DISS. ETH NO. 22230

3D EXPERIMENTAL INVESTIGATION OF THE HYGRO-MECHANICAL BEHAVIOUR OF WOOD AT CELLULAR AND SUB-CELLULAR SCALES

A thesis submitted to attain the degree of

DOCTOR OF SCIENCES OF ETH ZURICH
(Dr. sc. ETH Zurich)

presented by

ALESSANDRA PATERA

M.Sc. in Biomedical Physics, Università degli Studi di Torino

born on 18.02.1985
citizen of Italy

accepted on the recommendation of

Prof. Dr. Jan Carmeliet, examiner
Dr. Derome Dominique, co-examiner
Prof. Dr. Veerle Cnudde, co-examiner
Dr. Dominique Bernard, co-examiner

2014

Cover: Three-dimensional map of equivalent non-affine strains on the wood cell of Norway spruce softwood. Picture by Alessandra Patera and design by Andreas Rubin.

To my mother and my father, Matilde and Oronzo
To my beautiful niece, Annachiara
To my sister, Francesca

Tanto non mi importa quanto cielo dovrò strappare
Per coprire e accarezzare quel sorriso
Che neanche il mare sa di avere

Abstract

Many biological and engineering materials present a cellular structure, which provides them low density, high strength and high toughness. An exhaustive experimental and analytical investigation is carried out in this work in order to understand the response of these materials to environmental stimuli. This step is important in the context of evaluating their durability in different loading conditions. The focus is on softwood but the approach can be applied to other cellular materials. Wood is hygromorphic, responding to changes in environmental humidity by changing its geometry. The complex hierarchical structure of wood tends to deform during moisture sorption. The origin of the moisture induced deformation lies at the cellular and sub-cellular scales. High-resolution micro- and nano- X-ray tomography, combined with advanced tools for image analysis, are utilized to devise a solid non-destructive approach for the estimation of the swelling behaviour of softwood. Starting from the cellular scale, new findings in the anisotropic and reversible swelling behaviour of softwood and in the origin of swelling hysteresis in porous materials are explained from a mechanical perspective. Swelling due to moisture sorption displays also a non-affine component. A new sophisticated mathematical method for detecting locally the non-affine deformations in the cellular structure is presented in this work. The results highlight that the mechanical and moisture properties of wood highly depend on sub-cellular features of the wood cell wall. The experimental and analytical approach proposed in this thesis develops a line of research bridging the gap from sub-cellular to macroscale in cellular materials.

Riassunto

Molti materiali biologici e ingegneristici sono dotati di una struttura cellulare, che gli fornisce bassa densità, alta resistenza ed alta tenacità. In questo progetto, la risposta dei materiali a stimoli ambientali è indagata sperimentalmente e analiticamente. L'indagine rivela la sua importanza nella valutazione del tempo di vita utile (durata) dei sopra citati materiali, quando gli stessi sono soggetti a diverse condizioni di lavoro. Particolare attenzione è focalizzata sull'analisi del legno dolce (conifere); tuttavia, è possibile estendere l'approccio ad altri materiali cellulari. Il legno è un materiale igroscopico e reagisce, modificando la sua struttura geometrica, ai cambiamenti di umidità relativa. L'origine di queste deformazioni si estende su scale cellulari e sub-cellulari. Sistemi di micro- e nano-tomografia a raggi-X computerizzata ad alta risoluzione, in combinazione con metodi avanzati di analisi delle immagini, sono utilizzati per elaborare un approccio sperimentale non-invasivo sullo studio del rigonfiamento del legno. Su scala cellulare, nuove scoperte scientifiche sul comportamento anisotropo del legno, sulla sua reversibilità nel processo di rigonfiamento e sull'origine dell'isteresi in materiali porosi sono spiegate da un punto di vista meccanico.

Un nuovo e raffinato metodo matematico di registratura d'immagini non-affine è stato introdotto in questa tesi, per indentificare le deformazioni non-affini che occorrono localmente nella struttura cellulare del legno. I risultati mettono luce sull'intrinseca dipendenza del comportamento meccanico e igroscopico del legno da caratteristiche sub-cellulari della parete cellulare. L'approccio sperimentale e analitico proposto in questa tesi sviluppa una linea di ricerca in grado di superare il confine tra lo studio su scala sub-cellulare e quello su scala macroscopica in materiali cellulari.

Acknowledgment

Look deep into nature, and then you will understand everything better (A. Einstein). Four years ago I started my journey towards the incomprehensible and mysterious nature. I have not travelled in a vacuum in this journey, just in another country. And not alone, but with the support and encouragement of numerous people including my promoters, my family, my friends, colleagues and various institutions. This thesis represents the end of my journey in obtaining my Ph.D. At the end of my thesis I would like to express all my gratitude to all those people who made this thesis possible and an unforgettable experience for me.

First of all, I am extremely grateful to my research guide, my promoter Prof. Dr. Jan Carmeliet whose expertise, understanding, and patience, added considerably to my Ph.D. experience. He gave me the opportunity to work on this interesting and challenging topic and he helped me realize the power of critical reasoning. A very special thanks goes to my co-advisor, Dr. Dominique Derome, for all her energy, her enthusiasm, her encouragement, her inspiration and her great efforts to explain things clearly and simply. She makes me becoming an independent researcher but also a stronger person. I would like to thank her for all the fruitful hours spent together to talk about science and life. Under her guidance I successfully overcome many difficulties and learned a lot. I would like to thank her for being next to me in my difficult moments during these years. I will always keep in my heart all the support she gave to me in these moments. It was really precious for me!

I gratefully acknowledge the members of my Ph.D. committee: Prof. Dr. Veerle Cnudde and Dr. Dominique Bernard, for their time and interest in reading my thesis and for the fruitful discussions and suggestions on my work. I would like to acknowledge Prof. Dr. Anagnostou for accepting to be in my committee.

I am also extremely indebted to my former co-advisor, Dr. Michele Griffa, for providing necessary resources to accomplish my research work. I simply want to say ‘grazie’ to him for all these years, for his guidance and friendship. He has always been a valuable person to me!

A very important person for my Ph.D. that deserves more than one ‘danke’ is Stephan Carl. Without him, all my work on non-affine registration could not be so successful. He guided me during the programming part of the algorithm and he gave me always his essential technical support during all my beamtime at TOMCAT.

I want to say my thanks to Prof. Dr. Robert Guyer, from the University of Los Alamos, for all our fruitful discussion on hysteresis during his visits at EMPA.

I would like to kindly acknowledge Andreas Rubin for designing the cover of my PhD booklet.

During these four years, I had the opportunity to collaborate together with many researchers and technicians of my group and many other institutions. *In primis*, I would like to thank all the people of the Laboratory of Building Science and Technology. In particular, I would like to thank our secretary, Martina for all her efficient administrative work and for all her suggestions. I am really grateful to all my colleagues, Sreeyuth, Soyoun, Aytac, JaeBong, Marcel, Boran, Martin, Karol, Marc, Behrooz, Michela, Hannelore, Peter, Ahmad, Enrico, Vikram, George, Marcelo, Thijs, Ralph, Jonas, Kristina, Laurent, Guylaine, Andrea, Shanshan, Matthias, Roger, Viktor, Karim and all the people who gave me smiles and happy scientific and personal moments together. In particular, all the PhD students of my group, a big thanks for their friendship and for all our unforgettable moments out of the lab together.

I spent four intense years at EMPA, meeting a lot of people in the different laboratories. At EMPA, I met a lot of friends with whom I spent nice and funny moments. Starting from the beginning, I send a big hug to Renè, my first flatmate in the guesthouse, for helping me with the English and for his constant friendship through these years. To my first very good friend here, Brygida, thanks for everything! To Joanna, for the nice period we spent here together. To all my friends from EMPA and EAWAG, they are really a lot, but all of them gave daily an important contribution to let me feel at home, to give me moments of relax and for all our barbeque and party together. I am really happy to have still the opportunity to spend my time with each of you!

I want to thank Prof. Dr. Joris Van Acker, for letting me work in his group at the Ghent University, in Belgium, during a Short Term Scientific Mission in 2011. My gratitude goes in particular to Dr. Jan Van den Bulcke. We spent an intensive month together in the X-ray tomographic Centre, doing experiments days and nights. Chapter 6 is the result of our work together. I am really happy that I had the opportunity to meet Jan, nowadays not only a colleague but also a good friend.

I take this opportunity to sincerely acknowledge Prof. Dr. Marco Stampanoni. He has been supportive since the days I began working at the TOMCAT beamline, at PSI. All my gratitude goes to Marco for teaching me most of the theories related to the experimental part of my work and for providing insightful discussions about the research. I am extremely grateful to Dr. Rajmund Mokso for his scientific advice and knowledge. It is always nice to work with Rajmund and to learn from him! I would like to thank the TOMCAT group, in particular David, Konstantins, Anne, Gordan, Federica, Julie and Sally, for all their important support during the experimental work of my PhD and for being always nice with me. It is simply all my pleasure to become soon a member of this team!

I gratefully acknowledge the funding received towards my PhD from the Swiss National Science Foundation in the framework of the Sinergia project *“Multiscale analysis of coupled mechanical and moisture behaviour of wood”* under Grant number 125184. The project was also supported by the Swiss Federal Laboratories for Material Science and Technology (EMPA). Their supports are greatly acknowledged.

I take this opportunity to acknowledge my former professors from the Bachelor and Master studies, who encouraged me during these years of PhD every time I needed support. First of all, I would like to thank Prof. Dr. Giorgio De Nunzio, for his constant scientific support since the beginning of my PhD. My thanks go to Prof. Dr. Cristiana Peroni and Prof. Dr. Ferruccio Balestra, for helping me all the time before in Torino and then also when I moved to Switzerland and for supporting my enthusiasm towards research.

During these years, my family and my friends have always been there for me, for helping me in all the moments of my PhD and my life. Now, the main important people of my life deserve all my main important thanks directly from my heart.

First of all, my mother and my father…to give me this wonderful life and for surrounding my life with the most beautiful values, to give me all their love every single day since my birth! To make me smiling, loving, to give me energy, encouragement and freedom. To guide me all the time…and to give me the freedom to choose. Our love will never die! You’re the most beautiful thing of all

my life and I'll always fight to see you smiling, because your smiles make me smiling!
Thanks to my sister, Francesca, to be my best friend. Francesca, I know myself, but you know me more. I trust myself, but you trust me more. I love myself, but you love me more. Thanks for everything sis. A big thanks to her goes for the most important gift she gave me, my niece Annachiara. Her birth means really a lot for my life and for this Ph.D. Thanks to my brother in law, Salvo, for all your efforts in making the main important people of my life happy! Thanks for all what you've always done for me!

My thanks go to my second family, my best friends, Marco, Giancarlo, Tommaso and Andrea. I grew up with these four guys and they are really my brothers. I cannot imagine one day of my life without them. During these years, they shorten all the distances to support me in each single moment. My life is beautiful also because they are part of it! Especially my Marco, you were the one encouraging me the most since my school time. The one taking care of me during all my studies and all my life…with all your support and love. I will need you next to me for the rest of my life! Tommaso, although your 'vice-versa' skype camera, you're always there when I need to talk. Andrea and Giancarlo, you're my little big brothers…I really love you all guys, with all my heart! Thanks to all the group of friends from my hometown, in particular to Roberta, Maria Pina, Filomena, Dolores, Marco. To the group of friends from Torino, in particular to Anna, Claudia, Giuseppe, Daniele, Michele, Pierluigi, Rita, Flaviano, Shafiq, Marcello, Danilo. Thanks to my 'international' friend Ilenia. Thanks to Letizia. Thanks to all my colleagues from the University of Lecce and Torino and to my high-school friends, for being always an important part of my life. In particular, to the new mother, Marina, here all my best wishes.

Thanks to my cousin Danilo. Thanks to my guides in physics, my two cousins Maria Teresa and Luigi. Thanks to my wonderful cousins Anna Paola, Giuliana and Anna Maria. Thanks to my beautiful grandmother, 99 years old…the gold of our family. Thanks to my aunts and uncles, especially to zia Maria and zia Mimina…for being as mothers for me.

I want to acknowledge all the friends I met outside EMPA. I will always be grateful to my Italian group in Zurich, in particular to my little angel Elsa, to Giulio, Nadia, Marco, Matteo, Alice. A standing ovation for Francesco, firstly supporting me in Torino and now also in Switzerland. Our friendship is really beautiful… thanks for being always with me! I want to thank my two super crazy friends, Pierfrancesco and Andrea. It's thanks to them if I was always smiling in

the most difficult moments. I want to say thanks to the staff of the restaurant *Dialog* in Zurich, in particular to Pasquale, to give me the opportunity to not miss too much the Italian food with all his delicious dishes. I want to thank my ex-flatmate Eva, a good friend for me. And my current flatmate, Carmelo, *muu*!

The list of people who deserve my acknowledgment is really big. Besides this, several people have knowingly and unknowingly helped me in the successful completion of this project. They are really a lot in my life, to fulfil my life with joy and enthusiasm.

Before to conclude, I would like to spend some few words regarding my experience here in Switzerland during my PhD. I arrived in Switzerland four years ago, my first experience abroad. An unforgettable experience which let me growing up fast and happy! With a lot of efforts and a lot of bad days, I'm here…and today I know that there is nothing that counts the most to finish this journey with all the people who played a role next to me. Without all of them, my PhD could not be possible! My smile could not be possible!

Thank you for everything!

Alessandra

Nomenclature

This list of symbols is not exhaustive. Symbols that only appear locally in the text, or are self-explanatory, are not included. Scalar values are denoted with italic roman or Greek characters. In the text, vectors are indicated by bold characters.

Roman symbols

$\bar{\bar{A}}$	Affine matrix	-
$B_{l,m,n}$	B-spline functions	-
$\mathcal{C}$	Cost function	-
d_s	Sample diameter or thickness	μm
dx, dy	Artificial grid spacing	pixels
E	X-ray energy	keV
$g(x^{'})$	Object function	-
G_x, G_y	Artificial grid size	pixels
H	Entropy of the images	-
I	Intensity	number of photons
∇I	Gradient magnitude of the image	-
I_F	Fixed image	pixel×pixel
I_M	Moving image	pixel×pixel
$\bar{\bar{L}}$	Scaling matrix	-
m_a	Atomic molar mass	g/mol
N_A	Avogadro number	mol^{-1}
N_p	Number of pixels detector	pixels
$n_{x,y,z}$	Number of elements in the B-spline grid	-

p	Points in the artificial grid	-
$\mathcal{P}$	Penalty term	-
q	Filter function	-
$\bar{\bar{R}}$	Rotation matrix	-
$s_{x,y,z}$	Image size	pixel×pixel
$\bar{\bar{S}}$	Shear matrix	-
T	Transformation function	-
$\bar{\bar{T}}$	Translation matrix	-
T_{global}	Affine transformation function	-
T_{local}	Non-affine transformation function	-
$U(x)$	Displacement field	pixels
V	Volume	pixels^3 or μm^3
v_r	Reconstructed voxels size	μm^3
Z	Atomic number	-

Greek symbols

β	Swelling coefficient	-
β_α	Absorption term	-
γ	Penalty coefficient	-
ΔI	Intensity change in the image	-
δ_p	Phase shift term	radians
$\delta_{x,y,z}$	Spacing between control points	pixels
ε_{affine}	Affine strains	-
$\varepsilon_{n.a.,i}$	Non-affine strain components	-
η	Complex index of refraction	-
θ	Projection angle	°
θ_{beam}	Cone angle of X-ray beam	radians
$\theta_{\nabla I}$	Angle of gradient magnitude	°
λ	Wavelength	Å
$\xi_{x,y,z}$	Maximum number of iteration	-
$\Pi_{i,j,k}$	Control points of B-spline functions	-
$\Pi^{i,k}$	Feature points on the images	pixels
$\Pi^{j,l}$	Control points on the artificial grid	number of pixels

ρ	Density	g/μm^3
ρ_A	Atomic number density	(μm^3)$^{-1}$
σ_a	Absorption cross-section	μm^2
σ_p	Phase shift cross-section	μm^2
Φ	phase function	-
χ	Local minimum	-

Abbrevations

CT	Computed tomography	
ELW	Combined early- and latewood	
EW	Earlywood	
L	Longitudinal direction	
LW	Latewood	
M	Magnification	
MC	Moisture Content	
MI	Mutual information	
R	Radial direction	
RH	Relative humidity	
SSD	Squared pixel distance	pixel^2
T	Tangential direction	
TIE	Transport of intensity equation	

Table of Content

Contents

Chapter 1

Introduction

1.1 Background

Cellular structures, made of different materials and in different geometries, are found widely in nature and inspire the development of many artificial man-made materials. Examples of cellular structures in nature are wood, coral, plant steams, glass sponges, cork and cancellous bone. Wood and cork are honeycomb-like cellular materials with prismatic cells, somewhat like the hexagonal cells in bee honeycombs. Trabecular bones and plant parenchyma are foam-like cellular materials, with polyhedral cells. Man has made many artificial cellular structures, such as honeycomb-like materials used for lightweight aerospace, automotive and building components.

Cellular materials are made of an interconnected network of beams and/or plates resulting in a much lower density than the bulk material. The physical, mechanical and thermal properties such as density, conductivity, stiffness and strength of the bulk material can be dramatically changed by several orders of magnitude when organized into a cellular structure (Gibson and Ashby, 1999). Cellular solids can deform by the stretching or bending of the cell walls (Modén and Berglund, 2008). Most cellular materials are bending-dominated structures which are soft and absorb a lot of elastic energy during compression, while those that are stretching-dominated are much more weight efficient for structural applications (Ashby, 2013). The mechanical properties of cellular structures have been largely documented in literature (Gibson and Ashby, 1997).

Understanding the mechanical response of cellular materials subjected to environmental stimuli is crucial for optimum material design. The complex swelling behaviour of natural cellular materials with different architecture (e.g. geometrical heterogeneity, multi-layered cell wall, etc.) needs further investigations and the role of the geometry of cellular materials and cell wall composition on their hygro-mechanical properties should be assessed. Such study must be performed at cellular and subcellular levels to capture the exact mechanism at play. We focus here on the moisture induced swelling, with respect to their dimensional stability. In particular, moisture activated shape memory may be of interest in biomedical applications. Additionally, moisture variations such as buckling may cause undesired internal effects such as local deformations and even cracking due to an internal restraint of deformations. For these reasons, wood is an interesting material for setting up a sound experimental approach for studying the deformations at cellular and subcellular scales, such an approach can be also used for the study of other biological, cellular materials.

More specifically, this thesis aims at explaining experimentally the hygro-mechanical behaviour of wood, within a multi-scale approach. We adopted a non-invasive three-dimensional imaging technique to carry out our investigation, combined with sophisticated mathematical tools for in depth image analysis.

1.2 Sinergia Project: structure and objective of the research

This PhD project is part of SNF Sinergia project *"Coupled mechanical and moisture behaviour of wood"* which is introduced briefly in this section. The knowledge of mechanical and moisture properties of wood is crucial, since these properties determine to a great extent the durability and failure of wood elements exposed to varying mechanical and environmental conditions. For predictive purposes, computational models are used to forecast the relation between the applied loads (mechanical and/or moisture) and the respective hygrothermal and mechanical response. These computational models are mostly based on continuum mechanics, where wood is assumed to behave as a linear (visco) elastic (plastic) orthotropic continuum. However, when we realize that the particular behaviour of wood is driven by phenomena occurring at the cellular and sub-cellular levels, it is obvious that a continuum approach is a simplification of the real behaviour. Macroscopic mechanical and moisture properties of wood highly depend on lower level features such as cell geometry and orientation, or angle of the cellulose fibrils in the cell wall, which vary between growth rings. These features span the whole range of spatial scales, from nanoscopic (cell wall fibril aggregates), over microscopic (cell wall layers, cell geometry), and mesoscopic (growth ring of early- and latewood) to the macroscopic scale (wood). Therefore, macroscopic material properties, such as stiffness and moisture sorption isotherms (or moisture capacity), should be considered as apparent material parameters, which incorporate the physical behaviour of the different chemical constituents of wood, and their spatial arrangement in nano- and microscale geometry of cells and in growth rings composed of late- and earlywood. The relationship between the macroscopic apparent properties and the microscopic features is not fully understood to date. Furthermore, mechanical properties and moisture capacity are interrelated and such interaction is often in consistently taken into account in continuum models. As a consequence, the available continuum models may have a limited range of physical validity. In cases where microscopic details play an important role, a multiscale modeling approach is more appropriate, in order to understand the relative importance of microscopic features on the overall mechanical performance of wood. Multiscale models are basically a hierarchy of submodels, which describe the coupled mechanical and moisture behaviour at different spatial scales in such a way that the submodels are interconnected. The development of such models is a challenging task because of the following reasons:

- High resolution characterization of the geometry of wood at the nano- and microscale, which is a basis for multiscale modeling, depends on the resolution and the availability of advanced visualization techniques.

- Measurement of mechanical and moisture properties at lower scales is difficult to carry out and, although important technical improvements were recently made, few experimental techniques at sufficient low scales are yet available.

- Modeling of a natural material in 3D with realistic geometry at the micro- and nanoscale is not trivial.

The objective of this Sinergia research program was to investigate the relation between macroscopic mechanical and moisture properties of wood and its microscopic structure using a multiscale approach. Coniferous (softwood) species is the main type of wood used in building and civil engineering applications and presents a simpler structure than deciduous (hardwood) species. Thus, a softwood species, namely spruce (Picea abies), is considered as each species has a unique geometry, and cell dimensions, and different density. In terms of scope, the range of moisture loading is limited to the hygroscopic range (only adsorbed liquid, no bulk liquid) and mechanical loading is studied to the limit of failure (e.g. to the appearance of micro-damage). We will address wood from the macroscale of a few centimeters (10^{-2} m) to the nanoscale (10^{-8} - 10^{-6} m) which still includes subcellular features such as bordered pits and the different cell wall layers, is investigated. Contributions of the Sinergia project are improvements in the micro-meso-macro modelling and upscaling of a complex porous material, validation of the models at different scales by advanced experimental techniques, development of advanced experimental approaches for the combined study of moisture and mechanical loading and improvement of a macromodel to include nonlinear, hysteretic, and damage phenomena. The combination of such advancements allows to clarify the role of the nano- and micro-features of wood on its macroscale moisture and mechanical behaviour, which is crucial to ensure the durability of wood components exposed to varying environmental and mechanical loads.

1.3 Scope of the thesis

The main objective of the research presented in this dissertation is to develop a solid experimental and numerical method to investigate the physical behaviour of biological, natural and cellular materials at cellular and subcellular levels, such as wood. This PhD aims:

(1) To acquire high resolution 3D tomographic microscopy images of the cellular structure of Norway spruce (Picea abies) wood. High resolution X-ray tomographic images are acquired at TOMCAT beamline SLS, PSI Villigen and at the Centre of X-ray Tomography in Ghent University (UGCT).

(2) To investigate hysteretic swelling/shrinkage of wood under cyclic hygroscopic loading using an accurate image analysis techniques. We use 3D image registration algorithms for determining swelling/shrinkage strains from the tomographic datasets. In particular, we determine affine and non-affine strains, the former describing global deformations, while the latter local deformations occurring at cellular scale.

(3) In particular, to develop appropriate 3D image analysis techniques required for the study and the quantification of the non-affine deformations of wood at cellular and subcellular levels. The lumens surface during free swelling shows a form, which can be represented by a freeform surface. This freeform surface can be determined using control points connected together by a mesh. The surface is approximated using a control mesh guaranteeing a certain level of smoothness. Many representations of freeform surface exist in literature, but we use an approach of representing the free form deformation based on B-splines.

(4) To investigate the behaviour of some important sub-cellular features, such as bordered pits and middle lamella, by using nanotomography and to identify the influence of this behaviour on the swelling behaviour at cellular scale.

1.4 Outline of the dissertation

This dissertation consists of 9 parts and starts with a literature review in Chapter 2. Here, a general overview of wood as orthotropic material with its hierarchical structure is presented and the state of the art in experimental investigation of the physical behaviour of softwood is reviewed. An introduction to X-ray imaging of soft materials is given, together with a summary of currently available algorithms for imaging analysis.

The experimental procedures used in this thesis are described in Chapter 3. A main research gap is tackled with in Chapter 4, where an existing code for non-affine registration developed for medical applications is adopted in order to determine the non-affine deformations in the wood material.

In Chapters 5 to 8, the experimental results are presented and discussed. Chapter 5 presents the results related to homogeneous wood tissue, earlywood and latewood, during free swelling and an explanation for the origin of swelling hysteresis in wood is given. In Chapter 6, the swelling behaviour of combined wood tissues, composed of both earlywood and latewood of different density, is analysed. Chapter 7 describes the restrained swelling behaviour of wood and the impact of the restraint on the behaviour of wood at cellular scale, showing examples of cell wall buckling and moisture induced shape-memory. In Chapter 8, the investigation is downscales to subcellular level in order to investigate the role of singularities in the cell wall on the swelling behaviour of wood.

Chapter 9 summarizes the main conclusions of this thesis and presents recommendations for future research.

Chapter 2

State of the art

Wood in use, e.g. in material production, civil engineering and building applications, etc., is often subjected to mechanical and moisture loads which may lead to degradation and damage. Thus, a better knowledge of the hygro-mechanical behaviour of wood is important for improving the design of new and durable wooden components and structures. In addition, understanding the behaviour of cellular materials, such as wood, opens the doors for the development of new man-made materials.

This chapter describes first the hierarchical structure of softwood, a natural material. The interaction of wood with water and its anisotropic swelling behaviour are described. Then we introduce three-dimensional (3D) tomography as a tool of investigation of the swelling behaviour of wood. Finally, based on this overview, the needs for further research are pointed out.

2.1 Softwood, a natural cellular material

2.1.1 The structure of wood: from macro- to nano-scales

Wood is a natural cellular material with a complex micro-structural hierarchy. Wood is grouped into hardwood and softwood. Hardwood comes from angiosperm trees, like maple, birch, hickory, ash, oak, while softwood is wood from gymnosperm trees, i.e. conifers. Hardwoods and softwoods differ in their microscopic structure as the softwoods contain only two types of cells, tracheids and transverse ray cells. Hardwoods, however, have vessel elements that aid in water transport. In this work, the description covers the structure and properties of softwood, more particularly spruce (*Picea abies*).

Wood features and thus its material properties are orthotropic and we refer to the three orthogonal directions as: radial (R), tangential (T) and longitudinal (L), as shown in the wood structure (1) of Figure 2.1. The longitudinal direction is parallel to the long axis of the stem. The radial direction is perpendicular to both the growth rings and the long axis of the stem. The tangential direction is tangent to the growth rings. The softwood is composed by two types of cells, named tracheids (85-95%) and ray cells (5-12%). A typical softwood tracheid consists in 2-4 mm long and 0.01-0.10 mm wide hollow polyhedral tubes. The inner void volume of the cell is called the cell lumen and the material surrounding the lumen is named the cell wall. In temperate regions with seasonal climatic cycles, softwood tissues vary over the growing season, see growth ring (2) in Figure 2.1. During spring, the tissue, called earlywood, has thin cell walls and large lumens. Earlywood is usually light in colour and of low density. As the growth season progresses, the cells become smaller and the cell walls thicker. This part is named latewood and it is denser than earlywood. The region between earlywood and latewood may lead to transition wood.

Examining the earlywood structure, one can observe that the cell arrangement in the radial and tangential directions differs. The cells are assembled in straight rows in the radial direction and in a much more disordered way in the tangential one. This difference in cell arrangement leads to a lower stiffness in tangential direction compared to the one in radial direction. However, in latewood, the alignment of the cells and the higher density contribute to a more isotropic behaviour of this tissue. In other words, in latewood, the tangential and radial stiffness is similar.

In the living tree, the cells of the most recent growth rings, named sapwood, are active in transport of water from the root to the leaves and are usually water saturated. A valve-like feature, known as pit, see cell (3) in Figure 2.1, allows the passage of water in the tree by connecting cells. Aligned radially, ray cells are often organized in stacks of about ten cells, i.e. on top of each other in the longitudinal direction, and are only a single cell thick in the tangential direction. Inwards of this sapwood region, i.e. in the heartwood, there is no active water transport and the amount of water decreases, making lumens empty. In wood, as a building material, lumens are always empty.

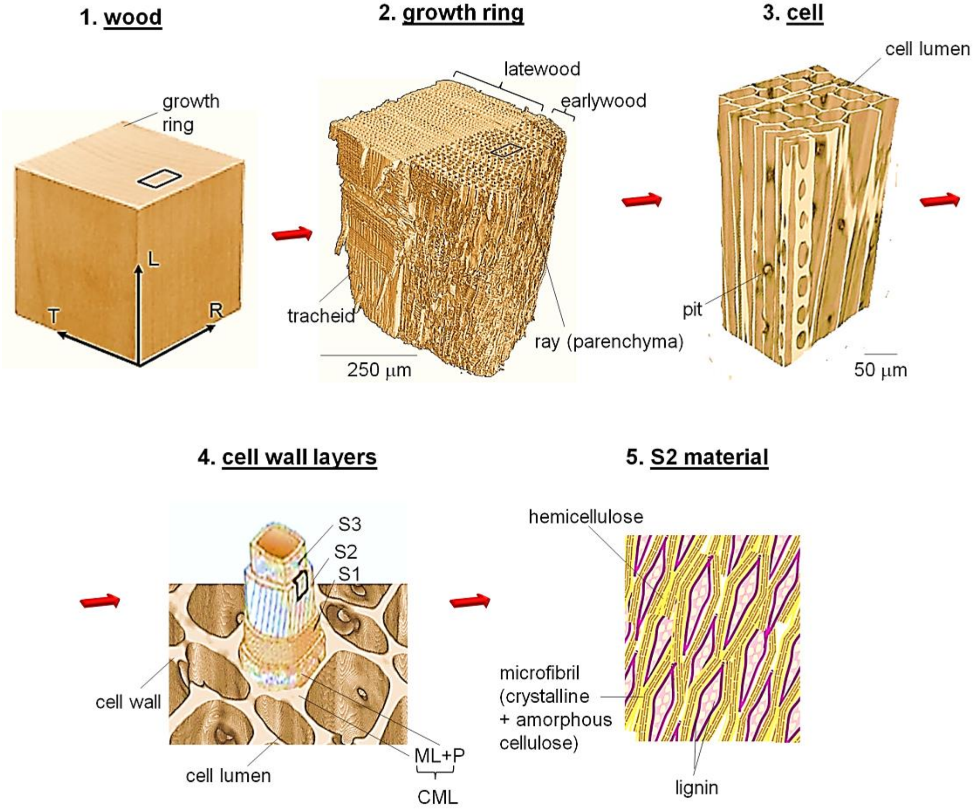

Figure 2.1: Schematic representation of the hierarchical structure of wood: from macro to micro scales, showing: 1. the growth ring, 2. the latewood and the earlywood tissues, 3. singularities in the cell wall, such as pits, 4. the cell wall layers and 5. the organization of the chemical components.

The softwood cell wall has a layered structure shown in (4) of Figure 2.1 which mainly consists of the primary wall (P) and the secondary wall (S), the latter is further composed of three layers: S_1, S_2 and S_3. Latewood has a thicker cell wall than earlywood due to the greater thickness of its S_2 layer, which is 1 to 2 μm in earlywood and 3 to 8 μm in latewood. The S_1 layer has a thickness of 0.2 to 0.5 μm in earlywood and 1 μm in latewood, while the S_3 layer is 0.1 to 0.2 μm thick in both tissues (Siau, 1995). As shown in Figure 2.1, the cell walls in wood are joined by an additional layer named middle lamella (ML) which holds the cells together. The P and ML layers of two adjacent cells are often considered as one, referred to as the compound middle lamella (CML).

The cell wall material can be regarded as a fibre-reinforced composite polymeric material as shown in (5) of Figure 2.1. The material consists of cellulose microfibrils, embedded in a polymeric matrix, oriented along the longitudinal direction with a slight angle in S_2 and with larger angles in S_1 and S_3. Two main constituents of the cell wall are the microfibrils, composed mostly of cellulose, and the cellular matrix, consisting mainly of hemicellulose and lignin. The hemicelluloses are amorphous polymers. Lignin is also amorphous but strongly branched. Lignin is present in the middle lamella and in the primary cell wall, but the largest quantity is found in the secondary cell wall (Srndovic, 2008). The wood anatomy leads to a pore structure with a very fine nano-pore distribution within the cell walls and middle lamella, with a surface area estimated to 300 m^2/g, and a second macro-pores system composed by the cell lumens linked via pits with surface area of about 0.2 m^2/g (Stamm, 1952). Furthermore, the polymeric components of wood have a very organised structure. The softwood microfibril is composed of cellulose crystals (3×4×30 nm) attached in single or multiple strips deposited parallel to each other during cell formation (Li and Renneckar, 2011). The cellulose microfibrils themselves are aligned and bound together into fibril aggregates or macrofibrils, of roughly 10-25 nm diameter. The cellulose microfibrils are running helicoidally along the cells. In the S_1 layer, the microfibrils are nearly perpendicular to the longitudinal axis of the cells. The orientation of the cellulose microfibrils varies in the different cell wall layers (MFA), typically from 10-30° to the vertical (longitudinal direction) in the S_2 layer to 70° in the S_3 layer (Dinwoodie, 1981). The mechanical properties of wood are strongly dependent on the microfibril angle within the S_2-layer. Large microfibril angles with the longitudinal direction result in low stiffness and high longitudinal shrinkage.

Further, the microfibril angle differs in both tangential and radial directions affecting the mechanical properties of the wood cell wall. The larger microfibril angles in the radial cell wall result in an increase in radial stiffness and a decrease in radial shrinkage (Holmberg et al., 1999).
The different features of the microstructure of wood give rise to a complex hygro-mechanical behaviour on larger scale.

2.1.2 Wood-water interaction: sorption and swelling

The properties of wood are strongly dependent on moisture content[1] (MC) in the hygroscopic regime. For Norway spruce, (*Picea abies* [L. Karst.]), which is the species under investigation in this thesis, the macroscopic swelling and shrinkage strains occur mainly between dry state and 28% moisture content and are known to be orthotropic. In this hygroscopic range, the moisture-induced deformation strains are typically in the order of 0.5% longitudinally, 4% radially and 6% along the tangential direction. Sorption in wood shows hysteresis between the adsorption and the desorption branches. The difference between the MC during adsorption and desorption for a given RH has been identified to be as high as 4% MC at mid-point of the hysteretic loop (Zillig, 2009). Water sorption is due to the presence of hydrophilic polymers making up the cell wall as they contain hydroxyl groups capable of attracting water molecules. The chemical groups which are highly attractive for the water molecules are called sorption sites and their affinity to water comes from their capacity to form hydrogen bonds with water molecules (Kollmann and Côté, 1968). The most sorption sites are found in hemicelluloses followed by cellulose and lignin (Christensen and Kelsey, 1959). It was found that the moisture content at RH=95% is around 50% for hemicellulose, 36% for cellulose (Beever and Valentine, 1958) and 23% for lignin.
The maximum amount of water, that can be accommodated within the cell wall is termed the fibre saturation point (FSP) is around 28% moisture content (MC) for softwoods, as measured intensively (Griffin, 1977; Hernandez and Bizon, 1994; Hill et al., 2005; Stone and Scallan, 1967). Higher moisture contents are due to the presence of liquid water in the

---

[1] Moisture content is the ratio of adsorbed water to the dry mass.

lumens. The equilibrium moisture content of wood is controlled by temperature (T) and relative humidity (RH). This dependence can be described by sorption isotherms. The sorption isotherm has a sigmoid shape and represents the equilibrium moisture states of wood with its surrounding environment achieved at constant temperature and relative humidity, in the hygroscopic range. The equilibrium moisture content is attained after either adsorption or desorption of water molecules. Higher temperature lowers the equilibrium moisture content of wood for a given relative humidity. As one example, we discuss Figure 2.2 which shows the main adsorption/desorption curves and desorption scanning curves.

Zillig (2009) measured the hygroscopic sorption and the water vapour permeability on spruce (Picea abies). All samples were cut from the same log. The hygroscopic sorption was determined by sorption tests at specified relative humidities, according to the standard EN ISO 12571 (2000). The samples were initially dried in an oven at 50°C and 10% RH. Afterwards, they were placed at constant conditions in desiccators over oversaturated salt solutions at 23°C. For each relative humidity, five samples were monitored until moisture content equilibrium. The main adsorption curve and several scanning desorption curves were determined. The measurement data are represented in Figure 2.2, a. As water adsorption and desorption occurs within the cell wall material, the cell wall and the overall cellular structure experience swelling and shrinkage, thus inducing swelling/shrinkage also at macroscale, as measured by Hernandez (1993). Figure 2.2, b shows that the swelling strains in the three orthotropic directions are almost linearly dependent on MC. Swelling strain hysteresis has been observed macroscopically, e.g. in the range of 1% for maple.

The source of swelling/shrinkage strains is attributed to the process of displacement of the polymer chains by the water molecules as they enter/exit the matrix of amorphous cellulose, hemicellulose and lignin. The cellular and the growth ring structures both affect the resulting moisture-induced deformations at the macroscale, as mentioned by Hernandez (1993).

Wood moisture sorption/desorption and swelling/shrinkage display hysteresis. Hysteresis of water sorption, in the hygroscopic range of wood, is related to a smaller number of hydroxyl sites available at a given RH to adsorb water molecules in adsorption than in desorption (Urquhart and Williams, 1924; Stamm, 1964). In greenwood (or wood from a living tree), water molecules are attached to the hydroxyl groups. When the wood dries, resulting in shrinkage of the wood, the hydroxyl groups are freed from water and start to bond to each other. During rewetting, most of the hydroxyl groups are not available anymore to the water molecules, resulting in less moisture adsorption compared to the amount of moisture present during the first desorption from greenwood state at the same relative humidity. With increasing moisture content, the swelling allows for the pairs of hydroxyl groups to break up again and eventually recover sorption sites. Thus, for the same relative humidity, there will be more water molecules remaining during desorption than during adsorption.

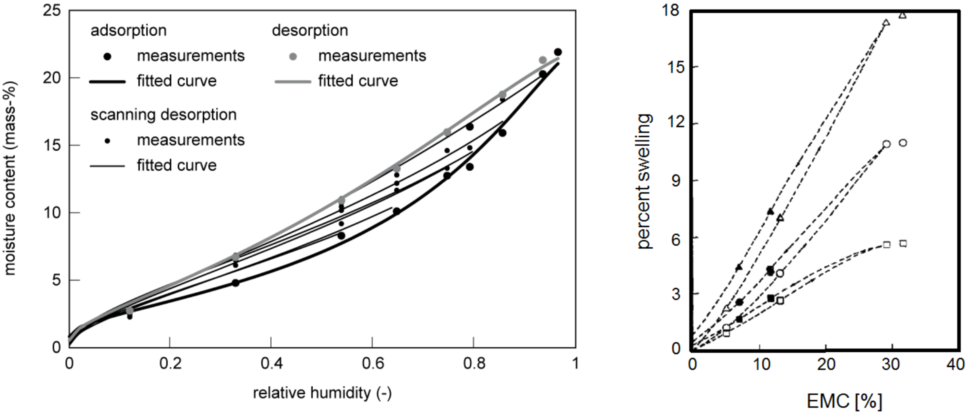

Figure 2.2: (a) Main adsorption and desorption curves of spruce wood and scanning desorption curves. Figure taken from Zillig, (2009). (b) Percent swelling of sugar maple as a function of the equilibrium moisture content at 25°C. Open and filled points correspond to adsorption and desorption states, while the upper, intermediate and bottom curves correspond to volumetric, tangential and radial swelling respectively. Figure taken from Hernandez (1993).

2.1.3 Anisotropic swelling behaviour of softwood

Wood swelling is found to be orthotropic. In earlywood, the swelling coefficient (β), defined as the slope of the linear relation of swelling strain (%) to moisture content (%), varies between 0.25 and 0.1, respectively in tangential and radial directions. In latewood, the values range between 0.2 and 0.5 in both directions. The combination of earlywood and latewood cellular tissues results in a layered material, with also orthotropic swelling properties. In Figure 2.3, swelling coefficients are plotted as a function of the relative density (density of wood normalized by that of the cell wall ρ=1500 kg/m^3) for softwood at different length scales. The data used in this figure, taken from Rafsanjani et al., 2013, are collected from different sources on softwood species (Vintila, 1939; Yao, 1969; Quirk, 1984; Watanabe et al., 1998; Pang and Herritsch, 2005; Derome et al., 2012). At cellular scale, anisotropy can be explained by the microfibril orientation and the particular cellular organization and structure. The microfibril angle can vary between radially and tangentially oriented cell walls, affecting the mechanical properties and swelling. The increase in the microfibril angle along the radially oriented cell wall results in an increase of the radial stiffness and a decrease of radial shrinkage. In earlywood, the cells are radially assembled in fairly straight rows, while tangentially they lie in a more disordered pattern. This cell arrangement in earlywood contributes to make the tangential stiffness lower than the radial one. Additionally, the ray cells act as reinforcement, resulting in an increase in the stiffness of the wood structure in radial direction (Holmberg et al., 1999). At macroscale, the anisotropic behaviour is explained as a result of the interaction between earlywood and latewood (Murata and Masuda, 2006). A computational upscaling approach of periodic honeycombs has been used to investigate the anisotropic swelling behaviour of two-dimensional cellular solids. Symmetric honeycombs show more swelling in tangential direction compared with irregular honeycombs. The alignment of cells in radial direction leads to a reduction of the swelling. As general conclusion, it has been observed that more geometrical disorder leads to less swelling anisotropy (Rafsanjani et al., 2012). It is known that the proportion of chemical components does not differ much between earlywood and latewood, (Bertaud et al. 2004, Johnson et al. 1961, Sundberg et al. 1996, Bertaud et al. 2002, Llyod 1978). The different hygro-mechanical behaviour of the earlywood and latewood cannot thus be explained based on chemical analysis.

The large volume fraction of the S_2 layer within the cell wall indicates that this layer may contribute significantly to the swelling behaviour. Swelling and shrinkage of the material composing the S_2 layer has also been investigated. A recent experimental investigation carried out on a pillar fabricated out of the S_2 layer material with high-resolution X-ray nano-tomography identified also an anisotropic behaviour of the S_2 layer. The anisotropy is found to be higher in the transverse plane of the cell wall and the swelling/shrinkage strains are larger in the direction normal to the cell wall compared to the direction parallel to the cell wall (Rafsanjani et al., 2014).

The orientation of the fibrils in the S_2 layer of the cell wall is a decisive factor for swelling and shrinkage (Požgaj et al. 1997; Perstorper et al. 2001). The longitudinal swelling/shrinkage is low due to the small deflection of the microfibril angle in the S_2 layer. The dimensional changes take therefore mainly place in the transverse plane (Perstorper et al. 2001). As a consequence, the swelling strains are the smallest in the longitudinal direction, amounting to 0.1–0.4%, while in the transverse direction the wood swells and shrinks more significantly, in the radial direction by 3–6%, in the tangential direction by 6–12%. The swelling in the different directions can be expressed by the following ratio: β_T: β_R: β_L = 20:10:1 (Niemz 1993; Niemz et al. 1993; Požgaj et al. 1997).

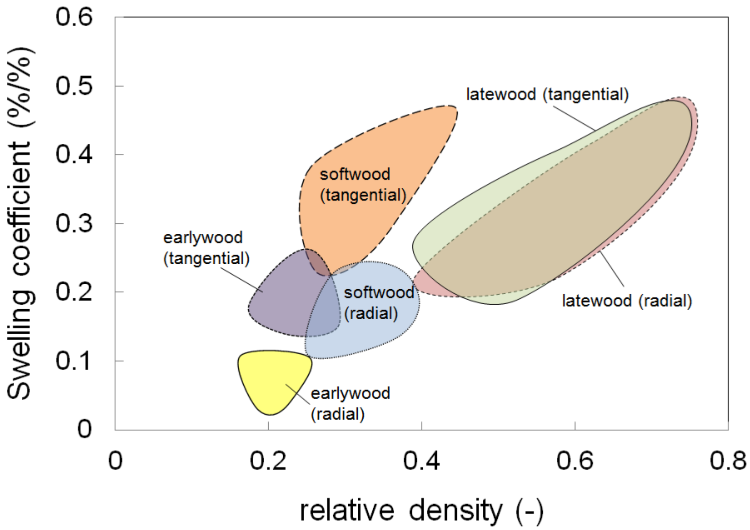

Figure 2.3: Swelling coefficients of latewood and earlywood for different softwood species and for different density. Figure adapted from Rafsanjani et al., 2013.

2.2 Characterization of swelling of wood

2.2.1 Experimental approach at different scales

Swelling and shrinkage of wood due to changes in MC have been measured at different scales. Traditionally, swelling is measured at the macroscale on samples (of a few cm size) exposed to change in RH. At growth ring level, local density and moisture-induced swelling behaviour of spruce wood samples have been investigated in 2D combining neutron imaging (NI) with digital imaging correlation (DIC) (Keunecke et al., 2012). It was found that the moisture induced strains largely depend on the wood density, the denser latewood part of the sample showing higher strains than earlywood.

At cellular scale, there are several studies addressing the dimensional changes of the material microstructure using 2D observational techniques, such as the environmental scanning electron microscopy (ESEM). In ESEM, the sample can be subjected to hygroscopic and mechanical loadings. However, only 2D information of the wood deformation of the outside surface is available (Turkulin et al., 2005).

The mechanical response of an orthotropic material such as wood to an applied load is inherently three-dimensional. Thus, two-dimensional visualization techniques for measurements of the deformation, such as (environmental) scanning electron microscopy and transmission electron microscopy, provide only partial information about the microstructure and the processes occurring in the material during loading, leading to limitations in the understanding of the complex behaviour of materials such as wood.

Understanding the moisture distribution in wood is important for evaluating its physical and mechanical behaviour. Tanaka et al. (2009) investigated the change in moisture content distribution in Japanese cedar (sugi) during drying using soft X-ray digital microscope.

However, wood exhibits a complex hierarchical structure at different length-scales, which requires a three-dimensional analysis. Therefore, 3D imaging of the wood micro-structure and its deformation becomes essential in understanding the hygro-mechanical behaviour of wood.

2.3 X-ray tomography: synchrotron and lab-based

X-ray computed tomography (CT), is a non-destructive technique to visualize objects three-dimensionally by combining the information of several projections acquired at different angles. The short wavelength of X-rays (ranging between 10 to 10^{-3} nanometers) provides high spatial resolution. X-rays with a wavelength longer than 1 Å (energies smaller than 12.4 keV) are called *soft X-rays*, while X-rays with a wavelength shorter than 1 Å are known as *hard X-rays*. Soft X-rays cannot penetrate as deeply into materials as hard X-rays, thus they are less suitable for investigating thick samples. X-ray tomography applications range from life sciences to materials science, including environmental and earth sciences.

A tomographic setup consists mainly in an X-ray source, a rotational stage and an X-ray detector. The latter is usually a photon flux measurement device where a scintillator detector detects the incident X-ray photons and converts them into visible light photons. The light is then collected and converted into an electrical signal by photodiodes. As the X-rays pass through the object, the beam intensity along any ray path connecting the source to a point on the detection plane is decreased compared with the propagation in the absence of the object. The decrease is due to the photon-matter interactions, mainly in the form of scattering and photoelectric absorption. Beer's law describes the macroscopic attenuation of the X-ray beam though a homogeneous material (Cnudde et al., 2013; Ingle et al., 1988; Beer, 1852). In the case of a monochromatic X-ray source, such laws states that

$$\mathrm{I} = \mathrm{I}_0 \exp(-\mu x) \tag{2.1}$$

with I_0 the beam intensity measured in the absence of the object, μ the linear attenuation coefficient for the material being illuminated and x the thickness of sample along the X-ray path. Considering a heterogeneous material made of a finite, discrete number of phases, Beer's law becomes

$$\mathrm{I} = \mathrm{I}_0 \exp[\textstyle\sum_i (-\mu_i x_i)] \tag{2.2}$$

where the sum is executed over the total number of material phases.

However, the attenuation coefficient is a function of the X-ray energy (E). Thus, the equation can be rewritten as an integral over the range of the X-ray spectrum:

$$I = \int I_0(E) \exp\left[\sum_i \left(-\mu_i(E) \boldsymbol{x_i}\right)\right] dE \qquad (2.3)$$

The main physical processes responsible for the macroscopic attenuation of an X-ray beam through a material within the typical hard X-ray energy range are the photoelectric absorption, Compton scattering and electron-positron pair production. The photoelectric effect occurs when the incoming X-ray energy is transferred to an inner electron causing its ejection. At higher photon energies, Compton scattering takes place. In this process, the incident photon is deflected from its original path by an interaction with an electron. The photon loses partially its energy, thus its wavelength increases. If a photon enters matter with an energy in excess of 1.022 MeV, a process called pair production occurs: an electron and a positron are created with the annihilation of the X-ray photon. Pair production becomes important only at energies above 10 MeV. In X-ray tomographic imaging of soft tissues, such as wood, the energy levels used range between 10 and 21 keV. At these energies, photoelectric absorption and Compton scattering are the two dominating effects.

A tomographic scan follows a two-step process: the acquisition of projections of the sample along the rays, at different angles while rotating the sample around an axis parallel to the vertical axis of the detection plane; the reconstruction, which calculates a 3D representation of the object, based on the projection images. A CT scan consists in the acquisition of three types of projection images (De Witte, 2010):

- *Dark fields*: Images acquired when the X-ray source is turned off. Such images contain the contributions of dark current and possible pixel offsets.
- *Flat fields*: the images I_0 acquired when the X-ray source is turned on but the sample is outside the field of view. This acquisition allows for the correction for spatial-temporal inhomogeneity in the X-ray beam profile.
- *Projections*: A set of projections is taken while rotating the sample at equiangular steps in a range of rotation of 180° for a short scan, used with parallel beam, or 360° for a full scan in the case of a conical beam.

These three types of projection images allow determining normalized projection images containing values between 0 and 1:

$$\mathbf{N(i,j)} = \frac{\mathbf{P(i,j)-D(i,j)}}{\mathbf{F(i,j)-D(i,j)}}, \tag{2.4}$$

where *N(i, j)* is the normalized intensity value of pixel *(i, j)* and *D*, *F* and *P* are respectively the dark field, the flat field and the projections.

Using an appropriate reconstruction algorithm, the projection images are used to determine a 3D representation of the sample, consisting of a certain number of volume elements (named voxels). Tomographic reconstruction can be performed with different methods. The linear attenuation coefficient μ in each volume element of the object can be calculated by the filtered back projection (FBP) algorithms (Smith, 1985).

Over the years, a new research field emerged in high-resolution X-ray tomography, called *micro-CT*. This method has been developed since the eighties using laboratory-scale X-ray source (Elliott and Dover, 1982; Elliott and Dover, 1985; Sato et al., 1981), gamma-ray sources (Gilboy, 1984; Gilboy et al., 1982) and synchrotron radiation (Bonse et al., 1986; Flannery et al., 1987; Grodzins, 1983). Important developments of synchrotron-based and laboratory-scale X-ray micro-CT can be mentioned. The high brilliant flux of synchrotron radiation results in a clear superiority in terms of achievable spatial resolution and signal-to-noise ratio (Baruchel et al., 2006), but the number of synchrotron facilities is limited due to their high cost. On the other hand, lab-based micro-CT systems have a lower X-ray flux but are more cost-efficient thus making desktop CT systems easier to access for a large number of researchers. More details on synchrotron and lab-based micro-CT follow.

Typical micro-CT setup: advantages and limitations

Synchrotron-based X-ray tomography provides 3D images with a spatial resolution 100–200 times larger than conventional medical CT systems. The main drawback of the technique, as well as in standard CT scans, lies in the sample size limitation, where the sample preferentially stands completely in the field of view (FOV) of the camera. In a synchrotron, electrons are accelerated to very high energies and injected in a quasi-circular storage ring, consisting of straight sections and bending or super-bending magnets. Third generation synchrotrons consist of different devices installed in the straight sections to produce photon fluxes and a monochromatic beam. When a particle is deflected from its original path, it loses energies by emitting high energy photons. These devices have magnets periodically positioned which force the electrons to follow a sinusoidal trajectory. Two types of magnets are commonly used: *undulators*, which produce a monochromatic beam and *wigglers*, which produce a polychromatic beam of high intensity.

Synchrotron radiation offers many advantages, making it a suitable tool for X-ray tomography. Firstly, it is highly brilliant. Brilliance is defined as the number of photons per second per unit source area, emitted per solid angle within a certain wavelength band. Normally, a wide energy spectrum of photons is obtained out of the electron acceleration. With appropriate methods and tools, it is possible to filter the spectrum within a very narrow bandwidth (ranging from eV to keV) such that the beam gets approximately monochromatic. The monochromaticity of the beam allows the quantification of the material properties and the identification of the different materials phases (Madonna et al., 2013) since beam hardening artefacts (Barrett and Keat, 2004) can be avoided. Further, its high collimation yields a more effective passage, through the sample towards the optical components with less radiation wasted. Also synchrotron radiation is spatially coherent. Spatial coherence allows measuring effects due to the wave nature of the photons, e.g., interference and diffraction effects, such as the diffraction produced by a circular slit. The monochromaticity and the high photon flux increase the image contrast and reduce the noise. All of these features result in high-resolution images, which allow the visualization and analysis of sub-micrometric details in μm-size samples.

The most common lab-based setup is the standard cone-beam micro-CT (Feldkamp et al., 1984; Turbell, 2001). In this configuration, the resolution is limited by the focal spot size of the X-ray source. A smaller focal spot size requires a reduced X-ray flux, making this system difficult and time-consumed. The conical beam geometry makes magnification possible, thus allowing the use of a wide range of technologies.

The non-destructive nature of the micro-CT method allows the investigation of the internal structure of an object without damaging it. In this way, it is possible to use the same sample for further analysis. This property is very important as it permits inspecting living objects, tracking down structural changes in a sample exposed to environmental changes (Rozenbaum, 2011; Van den Bulcke et al., 2009) or mechanical stress (Saadatfar et al., 2012; Zabler et al., 2008), also called *in-situ* CT.

However, several limitations in micro-CT systems have to be considered. In synchrotron systems, the voxel size is limited by the field of view, while at lab-based scanners it is dependent on sample size, X-ray source size, pixel size on the detector and magnification. A small sample size may lead to finite size effects or lack of representativeness in the response of the investigated system to the changes in the boundary conditions. Several imaging methods aim to overcome these difficulties, by enlarging the reconstructed area (Pfeiffer, 2004; Zamyatin et al., 2005), by reconstructing horizontally truncated data (Defrise et al., 2006; Vlassenbroeck, 2009) or by performing a mosaic scanning (Haberthür et al., 2010; Mokso et al., 2012), but the dependency of the voxel size on the sample size remains. Another effect that has to be considered in micro-CT is the sample positioning and the stability of the sample rotation. Optimal CT scanning requires a rigid and well-fixed sample which does not move during image acquisition. Additionally, due to the variety in sample size, shape and composition, no general protocols exist for micro-CT scanning. This implies that a wide range of parameters can be chosen, such as beam filtering, voltage, detector's exposure time, etc., which have to be optimized.

Although micro-CT is a powerful imaging tool, it presents also some limitations, such as noise, discretization effects and imaging artefacts. These effects are discussed next.

Like all imaging techniques, X-ray imaging is subject to noise. Image noise depends on many parameters, especially when a scintillator is used. Different software filters can be used to reduce noise in the reconstructed images. Another effect, called discretization, determines the limits of high-resolution X-ray CT, such as the lowest achievable voxel size as compared to the sample size. Due to the rotational movement, the sample can be approximated to a cylinder with a diameter d_s given by:

$$d_s = \frac{N_p o_p}{M} cos\, \theta_{beam} \qquad (2.5)$$

where N_p is the number of detector pixels, o_p the distance between the centre of two neighbouring pixels, M the geometrical magnification, defined as the ratio of the source-to-detector distance and the source-to-object distance and θ_{beam} the cone angle of the X-ray beam (Vlassenbroeck, 2009). In the case of a parallel beam, M=1 and $\theta_{beam} = 0$, the lowest achievable reconstructed voxel size v_r, or distance between the centres of two neighbouring pixels, is:

$$v_r = \frac{d_s}{N_p} = \frac{o_p}{M} \cos\theta_{beam} \tag{2.6}$$

All features smaller than this theoretical voxel size cannot be distinguished on the reconstructed dataset. The voxel size has not to be confused with the spatial resolution which is defined by the Modulation Transfer Function (MTF) of the complete imaging system, expressed in line pairs per distance unit. MTF can be theoretically defined as the response of the imaging system to sinusoids of different spatial frequencies. However, due to the complexity in defining the MTF, the voxel or pixel size is mostly used. Therefore, resolution can also refer to the number of pixels or voxels in an image.

Several types of artefacts can occur in tomography. Beam hardening is an artefact occurring with polychromatic sources, due to the energy dependence of the linear attenuation coefficient, which implies low-energetic (*soft*) X-rays to have a higher probability of being absorbed than high-energetic (*hard*) X-rays. This results in a *cupping effect*, which refers to the shape of a cross-sectional line profile with beam hardening. This effect can be reduced by using a beam hardening filter. Another artefact typical of cone beam geometry in lab-based CT is known as the *cone-beam effect*, which can be corrected by using an iterative reconstruction algorithm. In parallel beam, these two artefacts are reduced. Additionally, since the absorption signal is very small for soft materials, the contribution of the phase contrast signal to the projection image is no longer negligible. This phase signal, which is due to small angle refraction of the X-rays in the material, results in severe artefacts in the reconstructed slices when using conventional reconstruction algorithms for transmission CT. More information on phase contrast is given in the next paragraph. Several imaging and processing methods are suitable to benefit from this effect or to correct from phase effects (Boone et al., 2012; Cloetens et al., 1999; David et al., 2007; Weitkamp et al., 2011). Besides these major artefacts, other artefacts can occur: ring artefacts caused by failure of pixels in the detector (Sijbers and Postnov, 2004), streak artefacts due to highly attenuating inclusions (De Man et al., 1998), artefacts caused by sample instability or movements that cannot be completely removed, etc.

2.4 Acquisition of data: phase contrast on softwood

Despite the wide-spread use of absorption-based X-ray imaging, and its many applications, this technique is not ideal for all materials, especially light-element based materials, such as wood, as absorption is limited, providing poor contrast and spatial resolution. Furthermore, the absorption coefficients of soft tissue are very close to that of water, making it difficult to distinguish internal features and water in the light material (Paganin et al., 2002; Momose et al., 1996; Groso et al., 2006). In order to improve the contrast in X-ray imaging, phase contrast techniques have been developed in the last few decades for light elements. The phase shift cross section is a thousand times larger than the absorption cross section for light elements, indicating that the phase contrast technique is more sensitive to density variations than absorption based X-ray imaging. The absorption cross section, σ_α, of a target material is defined as:

$$\sigma_\alpha = (\mu/\rho) m_a / N_A \tag{2.7}$$

with μ/ρ the mass absorption coefficient, m_a the atomic molar mass and N_A the Avogadro number. When X-rays pass from one medium to another one, refraction is observed. Due to refraction, both the intensity and the phase of the X-ray beam are affected: the intensity is decreased along the incidence direction, because, by definition, some of the photons (the refracted ones) will travel along a different path than the incident one and the phase is shifted. One can calculate both absorption and phase shift from the complex index of refraction η, which is written for an homogenous material as:

$$\eta = 1 - \delta_p + i\beta_\alpha, \tag{2.8}$$

where δ_p is the phase shift term and β_α the absorption component. At wavelengths approaching a few angstroms, the real part can become larger than the imaginary part, meaning that phase contrast is more significant than absorption for hard X-rays. The two components can be written as following:

$$\delta_p = (\lambda/2\pi)\rho_A(\lambda r_0 Z) = (\lambda/2\pi)\rho_A\sigma_p \tag{2.9}$$

$$\beta_\alpha = (\lambda/4\pi)\rho_A\sigma_\alpha \tag{2.10}$$

where λ is the wavelength, $r_0=2.82\times10^{-15}$m is the Thomson scattering length (classical electron radius), Z is the atomic number, and ρ_A is the atomic number density (i.e., concentration of atoms per unit volume). From the equations of δ_p and β_α, the ratio between the two cross sections is defined as:

$$\sigma_p/\sigma_\alpha = (2\delta_p)/\beta_\alpha \tag{2.11}$$

In Figure 2.4, an example illustrates how a wave changes as it interacts with the material and how the ratio between the two cross sections decreases with increasing the atomic number. Figure 2.4, a, shows a plane wave which traverses a material with refractive index, η. This material absorbs a part of the wave, resulting in a change in amplitude, namely $\Delta|E|$. As the wave passes though the object the phase changes, $\Delta\phi$, resulting in a change in direction by the angle α. Figure 2.4, b, shows that phase contrast is beneficial for tissues which consist of materials of low atomic number (C, O and H), such as wood.

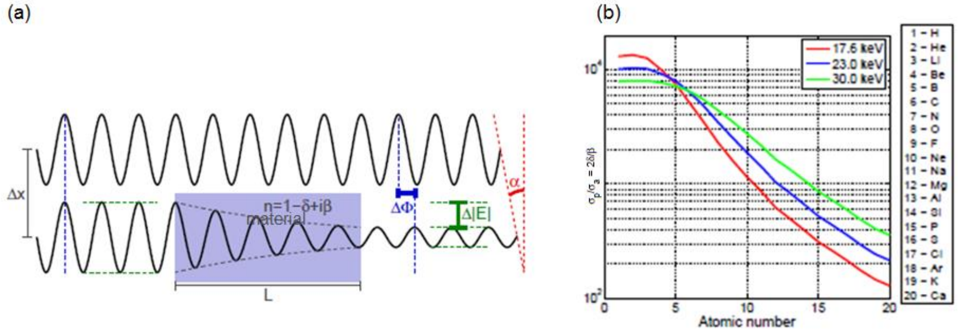

Figure 2.4: (a) Representation of the refractive index. (b) Ratio between the phase shift and the absorption cross sections plotted for various elements at various energies. Figure adapted from Jensen, 2010.

2.4.1 Algorithm of reconstruction using phase contrast information

Image reconstruction is a process that generates volumes from X-ray projection data acquired at different angles around the sample. Conventional CT reconstruction is based on the retrieval of the 3D distribution of the attenuation coefficient μ from its linear projections. Mathematically, a linear projection $P_\theta(x')$, also known as a *Radon transform*, of a function of two variables $g(\boldsymbol{x}) = g(x, y)$, is a projective transformation into the polar coordinate space (x', θ):

$$P_\theta(x') = \int_{-\infty}^{\infty} g(x)\delta_{Dirac}(x \cdot n - x')d^2x \tag{2.12}$$

where, $d^2\boldsymbol{x} = dx\,dy$, $\boldsymbol{n}$ is a unit vector normal to the projection beam forming an angle θ with one of the two axes of the reference frame of $g(\boldsymbol{x})$ and $\boldsymbol{x}$ is a vector on the projection beam. $\delta_{Dirac}(\boldsymbol{x})$ is the Dirac delta function.

This equation becomes, for a parallel projection data:

$$P_\theta(x') = \int_{-\infty}^{\infty} g(x, y)dy \tag{2.13}$$

where $g(x, y)$ is the object function in the transformed coordinates.

The 1D Fourier transform of the projection $P_\theta(x')$ in respect to the x' variable is found to be identical to the 2D Fourier transform of the object function $g(\boldsymbol{x})$ along a line passing through the origin of the 2D Fourier space and at angle θ. This is valid for a function of two scalar variables, which could be considered as an orthogonal slice of a function of three variables. This result is known as the *Fourier slice theorem* or the *central projection theorem*. Based on this theorem, the attenuation coefficient can be reconstructed and resolved in the form of a convolution (denoted by the asterisk) of the back-projection operator:

$$\mu(x, y, z) = \int_0^\pi d\theta \, q * g_\theta \tag{2.14}$$

where $\mu(x, y, z)$ is the 3D distribution of the attenuation coefficient and q is the filter function.

For low density materials, like wood, with low absorption contrast at all energies, conventional reconstruction methods have been improved by the introduction of phase-contrast imaging using the phase shifts in the X-ray beam rather than the differences in attenuation. Two methods based on phase contrast tomography are described below.

2.4.1.1 Modified Bronnikov algorithm (MBA)

When a monochromatic wave impinges upon a thin mixed phase-amplitude object with weak and almost homogeneous absorption, the intensity distribution at a small enough distance d is described by the Transport of Intensity Equation (TIE), (Teague, 1983; Peterzol et al., 2005; Langer et al., 2008):

$$I_\theta^d(x, y) = I_\theta^{d=0}(x, y)\left(1 - \frac{\lambda d}{2\pi} \nabla^2 \phi_\theta(x, y)\right) \tag{2.15}$$

where (x, y) are the coordinates on the detector plane, $I_\theta^{d=0}(x, y)$ is the beam intensity (after the normalization by the incident beam intensity, the so-called flat field cited before) measured at $d=0$, d being the distance from object to detector, θ is the projection angle, ∇^2 is the Laplacian with respect to the (x,y) variables. ϕ_θ is the phase function, which describes the cumulative phase shift induced by the object along a ray path from the source to the point of coordinates (x,y) on the detector plane. $\phi_\theta(x,y)$ is defined as:

$$\phi_\theta(x,y) = \frac{2\pi}{\lambda}\int_{raypath}\delta_p(x',y',z')dx'dy'dz' \tag{2.16}$$

When a plane wave impinges upon a sample, both the amplitude and the phase of the wave are perturbed. The TIE allows the retrieval of the phase information from intensity measurements only (Ishizuka et al., 2005). Eq. (2.15) can be written in the form:

$$\nabla^2\phi_\theta(x,y) = -\frac{2\pi}{\lambda d}\left[\frac{I_\theta^d(x,y)}{I_\theta^{d=0}(x,y)} - 1\right] = -\frac{2\pi}{\lambda d}g_\theta(x,y) \tag{2.17}$$

with

$$g_\theta(x,y) = \frac{I_\theta^d(x,y)}{I_\theta^{d=0}(x,y)} - 1 \tag{2.18}$$

Using the filtered back projection (FBP) and the Fourier slice theorem, an algorithm is derived by Bronnikov (Bronnikov, 1999; Bronnikov, 2006) and based upon the inverse Radon transform in higher dimension than what expressed in Eq. 2.13 allows for reconstructing δ_p:

$$\delta_p(x',y',z') = \frac{1}{4\pi^2 d}\int_0^\pi q * g_\theta d\theta \tag{2.19}$$

with g_θ the data function and q the filter function convolved with the data function. The filter function is defined as:

$$q(x,y) = \frac{|y|}{x^2+y^2} \tag{2.20}$$

The convolution between these two functions can be implemented in the Fourier domain by taking the two-dimensional Fourier transform. In the

Fourier domain, the filter function has the low-pass filter form given by (Bronnikov, 2002):

$$q(\xi,\eta)=\frac{|\xi|}{\xi^2+\eta^2} \tag{2.21}$$

In this filtered projection form, the reconstruction method suggested by Bronnikov is very interesting for a pure phase object ($I_\theta^{d=0}(x,y)=1$) since the 3D refractive index can easily be recovered from only one single tomographic dataset:

$$g_\theta(x,y)=I_\theta^d(x,y)-1,\theta\in[0,\pi] \tag{2.22}$$

The main assumption of this algorithm is that the object function g_θ is known. However, the ratio $I_\theta^d(x,y)/I_\theta^{d=0}(x,y)$ cannot be calculated in the case of a conical beam due to the change in magnification, except for a pure phase object (i.e. an object that only alters phase information). This problem has been solved by (Groso et al., 2006) by introducing a correction factor to the filter function:

$$q(\xi,\eta)=\frac{|\xi|}{\xi^2+\eta^2+correction\ factor} \tag{2.23}$$

This algorithm is called the Modified Bronnikov Algorithm (MBA). The correction factor can be calculated by using a semi empirical approach. A too small value leads to blurry results, while a too large leads to an elimination of the filter. Based on a single filtered projection, a good compromise can be obtained.

2.4.2.2 Paganin algorithm

The phase retrieval algorithm suggested by Paganin (Paganin et al., 2002) is based on the TIE as well and on the following assumptions:

(1) the object is homogenous and of known composition and density;
(2) the incident plane-wave radiation is monochromatic;
(3) the distance d between the object and the detector fulfills the near-field conditions.

To simplify the derivation of the Paganin algorithm, the point-source of X-rays is assumed to be at infinity ($d \rightarrow \infty$), as shown in Figure 2.5.

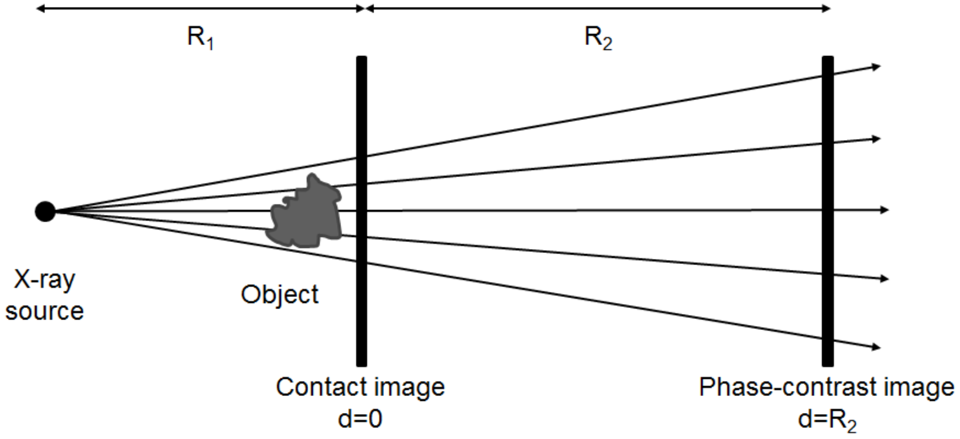

Figure 2.5: Scheme for phase contrast imaging using a point source. Paganin et al., 2002.

The Paganin algorithm is developed by taking the TIE as starting point, which describes the wave propagation (Teague, 1983):

$$\nabla_{\perp} \cdot \left(I(\mathbf{r}_{\perp}, d)\nabla_{\perp}\phi(\mathbf{r}_{\perp}, d)\right) = -\frac{2\pi}{\lambda}\frac{\partial}{\partial z} I(\mathbf{r}_{\perp}, d) \tag{2.24}$$

where $I(\mathbf{r}_{\perp}, d)$ indicates the intensity at distance d past the object and $\phi(\mathbf{r}_{\perp}, d)$ the cumulative phase shift phase, where $\mathbf{r}_{\perp}$ is the position vector in the x-y plane. Under the assumption of a homogeneous sample, the variation of phase and intensity can both be expressed in terms of variation of the thickness of the sample $d_s(\mathbf{r}_{\perp})$ in the plane perpendicular to the propagation direction:

$$I(\mathbf{r}_{\perp}, 0) = I_0 e^{-\mu\, d_s(\mathbf{r}_{\perp})} \tag{2.25}$$

and

$$\phi(\mathbf{r}_{\perp}, 0) = -\frac{2\pi}{\lambda}\delta_p d_s(\mathbf{r}_{\perp}). \tag{2.26}$$

The coefficients μ (linear attenuation coefficient) and δ_p (decrement from unity of the X-ray refractive index of the object material) are related to the complex-valued X-ray refractive index by Eq. (2.9) for δ_p and $\mu = 4\pi\beta_\alpha/\lambda$, where β_α is dimensionless. I_0 is the uniform intensity of the incident radiation.

By using the third assumption of near field conditions, $\partial I(\mathbf{r}_\perp, d)/\partial z$ can be approximated in the TIE by a 1st order finite difference equation. All these assumptions allow re-writing the TIE in terms of sample thickness:

$$\left(-\frac{R_2\delta_p}{\mu}\nabla_\perp^2 + 1\right)e^{-\mu\, d_s(\mathbf{r}_\perp)} = \frac{I(\mathbf{r}_\perp, d = R_2)}{I_0}. \tag{2.27}$$

This equation can be implemented using a Fourier transform and can be solved for thickness. Once the thickness is determined, the phase and the absorption can be calculated.

2.5 Image analysis

Datasets reconstructed with phase retrieval-based algorithms have better contrast and resolution, thus allowing achieving higher performance in image processing. There are several image processing techniques used in analysing images. The main two techniques are image segmentation and image registration, which are largely used for investing the behaviour of the material. However, prior to this analysis, tomographic datasets require a filtering procedure to make easier the segmentation. Examples of filters that are applied for reducing the image noise without removing significant parts of the image content are: non-local means, anisotropic diffusion or total variation (Gupta et al., 2005).

2.5.1 Segmentation of softwood cell-wall

Segmentation involves the classification of a picture element/volume (called *pixel* or *voxel,* for the whole volume) in different categories. In what follows, we will mainly refer to voxels, implicitly assuming that the same methods apply for pixels.

For the type of material investigated in this work, the two main categories are the solid phase of wood and air. Segmentation is important, for example, with respect to the accuracy in measuring volumetric swelling/shrinkage. One approach to image segmentation consists in classifying voxels based upon their grey value statistical distribution (histogram of grey values of voxels). The classification usually consists in finding thresholds for separating the overall histogram in different segments. In the case of only two voxel populations, the threshold leads to distinguishing a foreground (the solid material phase) from the background (the air). In this case, the segmentation is also called binarization. In thresholding-based image segmentation, it is important to select an adequate threshold value for extracting the object from its background. We present two methods, the Otsu (Otsu, 1979) and Bersen algorithm (Bernsen, 1986), based on a global and a local thresholding approach, respectively. Finally, we present two types of segmentation approaches called respectively region growing and active contour based on Chan-Vese algorithm.

2.5.1.1 Otsu algorithm: global thresholding

When a single threshold T is used to classify voxels independently of their spatial location within the image, the thresholding technique is called global. One such example is the Otsu algorithm based on the voxel grey value variance. The search of the optimal threshold relies upon a statistical analysis of the voxel grey value histogram. The statistical analysis is used to evaluate the ‘goodness’ of the threshold. Two variances are calculated once a guess of the threshold is found: the within-class variance and the between-class variance. A third variance, the intra-class variance, is defined as a weighted sum of the two classes’ variances:

$$var_{\varpi}^2(t) = \varpi_1(t)var_1^2(t) + \varpi_2(t)var_2^2(t) \tag{2.28}$$

where $\omega_{i\ ,\ i=1,2,}$ are the probabilities of the two classes being separated by a threshold t, and var_i the class variance. Otsu has shown that the problem of minimizing the intra-class variance in respect to the guess of the optimal threshold turns into a problem of maximization of the inter-class variance:

$$var_b^2(t) = var^2 - var_{\varpi}^2(t) = \varpi_1(t)\varpi_2(t)[\mu_1(t) - \mu_2(t)]^2 \qquad (2.29)$$

with μ_i the class average value. The class probabilities and the class averages are iteratively updated while new guesses of t are tried.

2.5.1.2 Bernsen algorithm: local thresholding

The main advantage of the Bernsen method, compared to the Otsu method, is that it is locally adaptive, i.e., it takes into consideration the grey voxel value distribution within the neighbourhood of a given target voxel, for each voxel in the image. In this method, local thresholds are calculated over neighbours and based on the voxel-wise average value, i.e., the average of the maximum, $I_{high}(i,j)$, and the minimum, $I_{low}(i,j)$, values within the local neighbourhood, where $I(i,j)$ represents the grey voxel value. If the contrast $C(i,j) = I_{high}(i,j) - I_{low}(i,j)$ (2.30) is below a certain threshold, then the neighbourhood consists of only one class defined as background or foreground, depending on the threshold value, obtaining a binarized image.

2.5.1.3 Region Growing

Another image segmentation method used in this work is known as region growing. The algorithm considers an initial “seed point”, from which a region (also called “blob”) grows, incorporating all the nearby voxels which respect certain criteria of mutual connectivity. In this way, all the voxels which follow similar criteria are added to the initial volume. The region growing algorithm used for this work is implemented in 3D in VG Studio MAX 2.0, a software for image analysis and visualization. More details on the algorithm can be found in Petrou & Bosdogianni, 2004 and in Patera et al., 2007.

2.5.1.4 Active contour based on Chan and Vese algorithm

A method for segmenting images was developed by Chan and Vese, 2001. This is a powerful and flexible method which is able to segment many types of images, including some that would be quite difficult to segment in means of "classical" segmentation – i.e., using thresholding or gradient based methods. The basic idea in active contour models or snakes is to evolve a curve, subject to constraints from a given image, in order to detect objects in that image. For instance, starting with a curve around the object to be detected, the curve moves toward its interior normal and has to stop on the boundary of the object.

2.5.2 Image registration

The analysis of body motion (deformation) is one of the more actively studied areas of image processing and computer vision. Motion analysis can be applied in different fields, including the extraction of camera motion, robot navigation, image registration, etc. (Szeliski and Coughlan, 1997). The common problem is to detect correspondences between regions in difficult images. We refer to this problem as image registration.

In this context, registration is a very important technique to match two or more images taken at different times or conditions. A broad range of registration methods have been developed over the years.

Image registration consists also in finding a geometrical transformation which tries to spatially align different images using to the minimization of a matching error, i.e. the distance measured between two images. In the last ten years, several approaches have been developed.

We first introduce some basic terminology.

<u>Target, fixed or reference image</u>: the image that is kept unchanged and is used as the basis for comparison.

<u>Source or moving image</u>: the deformed or geometrically transformed image, which has to be aligned with the target image.

<u>Transformation</u>: the function used to align the source with the target image.

Since large amounts of images can exhibit different degradation levels due to artefacts, noise, etc., it is difficult to outline a universal method applicable for any registration task.

Preliminary steps before proceeding to image registration may include:

<u>Pre-processing</u>: smoothing, deblurring, edge detection, segmentation, etc.

<u>Feature detection</u>: extracting points, lines, regions. These features are also called control points.

The determination of the specific location of features in images (target and source) must be as accurate as possible and the detection must not be sensitive to image degradation. The quality of the *feature matching* impacts strongly the performance of the registration procedure. A *transformation function* uses the coordinates of the control points to find the correspondence between the two images.

In 3-D, the coordinates of control points are given by:

$$\{(x_i, y_i, z_i), (X_i, Y_i, Z_i): i = 1, \dots, N\}$$

where

$$\begin{aligned} X_i &= f_x(x_i, y_i, z_i), \\ Y_i &= f_y(x_i, y_i, z_i), \\ Z_i &= f_z(x_i, y_i, z_i), \qquad i = 1, \dots, N. \end{aligned} \tag{2.31}$$

The general problem of image transformation is to find a single-valued function that interpolates or approximates

$$\{(x_i, y_i, z_i, f_i): i = 1, \dots, N\}.$$

A component of a transformation function can be represented by a variety of functions. The type of function selected should depend on the type of geometric difference between the two images and the accuracy of the feature extraction and points matching procedure.

In the following, we describe a linear transformation function called affine transformation.

2.5.2.1 Affine transformation for the estimation of the global strains in wood

The most commonly used registration transformation is the affine transformation, where changes in position, size and shape of a volume are described. The parametrization of a 3D affine transformation involves twelve parameters (three for defining translation, three for rotation, three for scaling and three for shear), which describe the function f, which relates each point $\bar{x}$ of the reference image to the corresponding point $\bar{x}' = f(\bar{x})$ of the moving image. The affine registration model is described by:

$$\bar{x}' = f(\bar{x}) = \bar{\bar{A}}\bar{x} + \bar{T}, \tag{2.32}$$

where $\bar{\bar{A}}$ is a 3×3 matrix of real numbers and $\bar{T}$ a column vector of R^3. The affine transformation is global in the sense that its parameters are independent from the image location. $\bar{\bar{A}}$ gives the contribution of shear, scaling and rotation and can be decomposed into the product of three matrices, while $\bar{T}$ is referred to the translation factor, as schematized in Figure 2.6.

In more details,

$$\bar{\bar{A}} = \begin{pmatrix} A_{11} & A_{12} & A_{13} \\ A_{21} & A_{22} & A_{23} \\ A_{31} & A_{32} & A_{33} \end{pmatrix} = \bar{\bar{S}} \cdot \bar{\bar{L}} \cdot \bar{\bar{R}} \tag{2.33}$$

$\bar{\bar{S}}$, $\bar{\bar{L}}$ and $\bar{\bar{R}}$ are respectively the shear, scaling and rotation matrices given by:

$$\bar{\bar{S}} = \begin{pmatrix} 1 & S_{12} & S_{13} \\ S_{21} & 1 & S_{23} \\ S_{31} & S_{32} & 1 \end{pmatrix}, \tag{2.34}$$

$$\bar{\bar{L}} = \begin{pmatrix} L_1 & 0 & 0 \\ 0 & L_2 & 0 \\ 0 & 0 & L_3 \end{pmatrix}, \tag{2.35}$$

$$\bar{\bar{R}} = \begin{pmatrix} R_{11} & R_{12} & R_{13} \\ R_{21} & R_{22} & R_{23} \\ R_{31} & R_{32} & R_{33} \end{pmatrix} = \overline{\overline{R_1}} \cdot \overline{\overline{R_2}} \cdot \overline{\overline{R_3}} \tag{2.36}$$

where $\overline{\overline{R_1}}$, $\overline{\overline{R_2}}$ and $\overline{\overline{R_3}}$ are the rotation matrices respectively along the three axes, using the Euler angles formulation for rigid rotation (Goldstein, 2002). Using a homogenous coordinate system (indicated by the symbol "~"), we obtain:

$$\bar{x}' = f(\bar{x}) = \bar{\bar{A}}\bar{x} + \bar{T} \Longrightarrow \tilde{\bar{x}}' = \tilde{f}(\tilde{\bar{x}}) = \tilde{\bar{\bar{A}}}\tilde{\bar{x}} \tag{2.37}$$

where

$$\bar{\bar{A}} = \begin{pmatrix} A_{11} & A_{12} & A_{13} & T_1 \\ A_{21} & A_{22} & A_{23} & T_2 \\ A_{31} & A_{32} & A_{33} & T_3 \\ 0 & 0 & 0 & 1 \end{pmatrix} \tag{2.38}$$

The coefficients along the main diagonal are related to the main strain tensor. In fact, the affine registration model assumes that each component of the displacement vector field, $U_{l,i\rightarrow j}(\bar{x}), l = 1,2,3$, is a linear combination of the spatial variables, meaning that the strain tensor components are constant over the domain of interest. Under the approximation of small displacement gradients, it turns out that:

$$\varepsilon_{affine,11} = \frac{\partial U_{1,i\rightarrow j}}{\partial x_1} = A_{11} - 1, \tag{2.39}$$

$$\varepsilon_{affine,22} = \frac{\partial U_{2,i\rightarrow j}}{\partial x_2} = A_{22} - 1, \tag{2.40}$$

$$\varepsilon_{affine,33} = \frac{\partial U_{3,i\rightarrow j}}{\partial x_3} = A_{33} - 1, \tag{2.41}$$

where $\varepsilon_{affine,11}$, $\varepsilon_{affine,22}$ and $\varepsilon_{affine,33}$ are the main affine strains along the three axes.

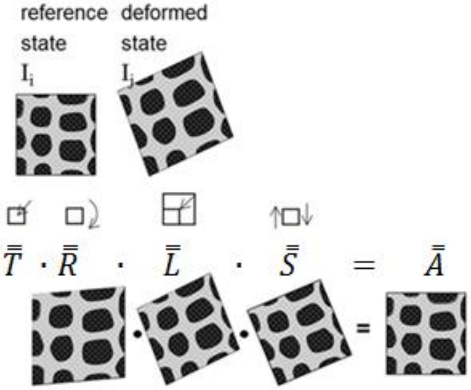

Figure 2.6: Schematic representation of the affine registration procedure for calculating the principal swelling/shrinkage strains by applying an affine transformation matrix composed of R (rotation), L (scaling) and S (shear) matrices, after applying the T (translation) vector.

The affine registration is a good approximation for describing global deformations. However, the occurrence of local deformations is not captured with this model. For this reason, we will introduce a non-affine registration model in Chapter 4.

2.6 Needs for further research

The origin of the anisotropic swelling behaviour of a natural and cellular material like wood cannot be understood at the macro-scale since its origin lies at the cellular and sub-cellular scales. Investigations on wood are carried out since many years, but only recent developments in 3D microscopy allow more detailed investigations, which allow the study of the role of geometry and the material behaviour of the cell walls. Robust methods for image acquisition and image analysis are needed. These methods allow to explore anisotropic moisture induced deformations of cellular microstructures. The relation between material structure and hygro-mechanical behavior of biological materials is not yet completely understood. This thesis aims at introducing a robust method for investigating the hygro-mechanical behaviour and its link to the complex matrix of structure of soft cellular materials, such as wood.

Not only an experimental approach has to be defined for accurate image acquisition, but also appropriate algorithms for image analysis and image registration have to be developed, which allow the investigation of the global and local deformations in complex-shaped materials such as wood.

Chapter 3

Experimental procedure

In this thesis, a typical experimental setup consists of a chamber with controlled environmental conditions to house the wood sample and an X-ray tomographic microscopy. The experimental work presented in this thesis has been performed at the TOMCAT (TOmographic Microscopy and Coherent rAdiology experimenTs) beamline of the Swiss Light Source (SLS), PSI Villigen and at the Centre for X-Ray Tomography of the Ghent University (UGCT) in Belgium. The wood samples can be subjected to different environmental conditions. Different configurations to fully investigate the cell wall structure, the cell features and wood behaviour during hygroscopic loading in free or restrained swelling conditions are designed and presented in this chapter. The design and manufacturing of the restraining device are presented. To complete the information acquired by imaging, the actual moisture content in the wood cell wall at different environmental conditions is measured by vapour sorption analysis. Thus, to conclude, the dynamic vapour sorption apparatus is described.

3.1 X-ray tomography on softwood: the different configurations

The identification of anatomical and physical properties of wood is important in wood science and technology (Mäkinen et al., 2008) and relies mainly on procedures performed at the microscale. The conventional approach consists of a microtome, a light microscope with a camera mounted on the top and an image analysis software. The anatomy and behaviour of wood has been documented in literature by using more advanced techniques such as SEM (Scanning Electron Microscopy), TEM (Transmission Electron Microscopy), AFM (Atomic Force Microscopy), CSLM (Confocal Scanning Laser Microscopy), etc. The main disadvantages of these techniques are the loss of three-dimensional information and the time required to obtain quantitative information. In addition to the aforementioned techniques, we mention X-ray tomography, which is extensively used in this work. It is a technique used in several research disciplines from the medical field (Fu and Kuduvalli, 2008), soil science (Taina et al., 2008), hydrology (Wildenschild et al., 2002), entomology (Fuchs et al., 2004), plant physiology (Lee and Kim, 2008) and material science (Cnudde and Jacobs, 2004). The wide range of applications has been made possible due to the recent improvements in terms of image quality, imaging speed and deposited radiation dose.

In the last thirty years, micro-CT, either lab-based or synchrotron, has become mainstream in biological material research. Lab-based micro-CT systems (Jakubek et al., 2006; Masschaele et al., 2007) have lower flux but are more affordable. The most commonly used lab-based X-ray setup is the standard cone-beam micro-CT (Feldkamp et al., 1984; Turbell, 2001), in which the conical beam provides a magnification of the sample located at any position between X-ray tube and detector (Figure 3.1 (a)). The detector may rely on different technologies, such as an amorphous silicon (a-Si) flat-panel detector combined with a relatively thick scintillator screen to obtain a high dynamic range. In this case, the achievable resolution is limited to the focal spot size of the X-ray source. Small spot sizes (below 1 μm) reduce the X-ray flux, resulting in high resolution micro-CT (<1 μm). However, due to the low signal-to-noise ratio and the low flux, they need a long exposure time and are therefore very time-consuming. Long scanning time produces instabilities in conditioning the samples, especially, as is here our case, where softwood samples are located in an environmental chamber and scanned after achieving a steady-state equilibrium at different relative humidity.

As synchrotron source has a high X-ray flux, but the X-ray beam is almost parallel, making geometrical magnification impossible without X-ray optics. The X-ray beam passes the monochromator, for selecting an energy with a certain bandwidth (Cnudde et al., 2013). This high flux can be detected by a thin scintillator screen, converting the X-rays to visible light (Figure 3.1 (b)). Geometrical magnification can be achieved with this configuration using Fresnel Zone plates (Chao et al., 2005; Chu et al., 2008), resulting in very high resolution.

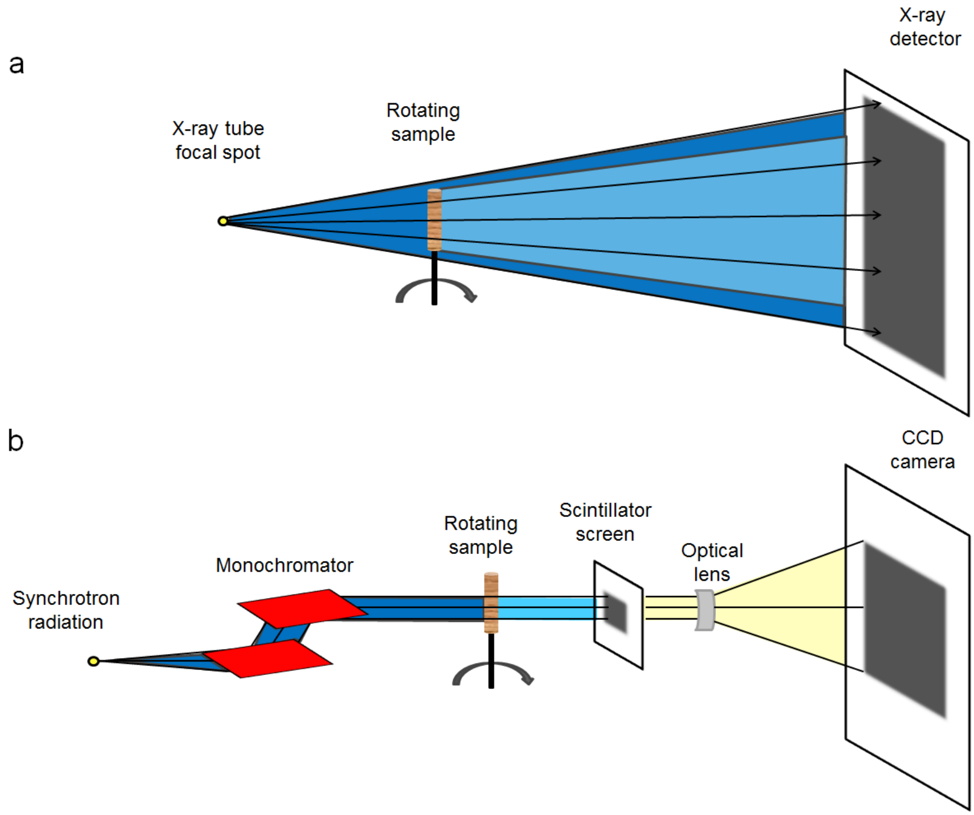

Figure 3.1: Schematic diagrams (a) of a typical lab-based micro-CT setup with a conical X-ray beam, (b) of a typical synchrotron-based micro-CT setup (from Cnudde et al., 2013)

Conventional tomography provides a 3D distribution of the local linear attenuation coefficient, which is stored as a stack of 2D slices equally spaced. By acquiring projection images from different directions, a 3D volume is reconstructed using a dedicated computer algorithm. After imaging acquisition and reconstruction, tomographic imaging analysis software is used to obtain quantitative results. The results can include anatomical analysis, revealing the cell wall features of softwood, and the observation of the physical properties of the samples under investigation. However, before starting with the imaging analysis, most of the reconstructed tomographic volumes require a pre-processing procedure which takes into account the limitations of the experimental setup and of the imaging tools adopted.

3.1.1 Lab-based tomography

UGCT (Centre for X-ray Tomography of the Ghent University) provides a unique combination of a top-quality high resolution PCXTM (Phase Contrast X-ray Tomographic Microscope) facility, specifically customized for investigating wood microstructure, and of a phase contrast tomographic image reconstruction software platform (Octopus) which gives access to the control of the reconstruction parameters. The lab-based micro-CT facility provides 3D dataset of samples within 1-2 hours of X-ray scanning and data reconstruction, as described in Masschaele et al., 2007. The main components of the CT scanner are the X-ray tubes, the sample stage and the X-ray detectors, see Figure 3.2. A motorized stage can be combined with either of the two X-ray tubes and either of the two X-ray detectors. Thus, two configurations are possible, one for high resolution up to 900 nm and one for the acquisition of large samples (up to 37 cm in diameter). The two detectors used during the experimental work are:

- Varian Paxscan 2520: with CsI scintillator, 1820x1460 pixels of 127µm pixel pitch;
- Photonic Science VHR: with thin gadox scintillator, 3600×3200 pixels of 7.74 µm pixel pitch.

The flexibility of the system allows choosing arbitrarily the reconstructed voxel size which can be selected within the range 200 µm to 50 nm. The X-ray source, a nano-focus tube, can reach a focal spot size of 1 µm. This configuration is used during the experiments presented in Chapter 6. More details on the experimental setup can be found in Dierick et al., 2014.

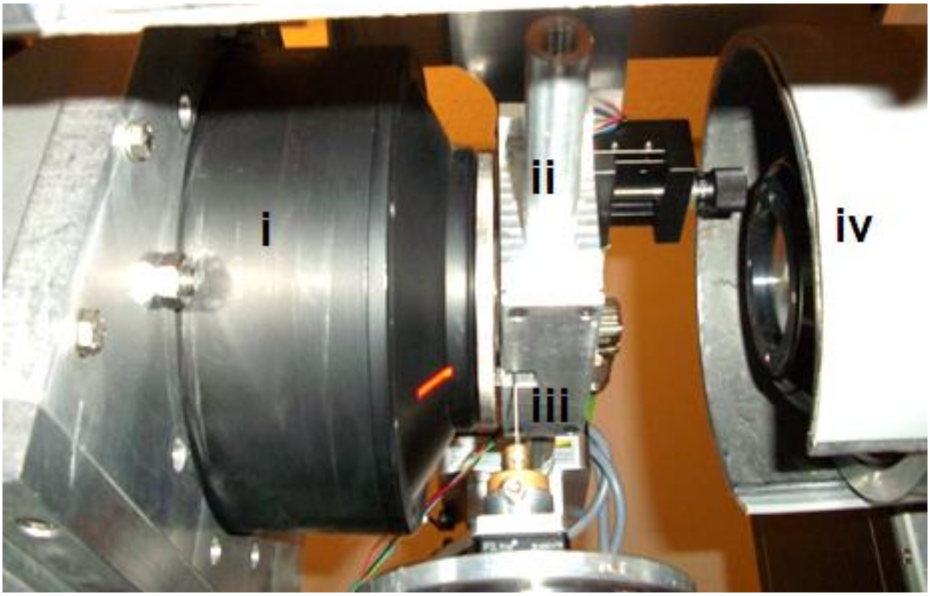

Figure 3.2: X-ray tomographic setup at UGCT, showing (i) the end of the X-ray tube, (ii) the environmental chamber, (iii) the wood sample and (iv) the detector.

3.1.2 Synchrotron-based micro-CT

A better contrast, higher resolution and faster imaging time can be achieved using synchrotron light than with lab-based setups. In particular, the photon density of third generation synchrotrons brings huge advantages compared with the traditional laboratory setup. Synchrotron radiation yields electromagnetic radiation characterized by a much higher brilliance, which provides increased spatial and temporal resolution to resolve details as small as 1 micron in millimetre-sized samples within few minutes.

3.1.2.1 TOMCAT beamline

Synchrotron radiation tomographic datasets were acquired at the TOMCAT beamline at the SLS of PSI, Villigen, Switzerland. The source is a 2.9 T bending magnet with a critical energy of 11.6 keV, which provides a photon flux between 8 and 45 keV. A double crystal multilayer monochromator (DCMM) is used to select X-rays with defined X-ray photon energy, i.e. for the TOMCAT, ranging between 12 and 20 keV. The monochromaticity of the X-ray beam makes quantitative measurements of material properties possible and vastly simplifies the identification of different phases, since beam hardening artefacts, distinctive for lab-based setup, can be avoided. Furthermore, monochromatic and high photon flux increases the contrast and reduces the noise. The almost parallel beam geometry common for synchrotron radiation tomography permits the accurate reconstruction of the volumes without cone artefacts.

The small source size (Σ_x=53 μm, Σ_y=16 μm), coupled with the high quality of the optical components, guarantee a highly transversally coherent beam even for TOMCAT, a rather short beamline (Marone et al., 2011). The coherence of the beam ensures that different imaging modalities can be exploited, enabling the optimal investigation of both low and high absorbing samples. In fact, an alternative to absorption tomography, phase contrast imaging is the best option for low-absorbing materials such as wood. Generally, the interaction of X-rays with materials directly depends on the atomic number. As wood is composed of approximatively 50% carbon, 44% oxygen and 6% hydrogen, thus elements with small atomic number, its interaction probability is small, which necessitates the utilisation of low beam energies for investigations (Mannes et al., 2010) and phase contrast imaging.

The photon intensity is detected by a scintillator-CCD-camera system. The TOMCAT X-ray detector consists of a Ce-doped $Y_3Al_5O_{12}$ single crystal scintillator able to convert the X-rays into visible light. This light then passes through an optical microscope, gets reflected in a mirror and is finally projected on a 2048 × 2048 pixels CCD camera with a 14 bit dynamic range. The specific microscope configuration is optimized for each experiment. Most of the synchrotron-based tomographic microscopy end stations are based on parallel beam geometry with a spatial resolution limited to a few millimetres. This configuration is used during the experiments related in Chapters 5 and 7.

3.1.2.2 Phase contrast nano-tomography on wood

One of the common approaches to achieve sub-100-nm resolution is full-field microscopy, i.e. where the whole field of view is imaged to a detector plane at the same time. Zernike phase-contrast hard X-ray nanotomography in the full-field mode of image acquisition was applied to image the bordered pits and middle lamella in the cell wall of spruce wood, as shown in Chapter 8. Nanoscopic configuration allows to perform local nanotomography with a nominal voxel size of sub-100 nm (Stampanoni et al., 2010).

For this configuration, the key optical elements are a condenser, to provide a homogeneous intense illumination of the sample and an objective lens, to provide a magnification of the image on the detector. The optimum resolution is then achieved by matching the numerical aperture of the illumination with that of the objective lens. Schematically, a beam shaper collects the light coming from the source and condenses the incoming radiation onto a 50 × 50 μm^2 top-flat square spot, producing a top-flat square illumination on the sample. The beamshaper is a 1 × 1 mm^2 in size, with 1-μm-thick gold structures (Gorelick et al., 2010). The outermost zone width is Δr=100 nm. A square central stop aperture (600 × 600 μm^2) has been used to block the zeroth order and the size of its shadows matches with the size of the beamshaper illumination magnified by the objective lens on the detector. The Fresnel zone plate magnifies this region into the detector located at 9 m of distance, resulting in a magnification factor of M = 110×.

At a distance of 80.7 mm from the Fresnel zone plate, the Zernike Phase Dots consists of a dot array which is aligned to the diffraction spots, generating Zernike phase contrast. For the work on middle lamella and bordered pits discussed in Chapter 8, we use the latest configuration of the nano-tomographic setup, in which the condenser and the Zernike Phase Dots have a circular shape, in order to allow the suppression of the halo artefacts. More details can be found in Vartiainen et al., 2014. The depth of the dots (d_{depth}=6.34 μm) can be adjusted to reach the desired phase shift, leading to a phase shift of $\pi/2$ at 10 keV. The sample is located between the condenser and the Fresnel zone plate (objective lens), as shown in Figure 3.3 (a). A Photonic Science VHR Image Star X-ray camera based on a full-frame transfer Kodak charge coupled device (CCD) with 3056 × 3056 pixels of 12 × 12 μm^2 size is located downstream and collects the raw projections with a 14 bit dynamic range. The camera features a full well capacity larger than 110 ke^-/pixel with a readout noise at 8 MHz of less than ten electrons and dark current smaller than 0.5 electrons/pixel/second. A film of 2.5 mg/cm^2

GdOS:Tb is deposited on a fiber optic taper (FOP), resulting in a final assembly of 12 × 12 mm^2 sized active input window with an optical resolution of 4 µm. For a magnification factor M = 110×, this setup yields a theoretical pixel size of 36 × 36 nm^2. The tomographic projections are reconstructed using a filtered back-projection algorithm with ring artefact removal, as described in Münch et al., 2009. A schematic representation of the experimental setup is shown in Figure 3.3 (b). The resolution of the system is limited by the Rayleigh criterion $R_{Rayleigh}$ = 122 nm.

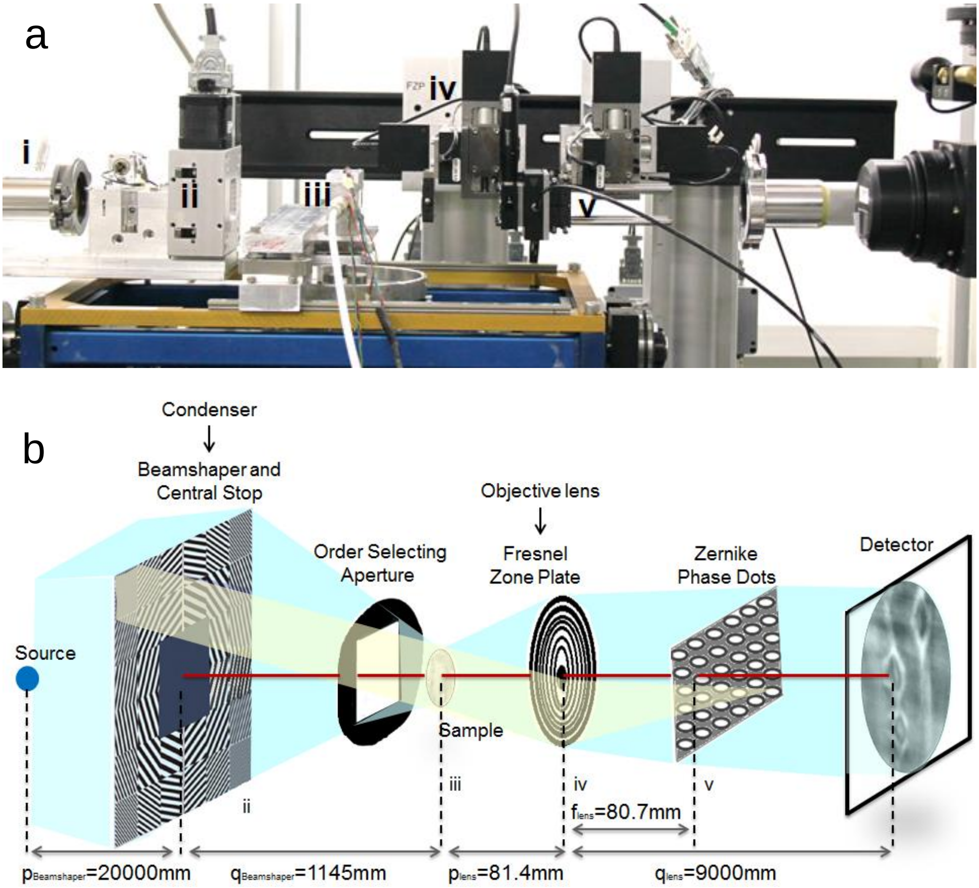

Figure 3.3: (a) Photo of the phase-contrast nano-tomography setup at TOMCAT, showing (i) the end of the X-ray tube, (ii) the condenser, (iii) the environmental chamber housing the wood sample, (iv) the Fresnel zone plate and (v) the Zernike

phase dots. The camera is located at 9 meter of distance from the (iv) and is not shown in the picture. (b) Schematic representation of the nano-tomographic microscopy (Stampanoni et al., 2010), with bordered pits imaged on the detector.

3.2 The environmental chambers

Two environmental chambers are built, adapted to each of the tomographic setups, with different designs and dimensions.

The climatic chamber used during the measurements at TOMCAT has interior dimensions of approximately 39 × 15 × 40 mm^3. Schematic representations of the environmental system and of the climatic chamber are shown in Figure 3.4 (a-b). The chamber has two windows of 15 × 15 mm^2, fitted with sheets of polyimide, which is transparent to X-rays. The bottom part of the chamber is screwed to a bridge that spans over the rotational stage of the tomographic setup. The top part acts as a sealed cap to enclose the space while giving access to the specimens. Additionally, the top has two holes for the data acquisition system (DAS) wires connecting to two solid state integrated RH/temperature sensors. A flexible membrane is attached to a sliding ring that wraps carefully around the rotational stage closing the gap without hindering the stage movement. The air inlet and outlet tubes are inserted into two ports thought the chamber walls. Another climatic chamber (Figure 3.5 (c)) has been manufactured to be adapted to the tomographic setup available at the Centre for X-Ray Tomography of the Ghent University (UGCT), in Belgium. In this case, the dimensions are approximately 92×30×60 mm^3 with two polyimide windows of 40×35 mm^2. The cover can slide on the lateral sides of the chamber in order to facilitate access (as needed for samples and sensors positioning).

3.2.1 The environmental conditions control system

An air handling system controls the air flow rate through the chamber and the relative humidity of the supply air, see Figure 3.4. The experiments are conducted under isothermal conditions provided by the TOMCAT room, so no cooling or heating of the air is necessary. A given relative humidity of the air is achieved by mixing dry and water vapour saturated air. The exact value of the relative humidity is measured downstream of the chamber with a dewpoint hygrometer. The hygrometer output is used to regulate the relative humidity in the mixing room. The environmental conditions, e.g. relative humidity and temperature, are monitored by a data acquisition system, where 4 channels measure different variables, such as temperature, RH, dew point, mixture ratio, partial vapour or enthalpy. The capacity relative humidity sensors have a typical resolution of 0.1% for relative humidity and 0.1 K for dew point temperature. The air velocity within the chamber is approximately 0.5 cm/s and the flow is laminar as verified by smoke visualization (see Figure 3.5).

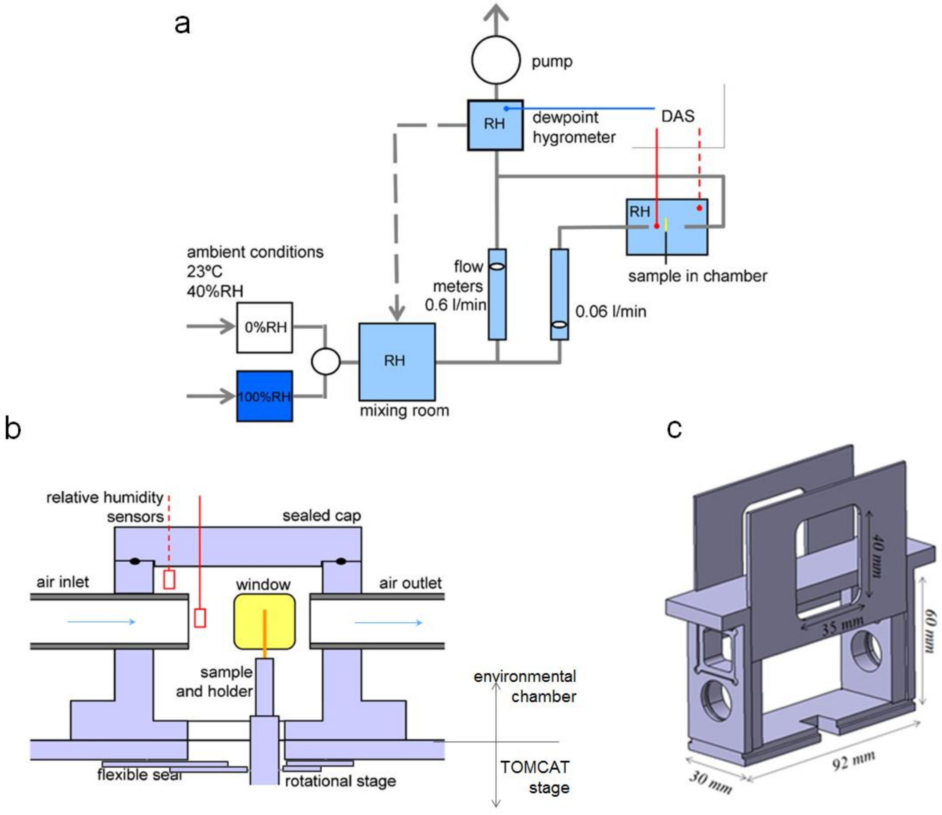

Figure 3.4: Environmental chambers and system to control air conditions around the sample: (a) schematic representation of the environmental control setup, (b) schematic representation of the environmental chamber used at TOMCAT and (c) of the chamber used at UGCT.

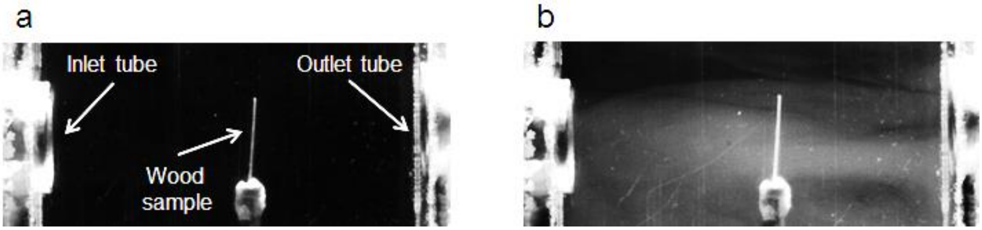

Figure 3.5: Smoke visualization for the observation of a laminar flow inside the climatic chamber, performed with high-speed camera and smoke generator. In (a) the inlet and outlet tubes and the wood sample are indicated. (b) Smoke is injected in the chamber to visualize the laminar flow.

3.3 PMMA restraining device

The hygro-mechanical behaviour of wood tissue is investigated under free swelling and under restrained conditions. For this second condition, a device is manufactured out of PMMA with laser ablation.

3.3.1 Selection of device material

The material of the restraining device must be stiff and transparent to X-rays. The need for X-ray transparency disqualifies stiff materials such as ceramics and metals. However, polymers are classified as moderately stiff materials, in a range similar to wood, with a Young's modulus between 0.1 GPa and 10 GPa. Also, given their lower density, polymers are quite transparent to X-rays. A readily available and known polymer is PMMA.

In terms of physical properties, PMMA is a polymer with excellent optical clarity, good weathering resistance, high tensile strength (48-76 MPa) and tensile modulus. This material is a quite stiff material with a Young's modulus ranging between 1.8 GPa and 3.1 GPa. The mechanical properties of polymers can vary with temperature and humidity. In the case of PMMA, Young's modulus slightly decreases linearly with increasing RH (Shen et al., 1985; Tobolsky and McLoughlin, 1952; Ishiyama, 2001). PMMA is reported to absorb very little water. We performed a dynamic vapour sorption (DVS, see section 3.4) measurement on a PMMA cube. In Figure 3.6, the PMMA moisture content (MC) is plotted versus RH. The

MC ranges between 0 and 0.3% for RH values between 5% (considered as dry state) and 90%. Thus, the amount of moisture adsorbed by PMMA in the hygroscopic range is negligible compared with the MC of wood in the same range. This leads to the very small deformations induced by moisture in PMMA. Swelling of PMMA by water sorption is equal to 0.4% at 25°C and 100% RH (Lacroix, 2007).

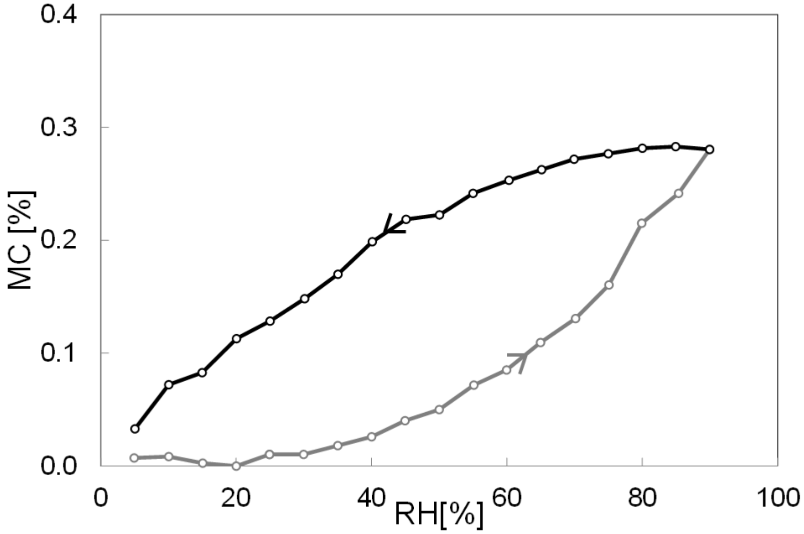

Figure 3.6: Adsorption (grey) and desorption (black) curves of PMMA acquired by dynamic vapour sorption apparatus.

The chemical formula of PMMA is $(C_5O_2H_8)_n$, and its density ρ is 1190 kg/m^3. In (Hubbell and Seltzer, 1995), the mass attenuation coefficient of polymer compounds is calculated at photon energies from 1 keV to 20 MeV with:

$$\mu/\rho = \sum_I w_i(\mu/\rho)_i \tag{3.1}$$

where w_i is the fraction by weight of the ith atomic constituent and $(\mu/\rho)_i$ is the mass attenuation coefficient of each constituent element. This results in a mass attenuation coefficient of $\mu/\rho = 0.5714\,cm^2/g$ in PMMA for E = 20 keV, indicating that this material is relatively transparent to X-rays (Seltzer, 1989). The transparency of PMMA is required to allow the X-ray to pass through the restraining device and to interact mainly with the wood sample. A monochromatic photon energy of 20 keV, which is the energy level used at the TOMCAT beamline of Swiss Light Source (SLS) during the current experiments, is reported not to produce damage to PMMA (Tynnyi, 1967). Thus, for its transparency to X-ray and its high stiffness, PMMA satisfies the requirements as the material out of which the restraining device is made.

3.3.2 Fabrication

A picosecond (ps)-laser ablation system is used to produce the device. Such laser system has many applications in micro-machining, such as micro-structuring surfaces, micro-cutting and micro-drilling thin materials up to a few millimetres thick. The ps-laser can ablate any type of material (polymers, metals, semiconductors, glasses, and ceramics) without mechanical force, without wear and tear and without thermal damages. The YAG (yttrium aluminium garnet)-laser operates at 1064 nm, 532 nm and 355 nm with repetition rates 0-500 kHz and average power up to 10 W at 1064 nm and up to 4 W at 355 nm. The scanning of the beam over the sample is possible either by precise XY stage with travel range 350×210 mm^2 or with galvanic scanner covering 50×50 mm^2 area. The sample is positioned in the path of the beam by a CCD camera with an accuracy better than 10 microns.

The material removal rate as a function of average power at 50 kHz frequency and 355 nm wavelength is calibrated on a 2 mm thick PMMA sample. The resulting depth and roughness are measured with the Tencor P-10 Surface Profiler. A stylus scans the sample across the grooves produced by the laser, which are schematically shown in Figure 3.7 (a). The depth as a function of power is plotted in Figure 3.7 (b). As can be seen, the material is not removed at power level of 50 mW, which appears to be below the ablation threshold for the parameters used. On the other hand, one can observe a strong increase of the removal rate at the power level of 1000 mW. Material melting takes place at this power level, which makes the ablation process similar to that of (nanosecond) ns-laser. The dependence of the removal rate on power was found to be quite linear in a 150-700 mW range. Finally, 500 mW is chosen as power level to produce the 0.5x2x4 mm^3 (depth, width and length) slot in the 4x4x4 mm^3 cubes and the 0.5x1x3 mm^3 slot on the 3x3x3 mm^3 samples. These cubes are first produced by an industrial nanosecond (ns)-laser ablation system, while the 2x2x2 mm^3 cubes, and all the slots in the cubes of three sizes, are cut by ps-laser ablation using wavelength of 355 nm, frequency of 50 kHz, and a hatch and spot-to spot distance of 3 μm. The 2 mm-thick devices require a scanning time up to 5 seconds at 300 mW power at each scan (in the X-Y plane), while the thicker samples needed 10 seconds for one X-Y scan at higher power (up to 500 mW). For the smallest cubes, the power is decreased down to 300 mW to reduce the melting effects, which are arising on the sample surface during multiple scanning. In total, 10 restraining devices are manufactured.

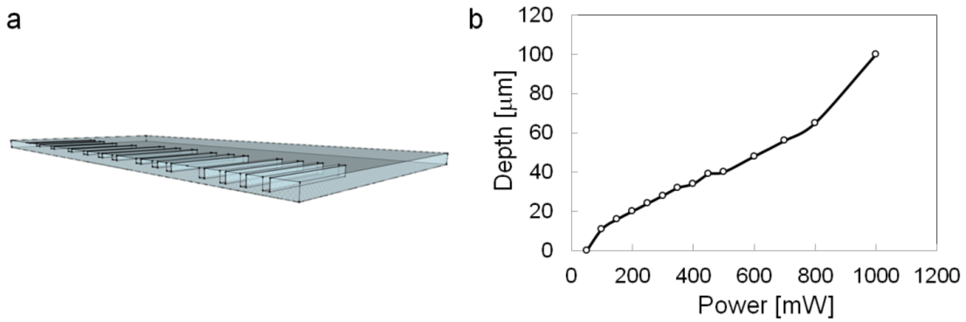

Figure 3.7: (a) Schematic representation of micro-machining by laser ablation at different power values (from 50 mW to1 W). (b) Depth of groove after one pass in X and Y directions versus power used.

The procedure followed to fabricate the slots is described below:

- The laser beam is scanned in the X-Y directions on one side of the cube to form the first part of the slot. At this stage the first half of the first slot has a conical shape.
- The sample is rotated 180° to continue the machining of the remaining part of the first slot.
- The first two steps are repeated for the manufacture of the second slot, perpendicular to the first one.
- A 0.5 mm diameter screw (corresponding to the slot height) is carefully used to remove the remaining material in order to get a rectangular

shape for the slot. The manipulation is controlled under an optical microscope.
- Finally, a silicon carbine paper is used to polish the inside surfaces of the slot.

3.3.3 Design of the restraining method

The aim is to design a restraining device which fits within an environmental chamber with controlled air conditions. Therefore, a passive mode of restraint during swelling is considered in this work, by producing a device that resists the swelling of the sample. A first complexity is posed by the natural cellular structure of wood, which makes it impossible to produce a wood sample with plane surfaces as cutting through cells results always in dented surfaces. The idea is to fabricate a solid restraining device that would restrict swelling in one direction. Another design constraint is that both the wood sample and its contact with the restraining device must fit within the field of view (FOV) of the microscopic setup to reach high resolution. So the chosen approach is to insert the sample into a slotted cubic device. The slot should provide two flat smooth surfaces to restrain the displacement of the sample undergoing swelling and should be visible in the FOV. In addition, the slot allows humid air to access the sample. The slotted devices are manufactured by picosecond (ps)-laser ablation, as explained in preceding section. The cube dimensions are optimized to provide an appropriate rigidity of the device and optimum space for image acquisition. For this purpose, a finite-element modelling parametric study is carried out to estimate the deformation of the device and slot boundaries under swelling pressures. The effective material properties arising in problems of hygro-elasticity are the elastic stiffness and the hygro-expansion coefficients. For modelling, the hygro-elasticity is considered equivalent to thermo-elasticity with moisture content playing the role of temperature. The swelling pressure of the spruce wood from dry to high RH is known to be about 2 MPA, based on macroscopic experiments (e.g. Virta et al, 2006). The selected material, PMMA, is elastic isotropically with elastic Young's modulus E = 3 GPa and Poisson's ratio υ=0.3. Different geometries are considered. The swelling load is applied as a uniform pressure on the top and bottom surfaces of the slot in a region of 1 mm wide through the whole opening and the deformation of the cube is calculated using the finite element package ABAQUS/Standard (Rising Sun Mills, Providence, RI, USA) through its Python scripting interface. The results of the simulations for different geometries of the cube and slot sizes in terms of the deformation in the y-direction are shown in Figure 3.8. The 2×2×2 mm^3 cube is subjected to higher deformations compared with the two bigger cubes under the above mentioned conditions. For cases b and c in Figure 3.8, the maximum central displacement in the y-direction ranges between 1.9 μm and 2.5 μm against the higher 3.2 μm vertical displacement in the 2×2×2 mm^3 cube. Smaller deformations occur in the 3×3×3 mm^3 PMMA cube under load, while intermediate values are found in the 4×4×4 mm^3 device. Based on this study, the 3×3×3 mm^3 and the 4×4×4 mm^3 cubes are selected as providing good restraint to the swelling of the wood samples.

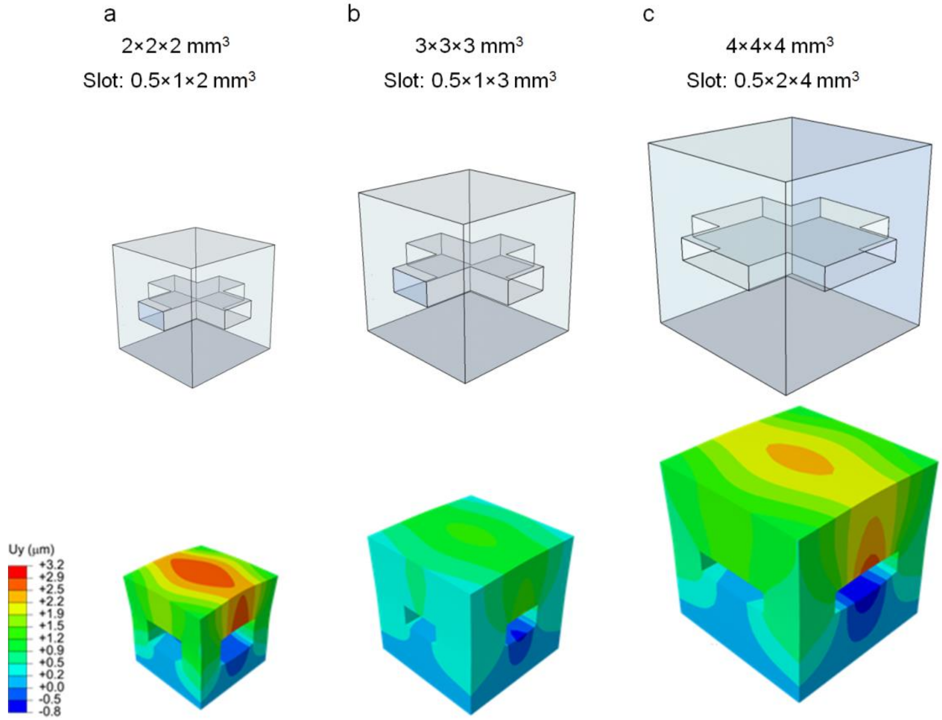

Figure 3.8: Geometry (above) and displacement field in y-direction (below) for three configurations of the restraining device, (a) 2×2×2 mm^3, (b) 3×3×3 mm^3, (c) 4×4×4 mm^3.

3.4 Dynamic vapour sorption machine

The dynamic vapour sorption instrument (VTI-SA+ Vapour Sorption Analyser), as shown in Figure 3.9, measures the mass of the sample as it adsorbs or desorbs moisture, respectively with increasing or decreasing RH with high precision. Identical conditions of temperature and humidity for the sample and a reference are achieved. The vapour sorption instrument is composed of two measurement pans, namely the sample and reference holders, suspended from the arms of an ultra-sensitive microbalance (0.1 μg sensitivity and ± 0.1% weighing accuracy) and located each in a different chamber. The chambers are linked to each other and subjected to identical environmental conditions, as they are located in a thermostatically controlled cabinet, within ±0.1°C in the range of 5 to 60°C. A constant flow of dry nitrogen gas, mixed with another nitrogen stream containing water vapour, maintains a set RH with an accuracy of "±" 1%RH in the 2 to 95% RH range. The RH is determined by a two-stage chilled-mirror dewpoint analyser. The apparatus can be programmed to execute a series of RH/T air conditions in terms of actual duration of steps or in terms of an equilibrium criterion. The running time, isotherm temperature, target RH, actual RH and sample weight are recorded throughout the isotherm run.

Figure 3.9: Photograph of the VTI-SA+ Vapour Sorption Analyser, with its control panel.

3.5 Summary

In this chapter, all the experimental procedures used in the following chapters are explained. In particular, three different configurations of X-ray tomography are described: synchrotron-based X-ray micro-tomography and nano-tomography, and lab-based X-ray tomography. The advantages of using synchrotron-based X-ray tomography for *in-situ* experiments are largely discussed. Especially for samples conditioned at steady-state equilibrium, the high flux of synchrotron radiation allows to acquire tomographic datasets in few minutes against the scanning hours needed with the X-ray tube source. Additionally, two different designs of environmental chamber adapted to the two main configurations (synchrotron-based and lab-based) are illustrated. In this work, hindered swelling of wood is also studied. Thus, the design and manufacturing of the restraining device is discussed. Finally, the last equipment used for measuring the mass of the samples at different RH levels, named DVS machine, is discussed. All these components are used in the following chapters. The next chapter discusses the registration method developed for identifying the local deformation, a needed tool for the analysis of the swelling and shrinkage of wood.

Chapter 4

Non-affine registration algorithm

In this chapter, we describe a quantitative method to analyse the deformations in cellular wood tissues when subjected to environmental changes. The goal of image registration in tomographic datasets of wood is to relate any point in the image sequence taken at different wet states to the dry state of the image, in other words, to find an optimal transformation between the two states.

Transformations used to align two images can be global or local. A global transformation is given by a single equation which maps the entire image. One global method, namely the affine transformation, has been previously introduced and described in section 2.5.2. The affine registration model allows to quantify the affine strains along the three orthotropic directions of wood. However, this model fails to identify the local deformations. Local transformations are much more difficult to describe considering that the image mapping depends on the spatial location (Brown, 1992). We propose a method to detect and quantify local deformations in cellular tissues using a non-affine registration model, based on B-spline functions. After a review of the previous works, a description of the basic idea of image registration is given. Then the local transformation model based on B-splines is mathematically described. Finally, the procedure of the algorithm is presented.

4.1 A survey of image registration techniques: affine and non-affine

Due to the importance of image registration in various application areas and given its complicated nature, a large number of image registration algorithms have been developed in the past. An exhaustive review of general-purpose image registration methods can be found in Brown (1992). One of the first works in this field appears in Roberts (1963), where projections of the edges of model polyhedral solids were aligned with image edges, thus enabling to detect and locate predefined polyhedral objects in the images. Over the years, image registration has been used mostly for medicine applications which explains that most of the algorithms have been developed in this field (Pluim and Fitzpatrick, 2003).

Applications of image registration in the medical field include combining data from different modalities e.g. computer tomography (CT) and magnetic resonance imaging (MRI), to obtain more complete information about the patient, monitoring tumour growth (Wyawahare et al., 2009), treatment verification (Gering et al., 1999; Gering et al. 2001; Staring et al., 2009), computer-aided diagnosis and disease following-up (Huang et al. 2009); surgery simulation (Miller et al. 2010); atlas building and comparison (Gooya et al. 2011); radiation therapy (Lavely et al., 2004; Foskey et al., 2005); anatomy segmentation (Collins and Evans, 1997; Frangi et al., 2003; Dornheimet al., 2005; Martin et al., 2008; Isgum et al., 2009; Gao et al., 2010; Zhuang et al., 2010); computational model building (Grosland et al., 2009) and image subtraction for contrast enhanced images (Maksimov et al., 2009). In contrast, much less algorithms for image registration are nowadays available for material applications.

A large number of software solutions have been developed, with main focus on medical image registration. Examples of free-open-source software packages include: source codes in Matlab and in C; Insight Segmentation and Registration Toolkit (ITK) (Ibanez et al., 2005); 3D Slicer (Gering et al., 1999; Pieper et al., 2004; Pieper et al., 2006); FLIRT (Jenkinson and Smith, 2001); source code in Elastix (Klein et al., 2010). Both 3D Slicer and Elastix are based on the ITK library.

In this thesis, we propose a method to detect and quantify local deformations in the cellular tissues using a non-affine registration model.

This type of registration employs a Free-Form Deformation (FFD) model based on B-splines (Rueckert et al., 1999). The code developed in this thesis has been adapted starting from this method, and written in Matlab.

Most of the algorithms presented in literature, such as the ones mentioned above, are based on the histogram of grey levels. Our idea is to combine the recognition of features in the material, performed with morphological operations, with an optimization method, in order to allow the detection of local deformations in complex biological materials such as cellular wood tissue.

4.2 Theory of image registration

Image registration is a method to map two different images, which are acquired with the same or different experimental setups. In image registration, the deformed image, also called *moving image* $I_M(x)$, is transformed to be aligned to the reference or original image, called *fixed image* $I_F(x)$. Both images have dimensions s and are defined in their spatial domain: $\Omega_F \subset \mathbb{R}^d$ and $\Omega_M \subset \mathbb{R}^d$ for fixed and moving images, respectively. In general, the transformation is defined as a mapping from the moving to the fixed image, i.e. $T: \Omega_F \subset \mathbb{R}^d \longrightarrow \Omega_M \subset \mathbb{R}^d$. The transformation that matches $I_M(x)$ to $I_F(x)$ is defined as:

$$T(x) = x + U(x) \tag{4.1}$$

where $U(x)$ is the displacement that makes $I_M(x + U(\boldsymbol{x}))$ to be aligned to $I_F(x)$. The goodness of alignment is evaluated by a distance or similarity measure $\mathcal{S}$, such as the correlation ratio, the sum of squared differences (SSD), or the mutual information (MI). These techniques will be described in this chapter, with particular attention to the sum of squared differences.

Commonly, registration is a problem of optimization in which a cost function $\mathcal{C}$ has to be minimized, resulting in $\hat{T}$:

$$\hat{T} = arg \min_T \ \mathcal{C}(T; I_F, I_M) \tag{4.2}$$

where $\hat{T}$ represents the set of points of the transformation between fixed and moving images for which the given cost function attains its minimum value. The problem of the identification of the non-affine transformation T becomes easily ill-posed and, therefore, a regularisation or penalty term $\mathcal{P}$ constraining the transformation T is introduced. Then the cost function is as follows:

$$C(T; I_F, I_M) = -\mathcal{S}(T; I_F, I_M) + \gamma\mathcal{P}(T) \tag{4.3}$$

where γ weights similarity against regularity. The cost function is described by the similarity term when γ tends to zero. A similarity measure is a function that takes two input images as parameters and computes a numerical value that quantifies the extent to which the two images are similar. The regularity term $\mathcal{P}(T)$ is designed to penalize control points displacements that potentially lead to naturally implausible deformations.

4.2.1 Image registration on wood

In general, the deformation of wood contains a non-affine component so that affine transformations alone are not sufficient to describe local deformations in wood tissues (Derome et al., 2011). Therefore, the transformation has to include contributions from both affine and non-affine components, or:

$$T(x, y, z) = T_{global}(x, y, z) + T_{local}(x, y, z) \tag{4.4}$$

The global transformation $T_{global}(x, y, z)$ is the affine transformation as described in Chapter 2. The local transformation $T_{local}(x, y, z)$ represents the additional term that is required in order to capture the local deformations. An elegant way to describe local deformations avoiding difficult parameterization methods has been introduced by Rueckert et al., 1999. The model is based on B-splines and it is known as the Free Form Deformation (FFD) model. FFD is a technique for manipulating any shape in a free-form manner. Basically, an object is deformed by manipulating an underlying mesh of control points. This section discusses the 3D case of FFD.

Let $\Omega = \{(x, y, z) | 0 \leq x < X, 0 \leq y < Y, 0 \leq z < Z\}$ denote the volume domain and Π be a mesh of control points $\Pi_{i,j,k}$ with uniform spacing δ and with number of elements $N = n_x \times n_y \times n_z$, represented schematically in two-dimensions in Figure 4.1.

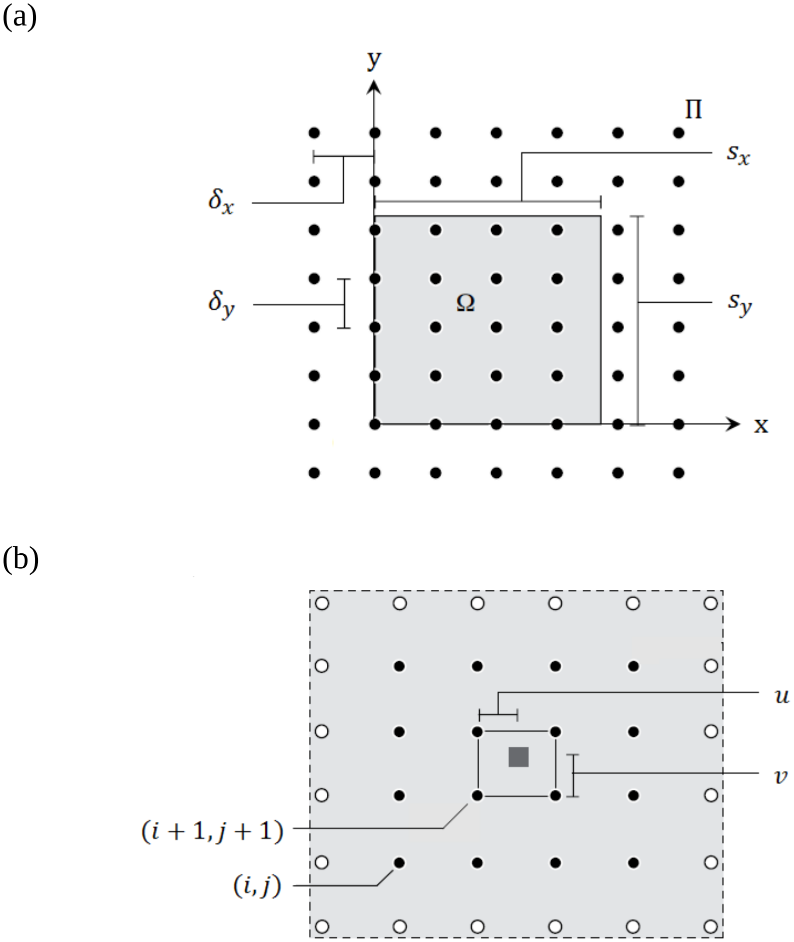

Figure 4.1: (a) A schematic two-dimensional configuration of the mesh of control points $\phi_{i,j}$, with the image shown in light grey. (b) A magnified portion of the image illustrating the computation of the transformation function. (to be continued)

(c)

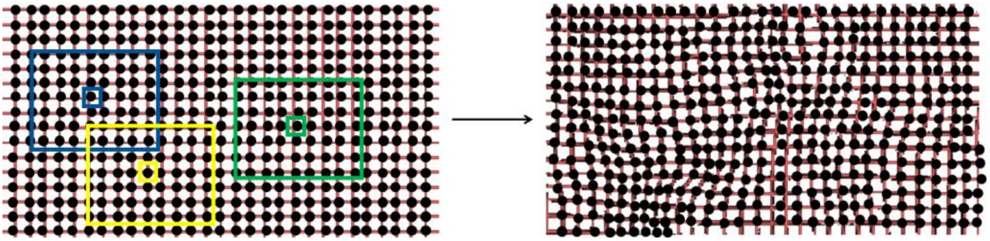

Figure 4.1: (c) An example of deformable mesh in which each point is locally controlled, as shown, for example, in the blue, yellow and green boxes.

Figure 4.1 illustrates the way in which the transformation function is computed. The pixel that is transformed is shown in dark grey. The control points that are not considered are marked in white, while the surrounding control points are shown in black. The set of control points is identical for all pixels. The weights for each of the control points change with the distances u and v, as shown in Figure 4.1 b. The transformation function $T_{local}(x, y, z)$ is written as the 3-D tensor product of 1-D cubic B-splines and is defined in terms of the control points $\Pi_{i,j,k}$:

$$T_{local}(x, y, z) = \sum_{l=0}^{3} \sum_{m=0}^{3} \sum_{n=0}^{3} B_l(u) B_m(v) B_n(w) \Pi_{i+l, j+m, k+n} \tag{4.5}$$

where $i = \lfloor x/n_x \rfloor - 1,\ j = \lfloor y/n_y \rfloor - 1,\ k = \lfloor z/n_z \rfloor - 1$ and where $\lfloor\ \rfloor$ means the floor of the number (i.e. the largest integer less than or equal to the number). The variables u, v, w are the fractional remainders of voxel coordinates between control points and represent the relative position of a voxel within its surrounding block of control points, see Figure 4.1 b. These variables are defined as: $u = x/n_x - \lfloor x/n_x \rfloor,\ v = y/n_y - \lfloor y/n_y \rfloor\ w = z/n_z - \lfloor z/n_z \rfloor$. B_l represents the lth, basis function of the B-spline, as defined below:

$$B_0(u) = (1-u)^3/6$$
$$B_1(u) = (3u^3 - 6u^2 + 4)/6$$

$$B_2(u) = (-3u^3 + 3u^2 + 3u + 1)/6$$
$$B_3(u) = u^3/6 \tag{4.6}$$

The control points $\Pi_{i,j,k}$ are the unknown parameters of the B-spline FFB. The degree of the non-affine transformation depends on the resolution of the mesh of the control points. The spacing between the control points determines the level of non-affine registration, i.e. a large spacing or low resolution results in a more global estimation of the deformations, compared with a smaller spacing (higher resolution) that models highly local deformations. At the same time, the number of control points determines the number of degree of freedom and the computational complexity.

The B-spline grid is constructed with the method of Lee et al. (1997). The method consists in the iterative refinement of a rough FFD grid in order to get a better approximation of the transformation. Let s_x, s_y and s_z be the object size in the three directions. The spacing between control points can be written as:

$$\delta_{x,y.z} = 2^{\zeta_{x,y,z}} \tag{4.7}$$

where ζ is defined as the number of maximum iterations needed to refine the B-spline grid as:

$$\zeta_{x,y,z} = min(\log_2 \frac{s_{x,y,z}}{4}) \tag{4.8}$$

4.2.1.1 Optimization problem

The parameters of the global and local transformations are determined by solving the optimization problem, i.e. by minimising the cost function defined in eq. 4.3.

Different optimization techniques can be used for the iterative alignment of the moving image $I_M(x)$ with the fixed image $I_F(x)$ with a certain control grid Φ. Three methods are mentioned:

- Quasi Newton Broyden-Fletcher-Goldfarb-Shanno (BFGS), which is a second-derivative line search method, a powerful method to solve unconstrained optimization problem (Shanno et al., 1970)
- Limited-memory BFGS (L-BFGS), which approximates the BFGS algorithm, however using less computer memory and widely used in machine learning.
- Steepest descent method, which is the simplest of the gradient methods. Given a function, the method approaches the minimum in a zig-zag way, in a direction opposite to the function gradient.

In BFGS methods, as well in all quasi-Newton methods, the gradient of the cost function needs to be computed iteratively, until convergence is achieved. In the algorithm, first a search direction is looked for and then the function is iterated along this direction with a step length satisfying the Wolfe conditions. The steepest descent method is simplified to a minimization problem along a line and approaches the minimum in a zig-zag manner, where the new search direction is orthogonal to the previous one. In regions far from the minimum, this method is more efficient than the others. However, it descends quite inefficiently compared to quasi-Newton methods closer to the minimum. More details on the optimization problems can be found in Ferraris et al., 2001.

4.2.1.2 Penalties

A penalty term is introduced in equation 4.3 to constrain the local transformation to be smooth. This term is described by Wahba (1990) as follows:

$$\mathcal{P}(T) = \frac{1}{V}\int_0^X \int_0^Y \int_0^Z \left[\left(\frac{\partial^2 T}{\partial x^2}\right)^2 + \left(\frac{\partial^2 T}{\partial y^2}\right)^2 + \left(\frac{\partial^2 T}{\partial z^2}\right)^2 + 2\left(\frac{\partial^2 T}{\partial xy}\right)^2 + 2\left(\frac{\partial^2 T}{\partial xz}\right)^2 + 2\left(\frac{\partial^2 T}{\partial yz}\right)^2\right] dx\, dy\, dz \tag{4.9}$$

with V denoting the volume of the image domain. We remark that the penalty term of a cost function is equal to zero in the case of an affine transform.

4.3 Modified FFD algorithm based on B-splines

In this section, we describe the different steps in which we adapted the above mentioned method to better describe the non-affine deformations in wood tissues.

The existing algorithm has been modified in order to improve the performance of the FFD for describing local deformations in complex materials, such as wood. An overview of the proposed method is given in Figure 4.2. Each step of the algorithm is described and demonstrated in an example in 2D, i.e. on an artificial image, in section 4.5.

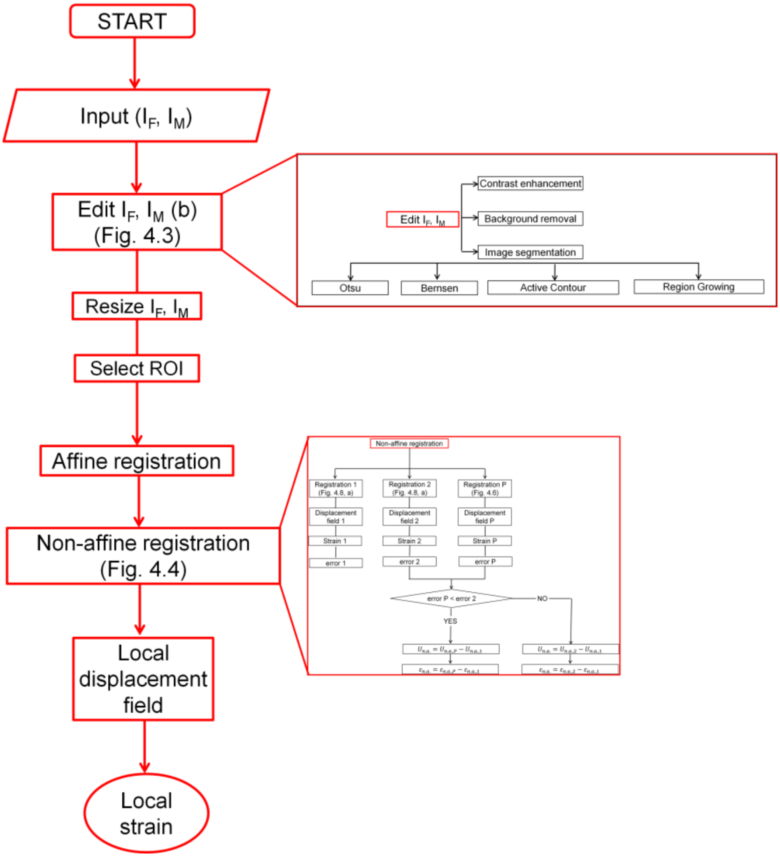

Figure 4.2: Flow chart of the non-affine registration algorithm adapted for investigating local deformations in the wood cellular tissue.

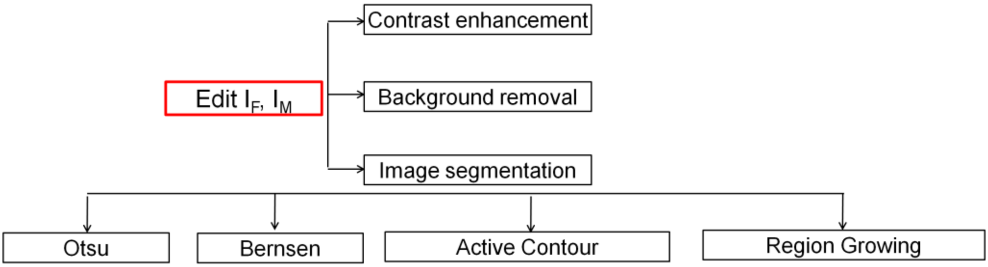

Figure 4.3: Description of the initial editing operations performed on moving and fixed image.

Two images, the *moving image* $I_M(x)$ and the *fixed image* $I_F(x)$, are given as input to the algorithm. Initial operations, [Edit I_F, I_M] in Figure 4.3, based on the histogram of grey-values can be performed on these images to improve the performance of the non-affine registration algorithm. Among these operations, we mention contrast enhancement, background removal or image segmentation. Four segmentation methods have been already described in Chapter 2, section 2.5.1 (Otsu, Bernsen, region growing and Chan-Vese algorithm). The fixed and moving images are resized to match each other in size and a region of interest (ROI) is selected. These steps allow to perform the registration of the images without correcting initially the images sizes and the continuity of the deformation in the whole ROI is considered.

Then, an affine registration is performed providing the global transformation $T_{global}(x,y,z)$. A set of initial points (generally 10) is manually determined on the images in order to help the affine registration algorithm. The choice (number and positions) of the initial points does not influence the performance of the registration procedure. After correction for affine registration, the fixed and the corrected moving images are subtracted to obtain the mis-registered deformations, related to places where local deformations occur. Based on this information, the non-affine deformations are obtained using non-affine registration.

Three approaches for non-affine registration are used. A flowchart of the non-affine registration algorithm is given in Figure 4.4. First, two approaches consist in performing the registration directly on the original images, i.e. on the intensity of the grey values. We refer to these two approaches as ‘Registration 1’ and ‘Registration 2’. ‘Registration 1’ is a rough and fast estimation of non-affine deformations in resized images, where the B-spline functions are largely constrained (increasing the weight γ of the penalty term in equation 4.3) in order to describe more the global deformations in the material. ‘Registration 2’ is performed directly on the original images with increasing the freedom of the B-spline grid, i.e. decreasing the weight coefficient γ of the penalty. In this way, the local misalignment can be more easily detected, although more artefacts coming from the high freedom of the B-spline grid can arise. To prevent these artefacts problems, we finally define the local deformations by subtracting ‘Registration 2’ from ‘Registration 1’ and the local transformation is calculated. However, there are cases in which these methods do not give the optimal solution. For this reason, we introduce a third registration technique. The third approach for non-affine registration is called point-based registration or ‘Registration P’. In this case, the input consists in a set of points in the two images. Different techniques for the detection of control points pairs in the images are used, which are referred to as manual, map, skeleton, harries or edges. All these techniques are described in section 4.3.1. The initial image pairs $\{\Pi^i(I_F),\ \Pi^k(I_M)\}_{i,k=1\ldots n}$ are added, in both images, to the points of the artificial grids $\{\Pi^j(G_F),\ \Pi^l(G_M)\}_{j,l=1\ldots m}$. A polynomial or affine transformation is used to transform the artificial grid matching $\Pi^j(G_F)$ with $\Pi^l(G_M)$. The initial pairs or feature points in the two images are selected in such a way to ensure a matching between image features in the images using correlation. The use of different methods for selecting the feature points in the images, combined with the artificial grid, represent the key features of the algorithm, explained in section 4.3.1. The registrations are compared two by two as follows. If the error, i.e. the difference between the two images after non-affine registration, given by ‘Registration P’, called error P, is smaller than the error calculated with the ‘Registration 2’, called error 2, then the local deformations can be estimated by subtracting ‘Registration P’ from ‘Registration 1’, where ‘Registration P’ detects the local deformations but, again, may be affected by artefacts due to the freedom of the B-spline grid. To avoid this problem, we proceed as for ‘Registration 2’, i.e. we define the local deformations by subtracting the displacement field calculated with ‘Registration P’ from the displacement field obtained with ‘Registration 1’. If error P is bigger than error 2, ‘Registration 2’ is considered for the final calculation of the local deformations and non-affine strains. This step ensures the selection of the best non-affine registration method for each case study. Once the optimization problem is solved by minimization of the cost function, the displacement field is determined and the local strain fields are evaluated and plotted.

The algorithm runs for a stack of images in a loop, performing a 2D registration image by image. The 2D approximation is valid in this case study, considering that the deformations of spruce wood along the longitudinal direction are negligible. This approach assumes that the local deformations in one direction are very precisely estimated (better than the voxel size) by the global affine.

transformation. For each registration step (i.e., 'Registration 1', 'Registration 2' and 'Registration P'), the non-affine (n.a.) strain fields are calculated from the gradient of the displacement field (U_x, U_y) in each direction ($\varepsilon_{n.a._x}, \varepsilon_{n.a._{xy}}, \varepsilon_{n.a._y}$) and the equivalent strain is calculated using the von Mises relationship (von Mises, 1913).

$$\varepsilon_{n.a.} = \sqrt{\varepsilon_{n.a._x}^{2} + 2 \times \varepsilon_{n.a._{xy}}^{2} + \varepsilon_{n.a._y}^{2}} \qquad (4.10)$$

The defined equivalent strain is a qualitative analysis to describe the deformation intensity in wood.

More details on strain tensors calculation can be found in Abd-Elmoniem et al., 2009.

Comparing three types of non-affine registration, i.e. 'Registration 1', 'Registration 2' and 'Registration P', we note the following. 'Registration 1' includes more constraints on the B-spline grid, thus performs a more global registration. 'Registration 2' and 'Registration P' give more freedom to the B-spline functions, thus allow the detection of more local features. Finally, the local deformations and strain fields are calculated as explained in Figure 4.4.

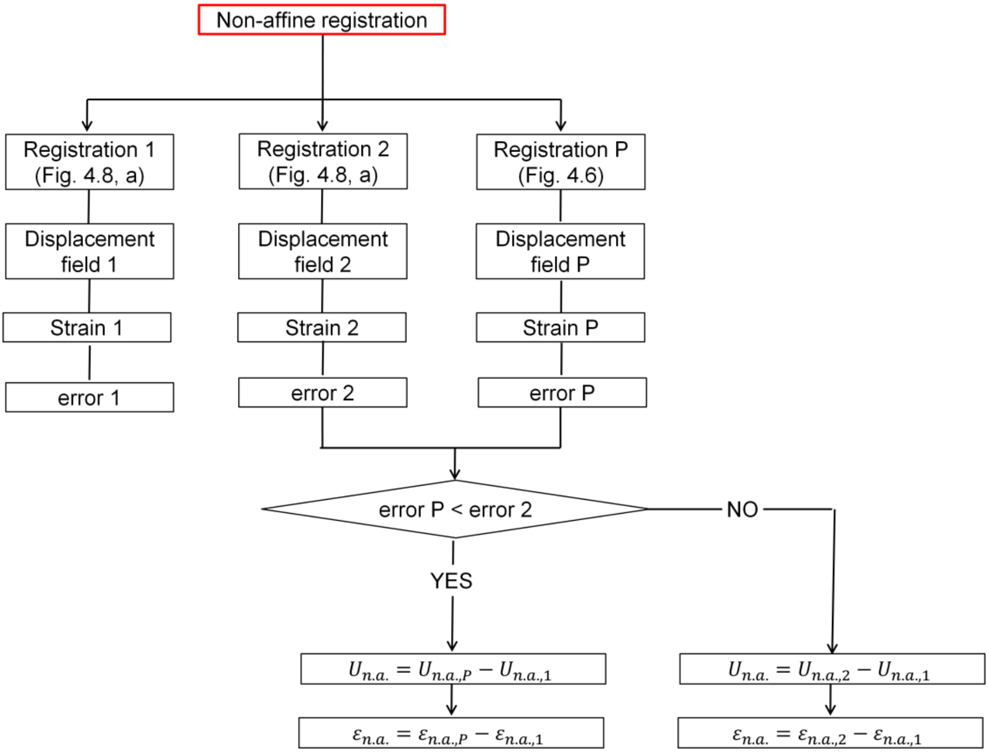

Figure 4.4: Overview of the non-affine registration algorithm with the three methods described in the text.

In order to make the algorithm easy and directly accessible, a graphical user interface (GUI) is created and a snapshot is given in Figure 4.5. Additional details on the parameters of the algorithm are given in the caption of the figure.

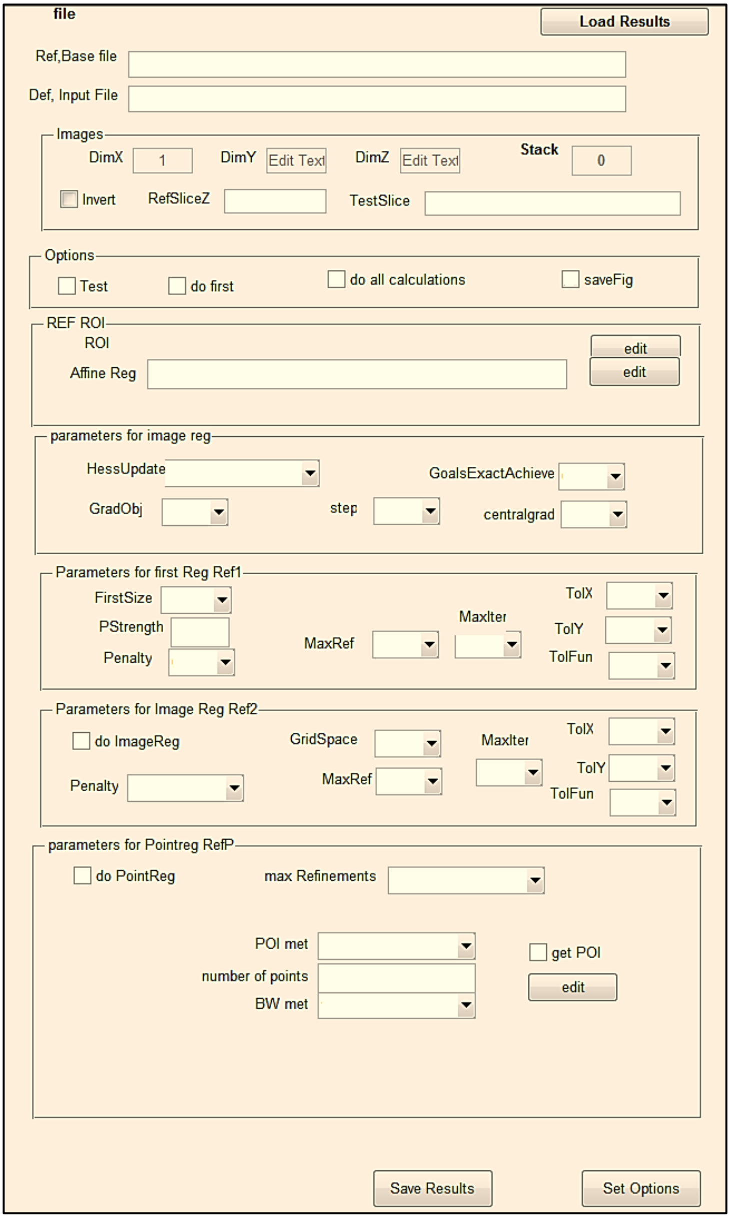

Figure 4.5: Graphical user interface (GUI) of the non-affine registration algorithm[i].

4.3.1 Key feature 1: acquire points in two images and correlate

The original FFD method allows introducing feature points, also called control points pairs, on the fixed and moving images by selecting them manually. If the region of interest is big or the algorithm needs to run for different image sequences, it is favourable to use automatic methods of selection of points on similar features in the two images. We introduce four types of morphological selection methods (see Figure 4.7):

- ‘Map’ is a simple procedure of tracking the borders of features using binary images and giving the coordinates of the borders as output.

- ‘Skeleton’ follows a skeletonization procedure consisting in the extraction of a region-based shape feature which represents the general structure of an object.

- ‘Harris’ is a method for calculating and displaying the feature points as Harris corners (Harries and Stephen, 1988). The Harris corner detector is a powerful tool due to its invariance to rotation, scale, illumination variation and image noise. It is a procedure to calculate

---

[i] Details of the GUI in Figure 4.5. In ‘file’, the two images, base and input, can be read together as a ‘.mat’ file containing the two image matrices or uploaded separately in their respective boxes. The whole stack can be loaded directly from the button ‘Load Results’. The images’ or volumes’ dimensions are indicated in the ‘Images’ box. In case of a stack, the image slice used for testing the parameters of the registration can be selected in ‘TestSlice’. In the ‘Options’, ‘Test’ allows the implementation of a first rough fast registration based on the intensity of grey values for testing the initial parameters. In case the parameters are corrected, one can do all the calculations and save the images. Otherwise, it is possible to continue only with intensity-based registration choosing new parameters, ‘do first’. In the RefROI box, the initial ROI and the initial landmarks on the two images are selected for affine registration. The dialog box ‘parameter for image reg’ contains the general parameters for non-affine registration chosen in this step. In particular, ‘HessUpdate’ represents the optimization problem and it contains the three options: BFGS, L-BFGS, steepest descend method. ‘GoalExactAchieve’ is the minimization loop, where two methods are available. ‘GradObj’ calculate the errors of the B-spline functions for each step as gradient (‘on’) or as a finite difference (‘off’). ‘Step’ defines the step size in the direction of the gradient in the line search method; ‘centralgrad’ is set to 1 when the error function is calculated as gradient or to 0 when finite difference. The box ‘Parameter for first Reg Ref1’ defines the parameters for ‘Registration 1’. The images are resized ‘FirstSize’ to run the first registration faster. ‘PStrength’ is set to high values when the registration is based on the initial landmarks, manually selected; in contrast, it is chosen as a small value when the registration is based mostly on the intensity of the histograms. The ‘Penalty’ is the γ coefficient in equation 4.3. ‘MaxRef’ is equivalent to ζ. ‘MaxIter’ defines the number of iterations. ‘TolX’ and ‘TolY’ are the termination tolerances on the function coefficients in x and y directions. ‘TolFun’ is the termination tolerance on the function value. Similar options in ‘Parameters for Image Reg Ref2’, referred to ‘Registration 2’. In this case, the grid space can be manually selected. In ‘Parameters for Pointreg RefP’, the main options are: method for features extraction and method for image binarization. Finally, before running the algorithm, click on ‘SetOptions’ and then on ‘Save Results’.

the local changes in an image by moving the feature point by a small amount in different directions. The corners are defined as image locations that have large intensity changes in more than one direction. The intensity change (ΔI) along some directions can be quantified by the sum of squared-difference (SSD):

$$\Delta \mathrm{I}(\breve{u}, \breve{v}) = \sum_{\breve{\imath},\breve{\jmath}} (I(\breve{\imath} + \breve{u}, \breve{\jmath} + \breve{v}) - I(\breve{\imath}, \breve{\jmath}))^2 \tag{4.11}$$

with $(\breve{u}, \breve{v})$ representing a shift between the two positions. If $\breve{u}$ and $\breve{v}$ are very small, the use of a Taylor approximation is valid:

$$I(\breve{\imath} + \breve{u}, \breve{\jmath} + \breve{v}) \approx I(\breve{\imath}, \breve{\jmath}) + I_x\breve{u} + I_y\breve{v} \tag{4.12}$$

where $I_x = \frac{\partial I}{\partial x}$ and $I_y = \frac{\partial I}{\partial y}$.

One can then calculate:

$$\left(I(\breve{\imath} + \breve{u}, \breve{\jmath} + \breve{v}) - I(\breve{\imath}, \breve{\jmath})\right)^2 \approx \left(I(\breve{\imath}, \breve{\jmath}) + I_x\breve{u} + I_y\breve{v} - I(\breve{\imath}, \breve{\jmath})\right)^2 = \left(I_x\breve{u} + I_y\breve{v}\right)^2 = \left(I_x^2\breve{u}^2 + 2I_xI_y\breve{u}\breve{v} + I_y^2\breve{v}^2\right) = [\breve{u} \quad \breve{v}] \begin{bmatrix} I_x^2 & I_xI_y \\ I_xI_y & I_y^2 \end{bmatrix} \begin{bmatrix} \breve{u} \\ \breve{v} \end{bmatrix} \tag{4.13}$$

The intensity change in a certain direction is thus identified by:

$$\Delta \mathrm{I} = \begin{bmatrix} I_x^2 & I_xI_y \\ I_xI_y & I_y^2 \end{bmatrix} \tag{4.14}$$

Finally, the corner positions are determined.

- ‘Edges’ is based on the Canny edges detection method (Canny, 1986). This detector is a multi-step process, which reduces firstly the image noise with a Gaussian filter. Then, the gradient magnitude of the image is determined:

$$\nabla I = \sqrt{\nabla I_x^2(x,y) + \nabla I_y^2(x,y)}, \tag{4.15}$$

and the angle of the gradient:

$$\theta = arctan\left(\frac{\nabla I_x(x,y)}{\nabla I_y(x,y)}\right). \tag{4.16}$$

with $\nabla I_x(x,y)$ and $\nabla I_y(x,y)$ the derivative of the image I in the x and y directions.

In order to determine the edges one pixel wide, a “non-maximal suppression” step is applied to select only the pixels on the edge with the highest gradient magnitude.

A problem that may arise is related to the risk of removing important parts of a connected edge during thresholding, for example in regions where the edge gradient magnitude fluctuates just above and just below the threshold. This problem is solved by using a hysteresis method, which consists in using two different thresholds t_{high} and t_{low} instead of one. Only the pixels with a value $t_{low} \leq \nabla I < t_{high}$ are considered if they form a continuous edge line with pixels where $\nabla I > t_{high}$.

In our approach, we use one of these methods to detect feature points in both the fixed and moving image. An example of application of these methods is illustrated in Figure 4.7. It is important to assure that we find the corresponding feature coordinates in both images. For this task, a normalized cross-correlation function is used to adjust each pair of control points. The algorithm moves the position of a control point by up to 4 pixels, in order to adjust the coordinates with an accuracy up to one tenth of a pixel. Then, the set of corresponding pairs is added to the nodes of the artificial grid, as shown in Figure 4.8.

4.3.2 Key feature 2: introduction of an artificial grid

An artificial grid is used to control the smoothness of the B-spline grid of the control points ($\Pi_{i,j,k}$).

Let s_x and s_y be the generic image I size in the x-y plane and $p_{x,y}$ the number of points in the artificial grid in x and y directions. We assume the grid to be rectangular and regular. The size of a grid element is determined as:

$$\begin{aligned} dx &= s_x / p_x \\ dy &= s_y / p_y \end{aligned} \tag{4.17}$$

The artificial grid is initially built for the fixed image (G_F). At this point, a transformation is performed on the feature points previously detected $\{\Pi^i(I_F), \Pi^k(I_M)\}$. The transformation used is generally a third order polynomial. An affine transformation is used when the number of pairs is less than ten, since three pairs is generally the minimum number required to fit a linear transformation, such as affine, and ten is the minimum for third order polynomial functions. Once the transformation is calculated, it is applied to the coordinates of the grid of the fixed image $\Pi^j(G_F)$, in order to find the corresponding grid nodes on the moving image $\Pi^l(G_M)$. Each point of the artificial grid is then added to the pairs of the control points in both images $\{\Pi^i(I_F), \Pi^k(I_M)\}$ to obtain Π_F and Π_M, as:

$$\begin{cases} \Pi_F = \{\Pi^i(I_F),\ \Pi^j(G_F)\}_{\substack{i=1\dots n \\ j=1\dots m}} \\ \Pi_M = \{\Pi^k(I_M),\ \Pi^l(G_M)\}_{\substack{k=1\dots n \\ l=1\dots m}} \end{cases} \tag{4.18}$$

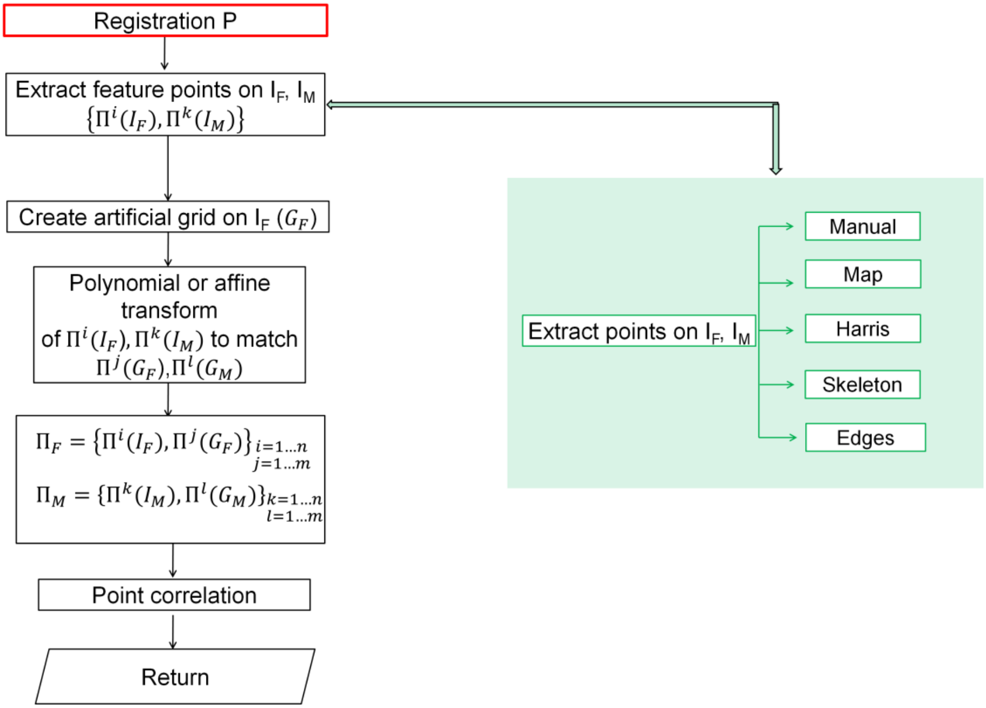

Figure 4.6: Flow chart of the point-registration algorithm with a list of methods for point extraction.

A graphical illustration of the flow chart for point registration, illustrating how the feature points are added to the artificial grid coordinates, is given in Figure 4.8.

Once these two steps are performed, the non-affine registration problem can be solved by performing first the intensity-based methods (‘Registration 1’ and ‘Registration 2’) and then the point-based method (‘Registration P’). The two intensity-based registrations methods are the critical steps of the algorithm as they incorporate the initial optimisation and minimisation problem in a sequential loop. Further explanation of the intensity-based method follows in the next paragraph.

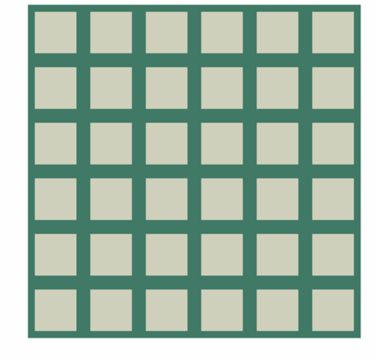

(a) Input Image

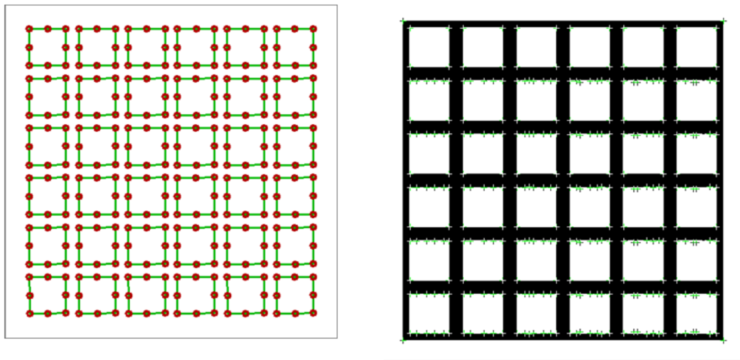

(b) Map (c) Harris

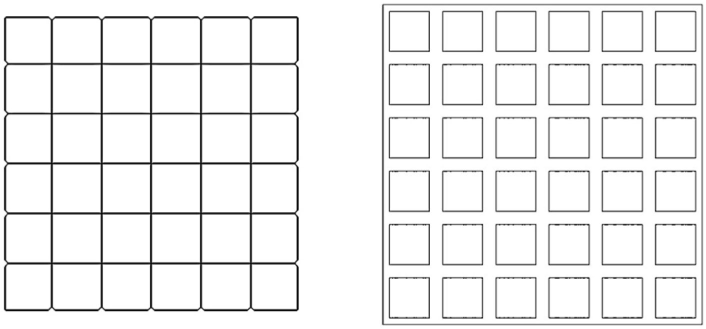

(d) Skeleton (e) Edges

Figure 4.7: Example of the four methods for feature extraction on a symmetric (a) input image, e.g. (b) map, (c) harris, (d) skeleton and (e) edges.

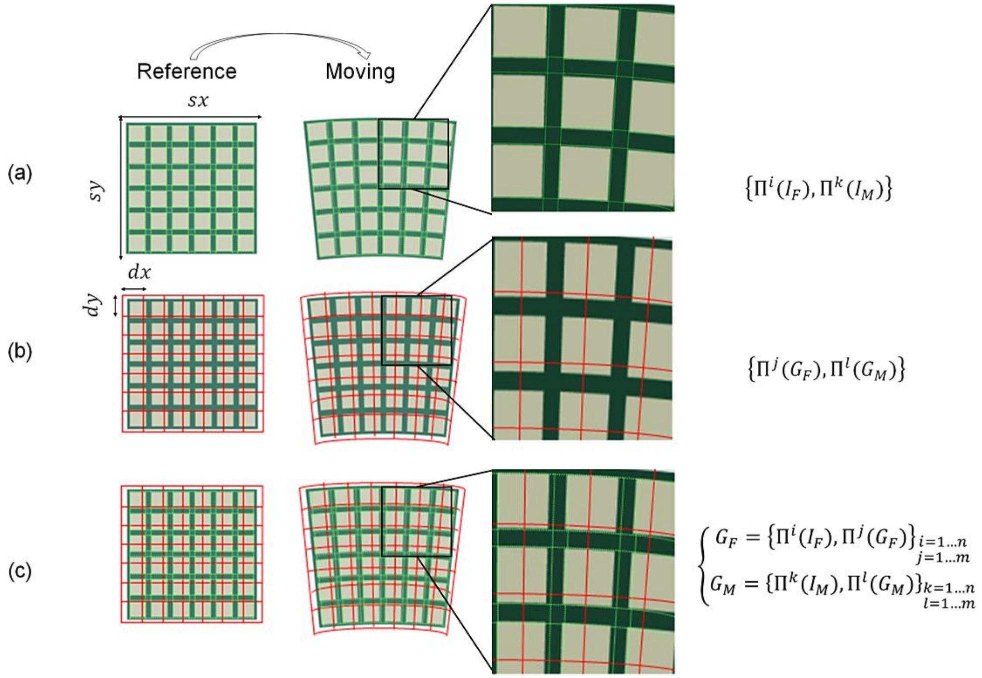

Figure 4.8: Graphical illustration of the different steps representing the two key-features of non-affine registration algorithm based on points. (a) The feature points are extracted on the reference and moving images. (b) An artificial grid is added on both images, as explained in Figure 4.6 and, finally, (c) the features points are summed to the nodes of the artificial grid in both, reference and moving images.

4.3.3 Intensity-based registration

4.3.3.1 Selection of options

As input, the reference and the moving images are given. Some options have to be first chosen: landmark, similarity and transformation type.

Landmark represents a set of initial control points, manually chosen in the reference and moving images, to control the initial B-spline grid. More specifically, if landmark is set to 0, the B-spline algorithm will start with an empty grid. If it is set to 1, a first grid is made by performing a point-registration and using the initial resulting grid. As default, landmark is set to 0.

Similarity is the second option, where two similarity criteria can be chosen: sum of squared pixel distances (SSD) or normalized mutual information (MI). Mutual information is based on the concept of information theory and expresses the amount of information that the fixed image contains about the moving image (Collignon et al. 1995, Viola 1995). The mutual information is maximized if the two images are completely aligned. However, the mutual information is not independent of the overlap between two images (Studholme et al., 1999). To avoid any dependency on the amount of image overlap, Studholme suggested the use of normalized mutual information (NMI) as a measure of image alignment:

$$\mathcal{S}(T; I_F, I_M) = \frac{H(I_F)+H(I_M)}{H(I_F,I_M)} \tag{4.19}$$

where $H(I_F)$ and $H(I_M)$ denote the marginal entropies of I_F and I_M. $H(I_F, I_M)$ denotes their joint entropy, which is calculated from the joint histogram of I_F and I_M.

Firstly, similarity is evaluated by comparing the histogram of I_F and I_M. As general rule, mutual information is applied if:

$$\sum |hist(I_M) - hist(I_F)| > 0.25 \tag{4.20}$$

In our study, similarity is chosen to be SSD, since the difference between the two histograms of grey levels (the reference and moving ones) is smaller than 0.25.

Then, a three step procedure follows. The steps consist of (1) a refinement loop, (2) an optimization problem in which (3) a minimization loop is implemented, which ends when a minimum is found. Figure 4.9 describes the algorithm in details.

4.3.3.2 Refinement loop

It is common to start the registration process using images that have lower complexity in order to increase the chance of successful registration. The images are iteratively smoothed with a gaussian filter and their sizes are reduced in order to make the algorithm operating faster. The Gaussian filter and the resizing procedure are implemented in a loop within the non-affine registration algorithm. Smoothing the input images is important when there is a considerable amount of noise or the noise pattern in the fixed and moving images is very different. The smoothness operation is not performed in the last step but the optimal transformation, as found in the previous iterations, is directly applied on the original image in order to obtain the final optimal transformation. The refinement loop ends when the number of iterations equals the maximum number of grid refinements $\zeta_{x,y,z}$, as defined in equation 4.9.

4.3.3.3 Optimization problem and minimization loop

Rueckert et al. 1999, describe the optimization problem in terms of minimizing a cost function, as given in equation 4.3, where the optimization proceeds in several steps in order to improve the computational efficiency. First, the affine transformation $T_{global}(x, y, z)$ is optimized, which corresponds to optimizing the similarity between the two images, where the penalty term of the cost function in (4.9) is zero. During the subsequent stage, the non-affine registration parameters are optimized. In each stage, a simple iterative gradient descent technique is used stepping in the direction of the gradient vector with a certain step size. The algorithm stops when a local minimum of the cost function is found, given by the condition that $\|\nabla \mathcal{C}\| \leq \chi$ for some small positive value of χ. The minimization loop based on the gradient descent technique is implemented within a line search strategy. The descent direction can be computed by various methods, as explained in paragraph 4.2.1.1. As line search strategy, two methods are available in the algorithm: the first is the simple one based on a parametric function; the second is a normal line search method with Wolfe conditions. A detailed description of line search strategy can be found in the book of Nocedal and Wright, 2006.

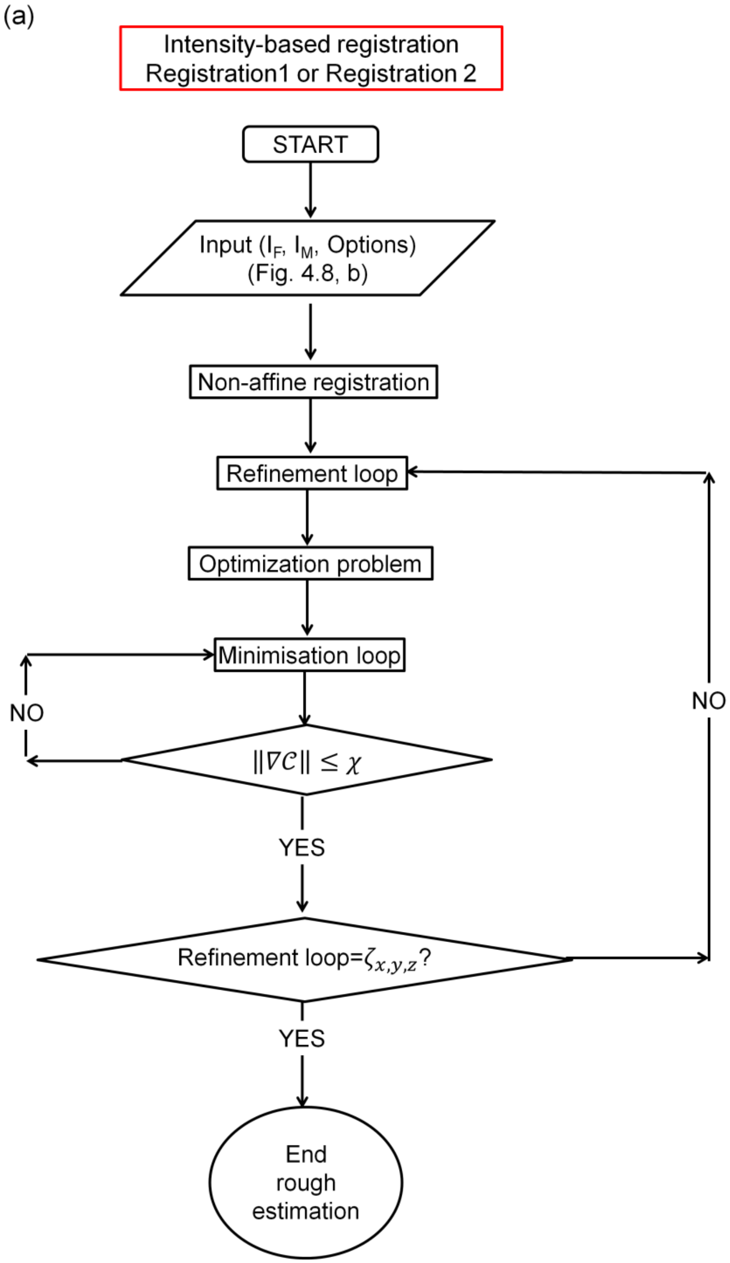
(a)
Intensity-based registration
Registration1 or Registration 2
START
Input (I_F, I_M, Options)
(Fig. 4.8, b)
Non-affine registration
Refinement loop
Optimization problem
Minimisation loop
NO
$\|\nabla C\| \leq \chi$
YES
NO
Refinement loop=$\zeta_{x,y,z}$?
YES
End
rough
estimation

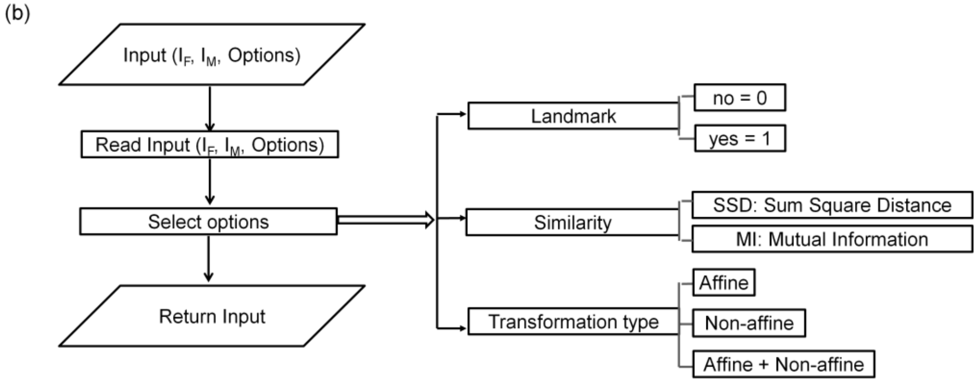

Figure 4.9: (a) Intensity-based registration algorithm. The inputs of the method and the options are specified in the grey box (b) as a subroutine of the main flow chart.

4.4 Validation of the algorithm with finite element results

The performance of the algorithm has been validated in 2D with an original fixed image I_F and a moving image I_M generated by a finite element calculation of a bending deformation, as shown in Figure 4.10a. In this example, we selected the steepest descend method to solve the optimization problem, since a better solution is found compared to the other two methods of optimization. Additionally, $\gamma = 0.01$ in ‘Registration 1’ and $\gamma = 0.001$ in ‘Registration 2’. In ‘Registration P’, we selected ‘map’ as method for point extraction. When the algorithm finds a minimum, the refinement loop is ended. The error between the reference and the deformed images is calculated for each registration type. In this case, the error (expressed as number of pixels) obtained from ‘Registration P’, i.e.0.006, is smaller than the error calculated with ‘Registration 2’, i.e. 0.009. Therefore, ‘Registration P’ is chosen for the calculation of the deformation fields and of the local strains, as reported in Figure 4.10.

The local strains calculated with our algorithm can be compared with the results of the simulation with finite element (Figure 4.11) obtained with the software Abaqus FEA. The results of simulation and registration algorithm are similar: the strains fall in the same range of value.

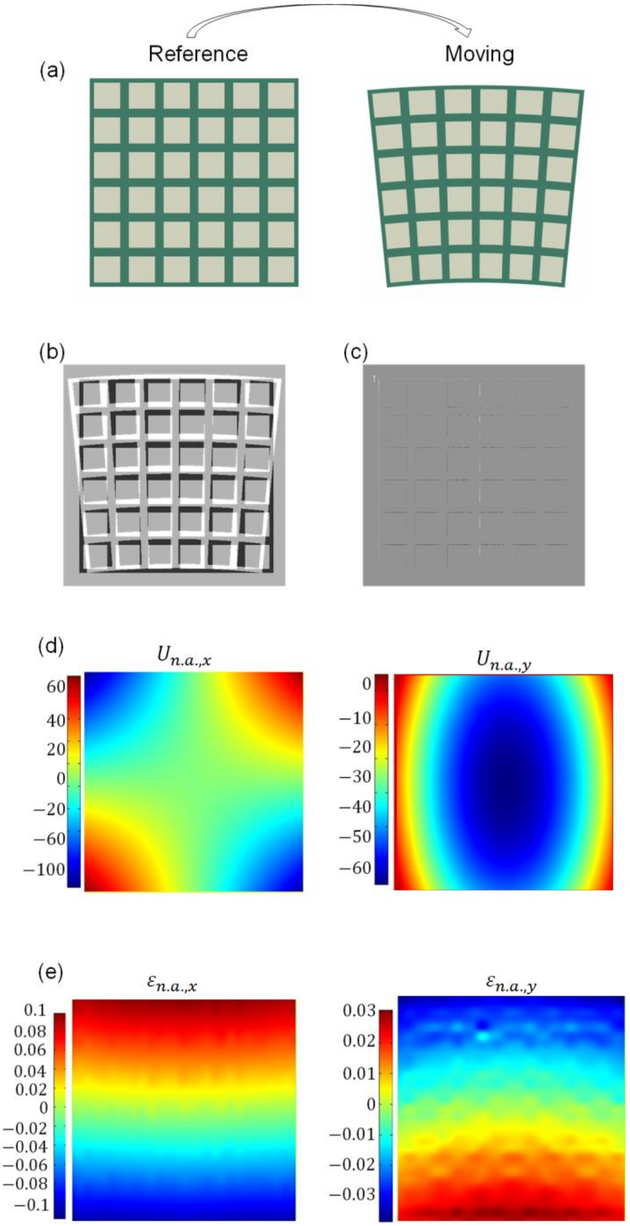

Figure 4.10: Example of application of the algorithm on an artificial image (a). The difference between reference and moving images is shown before registration (b), then after non-affine registration (c). In (d) the displacement fields in the two directions and in (e) the non-affine strains in the x-y plane are mapped on the reference image.

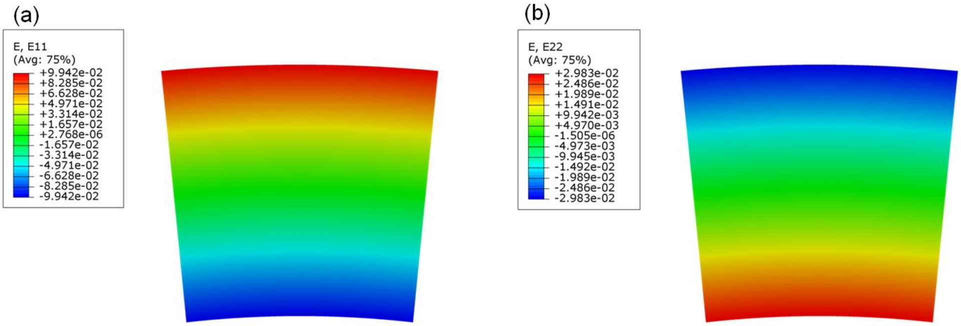

Figure 4.11: Strain fields plotted on the deformed image as result of finite element simulation, under assumption of homogeneous material. (a) The strain in x-direction (E11) is on the left side, (b) the strain calculated in y-direction (E22) is on right side.

It is important to note that the algorithm is implemented in 2D as most of the deformations in wood occur only along the tangential and radial directions. Therefore, before applying the non-affine registration algorithm, we first select a set of slices at the same plane in fixed and moving images. Then, we determine the optimal parameters for the three registrations methods, ‘Registration 1’, ‘Registration 2’ and ‘Registration P’. Finally, we run the algorithm in loop over the all stack of slices.

As a further note, the validation procedure used here could be done using more complex images, for example, on an artificially deformed grey level image of wood, exploring the capacity of the registration method in the presence of noise. Such further parametric validation is left for future work.

4.5 Conclusion

The non-affine registration algorithm introduced in this work is a powerful tool for detecting and quantifying the non-affine deformations in complex biological materials, such as wood. The algorithm contains a wide range of tools for image analysis: in particular, morphological operations, segmentation and linear and non-linear transformations. This work is mainly focused on the implementation of a non-linear transformation based on B-spline functions. Application of the algorithm follows in Chapters 6, 7 and 8.

Chapter 5

Hysteresis in swelling and in sorption of wood

In this chapter, wood-moisture interactions are studied at the cellular scale. Studies on moisture-induced deformations in wood have been described over the last century at the macro scale (lumber) and, recently, at the cellular scale with microscopy, such as reported by Murata and Masuda (2001b, a, 2006), Gu et al. (2001), Ma and Rudolph (2006), Sakagami et al. (2007). The different techniques used in these works are optical microscopy, confocal laser scanning microscopy and environmental scanning electron microscopy, which are all limited to two-dimensional inspections of the surface of a specimen.

We go one step further, employing a non-destructive technique to investigate wood tissue behaviour in different moisture states. As wood is a low absorbing material and swelling/shrinkage is a three-dimensional phenomenon, high-resolution synchrotron radiation phase-contrast X-ray tomographic microscopy is used for studying the cellular deformations.

The wood samples are either earlywood and latewood tissues, of different porosities and cell wall thickness. At the microscale, when considering wood tissues with uniform density, it is possible to decouple the effects of the growth ring layered arrangement of denser and lighter wood tissues and thus to focus especially on the role of the cell geometry and the cellular structure on these deformations.

This study is combined with a dynamic vapour sorption analysis for a better understanding of the origin of hysteresis in wood.

5.1 Homogeneous wood tissues

The wood species studied is Norway spruce (*Picea abies* (L.) Karst). A 10 × 10 × 10 mm^3 wood cube with excellent alignment of the wood grain along the cutting directions is chosen to provide homogeneous specimens of earlywood and latewood of uniform density (porosity). From this cube in wet state, 0.5 mm thick slices are cut with a microtome. A razor blade is then used to complete the cutting under a light microscope to produce thin toothpick-like pins of 500 µm × 500 µm × 8 mm in the tangential, radial and longitudinal directions, respectively. The individual wood cells are perfectly aligned along the longitudinal direction of the samples and each sample is composed of cells of similar size, as verified by optical microscopy. We use a set of four samples of different density: two denser latewood samples (LW1 and LW2) with thick cell walls and small lumens and two earlywood samples (EW1 and EW2) with thin cell walls and large lumens.

After cutting, the specimens are oven dried at 60°C. The dry samples are fixed vertically to a sample holder using cyanoacrylate glue and then kept in a desiccator in equilibrium with a salt-saturated aqueous solution, as an adsorption preconditioning close enough to the experimental starting point. For the preconditioning, we use the $MgCl_2$ salt, yielding a relative humidity of 33%.

Volume renderings of the four samples in dried state are shown in Figure 5.1. The 3D visualizations are performed with the software for image analysis and visualization VG Studio MAX 2.2.

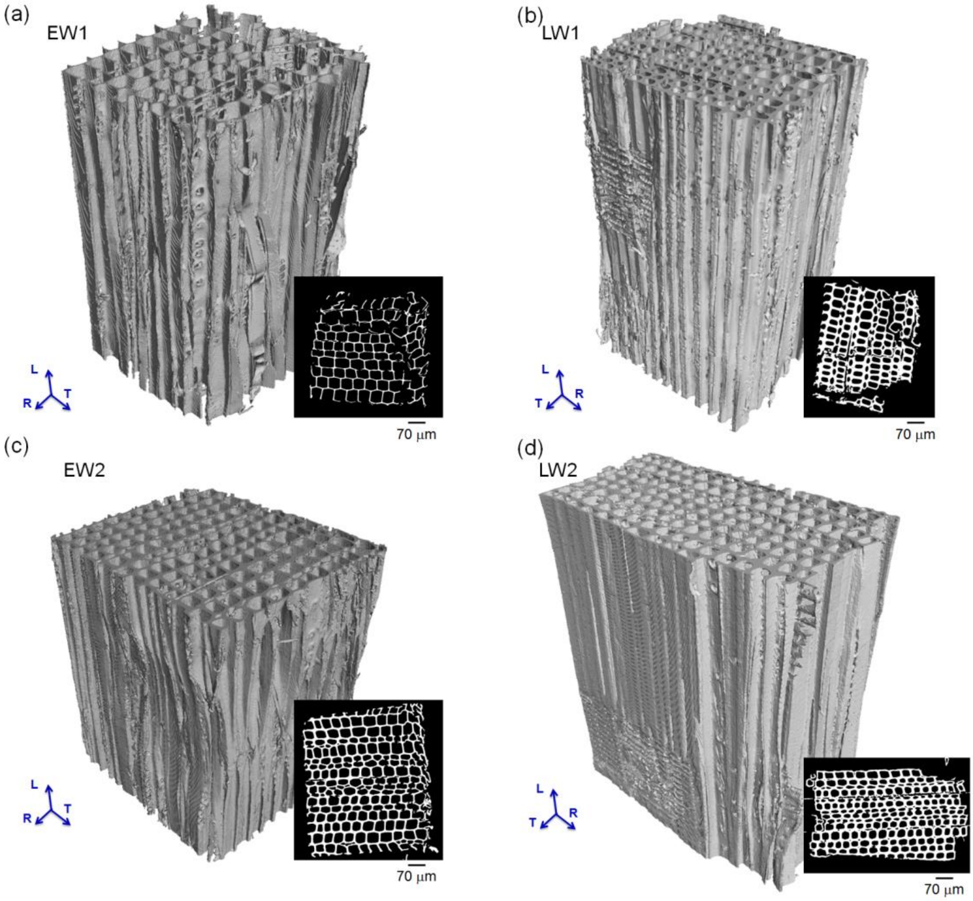

Figure 5.1: Volume rendered CT scans of the four wood samples with different porosity: (a,c) two earlywood (EW1, EW2) and (b, d) two latewood (LW1, LW2).

5.2 Experimental work

The general information on the experimental setup and the synchrotron radiation-based phase contrast X-ray tomographic microscopy (srPCXTM) can be found in Chapter 3. Information specific to this experiment follows. The wood samples are located inside an aluminium environmental chamber. During the experiments, the samples are exposed to cyclic variations in relative humidity (RH) for hygroscopic loops in adsorption and in desorption. Samples EW1 and LW1 are exposed to five relative humidity steps in adsorption (25% - 50% - 65% - 75% - 85%) and four in desorption (75% - 65% - 50% - 25%), then two additional steps to 10% and 25%RH. Sample EW2 is exposed to five relative humidity steps in adsorption (15% - 35% - 55% - 70% - 80%) and four in desorption (70% - 55% - 35% - 15%) and sample LW2 is conditioned to five relative humidity steps in adsorption (15% - 35% - 55% - 75% - 80%) and two in desorption (50% - 15%). The values within the brackets are the set values, the actual RH values in the environmental chamber are indicated in Figure 5.3. The RH conditions at each step are maintained long enough to ensure moisture equilibrium in the samples, i.e. one hour, as verified in advance by dynamic vapour sorption (DVS) measurements. Each experiment, including the total RH-protocol, lasted a total time of 12 to 16 hours.

The tomographic measurements are performed at the TOMCAT beamline of the Swiss Light Source, Paul Scherrer Institute, Villigen, Switzerland. The photons, after interacting with the sample, are captured on a 2048×2048 pixels CCD camera with a 14 bit dynamic range. The configuration used leads to a field-of-view of 720×720 μm^2 and a nominal pixel size of 0.35 μm/pixel. During our experiments, the sample-detector distance is approximately 30 mm, in the Fresnel zone (near field). The radiographic projections (generally 1024 with a 2× binning factor) are made at equiangular positions over a total rotation angle range of 180°. The exposure time for each radiographic measurement is around 75 milliseconds. Two flat-field (no sample) and two dark-field (no X-ray beam) images are acquired at the beginning and end of each tomographic scan, in order to compensate for the non-uniformity of the beam and the presence of above-average noisy (‘‘warm” and/or ‘‘hot”) pixels in the CCD detector. As wood has a low X-ray attenuation coefficient, the phase contrast tomography method is used. The difference in density at the boundary between air and wood is the source of phase contrast, thus in the X-ray index of refraction. The 3D spatial distribution of the index of refraction is estimated by an approach based upon a modified transport of intensity equation (Bronnikov 2002, Groso et al. 2006), as discussed in Chapter 2.

During our experiments, the detector is at a distance of approximately 30 mm from the sample, in its Fresnel zone (near field). 1001 (plus two dark fields and 2 flat fields) radiographic projections are made at equiangular positions over a total rotation angle range of 180°. After reconstruction, a tomographic dataset consists of 1024 radial-tangential cross section images (or slices) stacked at one pixel interval along the longitudinal direction. Each cross-section image has 1024×1024 pixels. As the mass of the sample is not recorded during X-ray tomography, we perform twin experiments using a dynamic vapour sorption instrument (VTI-SA+ Vapour Sorption Analyser, DVS), to obtain the actual moisture content. Thus, after the experiments, the samples are kept in a desiccator with desiccant (RH=0%) until the start of the DVS measurements. The sorption measurements are performed on the top portion of the tomographic samples (to exclude any cyanoacrylate glue) and on two additional earlywood and latewood samples, of similar densities, which are cut with razor blade from 2 x 2 x 2 cm^3 wood cubes. During the experiments, each sample is exposed to the same sequence of air relative humidity steps executed for their respective tomography experiments, as shown in Figure 5.2.

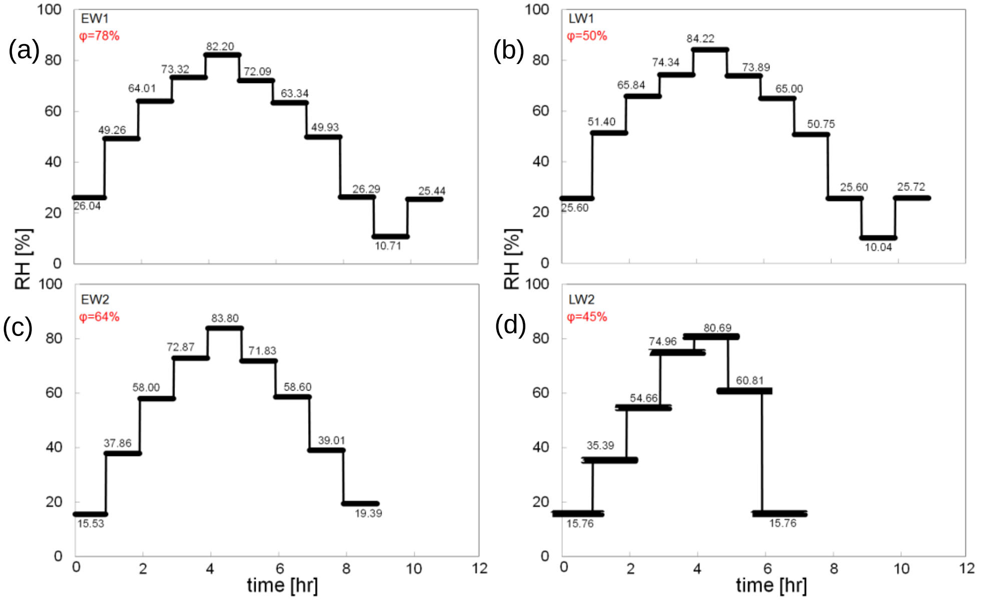

Figure 5.2: Hygroscopic loading protocols for the two earlywood (on the left) and the two latewood (on the right) samples. The values φ represent the porosity of the samples.

The sequence is repeated twice. Duration of one hour for each step is sufficient to achieve moisture content equilibrium.

5.3 Method of analysis

The tomographic data is analysed for the determination of the porosity and the swelling and shrinkage strains.

5.3.1 Determination of porosity

The cellular porosity (φ) can be defined as the ratio of the volume of the cell wall material to the volume enclosing the cell wall. Here we consider only the porosity due to the presence of the lumens. Thus we assume that the cellular wall material is solid, neglecting the porosity of the cell wall itself. By grey value thresholding, the tomographic datasets are transformed into binary datasets composed of voxels containing either cell wall material or air. Using the binary images, the wood volume is calculated by counting the number of material (white) voxels for each slice, summing up over all the stacked slices, and multiplying this value by the voxel size (0.343 μm^3). We implement here the thresholding method described in Bernsen (1986). As described in section 2.5.1.2, local thresholds are calculated taken into account neighbours and based on the pixel-wise mid-grey value, i.e. the mean of the maximum, $I_{high}(i,j)$, and the minimum, $I_{low}(i,j)$, grey values within the local neighbour, where $I(i,j)$ represents the pixel-wise grey value. If the contrast $C(i,j)=I_{high}(i,j)-I_{low}(i,j)$ is below a certain threshold, then the neighbour consists of only one class defined as background or foreground, depending on the threshold value. This thresholding yields a binarized image.

5.3.2 Determination of principal swelling/shrinkage strains using affine registration

Registration consists in the alignment of the moving to the reference image, by calculating the inverse of the transformation matrix and applying it to the deformed dataset. Affine registration, as described in section 2.5.2.1, is performed on the four datasets in order to determine the swelling and shrinkage strains along the radial, tangential and longitudinal directions. In this chapter, we assume that the affine deformation is a good approximation for describing the global deformation of the volume. We consider the state at 15% RH as the reference state (I_i) and we calculate the deformation from the reference to the states at the other RHs (I_j). The transformation matrix $\bar{\bar{A}}$, which includes twelve parameters describing the transformation, Eq. 2.32, is calculated with the software Slicer 3D (Pieper et al., 2004). Starting from these parameters and under the approximation of small displacement gradients, it is possible to calculate the principal strains along the tangential, radial and longitudinal directions.

5.3.3 Selection of the proper region of interest (ROI)

A methodology for the selection of the appropriate region of interest (ROI) is proposed. Given that any phenomenon should be studied at the appropriate representative elementary volume while the analysis of a too large dataset could require unnecessary long computational time, we perform the following analysis to select an appropriate ROI for each dataset. As first requirement, a ROI should exclude regions of the samples which present:

- deformations due to mechanisms other than swelling and shrinkage, such as buckling or deformations due to razor blade cutting;
- damages at the edges of samples;
- cracks through samples often due to sample preparation.

For each sample, we select three ROIs of decreasing cross-sectional dimensions, as shown in Figure 5.3 where ROI1 is the largest and ROI3 the smallest in each case. Each ROI volume consists of 1024 images along the longitudinal direction that are grouped into five stacks of 200 slices each, see Figure 5.4. The tangential, radial and longitudinal strains are calculated for each stack. Finally, for the obtained strains at each RH step, for each ROI, we determine the average strain values and the range of maximum and minimum values. A range is preferred to a standard deviation given that each dataset counts only five values.

Table 5.2 presents the sizes of three ROIs of each of the four samples, the number of wood cells, the number of rays stack and ray cells and the average range, also called error, on the radial and tangential strains. The ray stack is determined by counting the number of ray cells within each stack in the whole volume of interest. For each ROI, the errors, e, are given in adsorption and in desorption for the radial, e_R, and tangential, e_T, directions, respectively. Higher errors occur in regions which contain a larger or smaller number of cells, as shown in Figure 5.5. This analysis leads to conclude that the optimal ROI, i.e. the one with the smallest error or the most homogeneous behaviour, contains 20 to 50 cells. We deduce that, in smaller ROIs, localized cellular deformations due to the mismatch or restraint become more important versus the average affine deformation. For the continuation of the analysis, we use ROI1 for EW1 and LW1 and ROI2 for EW2 and LW2.

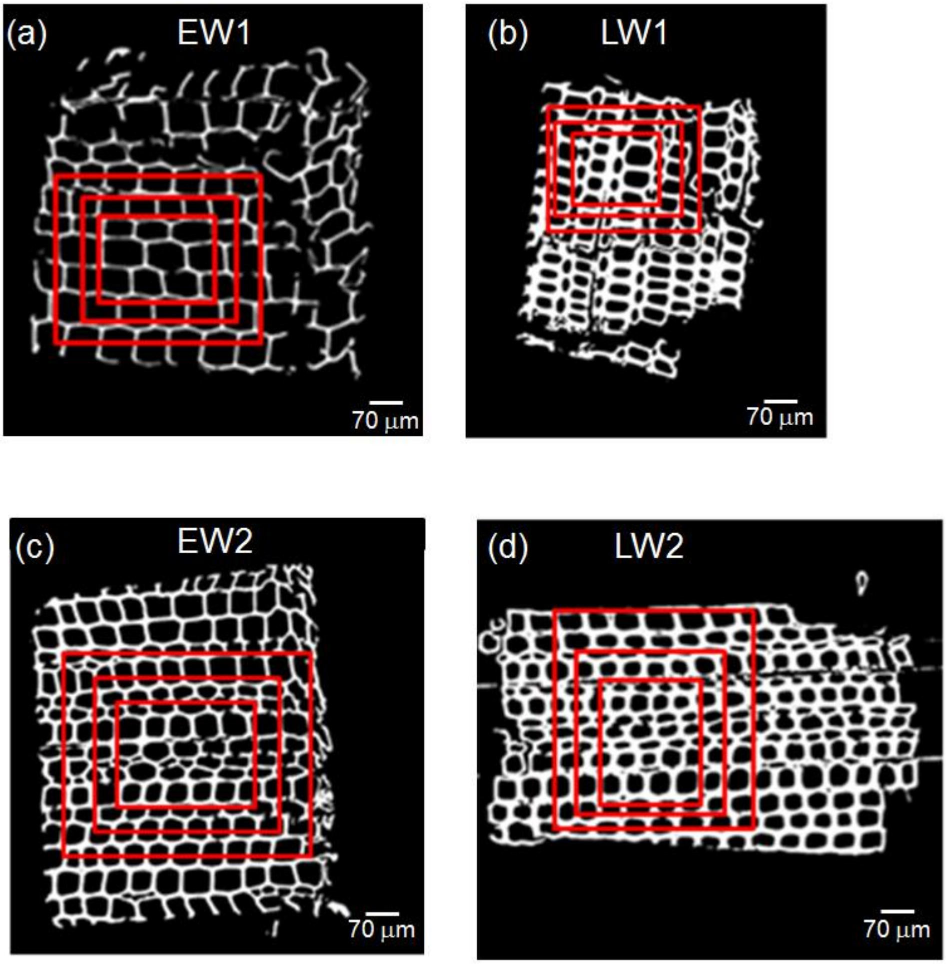

Figure 5.3: Binarized cross-sectional slice of samples (a) EW1, (c) EW2, (b) LW1 and (d) LW2. The white pixels correspond to wood cell wall material, the black ones to air. The outer region is ROI1, the middle one ROI2 and the inner one ROI3.

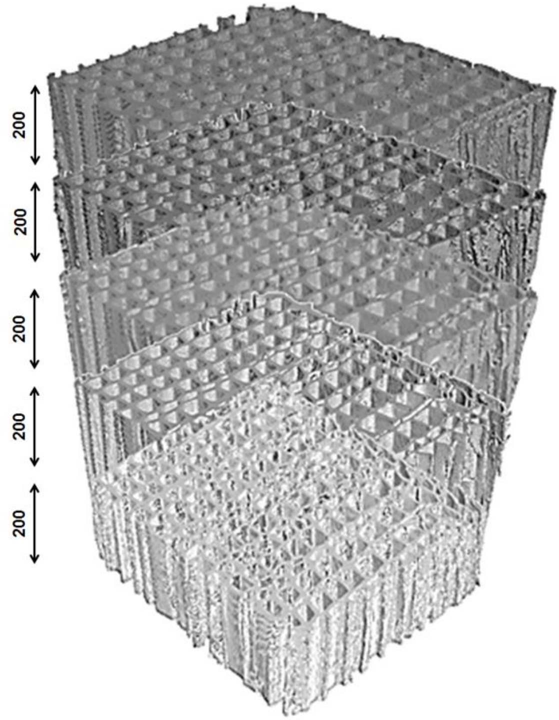

Figure 5.4: Example of 3D visualization of the five groups of 200 slices selected in the 1024-slices stacked volume in EW2.

Table 5.1: Total number of cells and ray stacks per sample. ROIs size, number of cells per ROI and error, i.e. range between minimum and maximum strains, in adsorption and in desorption. Text in bold indicate the optimum ROI for each sample.

	Sample EW1	Sample EW2	Sample LW1	Sample LW2
Total cells number	67	118	136	183
Ray stacks	6 (6-12 rays)	9 (5-10 rays)	9 (3-10 rays)	8 (3-12 rays)
ROI 1				
size [µm^2]	**210 x 140**	355,6 x 340,2	**210 x 140**	303,8 x 305,2
number of cells	**21**	129	**37**	60

average error in adsorption	**e_R= 0,031** **e_T= 0,033**	e_R=0,29 e_T=0,23	**e_R=0,048** **e_T=0,032**	e_R=0,13 e_T=0,21
average error in desorption	**e_R=0,032** **e_T=0,050**	e_R=0,12 e_T=0,10	**e_R=0,046** **e_T=0,052**	e_R=0,30 e_T=0,32
ROI 2				
size [μm^2]	105,7 x 105,7	**280,7 x 249,2**	105,7 x 105,7	**235,9 x 223,3**
number of cells	13	**46**	19	**25**
average error in adsorption	e_R=0,077 e_T=0,19	**e_R=0,034** **e_T=0,050**	e_R=0,11 e_T=0,046	**e_R=0,094** **e_T=0,15**
average error in desorption	e_R=0,17 e_T=0,14	**e_R=0,041** **e_T=0,085**	e_R=0,10 e_T=0,054	**e_R=0,045** **e_T=0,20**
ROI 3				
size [μm^2]	161,7 x 77,7	189 x 144,2	161,7 x 77,7	174,3 x 179,2
number of cells	11	15	12	11
average error in adsorption	e_R=0,039 e_T=0,12	e_R=0,076 e_T=0,065	e_R=0,18 e_T=0,11	e_R=0,32 e_T=0,19
average error in desorption	e_R=0,048 e_T=0,15	e_R=0,14 e_T=0,15	e_R=0,14 e_T=0,11	e_R=0,31 e_T=0,25

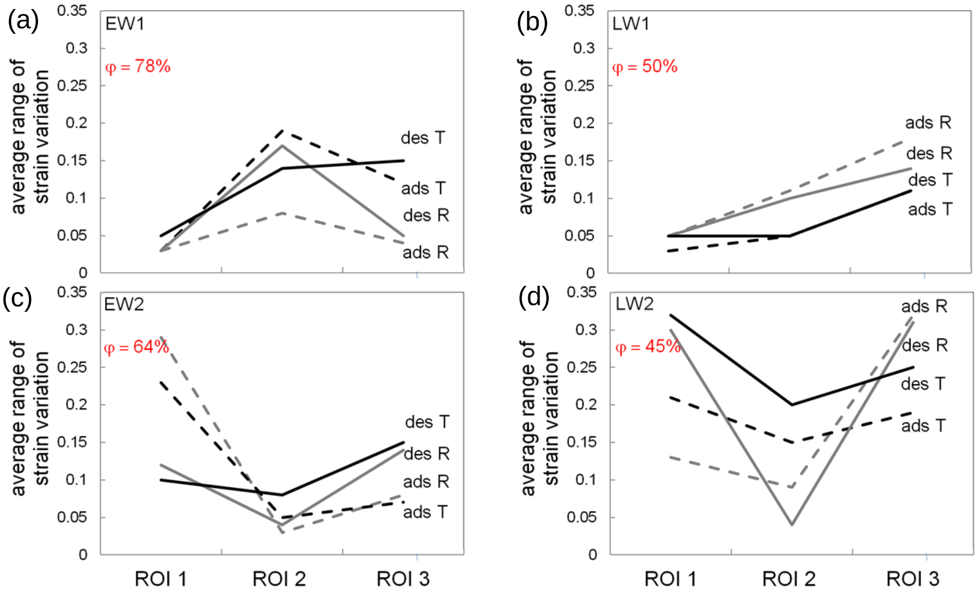

Figure 5.5: Average range of radial spruce (R) and tangential (T) strain variations in adsorption (ads) and in desorption (des) for the three ROIs for each of the four samples.

5.4 Results

5.4.1 Wood porosity and density

The binarization of the tomographic datasets at the reference state allows the determination of the porosity, determined as the ratio of wood (white) voxels compared to total (white and black) voxels of the domain, given in Table 5.2. Using the density of the cell wall material, i.e. 1500 kg/m^3 (Zillig 2008), the density of each sample is calculated, and given in Table 5.2. The four samples cover a range of porosity from 45 to 78%, i.e. a density ranging from 330 to 825 kg/m^3, which is representative of the density range found in spruce wood across the growth rings. The lighter earlywood, which contains larger lumen and thinner cell walls, presents the highest porosity, while the densest latewood consists of thick-walled cells with small lumens. Example of binarized slices for each sample is shown in Figure 5.3.

5.4.2 Swelling/shrinkage strains

The swelling/shrinkage behaviour of spruce wood is documented with high-resolution tomographic microscopy datasets. The strains are calculated for each dataset along the three orthotropic directions by affine registration. The tangential (in black) and radial (in grey) strains are given in Figure 5.6, while the longitudinal strain values are not presented as they are, as expected, less than 0.2%. The first column of the figure shows the swelling/shrinkage strains in tangential and radial directions of the four samples as a function of relative humidity, with decreasing porosity from top to bottom. The points are joined with a dash line in adsorption and with a solid line in desorption to indicate the sequence of the loading protocol (adsorption versus desorption).

Considering first the maximum swelling at higher RH (i.e. the difference between swelling strain at maximal and minimal RH), in tangential direction, as also reported in Table 5.2, the samples behave similarly except for the highest porosity sample which shows a lower swelling strain value. In radial direction, the highest porosity sample swells also much less than the other three. However here the two middle porosity samples (64% and 50%) swell less than the lowest porosity one (45%). The magnitude of the swelling strains is generally higher in tangential than in radial direction, and much more so for the highest porosity sample. The ratio of tangential to radial swelling differences is given in Table 5.2. Figure 5.7 presents the anisotropic swelling ratios during adsorption and desorption in function of porosity. It is clear the anisotropy increases with the porosity, while a quasi-isotropic behaviour (value ~ 1) is seen for the denser sample.

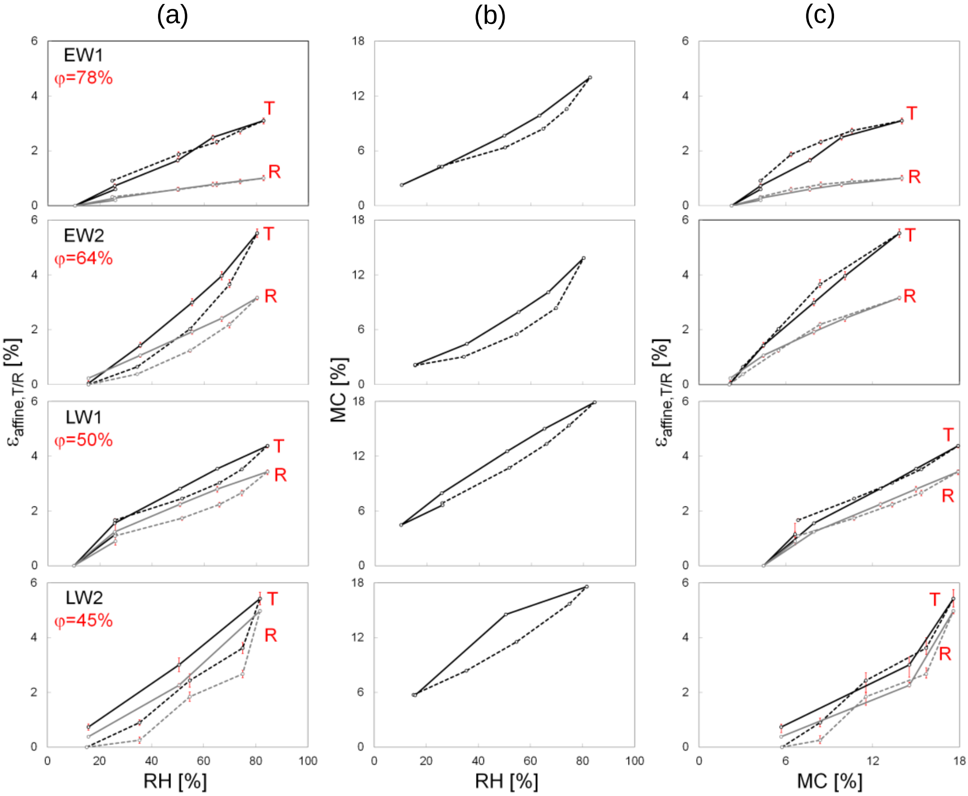

Figure 5.6: (a) Left column, strain vs. RH during adsorption (dashed line) and desorption (continued line) in tangential (black lines) and radial (grey lines) directions for earlywood samples EW1 and EW2 and latewood samples LW1 and LW2. (b) Middle column, sorption curves for the four samples in moisture content vs. RH. (c) Right column, strain in tangential and radial directions vs. moisture content for the four samples.

Table 5.2: Porosity, density, cell wall thickness, maximum swelling strain (between minimum and maximum RH) in tangential and radial directions, anisotropic swelling ratio of the four tissues.

	Sample EW1	Sample EW2	Sample LW1	Sample LW2
Porosity [%]	78	64	50	45
Density [kg/m^3]	330	540	750	825
Average cell wall thickness [μm]	3.7	5.2	5.9	7.5

$\Delta\varepsilon_{affine,T}$ (%)	3.1%	5.5%	4.4%	5.4%
$\Delta\varepsilon_{affine,R}$ (%)	1%	3.2%	3.4%	5%
Anisotropic swelling ratio	3.1	1.7	1.3	1.1

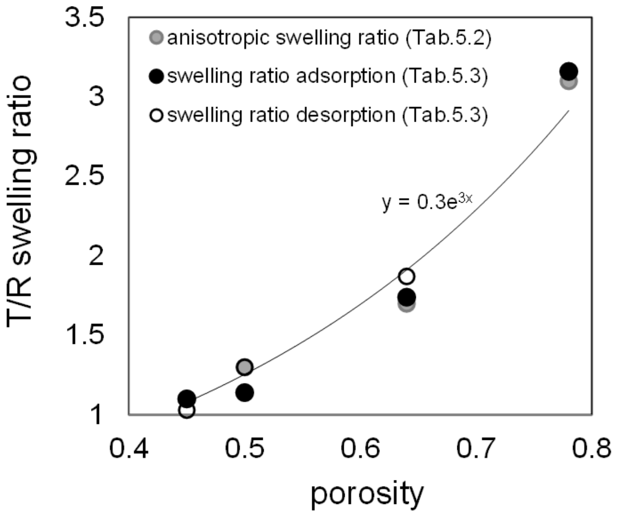

Figure 5.7: Tangential (T) to radial (R) swelling ratios versus porosity. The line represents the best fit of the swelling ratio versus porosity ratio. The grey dots are the values of the swelling ratio, as reported in Table 5.2. The filled and the empty black dots are the value β_T/β_R respectively in adsorption and in desorption as reported in Table 5.3.

5.4.3 Cell wall thickness

The cell wall thickness over the whole segmented dried volumes is computed with the software VG Studio MAX 2.0. The analysis allows the evaluation of the surface area per cell wall thickness. This study allows to consider the role of the cell wall thickness on the anisotropic behaviour of wood. The cell wall thickness ranges between 3.5 μm and 7.5 μm in the four samples. The average cell walls thickness for each the sample surfaces is reported in Table 5.2. More details are found in the Appendix. Tissues with higher porosities present smaller cell wall thickness values. As a consequence, the swelling ratio exponentially decreases with increasing cell wall thickness.

5.4.4 Hysteresis of swelling/shrinkage

All samples clearly show hysteresis in swelling/shrinkage strains vs relative humidity, except the one with highest porosity, as seen in the first column of Figure 5.8. We also observe that most strain-RH curves are closed loops, meaning that the starting and ending points of the respective adsorption and desorption coincides. Only the loop of sample LW2 is open, which may be explained by the fact that steady-state equilibrium was not achieved. Overall, the measurements display the expected reversibility of the sorption process.

To identify where lies the origin of the observed hysteresis, sorption isotherms were determined using a dynamic sorption apparatus, exposing the samples to the same steps in relative humidity as used during the srPCXTM measurements. All adsorption-desorption curves display a clear hysteresis of moisture content versus relative humidity, as shown in the middle column of Figure 5.6. Going one step further, combining the two first columns, the radial and tangential strains are plotted in function of moisture content for all the samples, in the third column of Figure 5.6. In all plots, the swelling and shrinkage strain curves almost collapse on each other. Hysteresis is thus reduced, even more so in the radial direction where it vanishes. The plots of strain versus moisture content illustrate that, at the same moisture content, the swelling strains produced by the swelling of the cell wall is the same, either in adsorption or in desorption for latewood. Since the adsorbed moisture is at the origin of the cellular structure deformation, which results in swelling/shrinkage strains, it is logical that the same amount of moisture entering or exiting the cell wall material leads to the same deformation of the cell material. This means that the main origin of the hysteresis has to be sought in the sorption behaviour and not in the swelling, which is directly related to the change in MC.

Moreover, we see that the strain-MC curves are quite linear over the total RH range with some small deviations. The slope of a linear trend line that fits the strain versus MC plots provides the linear swelling coefficient, β, reported in Table 5.3. The swelling anisotropy (β_T/ β_R) is then determined.

The results confirm the anisotropic behaviour of earlywood and the more isotropic behaviour of latewood. The swelling anisotropic ratios defined in that way coincide with the ratios obtained in Table 5.2. In homogeneous wood tissues, the absence of hysteresis in the swelling strains in terms of the moisture content indicates that the moisture content history does not play a role in the current deformation state.

Table 5.3: Swelling coefficients derived from linear fits on strains vs. MC results.

	Sample EW1 φ=78%		Sample EW2 φ=64%		Sample LW1 φ=50%		Sample LW2 φ=45%	
	T	R	T	R	T	R	T	R
β (adsorption)	0.21	0.068	0.48	0.28	0.24	0.21	0.43	0.39
β (desorption)	0.27	0.086	0.47	0.25	0.31	0.24	0.36	0.35
β_T/β_R (ads.)	3.2		1.7		1.1		1.10	
β_T/β_R (des.)	3.2		1.9		1.3		1.0	

A way to describe the importance of hysteresis is to determine the difference between desorption and adsorption curve. Thus, for the data of the first and second columns of Figure 5.6, we calculate:

$$\Delta MC = MC_{\downarrow}(RH) - MC_{\uparrow}(RH), \tag{5.1}$$

$$\Delta\varepsilon_{affine,T} = \varepsilon_{affine,T\,\downarrow}(RH) - \varepsilon_{affine,T\,\uparrow}(RH), \tag{5.2}$$

$$\Delta\varepsilon_{affine,R} = \varepsilon_{affine,R\,\downarrow}(RH) - \varepsilon_{affine,R\,\uparrow}(RH), \tag{5.3}$$

where MC, ε_T, ε_R are respectively the moisture content and the strains along the tangential and radial directions, while the arrows represent the desorption curve (↓) and the adsorption curve (↑). Then the curves are fitted with a second order polynomial function. Figure 5.8 shows the obtained values and the best-fit quadratic curves, thus the amount of hysteresis for sorption where RH and MC are normalized with respect to their higher values. We observe that the curves for the different samples with the different porosities follow the same trend, with a maximum at around a normalized relative humidity of 0.6. In order to compare and quantify the hysteresis in sorption and in swelling for the four samples, we calculate the area between the adsorption and desorption curves, i.e.,

$$< \Delta MC >= \frac{\int_{R1}^{R2} dR\, \Delta MC(RH)}{\int_{R1}^{R2} dR}, \tag{5.4}$$

$$< \Delta\varepsilon_{affine,T} >= \frac{\int_{R1}^{R2} dR\, \Delta\varepsilon_{affine,T}(RH)}{\int_{R1}^{R2} dR}, \tag{5.5}$$

$$< \Delta\varepsilon_{affine,R} >= \frac{\int_{R1}^{R2} dR\, \Delta\varepsilon_{affine,R}(RH)}{\int_{R1}^{R2} dR}. \tag{5.6}$$

The results of this calculation are reported in Table 5.4. As seen earlier, in earlywood, the swelling hysteresis is bigger in tangential than in radial direction, while the amount of swelling hysteresis is the same in both directions in latewood. We may conclude that hysteresis in swelling increases with wood porosity, but more data is needed to confirm the observed trend.

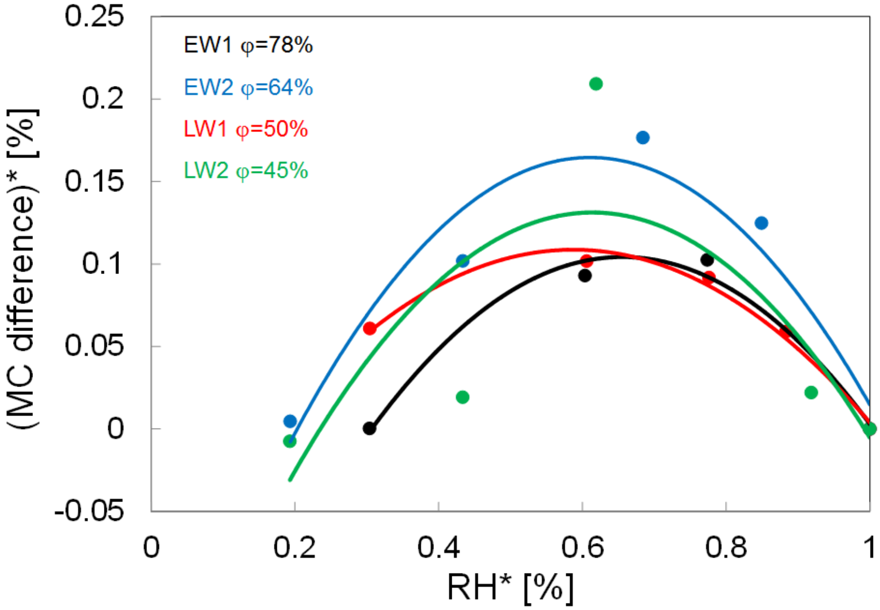

Figure 5.8: Normalized (*) moisture content differences versus normalized RH for the four samples.

Table 5.4: Area under the normalized ad- and desorption curves.

	Sample EW1 φ=78%	Sample EW2 φ=64%	Sample LW1 φ=50%	Sample LW2 φ=45%
$< \Delta MC >$	1.18	1.81	1.64	1.14
$< \Delta\epsilon_{affine,T} >$	0.08	0.73	0.46	0.92
$< \Delta\epsilon_{affine,R} >$	0.02	0.42	0.43	0.95

5.5 Discussion

5.5.1 Anisotropic swelling

Wood is a cellular material with a double porosity: a micro porous system of interconnecting cell lumens, which here is filled with moist air, and not participating to the swelling behaviour, and a nano-porous system of the cell wall material where vapour sorption is taking place. In the dry state, the cell wall has a porosity, although quite low, where water molecules can find readily available sorption sites. For further sorption to take place, i.e. above 2-3% moisture content, the sorption of water molecules pushes the polymeric chains apart, resulting in an increasing porosity, which may be assumed to be filled by water. This moisture-induced displacement has been demonstrated by molecular dynamics simulations (Kulasinski et al., 2014).

We have illustrated the swelling mechanism for four different wood tissues and have seen a clear dependence of anisotropy on the porosity. The wood sample with the highest porosity, thus consisiting of very thin cell walls, manifests the highest swelling anisotropy. As the cell wall is composed of a core, the S2 layer of varying thickness, bounded on both sides with restraining thin sheets, the S1 and S3 layers, it is known that thin earlywood cells have very little S2 material compared to the other tissues. So the anisotropy of highly porous wood tissue may come from a stronger presence (in proportion) of the corseting action of the S1 and S3 layers. Conversely, the quasi-isotropy of the low porosity tissues may stem from the overriding presence of the S2 layer. The experimental result confirms previous studies. Fengel and Stoll (1973) have measured the percentage of the thickness of the cell wall layers, showing that S2 is the thicker layer in both earlywood and latewood, but the two stiffer layers S1 and S3 represents a higher percentage volume in earlywood than in latewood (respectively 13% and 5% in earlywood and 9% and 3% in latewood). In Rafsanjani et al. (2013), it has been shown that the anisotropic swelling behaviour increases when the S1 and S3 layers are much stiffer than the S2 cell wall core material.

Further, at the cellular structure level, the presence of rays lying in the radial direction could also explain in part the anisotropy. On one hand, Table 5.1 shows that globally all samples have the same number of rays, although EW1 has less stacks. The rays could restrain the swelling of the thin walled tissues. However the thicker S2 layer of the low porosity tissues results in a bulky tissue that could override the reinforcing effects of rays.

To be more complete, a full discussion of the origin of anisotropy should also include the role of the cellular geometry and alignment, as wood structure is far from regular (disorder in alignment, in adjacency and in cell shapes) with earlywood cells that display a quasi-brick arrangement and the latewood cells which are more arranged like thick tubes. Simulation work indicates that part of the anisotropy may indeed stem from the variety of alignment, shape and wall thickness of the cells (Rafsanjani et al., 2012). In particular, the anisotropic swelling is found to increase when the sheath layers are much stiffer than the cell wall core material and the geometry of the honeycombs approaches a brick-like arrangement. As conclusion, the layered configuration of the cell walls may lead to the anisotropic behaviour both at the cell wall and at the cellular scale and beyond. Additionally, it is found in Rafsanjani et al. (2012) that the swelling anisotropy in periodic symmetric honeycombs is larger for low porosities while the presence of eccentricity in the cellular structure may significantly decrease the swelling anisotropy.

5.5.2 Linear swelling coefficients

The graphs of the right column of Figure 5.6 demonstrate that a change of moisture content results in a proportional change in strain. The cell wall reconfiguration due to shrinkage and swelling is thus independent of moisture content history, as shown by the absence of hysteresis in these strain-MC curves. Swelling is almost linearly related to moisture content in the hygroscopic range, although the sorption curve and the dependence of stiffness on relative humidity are far from linear. High MC can be reached due to the mechanical softening of the material, resulting in higher swelling strains and higher MC.

5.5.3 Origin of hysteresis

With the mechanism of swelling identified, we can now discuss what information could be obtained from the occurrence and magnitude of the hysteresis of moisture content versus relative humidity. For the following discussion, we use the chemical potential (μ) to describe the state of energy of the adsorbed water molecules. The chemical potential of water molecules in the air is related to the logarithm of RH at a given relative humidity. The sorption of a water molecule on sorption site requires a certain chemical potential, μ_0, (sorption is achieved via hydrogen bonding), where 0 refers to stress free conditions (free swelling). So if sorption and desorption would occur at μ_0, it would occur at the same relative humidity of the ambient air and no hysteresis would be observed. This is not the case for wood cellular tissues. We can thus consider that the chemical potential at absorption and desorption is different. Our hypothesis is that internal strains/stresses resulting from sorption, play a role in sorption hysteresis. The sorption sites in the material may be considered to be stretched by the neighbouring sorption sites being filled by water molecules. This stretching makes it for the site to adsorb extra water molecules. So the chemical potential at which the sorption site fills depends also on the strain. The chemical potential for sorption can be thus written as $\mu = \mu_0 + \lambda\varepsilon$. In reverse, desorption occurs only when sufficient shrinkage occurs around the sorption site to make it uncomfortable and make desorption desirable. The difference of forces induced by swelling and shrinkage is thus reflected by the difference of chemical potential required for ad- and desorption, which is actually the difference in relative humidity to obtain the same moisture content in a sorption loop (Guyer et al 2012).

The presence of a hysteresis loop in the sorption isotherms is a typical experimental observation for hygroscopic materials. Such hysteresis can be understood to be the results of different mechanisms: capillary condensation, fluid-fluid interactions or fluid-solid interactions. Since no capillary condensation occurs in wood cell material, swelling of wood clearly belongs to this last category, with fluid-solid interactions at the origin of the hysteretic swelling behaviour.

5.6 Summary

In this chapter, the hygro-mechanical properties of homogeneous wood tissues are investigated at cellular scales. In particular, four samples, two of earlywood and two of latewood, are studied. Earlywood has a more anisotropic behaviour compared with latewood which is, in contrast, isotropic. Anisotropy in wood is found to be exponentially dependent on the sample porosity. Additionally, the hysteretic behaviour of the four samples is observed in swelling and in sorption. Hysteresis disappears when the strains are plotted as a function of the moisture content, leading to conclude that hysteresis is a phenomenon related to sorption and not to swelling. In the next chapter, we extend our investigation to wood samples composed by both tissues, earlywood and latewood.

Chapter 6

Swelling of heterogeneous wood tissues

This chapter documents the sorption and swelling behaviour of combined wood tissues bridging growth ring, consisting of late and early wood tissues with different porosity. The aim is to identify the couplings and interactions between the swelling behaviour of the two tissues. In the previous chapter, it was found that latewood swells more than earlywood, and that the swelling/shrinkage strains are in the same range along the tangential and radial directions in latewood, indicating that latewood can be considered as isotropic. For earlywood, on the contrary the swelling/shrinkage strains are different along the tangential and radial directions, showing an anisotropic behaviour. In this chapter, we study the behaviour of two samples combining earlywood and latewood, subjected to adsorption and desorption loading. Then, a similar latewood/earlywood combined sample taken from the sapwood of a living tree (greenwood) is subjected to drying to document the first desorption curve, followed by an adsorption/desorption cyclic loading. X-ray tomography is used as a non-destructive tool and the phase-contrast method for volumetric reconstruction is adopted. The study is combined with a dynamic vapour sorption analysis. The results are analysed with affine and non-affine registration methods to document both affine and non-affine strains.

6.1 Experimental work

The experimental work is performed with X-ray tomography using the setup available at the Centre for X-Ray Tomography of the Ghent University, Belgium, presented in section 3.1.1. The datasets are reconstructed in phase-contrast modality with the Modified Bronnikov Algorithm (MBA), as presented in section 2.4.1.1. The air conditioning system for performing *in-situ* experiments is described in Chapter 3 and the environmental chamber used in this work is illustrated in Figure 3.1c. In total, we perform three experiments: two combined samples scanned during moisture sorption from dry to wet to dry conditions and one sample imaged directly from its green state and, successively, subjected to cyclic hygroscopic loading. The two experiments are described below.

6.1.1 Combined samples from dry to wet conditions

Two samples of Norway spruce (Picea abies) are investigated during rewetting from dry steady state conditions. A 10 × 10 × 10 mm^3 wood cube with excellent alignment of the wood grain along the cutting directions is chosen to provide wood specimens combined of earlywood and latewood. From this cube, 0.5 mm thick slices are cut with a microtome. A razor blade is then used to complete the cutting under a light microscope to produce thin toothpick-like pins of 500 µm × 500 µm × 8 mm in the tangential, radial and longitudinal directions, respectively.

During the experiments, the samples are exposed to cyclic variations in relative humidity (RH) for a hygroscopic loop protocol in adsorption and in desorption. Specifically, the wood samples are exposed to five relative humidity steps in adsorption (25% - 50% - 65% - 75% - 85% RH) and five in desorption (85% - 75% - 65% - 50% - 25% RH). The RH conditions at each step are maintained long enough to ensure moisture equilibrium in the samples, i.e. one hour, as verified in advance by dynamic vapour sorption (DVS) measurements. Each experiment, including the whole RH-protocol, lasts a total time of approximately 20 hours.

As experimental setup, the configuration adopted is the conventional X-ray tube for lab-based tomography, described in section 3.1.1, with a X-ray energy of 20 keV. Some parameters requiring optimization for the two samples, such as source to detector distance (SDD), object to detector distance (SOD), field of view (FOV), are specified in Table 6.1. The exposure time is of 2000 ms for both samples, resulting in the time needed to acquire a full dataset to be 73 minutes for sample ELW_1 and 91 minutes for ELW_2.

Table 6.1: Source to detector distance (SDD), object to detector distance (SOD), field of view (FOV) for the three combined samples.

	SDD [mm]	**SOD [mm]**	**FOV [pixels]**
ELW_1	107.35	5.56	1002×1603
ELW_2	107.35	5.56	1102×1603
GW	107.35	5.60	1641×1602

The optical configuration adopted in this case leads to an image size of $800.8\times800.8\ \mu m^2$ along the tangential/radial cross-sections and a pixel size of 15 μm.

Volume renderings of the two samples in dried state are shown in Figure 6.1. The 3D visualizations are performed with the software for image analysis and visualization VG Studio MAX 2.2.

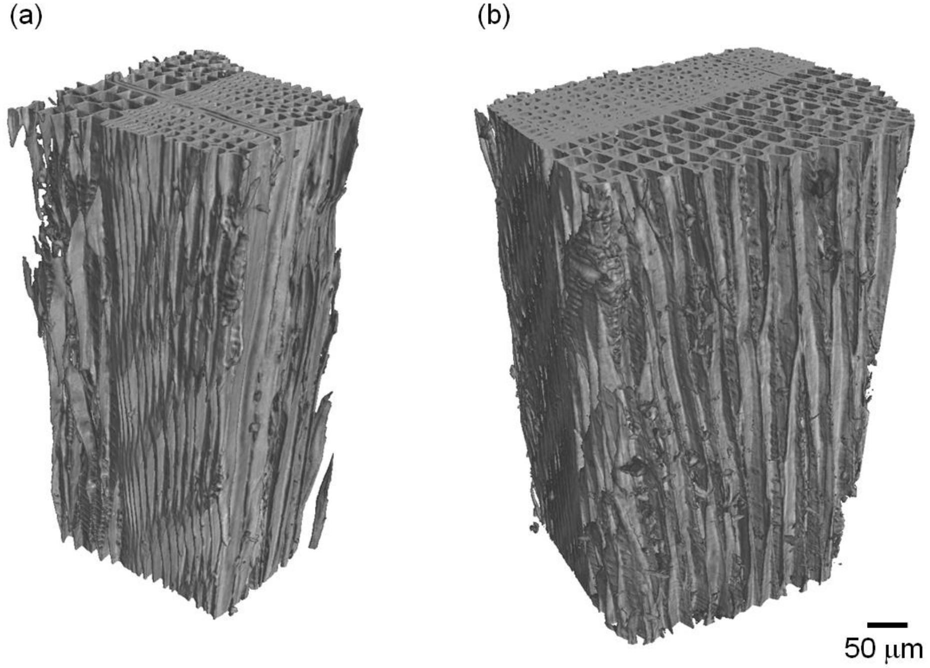

Figure 6.1: Volume rendered CT scans of the two combined wood samples: (a) ELW_1 and (b) ELW_2.

A main drawback of X-ray tomography is the inability to directly measure moisture content. In order to combine the deformations in wood due to hygroscopic loadings with the actual moisture content, we perform twin experiments using a dynamic vapour sorption instrument.

The three samples, after image acquisition, are kept in a desiccator with desiccant particles (RH~0%) until the start of the DVS measurements. The sorption measurements are performed on the top portion of the tomographic samples and each sample is exposed to the same sequence of air relative humidity steps that is executed for their respective tomography experiments. The sequence is repeated twice. Duration of one hour for each step is sufficient to achieve moisture content equilibrium.

6.1.2 Drying from the green state

This part of the experimental work focuses on understanding the hygro-mechanical behaviour of a wood specimen undergoing a loading protocol from green to dry state followed by a full hygroscopic cycle. A 500 µm × 500 µm × 8 mm wood sample is obtained from a trunk of a Norway spruce tree from the campus of the Ghent University. The final cut with razor blade is performed in the wet state under the optical microscope to ensure an excellent alignment of the wood grain along the cutting directions and that no cracks are present in the sample. After cutting, the sample is wrapped into a plastic foil and then kept in a refrigerator until the start of the experiments, in order to maintain its initial moisture/liquid.

The configuration parameters for the scans are given in Table 6.1.

The environmental chamber is conditioned at the highest relative humidity achievable by the control system machine, e.g. at 98% RH, and kept in this state for 40 minutes before insertion of the wood specimen. The green wood specimen (GW), composed half of earlywood and half of latewood, is then inserted in the chamber and the first tomographic scan is performed with the wood sample wrapped in plastic foil. After the first scan, the foil is removed in order to continue the hygroscopic loop. The loading protocol consists of a first desorption loop (98% - 85% - 75% - 65% -25% - 10% RH), followed by a full hygroscopic cycle in adsorption (10% - 25% - 65% - 85% RH) and in desorption (85% - 65% - 25% - 10% RH).

Three-dimensional visualization of spruce wood in its green state is shown in Figure 6.2a, where the lumen is almost fully filled with water. A feature, common in spruce wood and called resin pocket, is observed (see Figure 6.2b), having the form of an elongated lens amongst the cells but appearing empty of resin. As no resin is present in the pocket, it will not influence the hygro-mechanical behaviour of the sample.

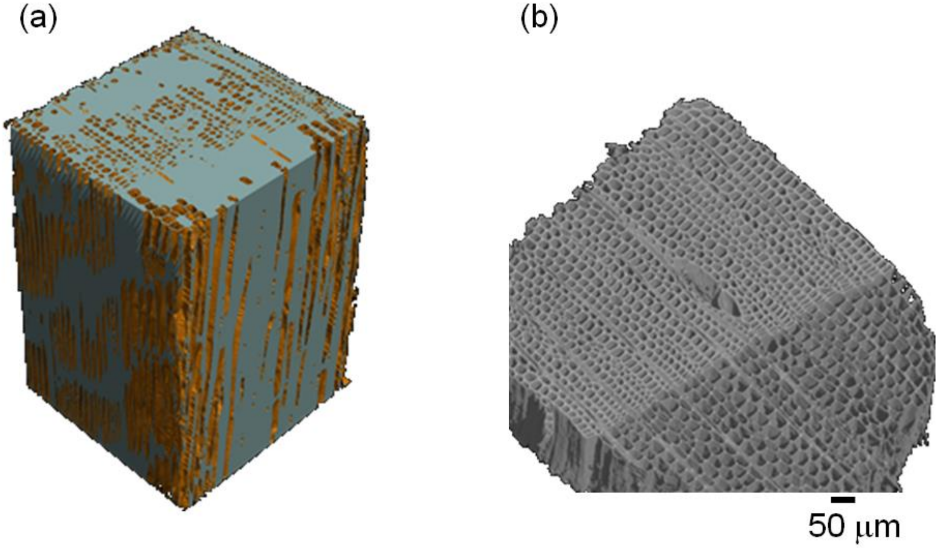

Figure 6.2: (a) Volume rendering of green wood sample with the lumens filled with sap. (b) Resin pocket in green wood in dry state.

6.2 Method of analysis

The tomographic datasets are first analysed for the determination of the swelling and shrinkage strains with affine registration, as described in section 2.5.2.1. Then, three-dimensional non-affine deformations are analysed with the non-affine registration algorithm described in Chapter 4. A further analysis is performed in this investigation, based on segmentation and morphological operations, in order to highlight the role of rays on wood behaviour. The procedure for isolating the ray cells from the cell wall of wood is explained next.

6.2.1 Ray cells in wood cell wall

The ray cells are segmented from the longitudinal/tracheid cells of the datasets in order to document their position within the specimen. This information is taken into account in the investigation of the influence of ray cells on the swelling/shrinkage behaviour of wood performed with non-affine analysis. The procedure of ray segmentation is performed with the software for image analysis and visualization Avizo Fire 8.1 and the main steps are illustrated in Figure 6.3. After volume rendering, an interactive thresholding method (Bankman, 2008) is used to segment lumens/voids and wood cell wall (Figure 6.3b). Then, an analysis to determine the orientations of lumens is performed. As rays are almost perpendicularly oriented to the tracheids, a filter based on orientation is applied to separate rays from lumens. Morphological operations of dilation and erosion are performed on the ray cells to determine the thickness of ray cell walls. Finally, a subtraction between the internal tubes of the segmented rays (in Figure 6.3c) and the same tubes after dilation is applied to extract the cell wall of the ray cells (Figure 6.3d). The results can be saved as 3D tiff files to be imported in VG Studio MAX 2.0 for the estimation of the cell wall thickness of ray cells.

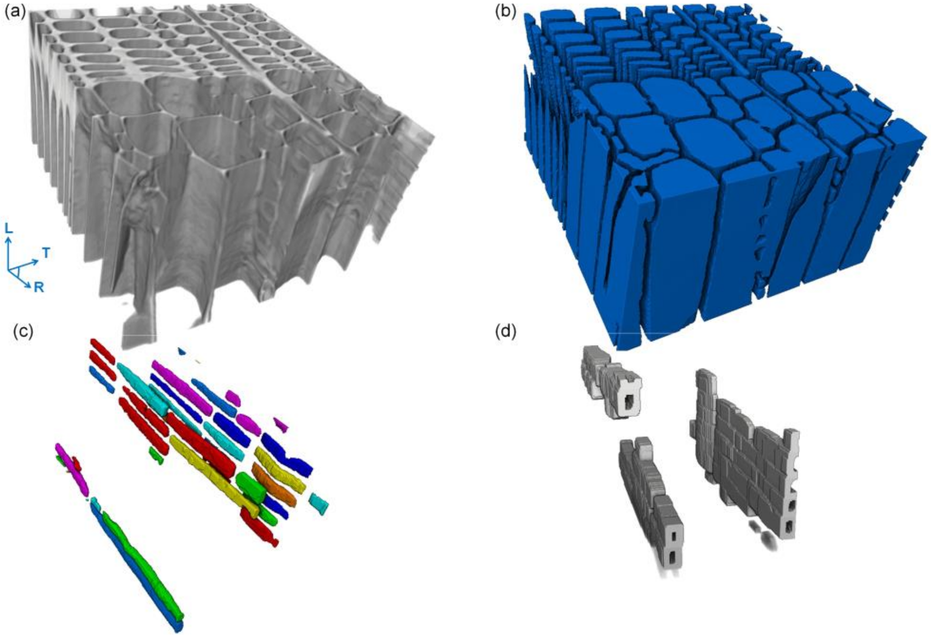

Figure 6.3: Example of ray detection and segmentation. (a) The volume is uploaded and volume rendering is performed. (b) The voids and lumens are separated from the cell wall through iterative segmentation. (c) Filter analysis is

applied on the segmented volume to obtain only the ray tubes. (d) The cell wall thickness of the rays is obtained using dilation and arithmetical operations.

6.2.2 Determination of swelling/shrinkage behaviour of wood cell wall

The affine registration (section 2.5.2.1) is performed on the three datasets of wood in order to determine the swelling and shrinkage strains along the radial, tangential and longitudinal directions between a reference state and each subsequent state. For each sample, three regions of interest (ROIs) are considered, one containing both earlywood and latewood tissues, one only earlywood and one only latewood. Then, the non-affine registration (see Chapter 4) is performed in order to capture locally the deformations of the wood cellular structure.

6.3 Results

In this section, we first show the results obtained by applying different algorithms of reconstruction in order to point out the importance of using phase-contrast techniques for wood materials. Then, the ray cells anatomy is documented at the cellular level. A descriptive discussion on the swelling/shrinkage behaviour of wood as result from affine and non-affine registration methods is then carried out.

6.3.1 Image reconstruction results

We use Octopus (Vlassenbroeck, 2009), which is a tomographic reconstruction package for parallel and cone beam geometry allowing the optimization of the parameters for phase-contrast correction. Several algorithms for image reconstruction in absorption and phase-contrast modality are implemented.

The reconstruction is first performed using the filtered back projection algorithm (FBP). Edge artefacts, background noise and low contrast are visible in Figure 6.4 a, where phase shift correction is not applied during image reconstruction. When applying phase filter to the original projections by using the MBA method as described in section 2.4.1.1, the absorption signal is eliminated and so the signal is converted to a dataset that contains only information about the phase coefficient of the sample. After applying the phase filter to the original projection data, the filtered data can be reconstructed by using the standard filtered back projection algorithm. We notice an improvement of the quality of the images (Figure 6.4 b).

Figure 6.4c shows the result achieved by using the Bronnikov Aided Correction (BAC), based on the Bronnikov approach (De Witte et al. 2009). In this case, the phase filter is used to correct the original projection images and obtain a pure absorption image, from which the attenuation coefficient of the object can be reconstructed.

Figures 6.4b and c include more information on the wood cellular structure as the noise is removed by filtering. However, Figure 6.4c shows a reduced contrast in terms of material versus background, which does not facilitate image post-processing.

Thus, in this work, we use the Modified Bronnikov Algorithm since it provides the most relevant information. After reconstruction, a bilateral filter is applied. It preserves the edges and reduces the noise. The filtering is performed in Morpho+, which is a software for image analysis developed at UGCT, in Belgium (Brabant et al, 2011; Boone et al., 2009).

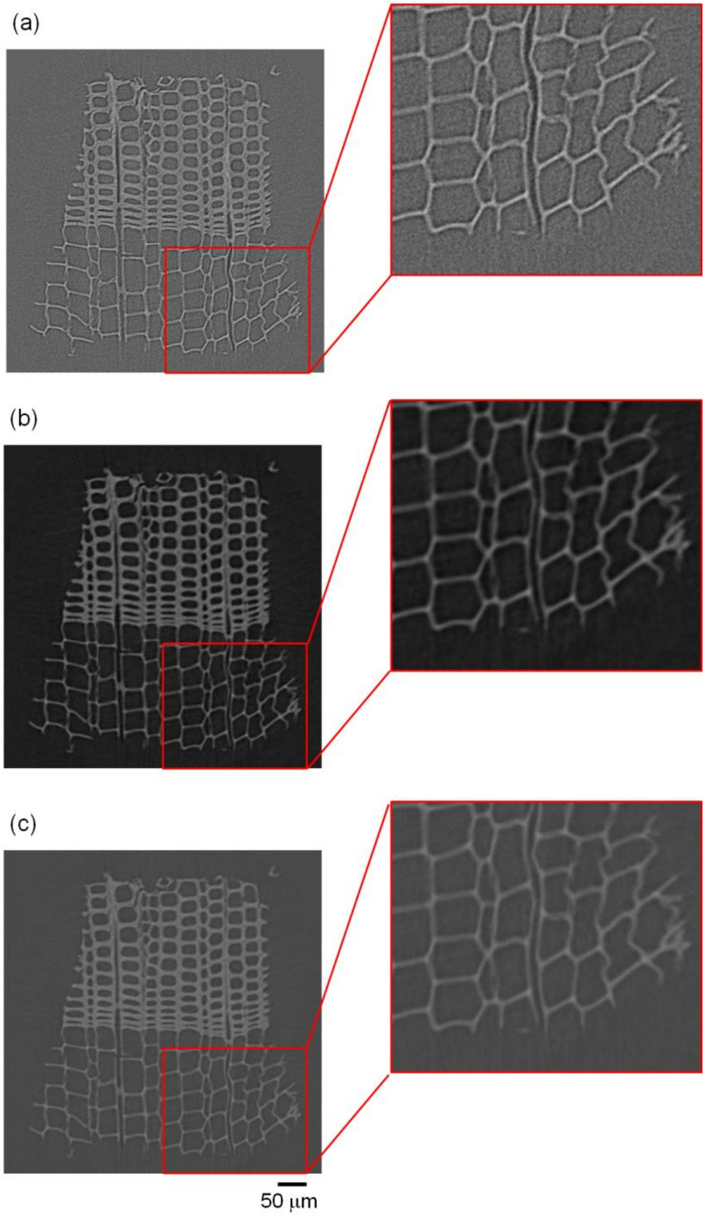

Figure 6.4: Cross-sectional view and a zoom on a region of sample ELW$_1$, where different methods of reconstruction are applied: a) FBP, b) MBA, c) BAC.

6.3.2 Ray cells in wood cell wall: anatomy

The rays anatomy of the two dry samples is extracted from the datasets. We observe that the ray cells are randomly distributed in the two tissues, earlywood and latewood. The thickness distribution of the cell wall is represented in Figure 6.5. Typical cell wall thickness for ray cells is found to vary between 5 μm and 6 μm, compared to the average cell wall thickness in earlywood of 4 μm and in latewood of 6 μm, found in Chapter 5. In total, 19 stacks (i.e. vertical arrays) of ray cells, composed of 2 up to 9 rays, are found in ELW_1 and the volume occupied by rays is equal to 7%. In ELW_2, 24 stacks of ray cells are counted, each composed by 2 up to 10 rays, occupying the 6% of the total volume. The porosity of the tissues and the volume occupied by ray cells over the total volume are given in Table 6.2 for each ROI of the two combined samples.

Table 6.2: Porosity (φ) and percentage of volume occupied by rays over the total sample volume (V_{rays}/V_{TOT}) for each ROIs in both samples.

	LW		EW		combined	
	ELW_1	**ELW_2**	**ELW_1**	**ELW_2**	**ELW_1**	**ELW_2**
φ (%)	43	48	75	73	60	61
V_{rays}/V_{TOT} (%)	3	3.2	2	3	5	5.5

It is known that rays may act as stiffeners in radial direction due to their orientation in that direction. Given the low stiffness of earlywood due to its thin cell walls, the stiffening effect of rays is much more important in earlywood compared to latewood, which shows a high stiffness due to its thick cell walls. Rays therefore contribute much more to the anisotropy in earlywood than in latewood. The affine and non-affine registration will further investigate the possible stiffening effect.

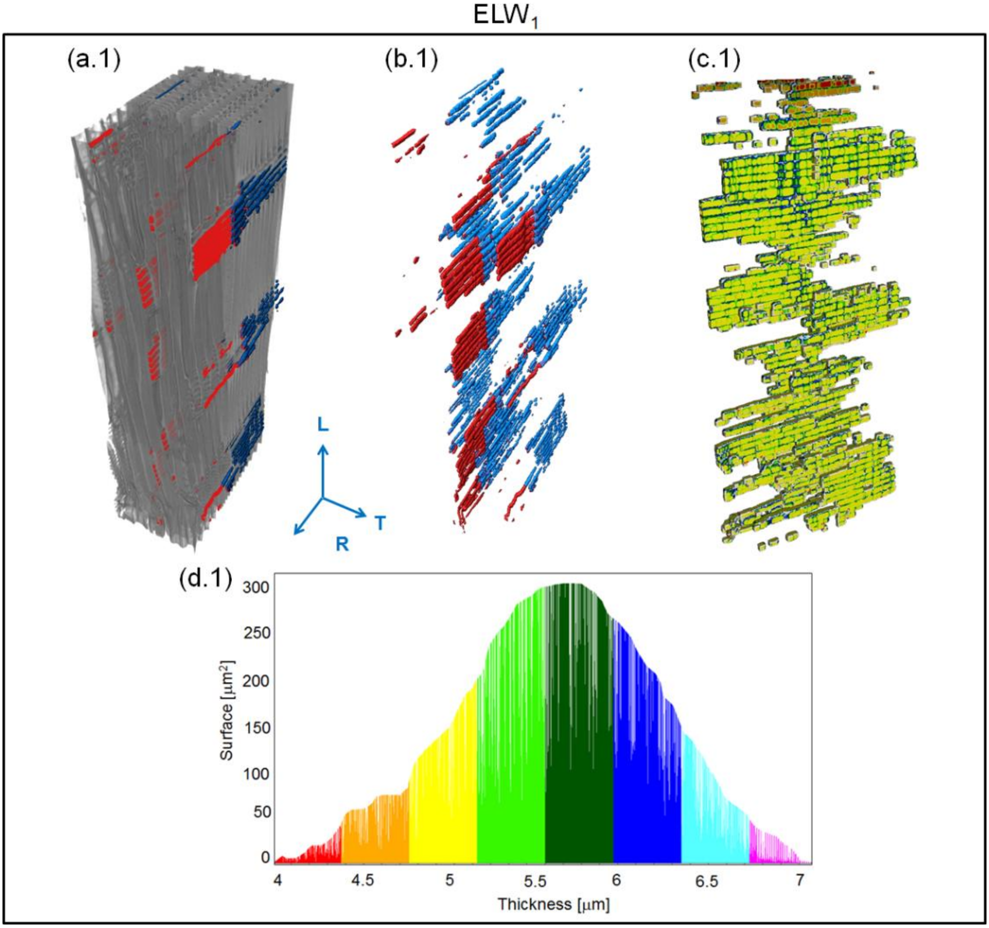
ELW$_1$
(a.1)
(b.1)
(c.1)
L
T
R
(d.1)
Surface [μm^2]
0
50
100
150
200
250
300
Thickness [μm]
4
4.5
5
5.5
6
6.5
7

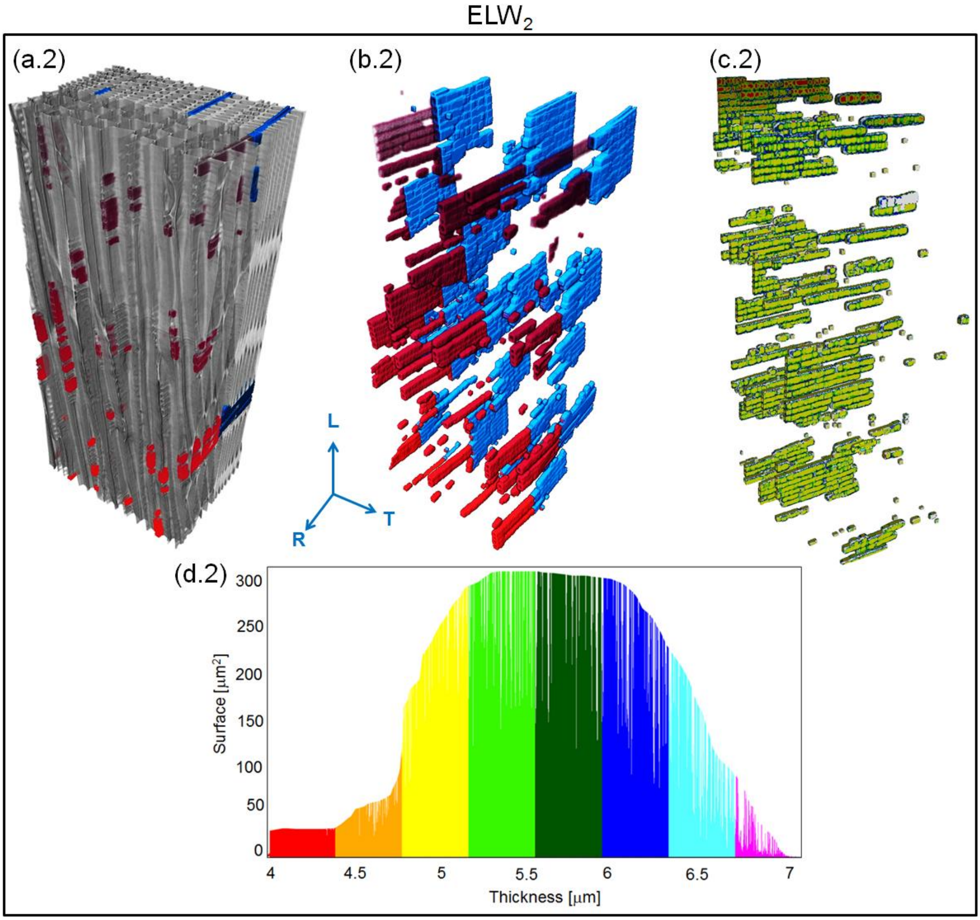

Figure 6.5: 3D distribution map of the rays for (a-d.1) ELW$_1$ and for (a-d.2) ELW$_2$ at dry state (RH=25). The ray cells in earlywood are coloured red and blue in latewood; (c) the 3D ray cell wall thickness and (d) the histogram of wall thickness values which colours are used for the distribution map of cell wall thickness.

6.3.3 Swelling/shrinkage strains

The swelling/shrinkage behaviour of spruce wood combined samples of earlywood and latewood is documented with X-ray tomography and image processing. The strains are first calculated along the three orthotropic directions using affine registration on three regions of interest (ROIs) containing earlywood, latewood and a combination of both tissues. We discuss the results of the two dry samples followed by our investigation on the greenwood specimen.

6.3.3.1 Affine swelling/shrinkage strains during cycling conditions

The three ROIs selected for the analysis of the two combined samples exposed to hygroscopic cycling from the dried state are illustrated in Figure 6.6a and b. The porosity and number of ray cells for each ROIs are specified in Table 6.2. The affine tangential ($\varepsilon_{affine,T}$) and the radial ($\varepsilon_{affine,R}$) strains are given in Figure 6.7 for the two dry samples ELW_1 and ELW_2, while the longitudinal strain values are omitted as they are very low. Each point corresponds to one tomographic dataset taken at one RH and this value is the average of 5 values of strains calculated in 5 stacks of 200 slices, as selected from the initial 1000 slices of the datasets. The left column of the figure shows the results for sample ELW_1 (a – e.1) while the right column refers to sample ELW_2 (a – e.2). Both samples present similar results for each ROI (EW, LW and ELW) analysed. The tangential and radial strains in the three regions are comparable within error bars. The affine swelling/shrinkage strains in the combined ROI (ELW) lie between the strains of LW and EW for both tangential and radial directions (Figure 6.7a and b). In latewood, the tangential and radial strains of ELW_1 are somewhat higher compared to the values in ELW_2. Hysteresis is observable in sorption and in swelling (Figure 6.7 a-b). Figure 6.7 d-e shows that hysteresis mainly disappears when the affine strains are plotted as function of MC, analogously as found in chapter 5.

We define the swelling strain difference in tangential ($\Delta\varepsilon_{affine,T}$) and in radial directions ($\Delta\varepsilon_{affine,R}$) as the swelling at 85% RH minus the swelling at 15%RH (taken zero) and the anisotropic swelling ratio as the ratio between $\Delta\varepsilon_{affine,T}$ and $\Delta\varepsilon_{affine,R}$. The results are reported in Table 6.3. The swelling difference is higher in latewood and lower in earlywood while the difference in the combined region is approximately the average between the swelling strains of the two homogeneous tissues of the sample.

The anisotropic swelling ratio in earlywood (EW) is around 1.5, while for latewood 1.0, meaning that swelling is anisotropic in EW and isotropic in LW, as already found in Chapter 5. The swelling coefficients β, calculated from the trend line of strain versus moisture content, in ad- and desorption and in tangential and radial directions, are reported in Table 6.4 for both samples. The anisotropic swelling ratios β_T/β_R in Table 6.4 can be compared with these reported in Table 6.3 and are found to be in the same range.

In Figure 6.8 we plot the anisotropic swelling ratio versus porosity, and observe that anisotropy, i.e. the ratio between tangential and radial swelling, is exponentially dependent on porosity. This result confirms the result obtained in the previous chapter and reported in Figure 5.8. Comparing the results for the single tissues (in Chapter 5, Table 5.2) with the results of the combined tissues (Table 6.3-4), we observe that the combined samples swell in general less. This reduction with 60% is attributed to the restraining effect of latewood on earlywood and vice-versa. Figure 6.8 gives also the swelling ratio for the homogeneous tissues (dashed line). We observe that the swelling ratio is lower for the combined tissues. This means that, due to the restraining effect of latewood on earlywood and vice-versa, swelling of combined wood becomes less anisotropic.

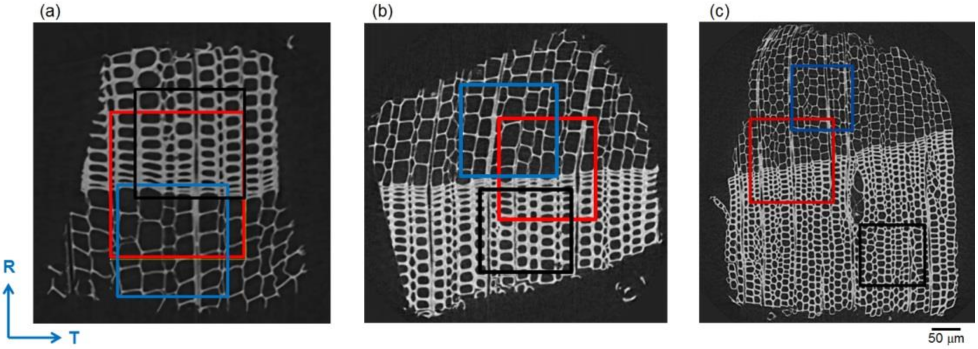

Figure 6.6: ROIs of earlywood (blue), latewood (black) and combined (red) used for calculating the strains of the two dried samples and of the green sample. (a) ELW_1 and (b) ELW_2 at dry states (RH=25%), while (c) greenwood at 10% RH after the second desorption curve.

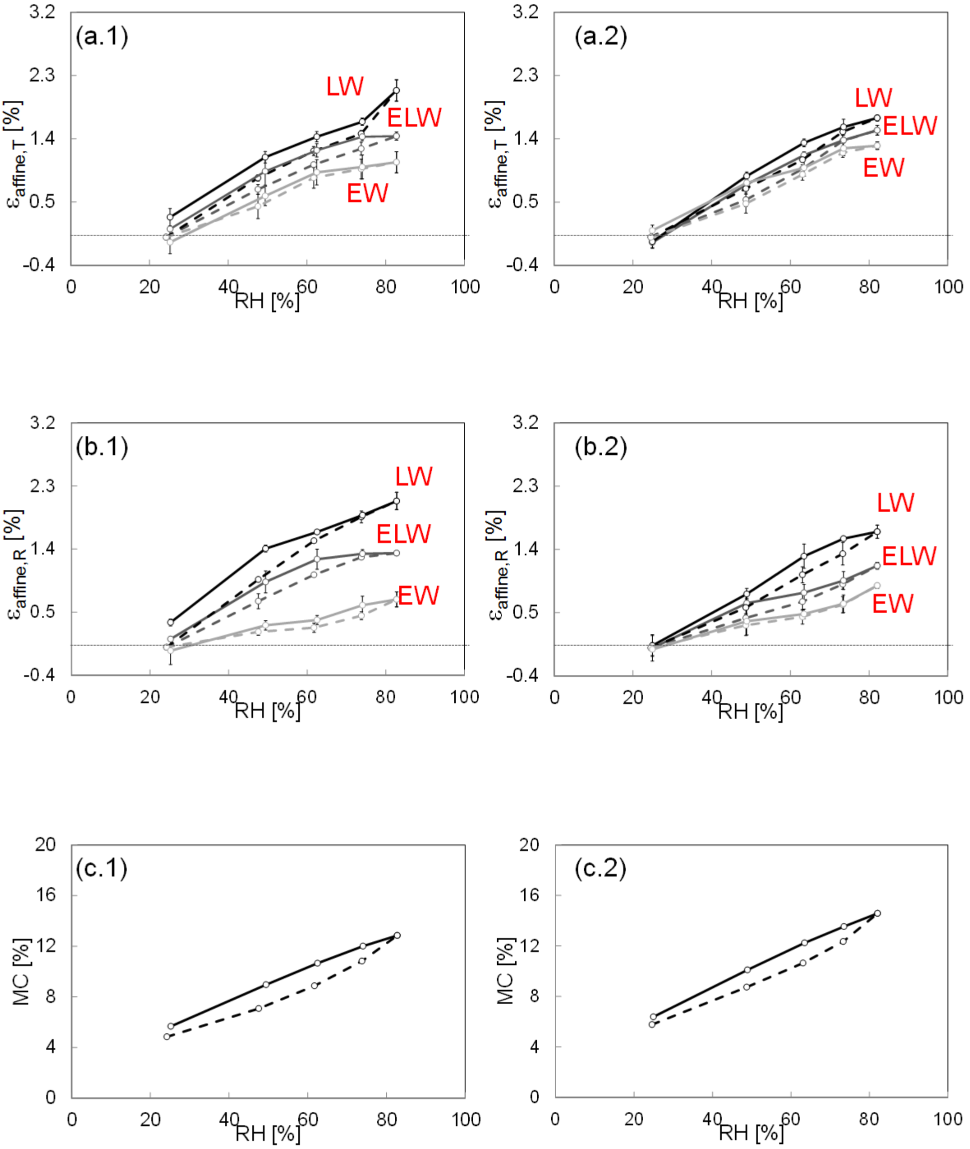

Figure 6.7: (to be continued)

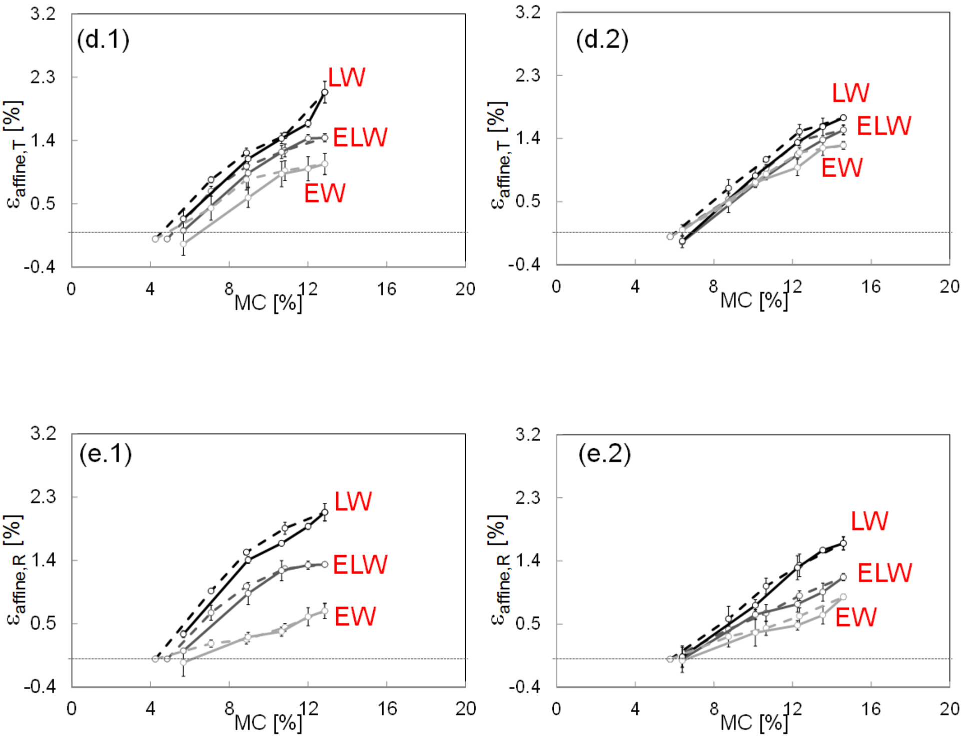

Figure 6.7 (continued): Swelling/shrinkage behaviour of ELW_1 (left) and ELW_2 (right), where the dataset at 25%RH is considered the reference state for this analysis. The tangential and radial strains are plotted versus RH in (a) and (b) respectively, while in (d) and (e) as a function of the moisture content. MC versus RH is shown in (c). The adsorption curve is indicated in dashed line, while the continued line indicates desorption. Black indicates latewood, grey combined early- and latewood and light grey earlywood. Each value is plotted with its corresponding error bar.

Table 6.3: Tangential/radial swelling difference (85%RH vs 25%RH, in adsorption) and anisotropy for samples ELW_1 and ELW_2.

	EW		LW		combined	
	ELW_1	**ELW_2**	**ELW_1**	**ELW_2**	**ELW_1**	**ELW_2**
$\Delta\varepsilon_{affine,T}$ (%)	1.1	1.3	2.1	1.7	1.4	1.5
$\Delta\varepsilon_{affine,R}$ (%)	0.7	0.9	2.1	1.7	1.3	1.2
Anisotropic swelling ratio (%)	1.6	1.5	1.0	1.0	1.1	1.3

Table 6.4: Anisotropic swelling coefficients and anisotropic ratio in adsorption and in desorption for samples ELW_1 and ELW_2.

	EW		LW		combined	
	$\mathbf{ELW_1}$	$\mathbf{ELW_2}$	$\mathbf{ELW_1}$	$\mathbf{ELW_2}$	$\mathbf{ELW_1}$	$\mathbf{ELW_2}$
$\beta_{T,ads}$	0.13	0.16	0.23	0.20	0.18	0.18
$\beta_{T,des}$	0.16	0.15	0.23	0.22	0.19	0.20
$\beta_{R,ads}$	0.08	0.10	0.24	0.19	0.17	0.13
$\beta_{R,des}$	0.10	0.10	0.23	0.20	0.18	0.13
$\beta_{T,ads}/\beta_{R,ads}$	1.6	1.6	1.0	1.0	1.1	1.4
$\beta_{T,des}/\beta_{R,des}$	1.6	1.5	1.0	1.1	1.1	1.5

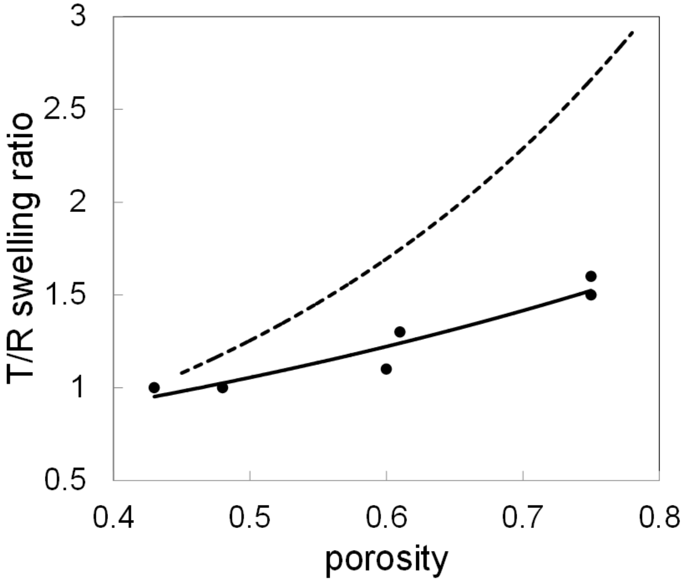

Figure 6.8: Anisotropic swelling ratio versus porosity for the six ROIs of ELW_1 and ELW_2 plotted as a continued line and compared with the anisotropic swelling ratios for homogeneous wood tissues (dashed line) as reported in Chapter 5.

6.3.3.2 Swelling/shrinkage strains of greenwood: first desorption and cyclic loading

Similarly to the dry wood samples, we analyse the green wood images with the affine registration method. For green wood, all the quantities are calculated considering the state at RH=10% after the second desorption curve as reference state.

Three regions of interest are investigated containing respectively pure latewood, pure earlywood and a region over the interface between the two tissues, see Figure 6.6c. The strains are calculated along the first desorption (Figure 6.9a and b), the first adsorption and the second desorption (Figure 6.9c to f). Figure 6.9g shows the moisture content versus RH, as measured with the DVS machine, reproducing the same conditions as during the tomographic experiment.

The sample starts from wet condition, i.e. 98%RH in the first desorption loop. The affine strains and moisture content, in the first desorption curves lie above the values calculated during the following cycling loading protocol in adsorption and desorption. For this reason, we can state that the first desorption curve is irreversible. In contrast, the states in first absorption and second desorption are reversible (closed loop).

The tangential/radial strain difference at 85% RH between first (d1) and second (d2) desorption loop in green wood is reported in Table 6.5 and calculated as:

$$\delta\varepsilon_{affine} = \varepsilon_{affine_{\mathrm{d1}}} - \varepsilon_{affine_{\mathrm{d2}}} \tag{6.1}$$

This strain difference is a measure for the permanent shrinkage strains present in wood after first drying. The permanent shrinkage strains in tangential direction are around 1% after first drying, while in radial direction they range between 0.3 and 0.55%.

It is remarkable that for greenwood, the combined tissues (ELW) display higher affine strains in radial direction than for both homogeneous tissues (EW, LW). This is in contrast with the results for the dry samples, where the strain values for the combined sample ELW were found to lie in between the results of the single tissues LW and EW. It is however important to note that the affine strains only represent part of the total strains. The total strains consist in an affine and a non-affine part. The affine strains refer to average volumetric strains, while the non-affine strains refer the local strains, like local bending and local shear deformations in the interface between the two tissues. In the next section, we determine the total strains, which give a more detailed picture of the interaction between the EW and LW.

Table 6.5: Tangential/radial strain differences between first and second desorption in greenwood sample.

GreenWood	LW	EW	combined
$\delta\varepsilon_{affine_{\mathrm{T}}}$	0.98	0.93	1.08
$\delta\varepsilon_{affine_{\mathrm{R}}}$	0.30	0.30	0.55

As a note, given that the initial dataset of greenwood, where the liquid fills also the lumens, cannot be segmented into cell wall and water, a simple calculation is performed to estimate the amount of water in this state. By binarizing the wet dataset, we found that 54% of the sample volume is either cell wall or water. At the next humidity step, when all the water is removed from the lumens, we found that 13% of the sample volume is cell wall. These values allow to make a very crude estimation of the liquid water content by volume in the lumens of around 40%.

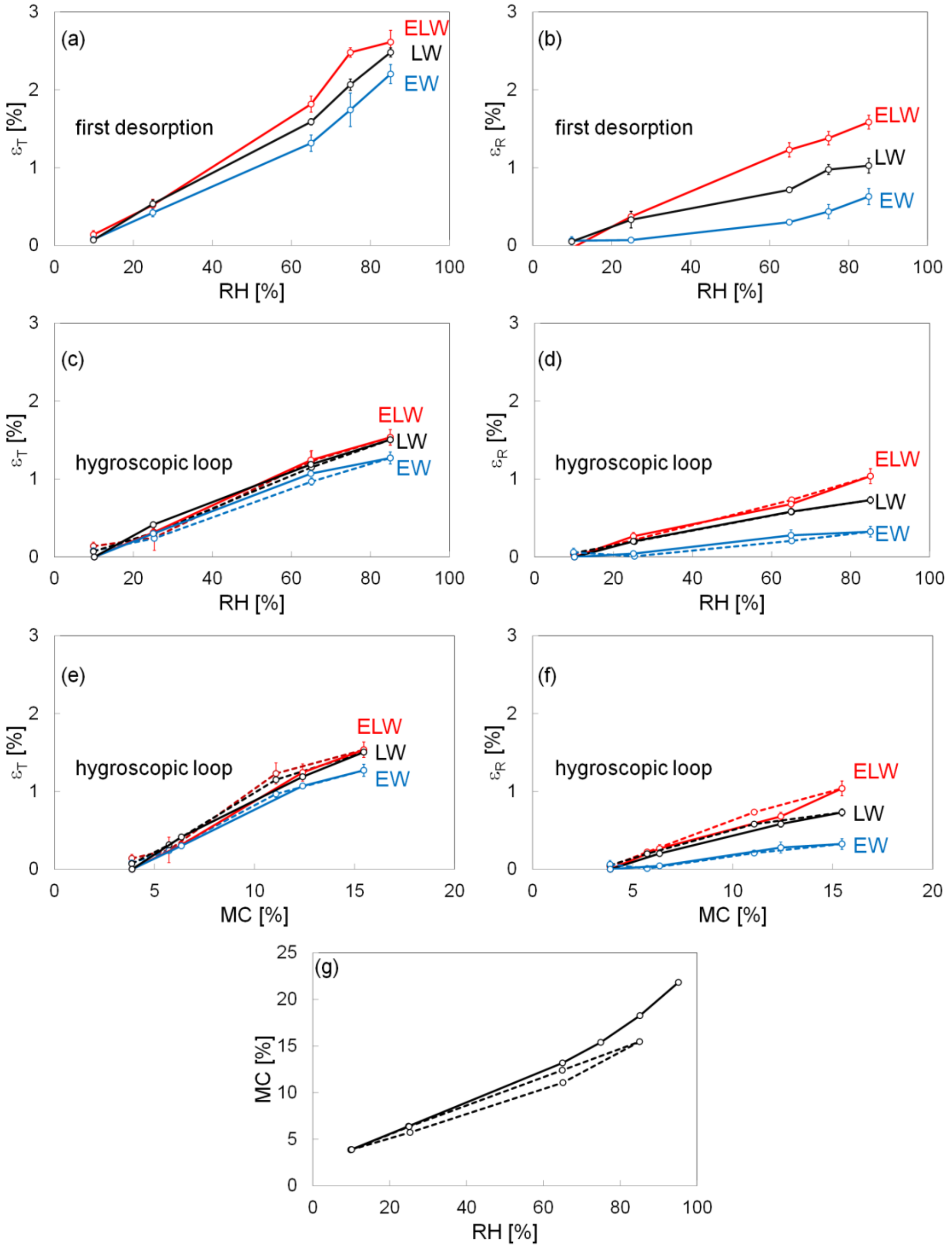

Figure 6.9: Swelling/shrinkage affine strains (tangential on the right and radial on the left) of three ROIs in green wood sample. The (a) tangential and the (b) radial

strains are plotted versus RH for the first desorption, with the dataset at 10% RH in the last desorption considered as the reference state for this analysis. The strains calculated during the hygroscopic loop in adsorption and desorption are plotted along the tangential and radial directions versus RH (c-d) and versus MC (e-f).(g) MC vs RH in the first desorption starting from 98%RH and in the whole hygroscopic loop. Strains are plotted with error bars. Red curves refer to the combined ROI, black to LW and blue to EW.

The results of the swelling difference $\Delta\varepsilon$, defined as difference between maximum swelling at 85%RH and the swelling at 10%RH, and the anisotropic swelling ratios are summarized for green wood in Table 6.6. We limit the analysis to the first adsorption and second desorption loop (d2). Comparing the values for greenwood to those of dry wood (Table 6.3), we observe that the sample of greenwood shows a much higher anisotropic swelling behaviour: T/R of 2.1 versus 1 for LW and T/R=4 versus 1.55 for EW. The greenwood sample is taken from the outmost portion of the woody stem, named sapwood. In this region, no maturation of wood has occurred yet, thus leading a softer wood material than the heartwood in the inner region. This means that sapwood, where the greenwood sample is taken from, shows a much more anisotropic swelling behaviour than heartwood.

Table 6.6: Tangential/radial swelling difference (85%RH, first and second desorption vs 10% RH on the second desorption) and anisotropic behaviour for green wood sample.

Greenwood	LW	EW	combined
$\Delta\varepsilon_{affine,T}$ (%) d2	1.5	1.3	1.5
$\Delta\varepsilon_{affine,R}$ (%) d2	0.7	0.3	1.0
Anisotropy (d2)	2.1	4.0	1.5

6.3.4 Non-affine strains analysis

The non-affine registration model is used to evaluate local events that do not follow the global behaviour of deformation. This analysis is performed on the two dry wood samples between the two extremes of a hygroscopic loading protocol: as reference and moving images, dry state (25% RH) and wet state (85% RH) are respectively taken. 200 cross-sectional slices are selected from the combined ROI of samples $ELW_{d,1}$ and $ELW_{d,2}$. For the greenwood sample, the wet state at 85%RH in the first desorption from green state is compared with the state at 10% in the second desorption for 200 slices, also including the combined ROI.

The criteria chosen for solving the optimization problem with the non-affine registration algorithm are described below. Initially, the algorithm runs on the resized volumes for a preliminary fast estimation. The registration approach based on the intensity of grey values intensity with the steepest descend method allows to compare the performance of the B-spline algorithm in two cases: the first on the resized volumes for a fast estimation (‘Registration 1’), where the B-spline functions are constrained to less freedom (γ=1.0E-2), while the second case, ‘Registration 2’, consists in giving more freedom to the functions (γ =1.0E-4). Additionally, the point-based registration algorithm (‘Registration P’) is applied with the method named ‘map’ for point extraction. We calculate the non-affine errors, as the difference due to misalignment between reference and moving images, slice by slice after non-affine registration. The results are reported in Figure 6.10a. ‘Registration 2’ gives the best approximation, showing less non-affine errors compared with ‘Registration P’. Therefore, we use ‘Registration 2’ for calculating the non-affine displacement and strain fields, by subtracting the displacements obtained with ‘Registration 1’ from the ones calculated with ‘Registration 2’. As mentioned in Chapter 4 and above, ‘Registration 1’ gives less freedom to the B-spline grid, describing a more global behaviour of wood. ‘Registration 2’ catches the local behaviour, as the penalty coefficient is lower. However, some artefacts in ‘Registration 2’ can arise due to high freedom of the B-splines. To avoid this problem, the difference between ‘Registration 1’ and ‘Registration 2’ is considered for evaluating the non-affine strains.

As example, the resulting displacement field is plotted in Figure 6.10b for $ELW_{d,1}$. We observes regions of positive and negative displacement for displacements along the *x*-axis (U_x) and along the *y*-axis (U_y). The directions *x* and *y* correspond to the two orthotropic directions of wood, i.e. tangential and radial, respectively. An interesting observation is that the vertical displacement field (U_y) in a region around a ray in earlywood shows a strong gradient from positive to negative values. This region is highlighted in Figure 6.10b by a box.

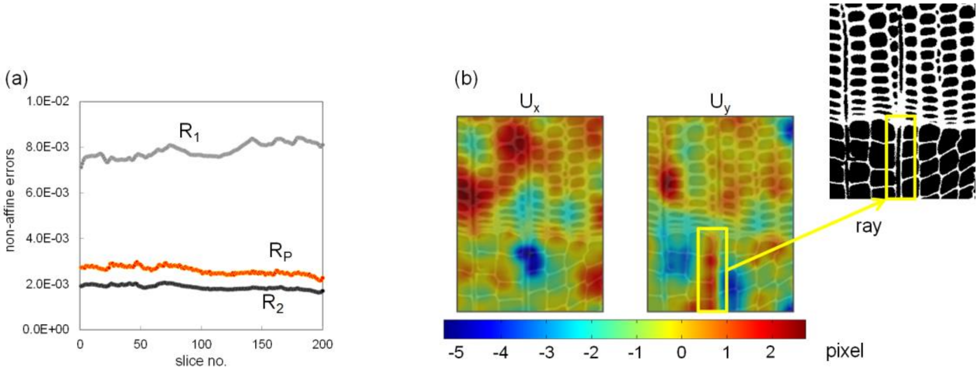

Figure 6.10: (a) Errors between reference and registered images after non-affine registration for each slices of the volume, using an intensity-based method for R_1 rough (grey) and R_2 free (black) estimation and a point-based registration R_P (orange). (b) Displacement fields in one slice of $ELW_{d,1}$ in pixels (1 pixel=0.8 μm)

The affine and non-affine strain fields are mapped in 2D on the cross-sections of the reference images. The non-affine strains are calculated as the gradient of the displacement field in each direction. In Figure 6.11, the total strain components (ε_{xx}, ε_{xy}, ε_{yy}) are plotted, which are given by the sum of affine and non-affine strains. We highlight 6 regions and name them 1 to 6 for simplicity. We observed that in tangential direction along the x-axis, higher total strains (ε_{xx}) are located at the interface earlywood/latewood (EW/LW). In particular, in boxes 1 and 4, we observe negative strains (blue regions) in a group of earlywood (EW) cells close to the transition area. These negative shrinkage strains are compensated by positive swelling strains in latewood (LW). This means that in regions where the EW cells are compressed, LW cells are in tensile state. These regions of combined compressive/tensile stresses point to a local bending occurring in these zones. Radially (i.e. along the y-direction), high strain (ε_{yy}) fields are found along the rays in the earlywood of sample ELW_1 (box 2), which indicate the restraining effect of rays on the soft earlywood cells during moisture sorption. A similar effect is visible in ELW_2, in the y-direction (box 3). Again, the regions with negative strains are accompanied by regions with high positive strains. This observation could indicate to a kind of slip behaviour between rays and surrounding material. However, we remark that a full understanding of the origin of the interacting local compression/tensile strain regions, and the restraining effect of the rays needs a more in-depth analysis, e.g. by a combined numerical/experimental analysis on cellular scale.

The three-dimensional renderings of the equivalent non-affine strains ($\varepsilon_{n.a.}$), are presented in Figures 6.12-13-14 for ELW$_{d,1}$, ELW$_{d,2}$ and greenwood. 2D cross-sections at different planes among the 200 slices are also shown. It is important to note that the equivalent non-affine strains are determined according to the von Mises relationship, as specified in equation 4.10.

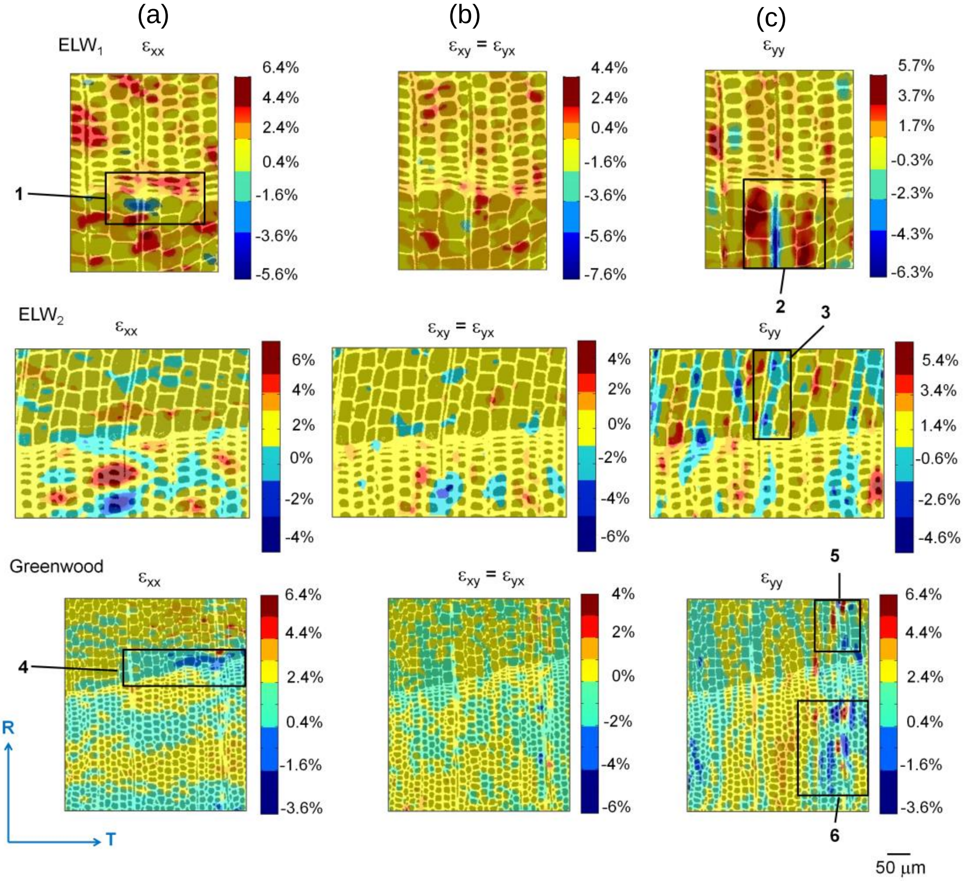

Figure 6.11: 2D map of total (affine plus non-affine) strains on the reference images for the three combined samples. The 6 regions discussed in the text are indicated.

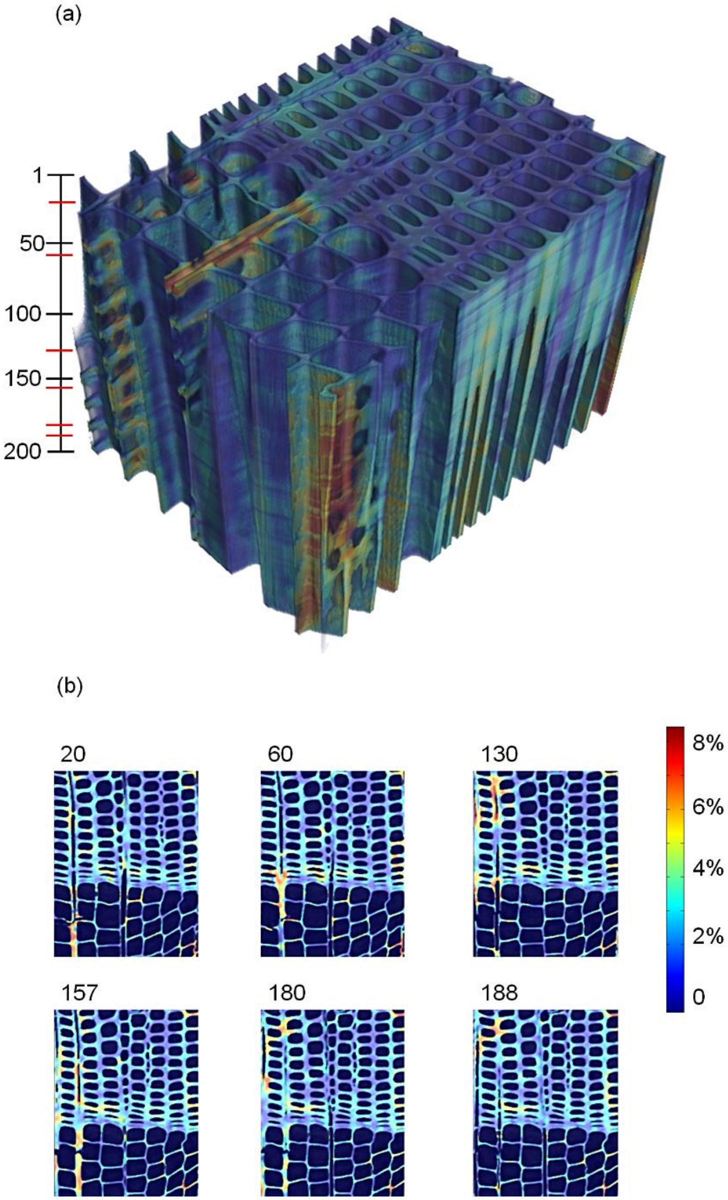

Figure 6.12: (a) Three-dimensional map of equivalent non-affine strains on the wood cell wall of sample $ELW_{d,1}$ for 200 slices, as indicated in the bar. (b) Cross-section cuts in the position indicated in red in the bar.

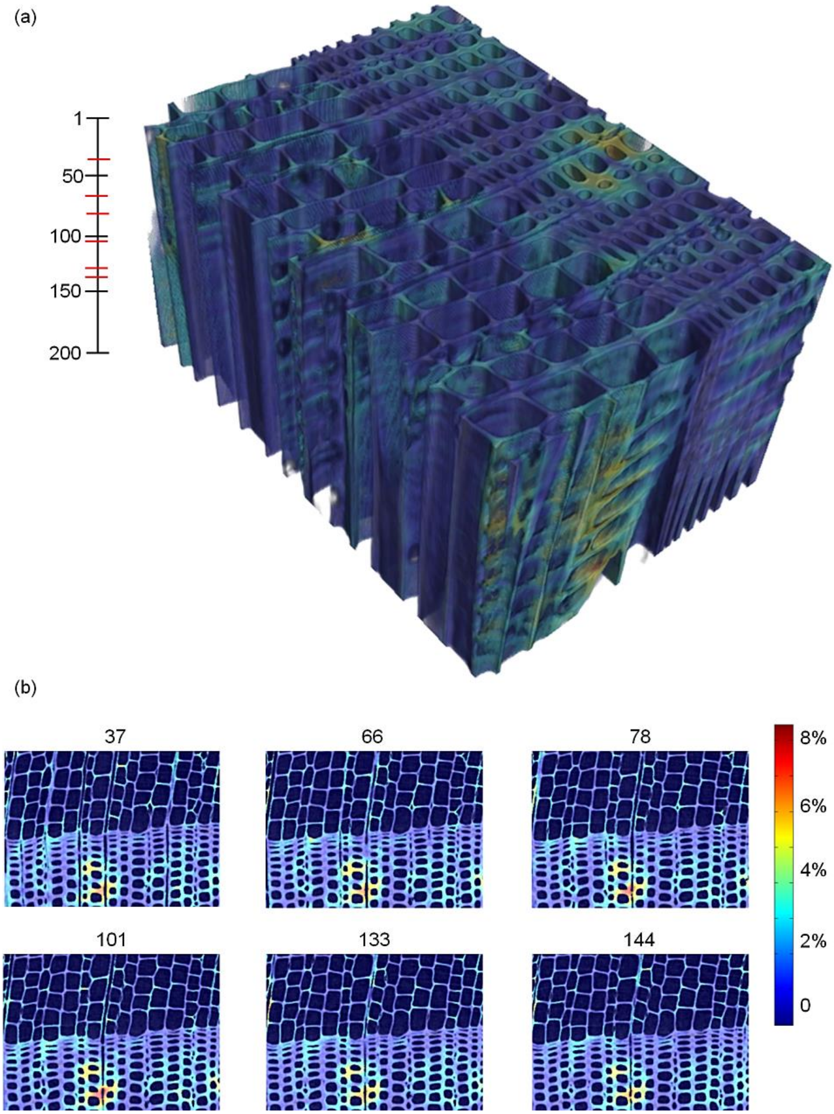

Figure 6.13: (a) Three-dimensional map of equivalent non-affine strains on the wood cell wall of sample ELW$_{d,2}$ for 200 slices, as indicated in the bar. (b) Cross-section cuts in the position indicated in red in the bar.

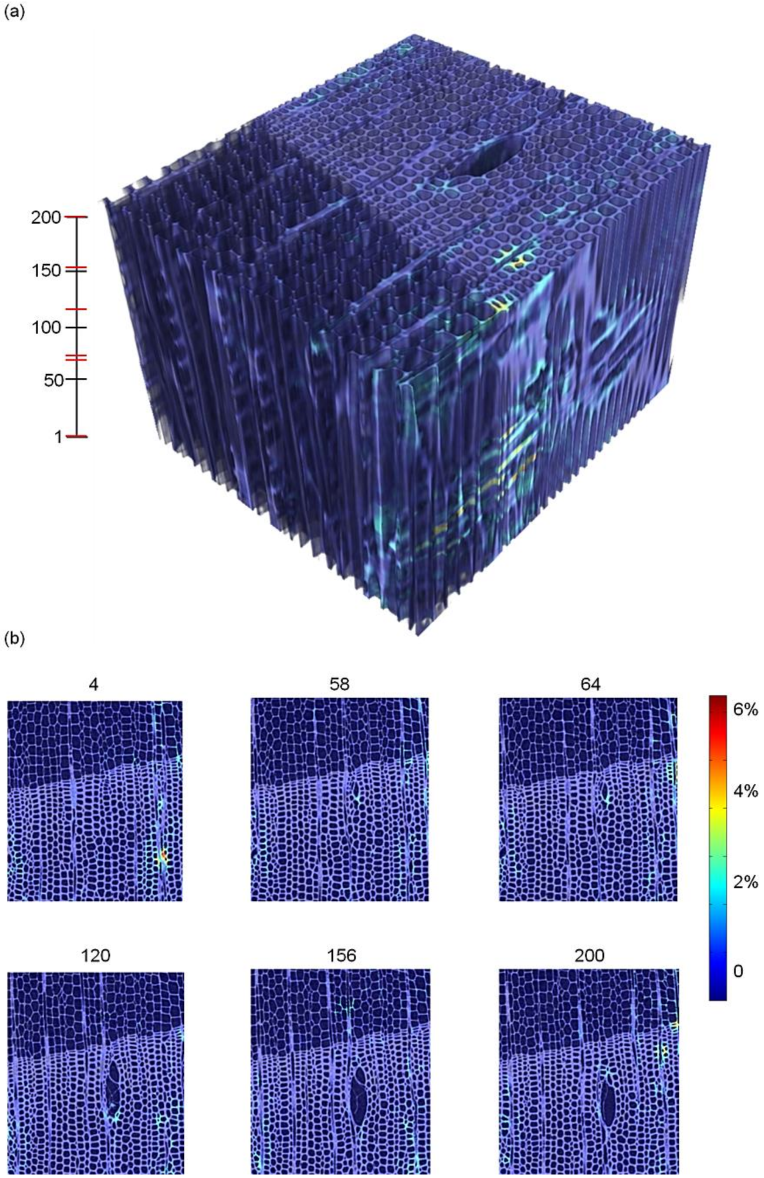

Figure 6.14: (a) Three-dimensional map of equivalent strains on the wood cell wall of green wood for 200 slices, as indicated in the bar. (b) Cross-section cuts in the position indicated in red in the bar.

Figure 6.12 shows that high values of equivalent non-affine strains occur in latewood cells close to the latewood/earlywood interface and close to the ray cells, especially in the earlywood layer. In Figure 6.13, we observe local regions of higher strains in a group of latewood cells surrounding ray cells. Greenwood shows low equivalent non-affine strains (Fig., 6.14), or a more affine behaviour, leading to the speculation that swelling behaviour of sapwood is different to swelling of heartwood due its more soft character . More discussion on the results follows in the next paragraph.

6.4 Discussion

6.4.1 Combined behaviour

We observe that the combined samples swell in general less than the single tissues. Also the swelling ratio is lower for the combined tissues. This means that, due to the restraining effect of latewood on earlywood and vice-versa, swelling of combined wood reduces and becomes less anisotropic. In the analysis of the non-affine strain components, we observed positive swelling strain values in latewood cells located at the interface latewood/earlywood and shrinkage strains in soft EW cells. This effect is visible in the tangential direction of wood. This means that in these regions of combined compressive/tensile stresses a local bending with respect to the interface LW/EW occurs.

6.4.2 On the role of rays

The analysis of rays cells show that they are randomly distributed between earlywood and latewood, occupying the same percentage of volume over the total sample volume. The ray cells seem to play an important role in making the displacement field less affine in the wood cell wall, especially in earlywood. Combining this observation with the anisotropic behaviour of earlywood, we can conclude that rays act as a restraint on the free swelling of wood. However, as the percentage of volume occupied by ray cells in earlywood is the same as the percentage of volume occupied by ray cells in latewood, we associate the fact that rays play a more important role in EW than in LW to the low cell wall thickness and low stiffness of the earlywood cellular structure. For this reason, the ray cells, with cell wall thickness higher than the earlywood cell walls, play a more important role in EW than in LW.

6.4.3 Sapwood versus heartwood

We speculate that the different behaviour of the greenwood sample compared with dry wood is related to the position in the tree trunk where the sample has been obtained from, i.e. close to the bark. As no maturation occurs in sapwood, we can conclude that this wood is softer, thus leading to a different behaviour. The behaviour of greenwood seems to be more affine as the non-affine strain values are very low.

The analysis of greenwood highlights an important observation related to the hysteretic behaviour of wood in the first desorption curve. As discussed in section 5.5.3, hysteresis is interpreted in terms of the accessibility of the hydroxyl groups in the wood to adsorbed water molecules. In the greenwood, the hydroxyls form hydrogen bonds with the adsorbed water and with other cell wall constituents. The cell wall is laid down in the fully swollen state. On drying, the adsorbed water is removed from the cell walls and the cell wall polymeric chains are drawn close together, forming new hydrogen bonds among themselves. Not all of these newly formed hydrogen bonds can be broken again during the sub-sequential adsorption and desorption loops. This explains why the first desorption curve lies at moisture content above all subsequent desorption curves.

6.5 Conclusion

This chapter extends the investigation of the hygro-mechanical behaviour of wood at cellular scale to samples including earlywood and latewood. The first part of the analysis is focused on the study of two combined samples subjected to hygroscopic cycle loading during tomographic scans. The volumes are reconstructed using the Modified Bronnikov Algorithm chosen for its optimal solution in getting high-quality results. The volume is divided in three regions of interest (ROIs), containing respectively pure latewood, pure earlywood and a region on the transition zone between the two tissues. The combined tissues, containing both earlywood and latewood, present an intermediate behaviour between the two homogeneous tissues in terms of strains and anisotropy. Overall, the behaviour of a combined region approaches more the behaviour of latewood, with an anisotropic ratio between 1.1 and 1.3.

The combined earlywood and latewood behaviour analysed in this chapter thus shows that, in general, latewood plays a major role on the growth ring transition regions. Anisotropy in earlywood is explained with respect to the restraining role of ray cells in the thinner material. This result is confirmed by the analysis of the non-affine strains. The volume occupied by ray cells is the same in latewood and in earlywood and the cell wall thickness of the ray cells is, in average, equal to 5.5 μm. It results that the thickness of ray cell walls is higher compared with the typical thickness of earlywood cell walls (~ 4 μm), explaining the reason why rays restrain more the earlywood material compared with latewood.

A greenwood sample is successively exposed to a full hygroscopic loading protocol from green to dry states and, again, in adsorption and in desorption. The lumen is filled with water when the sample is scanned in green state. However, the water leaves quickly the lumen as the sample is dried at the first desorption level, i.e. 85% RH. In greenwood, the material is softer than in dry wood, leading to a more anisotropic behaviour of both latewood and earlywood.

Having examined the behaviour of earlywood and latewood in a combined sample, we continue in the next chapter our study on understanding the swelling/shrinkage behaviour of the two tissues subjected to restrained swelling during moisture sorption. This investigation aims at giving more insights on the type of non-affine strains possible in the cell wall.

Chapter 7

Micro-scale restraint for humidity-induced swelling

Polymethylmethacrylate (PMMA) cubes are used to restrain the free swelling of wood subjected to relative humidity changes. The design and fabrication of the restraining device are presented in section 3.3. We use the device for restraining the swelling of wood during moisture sorption. The behaviour is captured with synchrotron X-ray phase contrast micro-tomography. The experiments highlight the capacity of the manufactured device to restrain swelling of wood and induce local deformation at wood cell level. The global behaviour is quantified with affine registration, while non-affine registration is applied to probe the local deformations of softwood during restrained swelling.

7.1 Introduction

In the previous chapters, the observations of free swelling/shrinkage of softwood led to the conclusion that, in addition to a global swelling, local deformations occur within the cellular structure. These deformations should be even more significant when the swelling of the wood cells is subjected to an external restraint during hygroscopic cycles. It has been reported that internal strains can influence the radial and tangential swelling of wood (Hittmeier, 1967). In Simpson and Skaar (1968), the swelling pressure during restrained swelling of red oak was measured with load cells. The swelling pressure is higher in tangential than in radial directions when the RH increases from dry to 50%RH, while the pressure is similar in the two directions when the RH increases from 50% to 80%RH. Most of these types of investigation on the mechanisms of restrained swelling of wood during moisture sorption are performed at the macroscale (e.g., Narayanamurti et al., 1954; Bolton et al., 1974; Moliński et al., 2010). Recently, micromechanical setups devised for tomography are developed in order to study the microstructure of various materials under mechanical loading. For example, Schneider et al. (2010) present a micro-compression device for bone testing and Zauner et al. (2012) a compression testing device to determine the cellular response of wood under mechanical loading. However, these systems cannot be used to expose the samples to varying RH conditions, due to the limitations in their designs. As few devices for micro-compression test set-ups are suitable for X-ray micro-tomography experiments under controlled RH and temperature conditions, a novel and simple method to restrain a microscopic piece of wood undergoing swelling is used in order to verify the occurrence of local deformations at cellular scale.

7.2 Experimental procedure

In this section, we present the procedure adopted for cutting the wood samples and inserting them into the PMMA cubes. Then, we introduce the experimental setup and protocol. The PMMA cubes are fabricated with laser ablation and the manufacturing of these cubes is explained in detail in section 3.3.

7.2.1 Preparation of the wood samples

The spruce wood samples (*Picea Abies*, L.Karst) are cut from 20×20×20mm^3 wood cubes into sticks of 0.5mm×0.5mm cross-section. The surfaces of the wood samples have to be as flat and smooth as possible, in order to fit in the slot of the restraining device and to be perfectly in contact with the cube slot's surfaces. Laser ablation is not appropriate for the wood samples preparation, since it leads to burning and material modification of the wood surface. Thus, the wood samples are mounted on a translational stage and cut by razor blade in 0.5 mm slices and then into sticks. Finally, the samples are manually cut along the longitudinal direction to the following lengths: 1mm for the 2×2×2 mm^3 cube, 1.5mm for the 3×3×3 mm^3 cube and 2mm for the 4×4×4 mm^3 cube. The samples are placed in a dry desiccator until placement in the restraining devices for testing.

7.2.2 Mounting of the samples

The wood samples, mounted in the restraining cubes, are first kept in a desiccator over desiccant for three days to reach dry state. After three days, the samples are visualized under an optical microscope in order to measure the size of the dry wood specimens. Then, one series of mounted samples is placed in an environment at 100% RH for three days and again visualized under the optical microscope. Figure 7.1 shows three images of the swollen wood samples inside the cubes captured with the optical microscope. The size of the samples is again measured and compared with the initial sizes of the dry samples. The wood samples mounted in the 2×2×2 mm^3 and 3×3×3 mm^3 cubes present too much swelling, leading to the conclusion that these cubes do not sufficiently prevent free swelling of wood. Additional observations highlight the presence of roughness on the slot surface and presence of cracks in the 3×3×3 mm^3 cubes, related to the pressure exerted by wood during swelling (Figure 7.1b). The visual comparison between the two states allows to conclude that the 4×4×4 mm^3 PMMA cubes exert a major constraint to the free swelling of wood compared to the two smaller systems. Therefore, we consider only the 4×4×4 mm^3 PMMA cubes in our testing program. The tangential and radial dimensions of two wood samples, one latewood and one earlywood, are reported in Table 7.1. These two samples are then inserted in two 4×4×4 mm^3 cubes to be restrained along the tangential directions and their position in the cubes is optimized under the optical microscope. Once inserted, the samples are observed under optical microscope in order to examine the smoothness of the slot surfaces and the quality of the contact between the wood samples and the slot surfaces. These two samples are then kept in a desiccator at ≈ 0%RH until the beginning of the tomographic scan. In this work, we will refer to these two samples as LW_T and EW_T (T stands for restraining along the tangential direction) During the experimental work, we will study the behaviour of two additional wood samples inserted inside the 4×4×4 mm^3 cubes, one latewood and one earlywood, subjected to restrain along the radial direction. We refer to the latter ones as LW_R and EW_R. The preparation of LW_R and EW_R samples (razor blade cut and insertion in the cubes) is performed at the TOMCAT beamline with the same procedure as for samples LW_T and EW_T (previously prepared at EMPA). We did not visualize by microscopy the initial sizes of LW_R and EW_R although the dimensions are comparable with the slot height. As a result, during insertion, the wood samples are somehow squeezed in the slot, leading to initial cell deformations. In total, four samples are presented in this work, two latewood and two earlywood samples, where each sample is subjected either to tangential or radial restraint during moisture sorption. The specific protocol is described in the next paragraph.

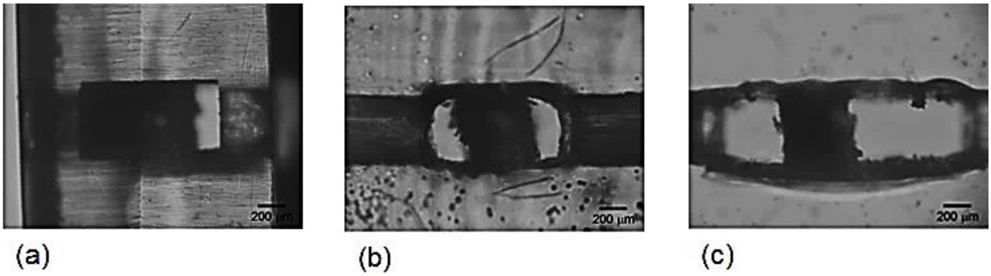

Figure 7.1: Photographs of three wood samples located respectively in (a) 2×2×2 mm^3, (b) 3×3×3 mm^3, showing cracks and surface roughness, and (c) 4×4×4 mm^3 PMMA cubes, acquired by optical microscopy.

Table 7.1: Initial dimensions of the wood samples before insertion into the cubes.

Samples/ Loading direction	LW_T	EW_T
Tangential	690 µm	520 µm
Radial	600 µm	460 µm

7.2.3 Setup configuration and experimental protocol

The measurements are carried out at the TOMCAT beamline of Swiss Light Source (SLS), Paul Scherrer Institute. The experimental setup consists of the synchrotron radiation X-ray tomographic microscope for image acquisition and an environmental chamber for conditioning the samples, as explained in detail in sections 3.1.2.1 and 3.2.1, respectively. The wood sample, prepared and located inside the restraining device, is mounted within an environmental chamber on a rotational stage and scanned with an energy of 20 keV and an exposure time of 40 ms. The detector to sample distance is optimized at 20 mm. A total of 1024 projections per tomographic scan is acquired with a standard CCD camera, PCO 2000. The microscopic configuration leads to a field of view (FOV) of 757×757 μm^2. We employ a 2× binning factor, which results in radiographic images of a 1024 × 1024 pixel effective resolution. This converts into an effective spatial resolution of 0.74 μm/pixel. As a note, the sample is exposed to only 40 seconds of X-ray radiation during one scan, a main advantage of using synchrotron radiation X-ray tomography instead of conventional CT towards ensuring that the sample is not damaged, nor deformed by X-rays.

The reconstruction is performed in two steps. First the phase shift introduced by the wood is retrieved using the Paganin algorithm, which is based on the homogenous object assumption (Paganin et al., 2002) and derived from the 'transport-of-intensity equation'. This is well applicable for cellular wood samples, considered as homogenous objects for X-rays meaning that the 3D complex refractive distribution consists of only two components: wood and air. Under the approximation of "homogeneous" object, the real and the imaginary parts of the refractive index representing the phase shift and attenuation are proportional to each other and can be calculated from the images acquired at a single propagation distance, as explained in section 2.8. After the phase retrieval step, we used the Fourier based tomographic reconstruction method (Marone et al., 2012) to obtain the 3D volumes.

The four wood samples, LW_T, LW_R, EW_T and EW_R, located inside the 4×4×4 mm^3 PMMA cubes, are exposed to relative humidity cycles from RH=15% to RH=85% in adsorption and desorption. Specifically, the experimental protocols are as follows:

LW$_T$: 15 – 25 – 65 – 75 – 85 – 75 – 65 – 25 – 15% RH;
LW$_R$: 15 – 65 – 85 – 65 – 2% RH;
EW$_T$: 15 – 25 – 65 – 75 – 85 – 75 – 65 – 25 – 15% RH;
EW$_R$: dry – wet – dry, as the malfunction of the control system prevented the determination of the exact conditions in the environmental chamber.

Each RH condition is maintained approximately for one hour before the acquisition of the tomographic scans in order to ensure moisture content equilibrium.

A three-dimensional visualization of the four systems is presented in Figure 7.2. Volume rendering is performed on the reconstructed datasets for the four samples at dry state with the image processing package Fiji (Schindelin J., 2012), which allows to identify the edges and the contact zones between the cube and the wood sample. Generally, we observe contact areas for most of the samples between sample and smooth slot surface. However, the radial earlywood sample shows a rougher slot surface than the other three systems although the contact between wood sample and both surfaces is still good. The wood samples, squeezed inside the PMMA cubes, reveal deformations of some cells at the edges, especially for the two latewood specimens, LW$_T$ and LW$_R$.

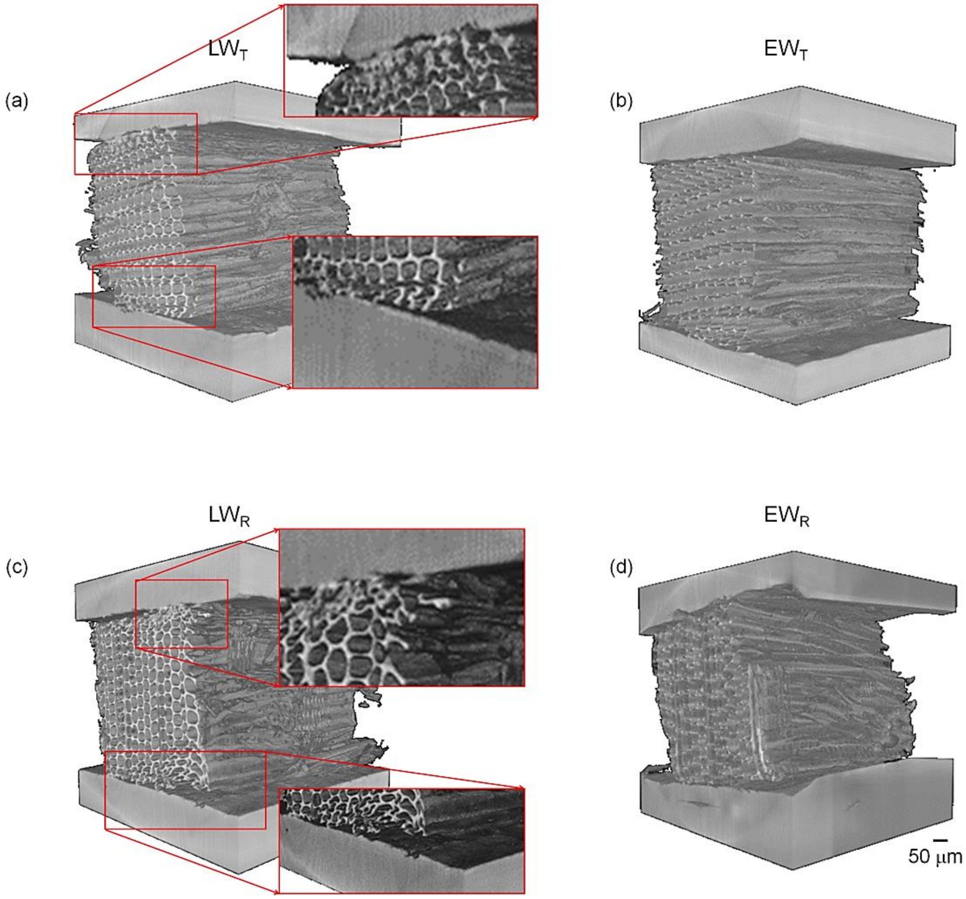

Figure 7.2: Volume rendering on four datasets at 10%RH for (a) latewood in tangential direction, (b) earlywood in tangential direction, (c) latewood in radial direction and (d) earlywood in radial direction. Zoomed regions highlight where latewood cells at the surface of the sample are deformed due to insertion in the cubes.

7.3 Results and discussion

In this section, the adequacy of the PMMA device for restraining wood swelling is demonstrated by 2D and 3D image analysis. Then, the deformations of the cellular wood tissues are further investigated and reported, in affine and non-affine analysis.

7.3.1 Two-dimensional image analysis at the interface wood/device

For this analysis, two datasets, acquired at 15% RH and 85% RH for each sample, are used. The main technique adopted for investigating the 2D swelling/shrinkage is based on the affine registration model, using the image analysis and visualization toolbox available in Matlab. As explained in previous chapters, affine registration consists in aligning two images by removing the global geometrical differences due to translation, rotation, shear and scaling. Four initial control points given as input to the algorithm are selected across the wood/device interface of the PMMA slot in order to quantify possible deformations of the cube after moisture sorption. The images are first analysed selecting only the PMMA regions and an affine registration is performed on the PMMA regions only to determine the displacement of the PMMA slot surfaces. The results are reported in Table 7.2, which highlights that the deformation of the cube slot surfaces due to the swelling of wood from 15% RH to 85% RH is equal, in percentage, to 0.5% of the slot height in the cube containing the LW_T, 0.3% for LW_R, 0.2% and 0.04% for EW_T and EW_R, respectively. The displacement of the slot surfaces due to the swelling of the wood sample is much higher for latewood, which is a stiffer material, than for earlywood.

Figure 7.3 shows a comparison between dry and wet state of the system. The insertion of the wood samples into the PMMA slots provokes a collapse of some cells at the edges of the sample at 15% RH. The initial collapse of groups of cells cannot be avoided with such device. This represents the main drawback of the design. An alternative method would require a better wood sample preparation to make it fitting in size into the cube slot. However, this step would require laser cutting procedure, thus provoking a cell damage, or focused ion beam (FIB) preparation, which means longer and more difficult sample preparation. Adjustments could be made also on the restraining device design, following a similar approach as presented Zauner et al. (2012) but with smaller size to fit inside the environmental chamber. The scans at 85% RH show that the cell collapse increases during the swelling, as highlighted in red rectangle in Figure 7.3. We see that, as the wood samples undergo sorption of water, the cells at the edges of the sample and in contact with the restraining surface undergo buckling. Buckling occurs in LW and EW tissues, but to a less extent in the bulky latewood. We remind that the samples were cut with a razor blade, thus, most likely, initially in some deformed or disturbed state due to the cutting and due to the insertion into the cube. Such state must facilitate the occurrence of buckling. For example, the group of cells highlighted in LW_T shows a stack of ray cells in dry state, which collapse in wet state due to the restraining role of the cube slot. Buckling of groups of cells is observable also in EW_T, LW_R and EW_R.

The detailed investigation on the occurrence of local deformations and buckling process is performed below with non-affine registration.

Before proceeding to sample analysis, we discuss shortly the behaviour of the restraining device. The wood sample exerts a pressure on the PMMA cube, due to the restrained swelling. We predicted by FEM simulation that the maximum displacement along the y-direction under the conditions of a cube of size 4×4×4 mm^3 with a slot cross section of 0.5×2 mm^2 would be equal to 2.8 μm. The maximum displacement, measured in the experiments for RH=85%, is found to range between 0.22 μm and 2.36 μm, as reported in Table 7.2. This result shows the adequacy of the design of the restraining device.

Table 7.2: Maximum increase of the height of the cube slot under the swelling pressure of the four samples.

PMMA Samples /	Latewood		Earlywood	
Loading direction	Absolute	Percentage	Absolute	Percentage
Tangential	2.36 μm	0.5%	0.79 μm	0.2%
Radial	1.52 μm	0.3%	0.22 μm	0.04%

Lacroix (2007) reported the free swelling of PMMA at 100% RH to be equal to 0.4% and a quasi-linear dependence of swelling with respect to RH. Using this value, we can estimate the swelling of PMMA from lab conditions of 50%RH to 85%RH equal to a strain of 0.14%. The strain ε_{PMMA} equals

$$\varepsilon_{PMMA} = \frac{\Delta L}{L_0} \tag{7.1}$$

where ΔL is the change in height of the slot and L_0 is the initial slot height measured at lab condition, i.e. 500 μm. From eq. 7.1, it results that ΔL=0.7 μm. This means that, for a displacement of 2.36 μm, 1.66 μm is due to the swelling pressure exerted by the wood sample while the remaining displacement is associated to swelling of the PMMA cube.

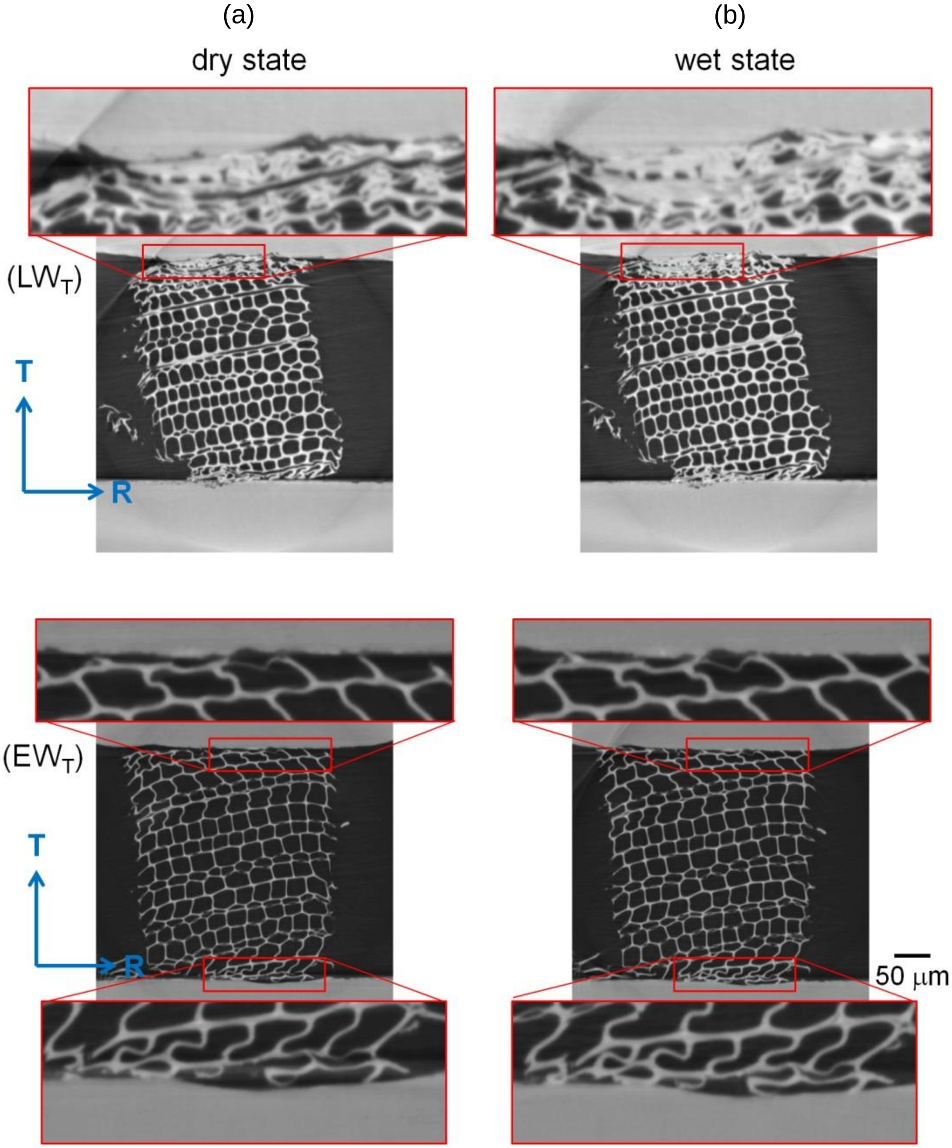

Figure 7.3: (to be continued)

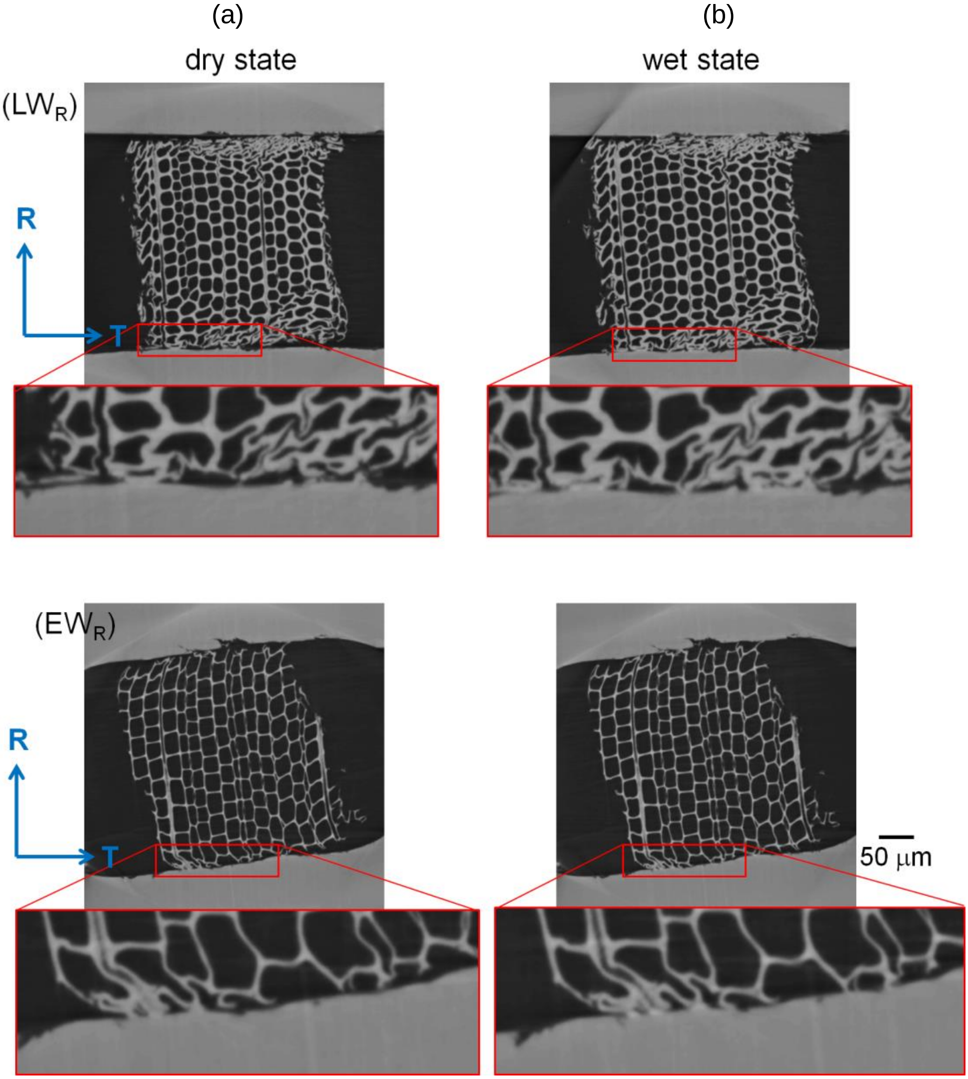

Figure 7.3 (continued): 2D cross-sectional view of wood samples inside the PMMA cubes, at two different RH conditions, (a)dry and (b) wet. Regions of interest (in red rectangles) are zoomed in.

7.3.2 Three-dimensional affine analysis of wood samples

The four datasets are analysed in 3D in order to determine the global swelling/shrinkage in the tangential and radial directions. As observed previously, in Chapters 5 and 6, the measured longitudinal strains are very small and are not presented further during this analysis.

We observe that the samples LW_T and EW_T show a good contact with the PMMA slot surface during the hygroscopic protocol in adsorption and in desorption, except for two RH conditions in desorption at 25% and 15% RH. Sample LW_R shows more contact at 85% RH and then a lower level of contact in the other RH values. For sample EW_R, unfortunately, no full contact with the restraining device was observed, and for this reason this dataset is omitted from further 3D analysis.

We consider regions of interest (ROIs) in the centre of the wood samples and at the edges in contact with the PMMA cube, containing 29 up to 60 cells(see Figure 7.4). In LW_R we consider only a region in the centre due to the irregular contact of the sample with the device.

We determine the porosity, the cell wall thickness and the affine swelling/shrinkage strains in the tangential and radial directions. The porosity and the average cell wall thickness are measured on the whole volume of the sample by using the software for image analysis and visualization VG Studio MAX 2.0, while the affine registration for the calculation of the affine strains is performed with 3D Slicer (Pieper et al. 2004).

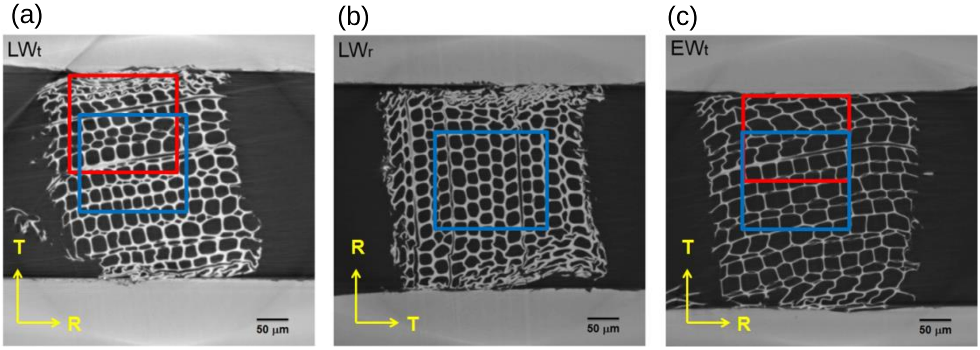

Figure 7.4: ROIs considered for this analysis of (a) LW_T, (b) LW_R and (c) EW_T. ROI 1 in blue and ROI 2 in red.

The cellular porosity is defined as the ratio of the lumen volume to the total volume of the ROI. The volumes are binarized by thresholding and the cell wall material is considered by counting the number of white voxels from the binarized images. As thresholding method, we use the region growing algorithm, as explained in section 2.5.1.3. The criteria used is pixel intensity. The sample porosity varies between 54% in latewood up to 65% in the earlywood tissue.

The swelling/shrinkage strains are determined by affine registration as explained in detail in the section 2.5.2.1. In general, a 3D affine transformation is a good approximation for describing the deformation between the two volumes, especially for the ROIs 1 in the centre of the samples. We have to keep in mind though that, in the ROIs 2 at the edges of the sample, non-affine deformations occur due to restraining of the swelling. We consider the state at 15% RH as the reference state. We split each dataset into 5 stacks of 150 slices each and register each stack, allowing to calculate the average strains in each direction with respective standard deviations.

The results of this calculation are reported in Figure 7.5 for ROI 1. In LW_T, we observe almost isotropy, as the radial affine strains are similar to the tangential ones. When latewood is restrained along the radial direction (see LW_R sample), the radial strain becomes smaller, while the tangential strains are quite large, resulting in a strong anisotropy. For the earlywood sample EW_T, we observe tangential strains similar to the radial ones, which is markedly different from the anisotropy seen in Chapters 5 and 6.

In ROIs 2 shown in Figure 7.6, thus at the edge of the samples LW_T and EW_T, we observe that tangential strains are almost nil during sorption, remaining so during the first steps of desorption, to decrease linearly from 65%RH and below. Thus, at the edge of the sample, we speculate that, after a sorption loading where free swelling was prevented, in desorption, when the restraining effect stops, a free shrinkage can be recovered. We note that the (linear) shrinkage from 65%RH is almost within the normal range of free shrinkage, as observed in Chapter 5, where latewood and earlywood samples show a range of tangential strains at 65% between 2.5% 3.5%.

The hysteretic behaviour of wood observed in free swelling, as documented in Chapters 5 and 6, is almost not observed in restrained swelling (see ROIs

1 of LW_T and EW_T). We hypothesize that, due to the restraining pressure on the wood cells, sorption and swelling are reduced. As a consequence also, the displacement in adsorption and in desorption is similar and hysteresis in restrained swelling is reduced.

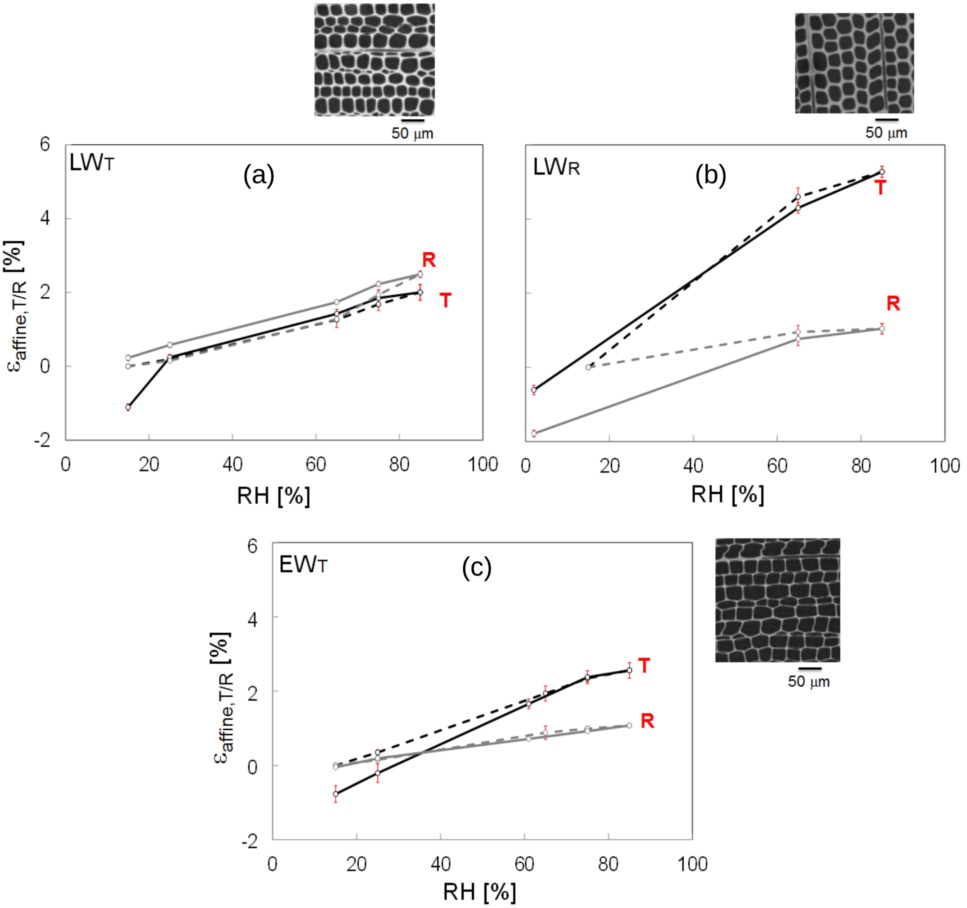

Figure 7.5: Tangential strains (black line) and radial strains (grey line) calculated for ROI 1 in (a) LW_T, (b) LW_R and (c) EW_T. Continued lines for desorption conditions and dashed lines for adsorption conditions. The error bars are the standard deviations on each measurement point.

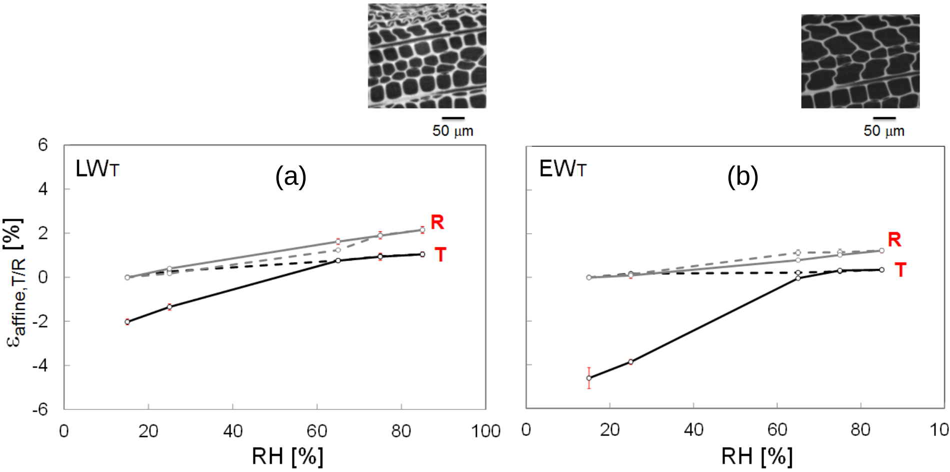

Figure 7.6: Tangential strains (black line) and radial strains (grey line) calculated for ROI 2 in (a) LW$_T$ and (b) EW$_T$. Continued lines for desorption conditions and dashed lines for adsorption conditions. The error bars are the standard deviations on each measurement.

Table 7.3 includes the maximum tangential and radial swelling strains ($\Delta\varepsilon_{affine}$), i.e. considering the reference state at 15% and the moving state at 85%, and the tangential to radial swelling ratios. The results reported in Table 7.3 show that the tangential to radial swelling ratios are equal to 0.8 in latewood sample subjected to tangential restraint and 5.3 for the latewood sample restrained radially. In chapter 5, this ratio for homogeneous tissues of similar density (50%) is around 1.3. Thus, under tangential restraint, the device reduces the tangential swelling, resulting in a reduction of the swelling ratio from 1.3 to 0.8. When the restraint is in the radial direction, the radial swelling is markedly hindered and the ratio augments from 1.7 to 5.3. For the earlywood sample, the restrained swelling in tangential direction leads to a ratio of 2.4, which indicates a hindering of tangential swelling when compared to the ratio value of 1.7 reported in Chapter 5.

The ratio in ROI 2 at the edge of LW$_T$ is 0.5, which is much lower than the 0.8 in the centre, indicating also more restraining. ROI 2 at the edge of EW$_T$ shows a ratio of 0.25, compared to the 2.4 in the centre, showing the large constraint in tangential direction in earlywood. Thus restraining is higher at the edges of the samples compared to the centre regions.

Table 7.3: Cell wall thickness and porosity of the whole sample, cells number, tangential/radial swelling and T/R swelling ratio of ROI 1 and ROI 2 as shown in Figure 7.5, for three samples.

	LW_T		LW_R	EW_T	
	ROI 1	ROI 2	ROI 1	ROI 1	ROI 2
Average cell wall thickness [μm]	7.5		6.0	5.7	
Porosity [%]	54		60	65	
Cell number	60	49	46	51	29
$\Delta\varepsilon_{affine,T}$ [%]	2.0	1.0	5.3	2.6	0.3
$\Delta\varepsilon_{affine,R}$ [%]	2.5	2.1	1.0	1.1	1.2
Anisotropic swelling ratio	0.8	0.5	5.3	2.4	0.25

To complement the 2D analysis described in the previous section, we performed a three-dimensional affine registration on the four PMMA cubes. Here, we considered the whole stack of 750 images at 15% and 85% RH and we cut out the regions containing the wood sample, so only the volumetric deformation of the PMMA cubes us described. The results are reported in Table 7.4. The volumetric swelling of PMMA ranges between 0.32% and 0.55%. We conclude that the volumetric swelling of PMMA is negligible compared with the swelling in wood, which equals in average equal to 6-7%.

Table 7.4: Volumetric swelling of the four PMMA cubes under wood swelling pressure and hygroscopic loading.

Loading direction	LW_T	LW_R	EW_T	EW_R
Volumetric swelling [%]	0.55	0.35	0.42	0. 32

7.3.3 Non-affine strain analysis

The affine strains give a good approximation of the global swelling/shrinkage of wood samples subjected to restraint. However, the local deformations of wood, in particular in the regions in contact with the slot, are not completely described with affine registration. As an example, we study in detail the non-affine strains in the two samples, latewood LW_T and earlywood EW_T, subjected to restraint along the tangential direction.

We consider these two samples since the restrain effects are most significant. The PMMA cube is excluded from the region considered for this analysis, thus here the ROI include the full cellular wood structure between the slot surfaces. The comparison is done between 15% and 85%RH in adsorption. The optimization problem is solved with the L-BFGS criteria and the minimum error is found for 'Registration 2', and used for the calculation of the strains.

The non-affine strains in *x* and *y* directions are mapped in 2D for the two samples in Figure 7.7. We observed that LW_T presents high non-affine strains in the regions in contact with the restraining device. The effect is less visible in EW_T, where only few cells are influenced by restraint. At first glance, we observe quite similar strains distribution in latewood and earlywood:

a) Vertically oriented regions of high compressive strains, $\varepsilon_{n.a.,yy}$, (blue regions) along the tangential direction which are due to the restraint in tangential (y-direction).

b) Occurrence of local regions of high tensile strains, $\varepsilon_{n.a.,xx}$, in between the regions of high compressive strains, indicating a bending or buckling deformation pattern.

c) We observe also high strains, $\varepsilon_{\mathrm{n.a,xx}}$, in the not-restrained direction and also regions of high shear strains. This deformation pattern indicates a 2D behaviour, where the bending/buckling in y-direction is accompanied with bending/shear in the other direction.

We zoom on three regions of interest: top (in yellow), central (in green) and bottom (in orange), as shown in Figure 7.8. Please note the different scale bars for the different regions. The equivalent non-affine strains are calculated with eq. 4.10. In LW_T, the maximum value of 12% is found on the top and bottom regions. In these regions, we clearly observe buckling of groups of cells where the highest non-affine strains are located. In the central part, the non-affine strains are lower, reaching a maximum of 6%, only in few cells. The same cells show a high non-affine component in the radial plane ($\varepsilon_{n.a.,xx}$, in Figure 7.7).

In EW_T , most of the high non-affine strains are located in the bottom and central part of the sample. Most of the cell buckling in EW_T occurs at the bottom region, reaching a peak of 8% locally. In the top region of EW_T, the maximum non-affine strain (~12%) is only reached in one cell. This cell is visible also in the comparison between dry and wet state in Figure 7.3 and we clearly see that this cell undergoes locally large deformation This cell was highly deformed during sample preparation with razor blade or by the insertion process. When wetting and drying, we observe a kind of shape-memory effect on this cell (Figure 7.9). In fact, the angle that the cell forms with plane parallel to the PMMA slot is equal to 40° at 15%RH in adsorption, then it decreases to 26° during moisture sorption at 85% RH and goes back to 38° at 15%RH in desorption. This means that, when wetting again, the cell initially highly deformed by the cutting will try to regain its original cell shape (memory of initial shape) leading to high local non-affine deformation.

Despite the fact that the contact region on the top led to a high global restrain of the tangential swelling, as suggested by the low affine strains in Figure 7.6, it seems that the pressure due to the contact is not high enough to provoke buckling of the cells on the top.

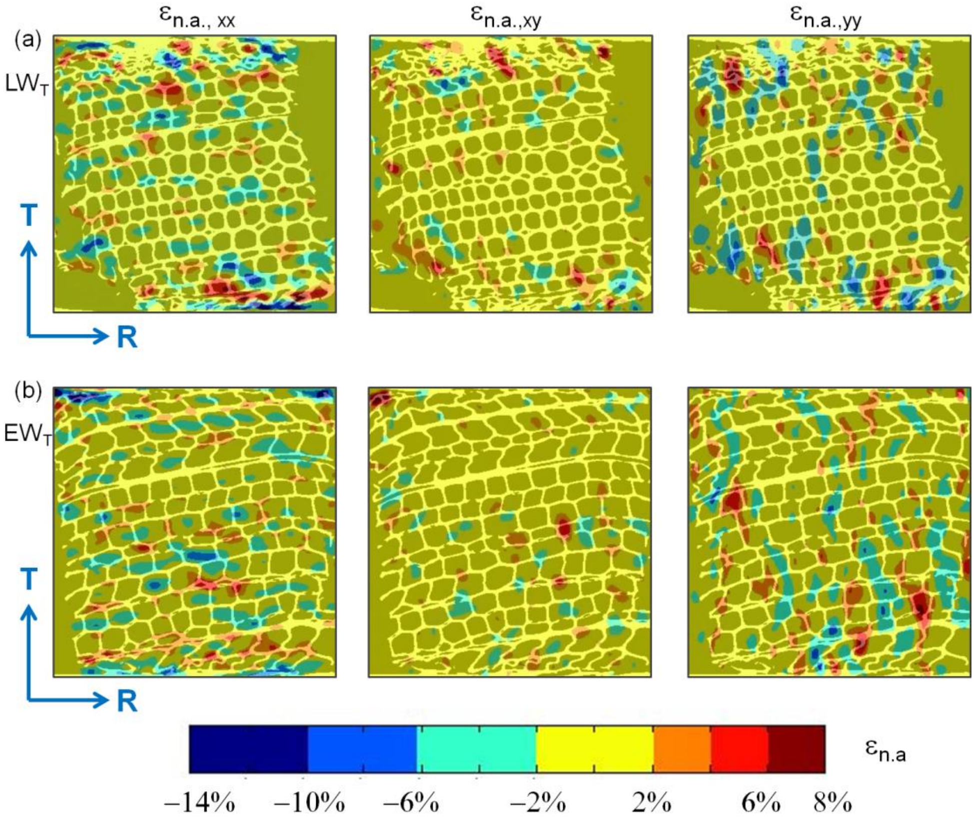

Figure 7.7: 2D map of non-affine strain components for (a) LW_T and (b) EW_T in the *x*-*y* plane.

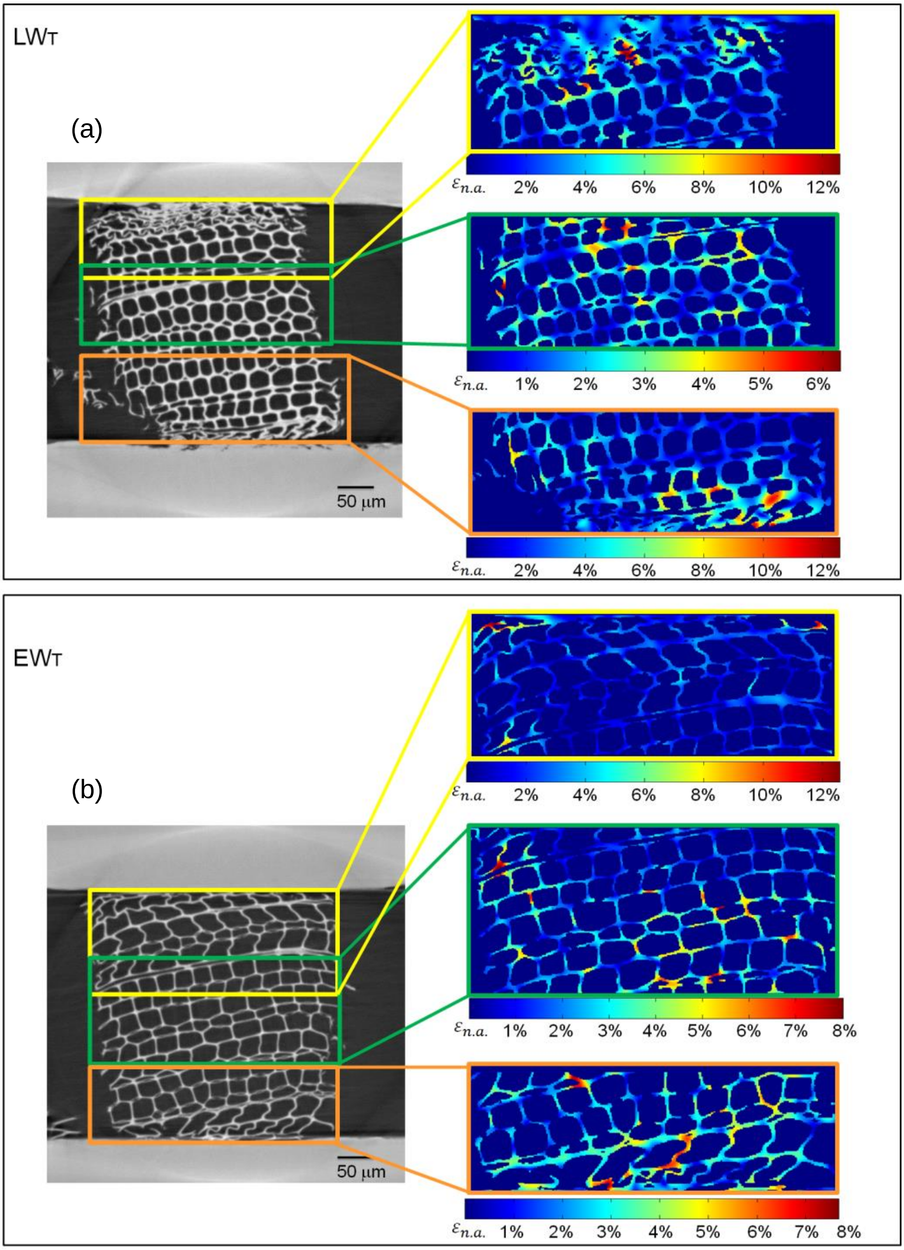

Figure 7.8: 2D map of the non-affine strains in three different regions of the wood sample. The results are reported for (a) LW_T and (b) EW_T between the 15% and the 85% RH states.

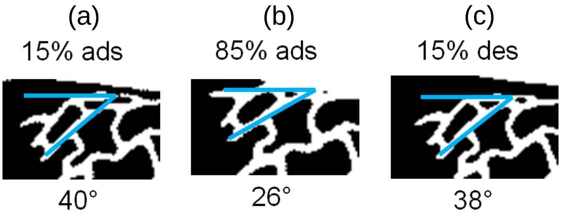

Figure 7.9: Shape-memory effect on the cell undergoing large deformations and highlighted in the yellow region of sample EW_T.

To further highlight the occurrence of moisture-induced shape-memory effects in wood, we consider a ROI in LW_R at the outer edges of the sample (see blue rectangular in Figure 7.10). This region shows cells that are cut/damaged during the sample preparation process. These initially deformed cells are expected to show high non-affine deformation, indicating a shape memory of the original cell shape. Figure 7.10b shows the 3D map of the equivalent non-affine strains and a slice cut out in the middle of the volume. The components of the non-affine strains are mapped on the same slice in Figure 7.10c. In Figure 7.10b (right), we observe high equivalent non-affine strains in the cell walls at the outer edge. A comparison with Figure 7.10c shows that these strains are due to high tensile non-affine strains, $\varepsilon_{n.a,xx}$, in horizontal cell walls and, to a less extent, to high tensile strains, $\varepsilon_{n.a,yy}$, in vertical cell walls. These tensile strains cannot be explained by the restraining of the PMMA device, but only to a deformation induced by shape memory. We consider a possible realignment of the different polymers (Derome et al., 2012) to justify the phenomena. In fact, it may be that during sample preparation with razor blade, initial deformations are induced on the sample, resulting in a warping of the stiff cellulose fibrils. Fibrils are less sensitive to moisture compared to the matrix, due to their high content in crystalline hydrophobic cellulose. Thus, it is suspected that fibrils can remember their original relative position and geometry. A “permanency” of the geometry could be embedded in the cellulose fibrils at the time of its synthesis by the living cells and its deposition in the external skeleton (Derome et al., 2012). Such hypothesis is also considered by Burgert et al (2009).

As clearly observed, cell buckling phenomena are widely visible in these experiments. Under mechanical restraint, sorption of water leads to stresses provoking buckling. A case of buckling under radial restraint is discussed for a ROI in sample $\mathrm{LW_R}$.

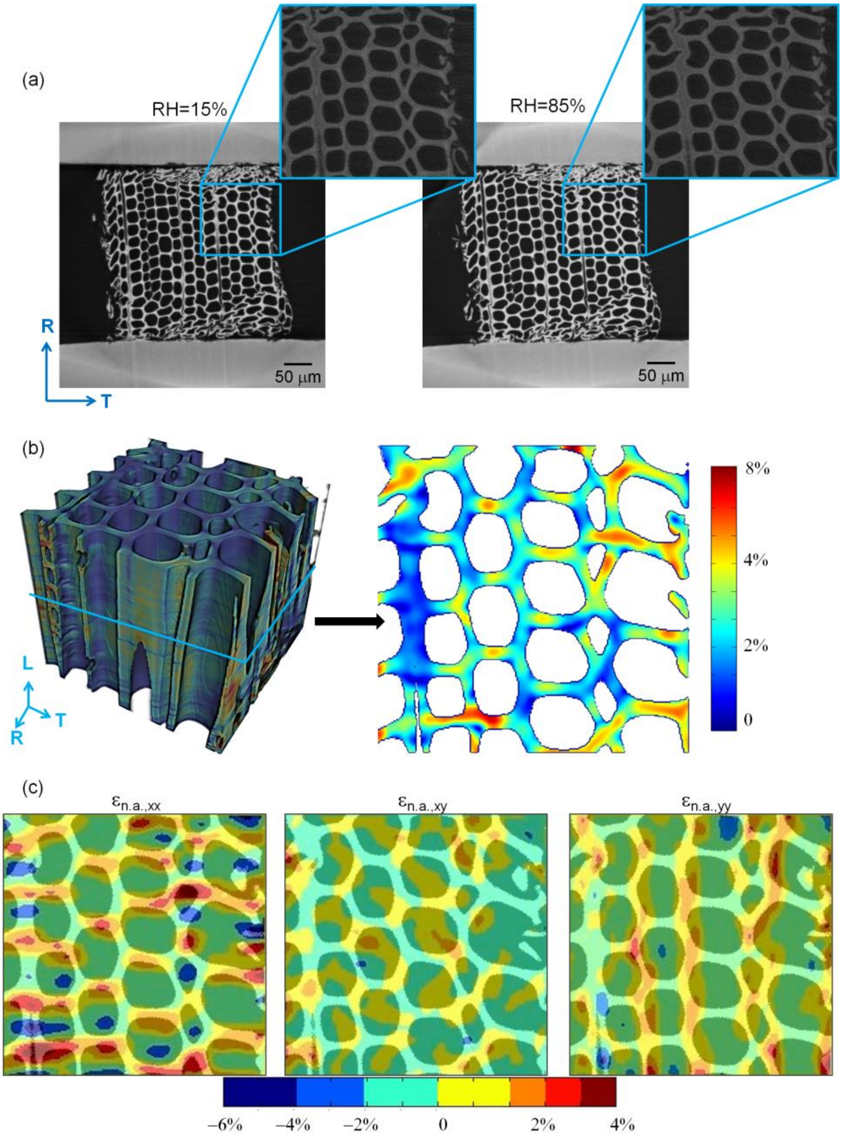

Figure 7.10: (a) $\mathrm{LW_R}$ sample, dry (left) vs wet (right), with a zoom on the ROI (in blue) where shape-memory is observed. (b) 3D map of the equivalent non-affine

strains, with a slice cut out in the middle of the volume and (c) the components of the non-affine strains in tangential (xx) and radial (yy) directions.

We already observed in LW_R the buckling of a group of irregular cells initially deformed during insertion of the wood sample in the cube. We analyse now in more detail a region highlighted in the yellow box in Figure 7.11a. In the figure, we report the equivalent non-affine strains and their strains components. We observe high values of non-affine strain (~8%) in two regions, for which buckling is highlighted in Figure 7.12a. The observed buckling accords well with the typical buckling mode of regular periodic honeycomb structure under radial restrain as reported in Derome et al. (2012). This buckling mode is characteristic for honeycomb structures subjected to axial compressive stresses as shown in Figure 7.12b.

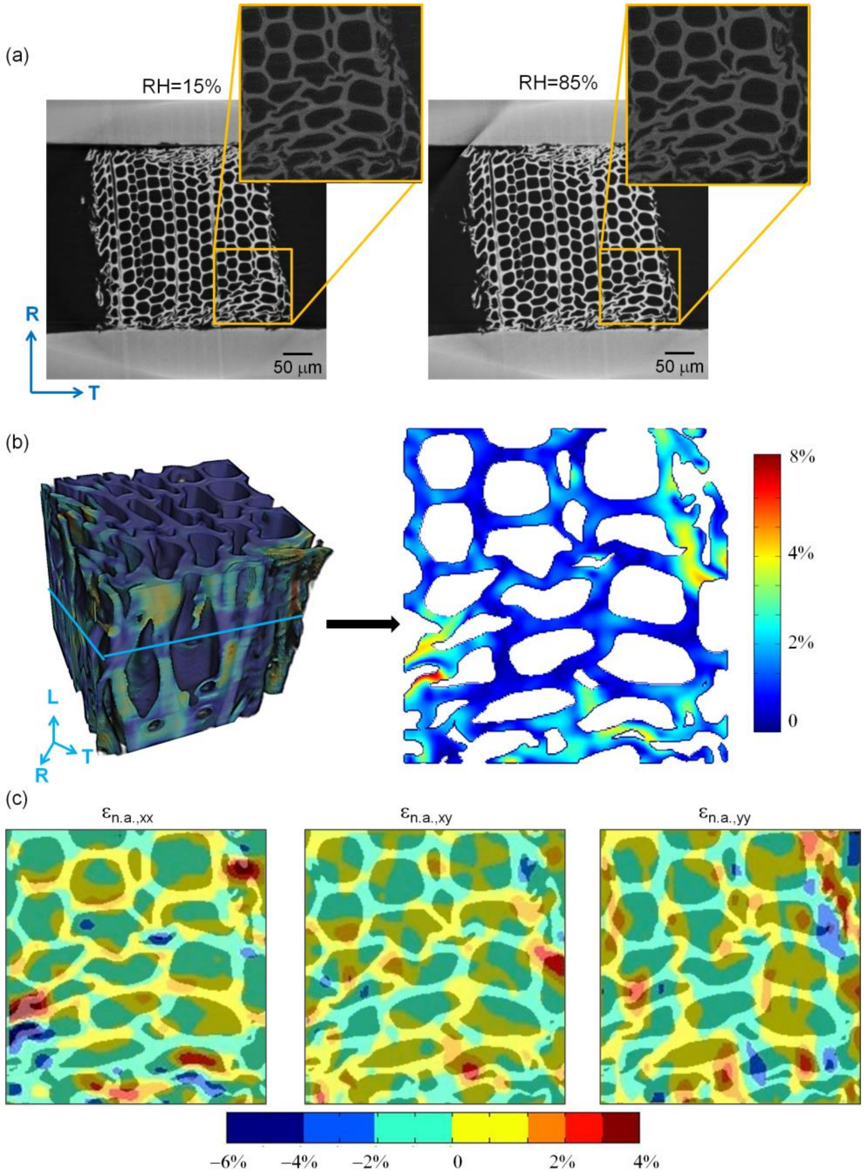

Figure 7.11: (a) LW_R sample, dry (left) vs wet (right), with a zoom on the ROI (in blue) where buckling is observed. (b) 3D map of the equivalent non-affine strains, with a slice cut out in the middle of the volume and (c) the components of the non-affine strains in tangential (xx) and radial (yy) directions.

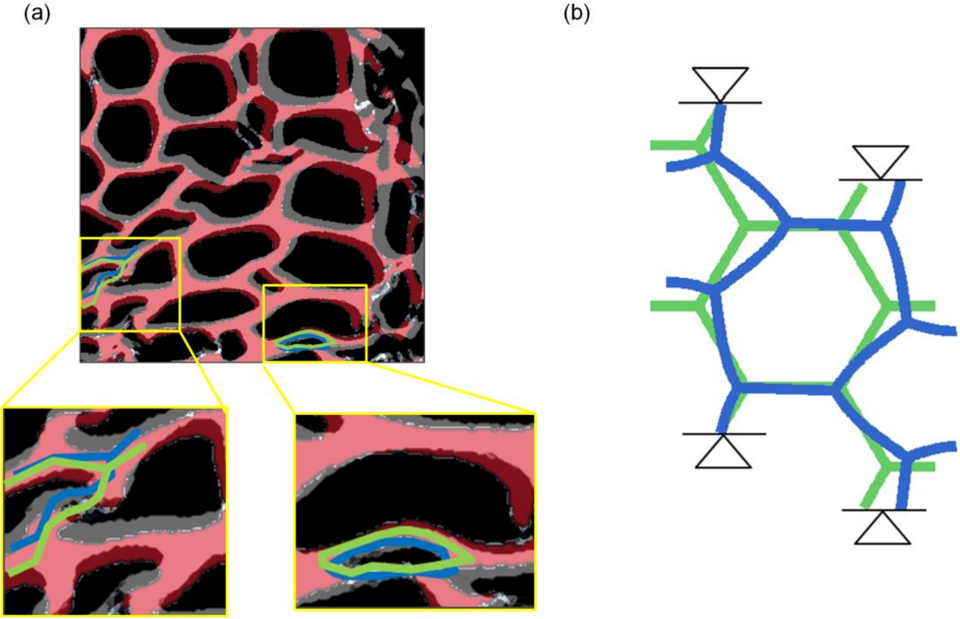

Figure 7.12: Sample LW_R: (a) Superposition between dry state at 15%RH (in red) and wet state at 85%RH (in grey), showing buckling under radial restraint. The cells undergoing buckling are highlighted in green for dry and in blue for wet states. (b) Schematic representation of typical buckling of a regular periodic honeycomb structure under radial restraint (from Derome et al., 2012).

7.4 Conclusion

In this chapter, we showed that the restraining device successfully prevents the free swelling of wood during moisture adsorption, thus modifying significantly the amount of swelling and its anisotropy. This restraining experiment is also appropriate for characterizing localized non-affine deformations in the wood cells, such as cell wall buckling. Studying one cell undergoing large deformation during moisture sorption, we observe that this cell, which was initially highly deformed due to the sample preparation process, recovers its original shape when wetting. This regaining of cell shape after wetting is referred to as moisture-induced shape memory, and is an effect that is known in biological materials. The experimental approach presented in this chapter, together with the results of Chapters 5 and 6, leads to a basic understanding of the swelling behaviour of cellular wood in response to environmental stimuli. However, to still better understand swelling, a further downscaling of our experimental approach will be fruitful for setting up a complete integrated approach. We investigate sub-cellular features of the cell wall material in Chapter 8.

Chapter 8

Hygroscopic swelling and shrinkage of bordered pits and middle lamella probed by phase-contrast nano-tomography

This work documents the capacity of synchrotron radiation-based phase-contrast X-ray tomographic nanoscopy to capture ultra-structural features in the wood cell wall undergoing changes in moisture content. The investigation is mainly focused on two features of the wood cell wall: bordered pits and middle lamella material. In the introductive part, first a literature review is presented, followed by a detailed description of the sample preparation. Then we document the *in-situ* nano-tomographic experiments and finish with a discussion on the relevance of studying these specific singularities of the wood cell wall.

8.1 Introduction

On bordered pits

We describe the anatomy of bordered pits and the function of these valves in trees. Bordered pits are most interesting features in softwood, which control the transport of water between cells. Bordered pits are passages through the cell walls of xylem conduits (vessels and tracheids) formed by a separation between the secondary walls from the compound middle lamella. The entry opening has a diameter of 3-7 μm and is called the porus or pit aperture. In the central plane, a membrane spans the pit chamber, which thick centre is called the torus (diameter 5-10 μm, thickness 100 to 500 nm depending on the species), while the thin remaining part is called the margo. Figure 8.1 shows the internal structure of a bordered pit and visualises the pit after aspiration. Bordered pits in Picea tracheids are larger and more abundant in earlywood than in latewood (Koran, 1974). In Picea mariana tracheids, bordered pits have a diameter of 16.4 μm in earlywood, while in latewood they have only a small diameter of 6.1 μm (Koran, 1974).

Furthermore, studies on permeability in living wood highlighted that after air drying, the water permeability decreases with 1-3 % with respect to its initial value (Erickson and Crawfort, 1959). Such large changes of permeability are of great importance in wood preservation and in studies of water conduction in the living tree. Drying wood generally causes the torus to be displaced coming into contact with one of the pit borders. This phenomenon is referred to as pit aspiration. Pit aspiration provokes the closing of the pit; the pit membrane and the torus move across one side of the pit aperture to seal it and prevent the fluid flow through the pit, as shown in Figure 8.1, (Petty, 1972).

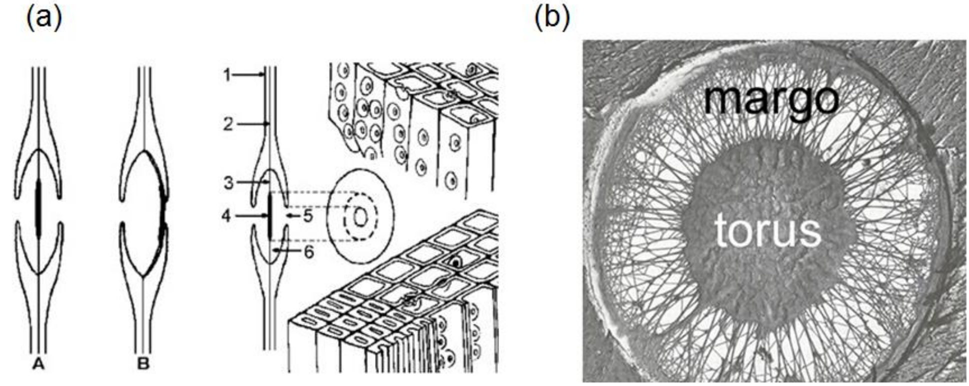

Figure 8.1: (a) Representation of an earlywood bordered pit in section transverse to the pit membrane. On the left, (A) Un-aspirated situation, (B) Aspiration of a bordered pit during drying, i.e. the torus is pulled across the pit chamber by surface tension forces. On the right, typical earlywood bordered pit: 1 tracheid wall

(secondary wall), 2 middle lamella (and primary wall), 3 margo strands, 4 torus, 5 pit aperture, 6 pit chamber (from Petty, 1970). (b) Scanning electron microscope image of a pit membrane, showing the torus and margo of conifer tracheids (Pittermann et al., 2005).

Liese and Bauch (1967) studied the structure of bordered pits in earlywood and latewood tracheids of conifers and the pits aspiration process using a microscope and permeability studies. The results show a linear dependence of the pit closure on the membrane structure (e.g., thickness and shape) in species like Pinus and Picea. The number of pits per tracheids varies from 50 to 300 in earlywood with only 10 to 50 rather small bordered pits in latewood (Stamm, 1970), meaning that the permeability of latewood specimens is higher than in earlywood for seasoned wood while it is lower in green wood (Petty and Preston, 1969). Although very detailed anatomical statistical studies of bordered pits with respect to their function are existing (e.g. Domec et al., 2006), the techniques used, i.e. electron microscope combined with permeability, are invasive and two-dimensional. The main findings of these studies reveal the anatomical structures of bordered pits in different species and their role in controlling water flow. Fujii et al. (2001), for example, revealed that the sizes of the openings between the margo strands are likely to be the hydraulic bottleneck controlling water flow between tracheids because water must move laterally through the membrane. However, the need for a three-dimensional mapping in order to better understand the pit function in the context of wood complex vascular network has been highlighted by Choat et al (2006). Additionally, little is known on the geometrical changes of bordered pits during moisture adsorption/desorption. In this work, we document in 3D the hygro-mechanical behaviour of two bordered pits and we highlight the capacity of synchrotron-radiation nano-tomography to document *in-situ* the hygroscopic behaviour of such small features in the complex cellular structure of wood.

On middle lamella

The middle lamella (ML) is a layer that glues the wood cells together. Contrary to the cell wall, especially its thickest layer S_2, the middle layer is free of cellulose. The transition from the middle lamella to the adjacent cell wall layers is not clearly visible in microscopic sections; hence in anatomical studies ML is often combined with the primary cell wall and is referred to as the compound middle lamella (CML). The volume fraction of the compound middle lamella in coniferous wood is ca. 10-12% of the woody tissue volume (Fergus et a1., 1969). The middle lamella is largely isotropic and appears homogeneous under scanning electron microscope. It is composed of an amorphous matrix of pectin with a high concentration of lignin. Cell wall corners of spruce wood are highly lignified (e.g., Downes et al., 199l; Wimmer and McLauglin, 1996), as is the compound middle lamella (Fergus et al., 1969). Pectin is the ultra-adhesive constituent of the middle lamella which role is to connect neighbouring cells to one other. Moreover, due to its amorphous structure and lack of cellulose, ML appears dark without exhibiting birefringence under polarized light. The thickness of the middle lamella ranges from a few tenths of a micrometre up to 5 μm in the cell-wall corners (Skyba, 2008). Due to its small thickness and lack of cellulose, the structure and mechanical behaviour of the interface between two adjoining tracheids have been ignored for years. A recent study of Raghavan et al. (2012) aimed at investigating the deformation and failure mechanisms of double cell walls consisting of compound middle lamella, S_1, and S_2 layers. *In-situ* SEM compression tests were performed on a 3 μm thick pillar fabricated with focused ion beam (FIB) to study its mechanics and deformations response. Lower strength and stiffness values compared to the secondary cell wall were obtained in the compound middle lamella. Failure was found to occur at the interface between the S_1 and S_2 layer. Cracks were observed at the S_1-S_2 interface, whereas the CML remained crack free. This observation suggested that the CML has more resistance to cracking than the individual cell walls. However, local deformations in wood seem to be strongly dependent on the middle lamella. In fact, a relaxation mechanism in the matrix between the cellulose fibrils, inducing irreversible deformations in spruce wood, has been observed by *in-situ* synchrotron micro-focus experiment on a wet wood foil. The origin of this relaxation was found in the matrix between the cellulose fibrils or in the middle lamella (Keckes et al., 2003). However, the behaviour of the middle lamella has never been investigated during hygroscopic loading. How does the middle lamella influence the swelling behaviour of wood induced by moisture sorption? In this work, we aim at answering this question in order to give a more general understanding of the wood swelling behaviour at cellular and sub-cellular scales.

8.2 Experimental work

As the nano-scale work performed looks essentially at two different features, two sample preparations and image acquisition with nano-tomography are presented.

8.2.1 Sample preparation

For bordered pits study

The study of bordered pits requires a sample size of approximately 50×50 μm^2 cross section to fit within the field of view. The wood thin sticks are cut with razor blade from 10 × 10 × 10 mm^3 oven-dry cubes of Norway spruce (*Picea abies*), under an optical microscope. The thin wood sticks tend to bend during moisture sorption; therefore, the samples need to be kept in place during the whole hygroscopic protocol. We propose a sample holder where both ends of the sample are kept in place. The sample holder is small enough to fit on the sample stage within the environmental chamber (see section 3.2) and is made of a material transparent to X-rays, i.e. polyimide foil. The section of this sample holder fits into the field of view. A cylinder-shaped sample holder is selected to allow a uniform X-ray path, independent on the rotational angle. The cylindrical sample holder is made by linking two small PMMA cylinders at both ends. The diameter of the cylinders is 8.6 mm. The bottom cylinder has a pin holder containing a magnet for insertion on the magnetic rotational stage of the TOMCAT setup. The polyimide foil is rolled and glued around the two cylinders, which are kept together by a thin aluminium wire. A pre-cut circular hole allows access inside the tube, to cut out a centre piece of the aluminium wire. The sample holder is then ready to receive the wood sample, where the ends of the wood sample are glued to the ends of the aluminium wire (Figure 8.2, a-b).

Such samples are prepared before the experiments and kept in a desiccator with desiccant particles until the beginning of the tomographic scans.

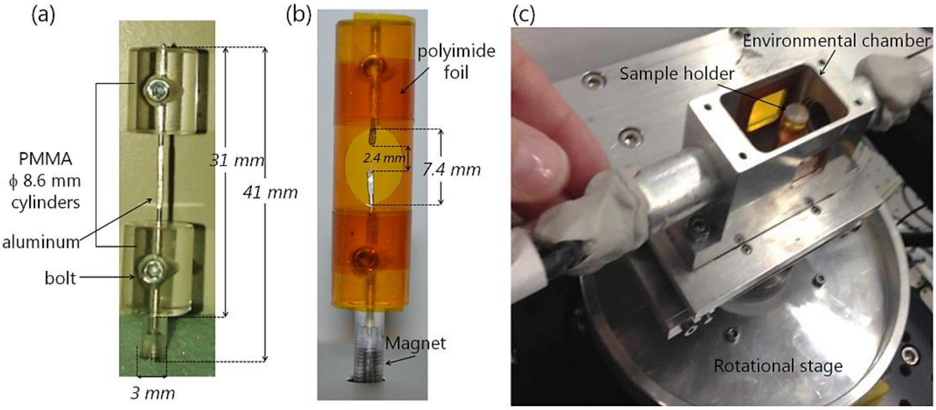

Figure 8.2: (a) Components of the sample holder, (b) finalized with polyimide foil and with access window for inserting and gluing the wood fibre. (c) A view from the top of the sample holder inserted in the environmental chamber.

For middle lamella study

For this study, the middle lamella needs to be isolated from the surrounding wood tissue. Two micro-pillars are prepared by focused ion beam (FIB) machining. Each micropillar is machined with two different FIB setups, the first available at the Empa Dübendorf in the Laboratory of Reliability Science and Technology, while the second pillar is prepared at the Laboratory of Mechanics of Materials and Nanostructures at Empa Thun.

The first micropillar is prepared from an earlywood sample with initial size of 1×1 mm. This sample is milled into a rectangular micropillar of 2×2 μm size using a dual FEI Strata 235 gallium (Ga) FIB system, combined with scanning electron microscope (SEM). The sample surface is coated prior to FIB with an approximately 8 nm thick gold layer in order to minimize charging and drift during SEM imaging and FIB milling of the wood. During the preparation of the sample, a beam acceleration voltage of 30 kV has been used and a side wall milling method is chosen. The current is initially set to 20 nA for the coarse milling and then it is varied from 1nA to

300pA for the polishing of the micropillar to reach its final thickness. The first micropillar is obtained from an earlywood tissue with a cross-sectional dimension equal to 1.3 µm and height of 13 µm. The first micropillar is shown in Figure 8.3, referred to as ML1.

The second micropillar is prepared from an earlywood sample with initial size of 1×1 mm. In this case, the wood fiber was sputter-coated with several nm of Au-Pd to prevent charging of the insulating material. A Tescan Lyra dual beam FIB/SEM workstation is used for the machining of the pillar. The material around the final pillar location is first removed in a coarse milling step using a 30 keV ion beam with 6-8 nA ion current, leaving an area of approximately 10 x 10 µm^2. In a second fine milling step with an ion-current of 1 nA, the free standing area is reduced to a circular diameter of 3 µm. Thereafter, the Au-Pd coating is renewed for further milling. In a last step, the specimen is polished to the final diameter of 0.9 µm using low ion current conditions (30 keV, 75 nA) to minimize FIB-damage. In Figure 8.3, the second sample is shown and indicated as ML2.

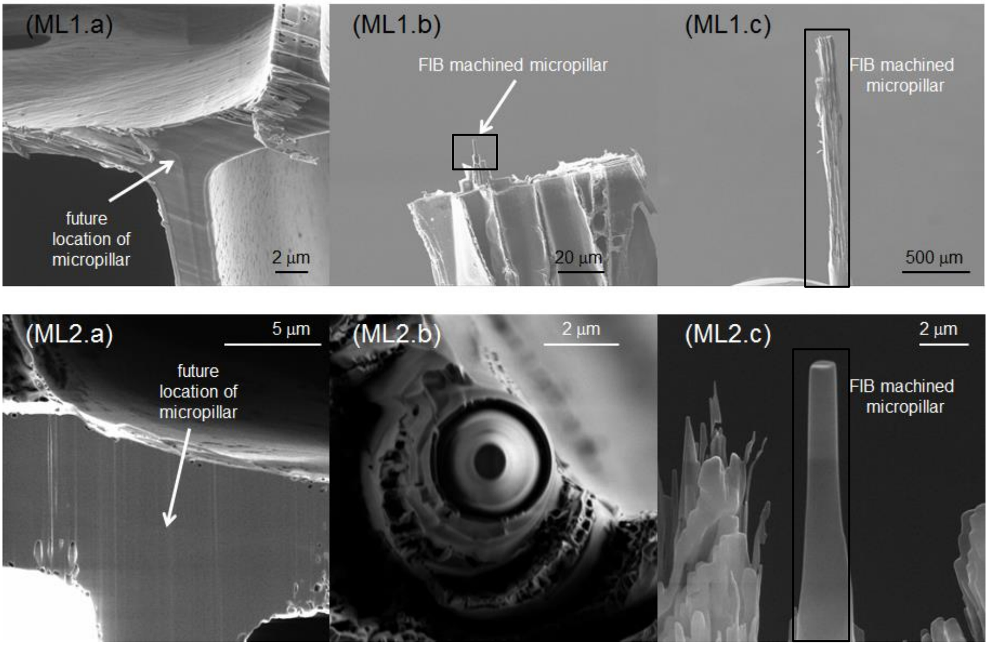

Figure 8.3: Preparation of micropillars ML1 and ML2 with FIB milling. (a) The future sample location is identified with FIB/SEM visualization. (b) Machining of the micropillars with FIB and (c) a close look to the machined samples. The black rectangles indicate which part of the samples is imaged in nano-tomography.

8.2.2 Experimental protocol

The samples are located inside the environmental chamber (described in section 3.2), as shown in Figure 8.2c. Before starting the hygroscopic loop, the chamber top is closed and the control system set at 10% RH to impose the equilibrium of the sample at reference state (referred to as dry state).

During the experiments, the samples are exposed to cyclic variations in relative humidity (RH) for hygroscopic loops in adsorption and in desorption. Sample with bordered pit 1 is exposed to four relative humidity steps in adsorption (10% - 50% - 75% - 90%) and three in desorption (75% - 50% - 10%). Sample with bordered pit 2 is only exposed to dry (10% RH) and wet (80% RH) states. The two samples with machined middle lamella pillars undergo a full hygroscopic loading protocol, with four relative humidity steps in adsorption (10% - 50% - 75% - 90%) and three in desorption (75% - 50% - 10%). The RH conditions at each step are maintained long enough to ensure moisture equilibrium in the samples, i.e. 40 minutes, for a total of 48 hours of experiments.

8.2.3 Image acquisition

The experimental setup has been described in section 3.2.2.2. In a first setup, the regions of the sample containing bordered pits have to be identified. This is done with the micro-setup of 0.7 μm nominal pixel size. Then, the nano-setup is used. A total number of 361 equiangular projections per tomographic scan between 0° and 180°, including 10 dark fields and 30 flat fields, with 728×728 pixels are captured on a CCD camera with a 14 bit dynamic range and an exposure time of 150 ms each, resulting in a total scanning time of approximately 34 min. The dimension of the field of view is 36×36 μm in the horizontal and vertical directions. This brings to an effective reconstruction pixel size of about 50×50 nm. Scans are performed with energy of 16 keV and no binning factor.

8.3 Image processing

The reconstructed tridimensional datasets are analysed with different software. In total, four datasets are acquired: two of middle lamella and two of bordered pits. VG Studio MAX 2.0 is used for the 3D renderings of the datasets of middle lamella, for segmenting the images and analysing the volume of the material. Figure 8.4 shows the volume renderings of the two pits and the two micropillars of middle lamella analysed in this work. Then, the affine registration on the two datasets of middle lamella is performed with the software 3D Slicer. Finally, we detect the local strains with our algorithm for non-affine registration, as explained in Chapter 4. In this case, ‘Registration P’ gives the optimal solution for both pits and middle lamella datasets with ‘map’ as method for extracting the feature points on the segmented images. The optimization criteria used is the steepest descend method for all the datasets.

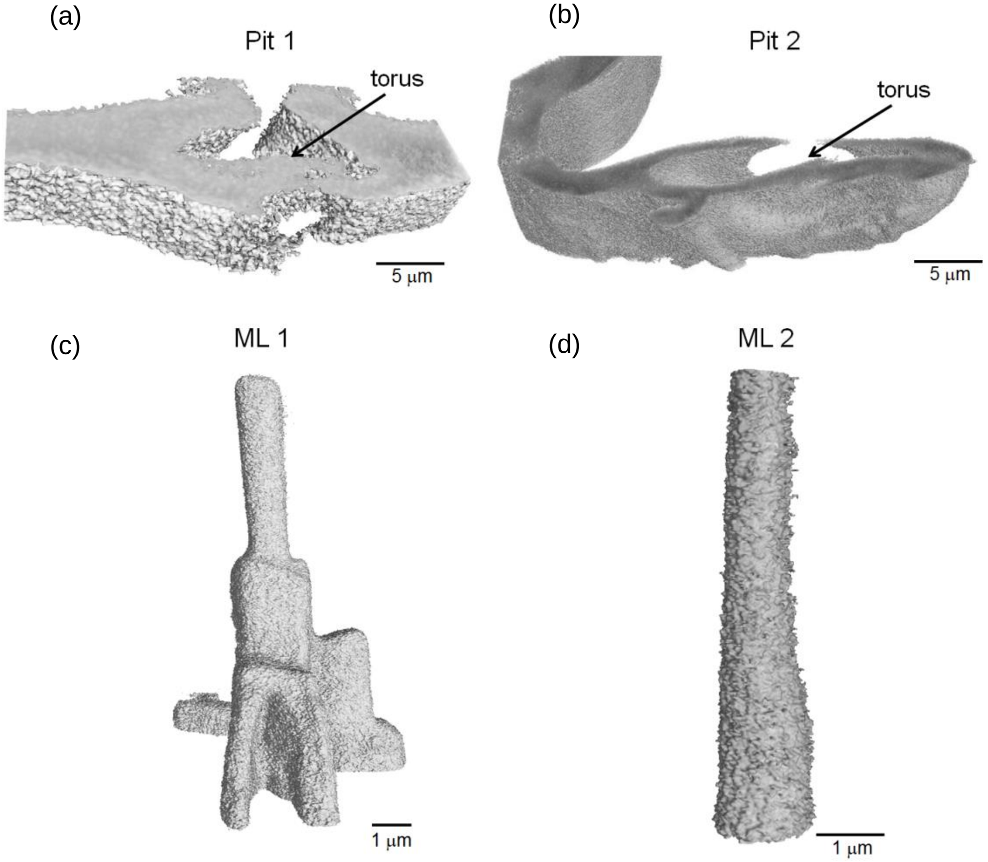

Figure 8.4: Volume renderings of (a, b) the two pits (on the top) and (c, d) the two micropillars (on the bottom).

8.4 Results and discussion

In this paragraph, we present the main results obtained from the analysis of two datasets of middle lamella micro-pillars and two datasets of bordered pits. Affine registration results are presented for the micro-pillars while non-affine registration is performed on the four datasets.

8.4.1 Behaviour of bordered pits during moisture sorption

Two bordered pits are selected in the two earlywood samples and subjected to a loading protocol. We present the non-affine strains of bordered pit1, which has a diameter of 9 μm at 10% RH. The non-affine strains are calculated for the full hygroscopic loop: 10% - 50% - 75% - 90% - 75% - 50% - 10%, with RH=10% in adsorption considered as reference state. Figure 8.5a shows a cross-section of the bordered pit at different RH levels. The pit is slightly tilted ($\theta°_{\text{tilting}}$) with respect to the horizontal axis (as indicated in figure 8.5a) with an angle of 74° at 10% RH. This angle decreases to 67° at 90% RH during adsorption, and returns to its original value at 10% RH in desorption, as shown in Figure 8.5b. This effect explains that the wood sample housing the bordered pit returns to its initial position after being subjected to an adsorption and desorption cycle.

We do not report affine strains of bordered pits as the deformation of these features appears to be more local. For this reason, the non-affine registration method is used. The equivalent non-affine strains are calculated using eq. 4.10 and mapped in 2D on the reference image, as shown in Figure 8.5c. Note the different maximal values used in the scale bars. The non-affine strains at 50%RH range between 6% and 8%. The strains increase to a maximum of 10% at 75% RH. Here, the torus starts to move towards the pit opening on the right, resulting in a local displacement which reaches its maximum (~12%) at RH = 90%. In desorption, the local non-affine strains disappear between 75% and 50%RH. A high non-affine strain of 8% is observed at 10%RH, showing that locally in the torus some permanent strains may remain after cycling.

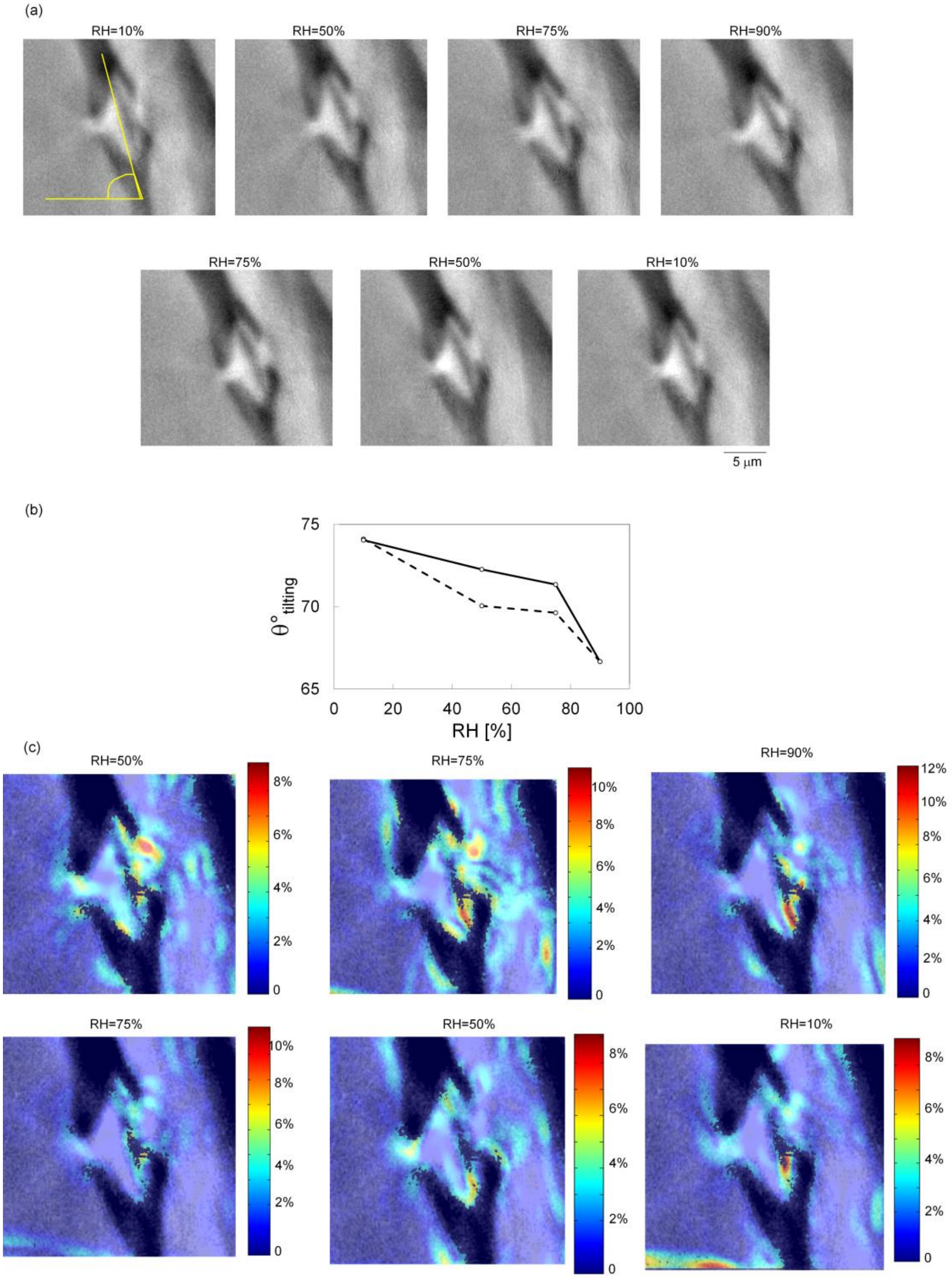
(a)
RH=10%
RH=50%
RH=75%
RH=90%
RH=75%
RH=50%
RH=10%
5 μm
(b)
75
70
65
θ° tilting
0
20
40
60
80
100
RH [%]
(c)
RH=50%
8%
6%
4%
2%
0
RH=75%
10%
8%
6%
4%
2%
0
RH=90%
12%
10%
8%
6%
4%
2%
0
RH=75%
10%
8%
6%
4%
2%
0
RH=50%
8%
6%
4%
2%
0
RH=10%
8%
6%
4%
2%
0

Figure 8.5: (a) Cross-sectional view of pit 1 at different RH values in adsorption (10% - 50% - 75% - 90%) and in desorption (75% - 50% - 10%) used for the analysis of (b) the tilting angle in adsorption (dashed line) and in desorption (continued line) and (c) the equivalent non-affine strains.

Pit 2 is located at the edge of a cell wall, where the sample is mechanical damaged by razor blade cut. The pit has a diameter of 23 μm. Figure 8.6 shows the non-affine strains between dry (reference at RH=10%) and wet (moving at RH=80%) state in adsorption. The torus is partly damaged during sample preparation, and, as a result, the torus is pushed on one side of the pit opening. Some movement is visible. The non-affine strains in *x*- and *y*-directions range between 2% and 4%. We do not observe large local deformations, which most probably can be attributed to the initial collapse of the torus on the opening of the bordered pit.

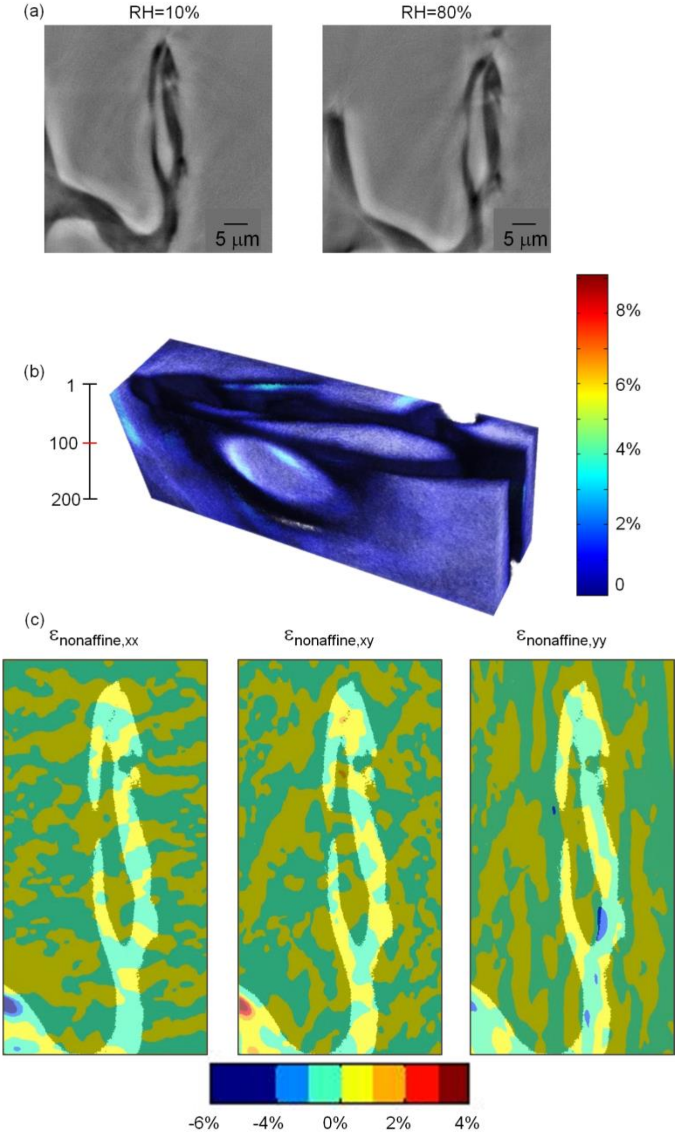

Figure 8.6: (a) Cross-sectional view of pit 2 at two RH values used for non-affine registration and calculating (b) the equivalent non-affine strain over the volume and (c) the components of non-affine strains along the *x*, *xy* and *y* directions.

8.4.2 Behaviour of middle lamella micro-pillars during moisture sorption

The first sample of middle lamella, presenting a very nice geometry and a good contrast, is used to determine first the affine strains with 3D Slicer as shown in Figure 8.7b. The affine strains in adsorption lie above the desorption curve. This effect may be due to presence of some initial deformations caused by a lack of pre-conditioning of the sample. The black curve represents the strains in the *x*-direction, corresponding, in this case, to the tangential direction of wood, while the radial strains, *y*-direction, are plotted in grey. The tangential strains are slightly higher than the radial strains in adsorption for 50% and 75% RH. The maximum affine strain at 90%RH reaches 5.3% and 5.4%, respectively in tangential and radial direction. In desorption, the two curves almost overlap. We may thus conclude that the behaviour of ML1 is isotropic. VG Studio Max 2.0 is used to segment the volumes at each RH level using the region growing algorithm and calculating the amount of volume at each state. In this way, the volumetric swelling strains are determined as:

$$\varepsilon_V = \frac{V_{RH\%} - V_{10\%}}{V_{10\%}} \tag{8.1}$$

Figure 8.7c, reports the volumetric strains as a function of RH. We observe that the adsorption curve lies again above the desorption curve and reaches a maximum at 90% RH.

We use the non-affine registration algorithm for comparing two states in adsorption, i.e. dry (RH=10%) and wet (RH=90%), see Figure 8.8a. The equivalent non-affine strain distribution (calculated with Eq.4.10) is shown in Figure 8.8b, and its components in Figure 8.8c. We observe a non-uniform strain distribution over the cross-section of the sample, where both positive (tensile) and negative (compressive) strains appear. These neighbouring zones of tensile and compressive strain indicate local bending or slipping of different layers in the sample. The non-affine strains range between -8 and 8% and are slightly higher than the affine strains (max. 5.4%).

The results for ML2 are shown in Figure 8.9. In this case, the datasets are very noisy due to the sample preparation and uneven surface. This does not allow to acquire accurate information for a detailed analysis. The volume renderings of ML2 at the different RH levels are reported in Figure 8.9a. The analysis of this datasets is limited to the calculation of affine and volumetric strain, reported in b and c of the same figure. The strains in adsorption lie above the strains in desorption, as observed for ML1 and the tangential and radial strain curves almost overlap. The volumetric strains in ML2 follow a similar trend as the volumetric strains in ML1, with the adsorption curve above the desorption one and a maximum of 10% volumetric strain at 90%RH. The results of affine and volumetric strains are summarized in Table 8.1 for ML1 and ML2. The values of both experiments agree very well.

Comparing the volumetric affine strain values of the middle lamella obtained in this study of 10% to the values up to 25% obtained for a micropillar of the S2 layer by Rafsanjani et al (2014), we conclude that the ML swells much less than the S2 layer. We further conclude that, although the ML shows an isotropic affine deformation behaviour, local non-affine strains may highly vary between tensile and compressive behaviour, in different directions. More research is needed to fully explain this difference between affine and non-affine behaviour.

When comparing the affine strains of the ML with the global earlywood and latewood tissue, we may conclude that the maximal strains for ML (5.5%) are in the same range as the affine strains for earlywood in tangential direction (4.3%) and for latewood in tangential (4.8%) and radial directions (4.2%), and are higher than those for earlywood in radial direction (2.4%). The understanding of the interaction between the different layers during swelling needs further analysis, using e.g. a multiscale modelling analysis (see e.g. Rafsanjani et al., 2013).

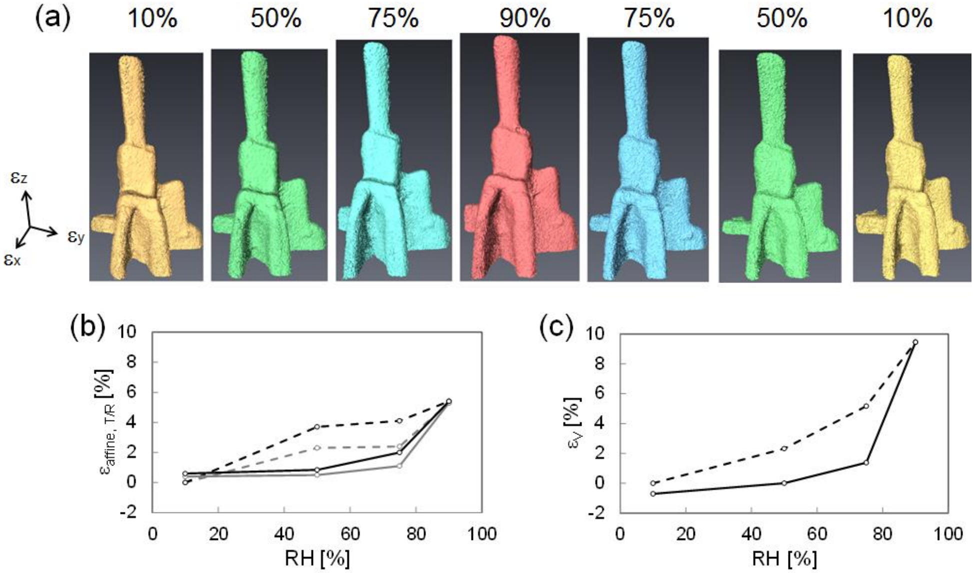

Figure 8.7: (a) Volume renderings of ML1 in adsorption (10% - 50% - 75% - 90%) and in desorption (75% - 50% - 10%) used for the analysis of (b) the affine strains in adsorption (dashed line) and in desorption (continued line) and (c) the total volumetric strains.

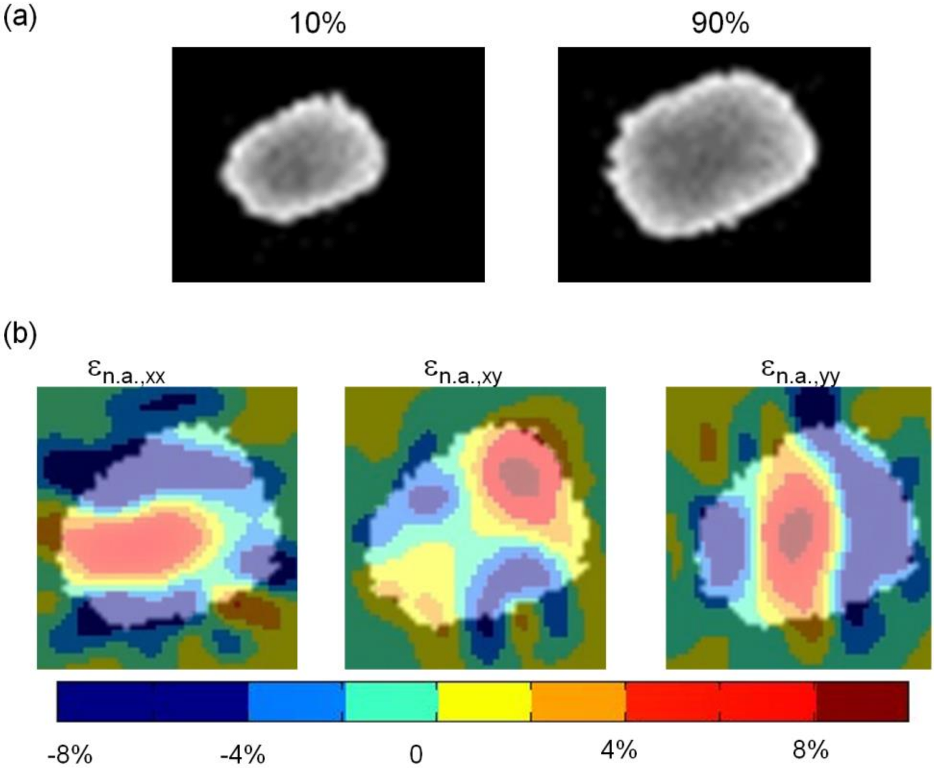

Figure 8.8: (a) Cross-sectional view of ML1 in the reference and moving states. (b) 2D map of the non-affine strain components in the *x*-*y* plane.

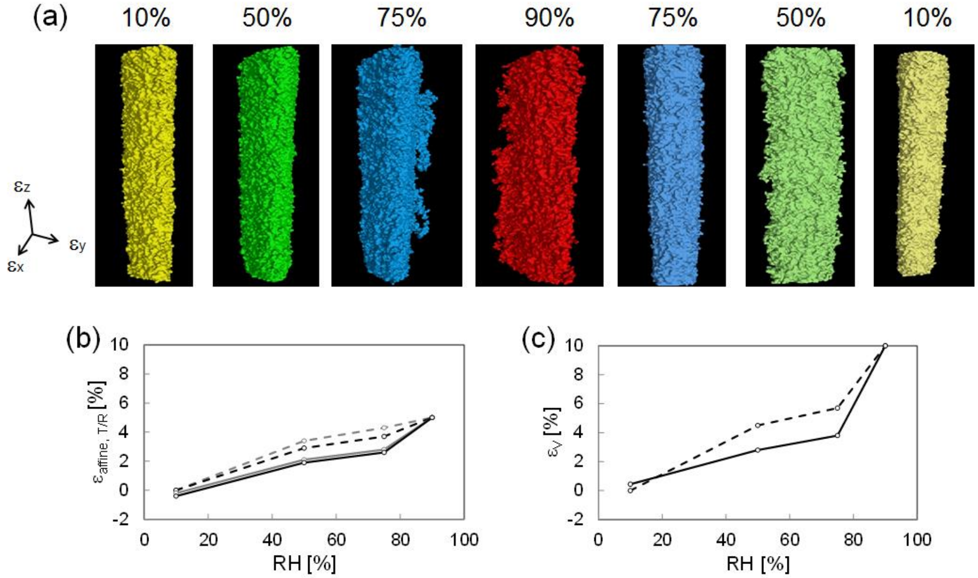

Figure 8.9: (a) Volume rendering of ML2 in adsorption (10% - 50% - 75% - 90%) and in desorption (75% - 50% - 10%) used for the analysis of (b) the affine strains in adsorption (dashed line) and in desorption (continued line) and (c) the total volumetric strains.

Table 8.1: Maximum affine swelling in *x*-*y* directions and maximum volumetric swelling for the two samples of middle lamella.

	ML1	ML2
$\Delta\varepsilon_{affine,x}$	5.3%	5%
$\Delta\varepsilon_{affine,y}$	5.4%	5%
$\Delta\varepsilon_{V}$	9.5%	10%

8.5 Conclusion

The swelling behaviour of two sub-cellular features in the wood cell wall is studied in this chapter, with the aim at giving a complete picture of the swelling behaviour of wood at two scales of observation: cellular and sub-cellular. We observe that non-affine swelling deformations occur in bordered pits of earlywood, also showing a movement of the torus towards the pit surfaces. Further studies on the deformation of bordered pits during hygroscopic cycling and its effect on permeability can bring new insights on the change of permeability in dried wood caused by subsequent wetting/drying. The swelling of another sub-cellular feature, the middle lamella, is investigated also in this chapter. The ML is found to swell less than the S2 layer in the wood cell wall. Although the ML shows an isotropic affine deformation behaviour, non-affine strains may occur locally, indicating a local bending or slip between subcellular layers.

Chapter 9

Conclusion and Outlook

Understanding cellular materials, such as wood, and revealing the relation between cellular structure and swelling behaviour can be of relevance for many other biological and engineering materials. The aim of the present research is to build up an experimental approach based on advanced image analysis for studying the hygro-mechanical behaviour of wood at cellular and sub-cellular scales. This thesis focuses mainly on the experimental documentation of the swelling behaviour of softwood, the origin of swelling hysteresis and the occurrence of anisotropy in different wood tissues. The method can be extended for studying the coupled hygric and mechanical deformations of many biological and cellular materials with a non-destructive approach at cellular and sub-cellular scales. The main conclusions of the present work are summarized in this section.

9.1 Synthesis

The main findings regarding the anisotropic behaviour of different wood tissues are summarised in this paragraph. The anisotropic swelling ratios, i.e. the ratio between the tangential to the radial swelling, discussed in Chapters 5, 7 and 8, are reported in Table 9.1 and plotted in Figure 9.1 for homogeneous tissues (earlywood and latewood) in free swelling, in restrained swelling and for heterogeneous (combined late- and earlywood -) dry and green wood tissues. Earlywood swells anisotropically during moisture sorption. Latewood shows a quite isotropic swelling behaviour, in homogeneous and combined tissues. The swelling of earlywood becomes more isotropical when combined with the more isotropic swelling latewood. The anisotropy of earlywood and latewood tissues is importantly modified in restrained swelling experiments due to the lowering of swelling in the restraining direction. In green wood, both earlywood and latewood show important swelling anisotropy, while, in the interface between the two tissues, green wood behaves more isotropically.

The linear swelling coefficients for dry wood, defined as the slope of the linear relation between strains and MC, are plotted in Figure 9.2. The plot summarizes the results discussed in Chapters 5 and 6 for different wood tissues. The swelling coefficient ranges from 0.1 to 0.5, with lower values for earlywood in radial direction, which is attributed to restraining by the rays. There is no direct relation of tangential swelling coefficient and porosity and a slight decrease of radial swelling coefficient with porosity, which indicates that the cellular structure plays also an important role. Such cellular structure features must include anisotropy of cell layer materials, layered structure of the cell wall and geometry of the cell.

Table 9.1: Anisotropy of earlywood and latewood in free swelling (Chapter 5), of regions of interest in combined dry and green (GW) wood samples (Chapter 6) and of regions of wood with minor (ROI 1) or major (ROI 2) restraint during moisture sorption (Chapter 7)

	Chapter 5		Chapter 6			Chapter 7	
Anisotropy	**Free swelling**		**Combined**		**GW**	**Restrained swelling**	
	EW1	EW2	ELW_1	ELW_2	GW	ROI 1	ROI 2
EW	3.1	1.7	1.6	1.5	4.0	EW_T:2.4	EW_T:0.25
LW	1.3	1.1	1.0	1.0	2.1	LW_T:0.8 LW_R:5.3	LW_T:0.5
EW+LW			1.1	1.3	1.5		

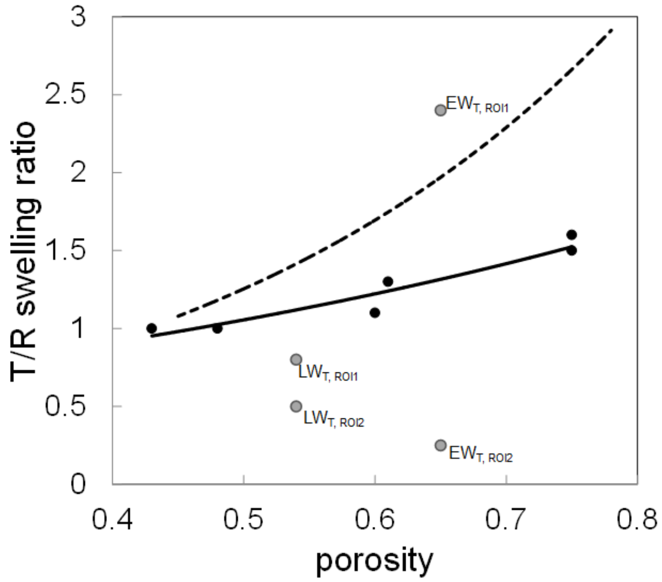

Figure 9.1: Anisotropic swelling ratio versus porosity for earlywood and latewood samples in free swelling (dashed line), in combined dry tissues (continued line and black dots) and in restrained swelling (grey dots).

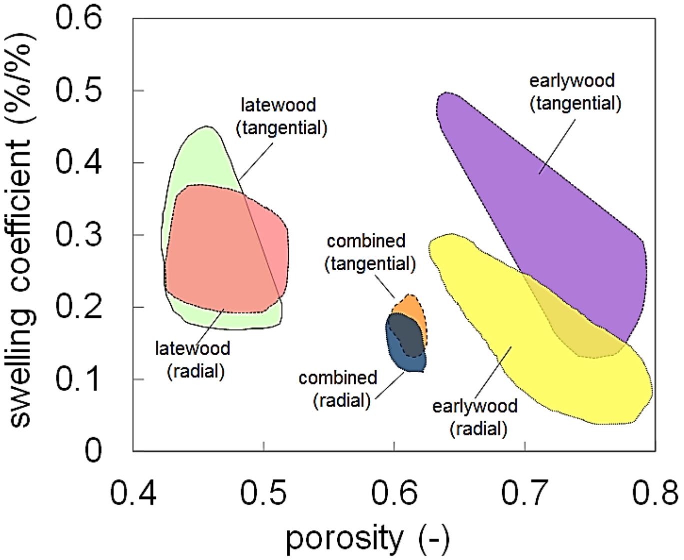

Figure 9.2: Swelling coefficients of latewood and earlywood for different porosity.

9.2 Contributions

Experimental methods advances:

- Development of a non-destructive 3D experimental imaging approach for understanding the influence of environmental changes on the cellular behaviour of wood, which consists in subjecting carefully prepared wood samples to an *in-situ* RH loading protocol and micro-imaging of their geometric changes. This approach is applied on the complex cellular structure of wood at cellular and sub-cellular scales (such as pits and cell wall layers) using micro- and nano-CT, respectively.

- Development of an environmental chamber and relative humidity control systems for the different configurations and scales of CT setup, i.e. the X-ray tube and the synchrotron-radiation source.

- Development of advanced sample holders for micro- and nano-tomographic setups, such as the restraining device and the magnetic holders for very thin samples.

Advances in image analysis:

- Integrated use of different advanced tools for processing tomographic images in 3D: especially image pre-processing operations in combination with algorithms for phase contrast and image post-processing operations integrated with different tools for segmentation and image affine registration.

- Development of a new image registration technique for detecting the non-affine deformations in wood induced by moisture content changes, a material with complex cellular structure and behaviour. In our case, wood swells and shrinks more along the tangential and radial directions than in longitudinal direction, allowing us to investigate the non-affine strains in 2D. The complex cellular structure of wood is a good example for testing the performance of an algorithm which combines several morphological operations to an optimization problem. The algorithm is able to recognise different features in the wood cell wall (cell edges, cell corner, and skeleton), to extract the features coordinates, to compare these features in two different states (reference and moving/deformed) and to find the optimal transformation, using B-spline functions, which maps the features of the moving state into the features of the reference state. This technique is called point-based registration. This new image registration method is added to two procedures of registration based on the intensity of grey values, in order to ensure the optimal performance of the non-affine registration method.

- Development of a data analysis approach, which combines understanding of the affine behaviour of the material with the occurrence of local non-affine deformations in the cellular structure. The affine strains are calculated in 3D. The affine registration model is a good approximation to explain the global deformation behaviour of wood but it fails in detecting the local non-affine strains. For this reason, the non-affine registration model is required in order to investigate locally the deformations in wood and to quantify the non-affine strains and the total strains. The total strains are finally mapped on the cellular wood structure for further analysis. The approach developed shows the capacity to highlight zones undergoing bending, the restraining effects of rays, shape-memory effects and cell wall buckling.

Advances in understanding wood swelling:

- Understanding of the swelling behaviour of earlywood and latewood at cellular scale. The anisotropic behaviour of the cellular material is investigated for different wood cellular geometries. A main conclusion is that the swelling anisotropy depends exponentially on the porosity. Wood tissues with higher porosity present a more anisotropic swelling behaviour compared with the less porous latewood tissues. It is found that the anisotropy can importantly be reduced/increased dependent on the direction of restraint. In samples combining both earlywood and latewood, the overall behaviour is more dominated by the swelling of latewood.

- Understanding of the occurrence of hysteresis in wood. This thesis demonstrates that hysteresis appears when swelling and moisture content are considered as a function of relative humidity, while it disappears when swelling is plotted versus moisture content. This shows the main origin of hysteresis to be due to sorption, thus leading to the conclusion that the same amount of moisture entering or exiting the cell wall material leads to the same swelling deformation of the cell material.

- Detecting local deformations in the earlywood and latewood as occurring in localized manner along the ray cells, especially in earlywood, underlines the restraining role of rays on the cellular material swelling. It is found that the restraining effect of the rays on the swelling is more important for cellular material composed of thinner cell wall materials, since the cell wall thickness of the rays is higher than the cell wall thickness of earlywood tissues.

- Understanding the swelling behaviour of green wood when it is dried for the first time, i.e., the first desorption curve, which is shown to be irreversible, leading to the appearance of permanent strains. In contrast, the adsorption and second desorption curves are reversible. The behaviour of a green wood specimen during sorption is found to be strongly different compared with dry wood materials. This is related to the fact that no maturation occurs in green sapwood, thus the material is softer than in dry heartwood, leading to a more anisotropic behaviour of both latewood and earlywood. Additionally, it is found that the swelling in greenwood is more affine as no large non-affine deformations occur locally.

- Understanding the swelling of wood subjected to restraint during moisture sorption. It is observed that the swelling of cell wall structure is prevented by the presence of a restraining device. This restraint introduces important local deformations of wood such as cell wall buckling. A buckling mode of axial compressive type is found in a group of cells which are subjected to restraint along the radial direction.

- Shape-memory effect is observed in initial highly deformed cells due to sample preparation, which regain their original cell shape when rewetting.

This memory effect is probably related to a possible realignment of polymers.

- Understanding the role of singularities in the softwood cell wall at sub-cellular scale, such as bordered pits and middle lamella. *In-situ* experiments with phase-contrast synchrotron-radiation nano-tomography allow us to image the deformations in bordered pits during hygroscopic loading. It is found that middle lamella shows an isotropic swelling behaviour. Non-affine strains may occur locally in the middle lamella, indicating a local bending or slip between subcellular layers.

9.3 Perspectives

Based on this thesis, a number of directions for further research can be formulated. These issues are discussed here:

- This work shows the potential of image analysis in investigating global and local deformations in complex materials. Since the cellular swelling of softwood is predominant along radial and tangential directions, while it is almost zero longitudinally, the strain registration algorithm has been developed in 2D. For studying different materials, a 3D version of the algorithm needs to be implemented. Another possible improvement on the algorithm is related to computational time. Running a stack of 200 slices of 1000×1000 pixels cross-sectional size on one processor requires at the moment of this thesis 24 hours. The code could be implemented in parallel with multiprocessor imaging. Further progress of the algorithm should tend towards an improved selection of the constraint on the B-spline functions instead of using an artificial grid. In this way, the method could be used for studying the behaviour of different existing materials detected in 2D or in 3D.

- For wood datasets obtained in the same modality, we can use the squared sum of intensity differences (SSD) as similarity criterion. However, there are cases, especially in medicine, where the two datasets, i.e. reference and moving, are acquired with different configurations leading to contrast enhancement (i.e., pre- and post- contrast agent with magnetic resonance imaging). In these cases, another similarity criterion could be used, e.g. insensitive to intensity changes (Rueckert et al., 1999). Such a method can be widely used in material science and in medicine for detecting locally the object deformations.

- The behaviour of green wood and the first desorption curve at microscale should be explored in more detail by doing repeat experiments on green samples in wet conditions. Understanding the role of a living tree with respect to permeability studies at micro- and nano- scales will give more insights to understand fluid transport and effect of draught in trees.

- Further understanding of the origin of swelling behaviour by downscaling to molecular scale. Experimental investigation of the chemical composition with respect to the cell arrangements and chains ordinations along the wood fibres combined with molecular dynamic simulations would provide new insights in understanding the role of each sub-cellular features to the global frame of wood material in a multiscale framework.

- The affine and non-affine swelling/shrinkage strains can be used for validating a 3D multi-scale model of the behaviour of wood.

- The moisture shape-memory effect is seen in a variety of polymers and biological materials. Further investigations based on experiments and combined with a modelling approach are required for understanding the mechanisms that govern the ability of certain materials to recover their original shape after moisture loadings.

Appendix

In the appendix, we report the cell wall thickness of the wood specimens analysed in Chapters 5 and 7. The procedure for mapping the cell wall thickness is briefly described. We use the software for image analysis and visualization VG Studio MAX 2.0. In particular, we use a module named *wall thickness analysis* in order to examine objects for areas in which the wood cell wall thickness is within a defined permissible interval. Connected areas are combined into one component for which the position, minimum/maximum wall thickness and volume are specified. The resulting components are colour-coded for a 3D visualization. Figure A.1 shows the 3D distribution map of the cell wall thickness of four homogeneous tissues, EW1, EW2, LW1 and LW2. Figure A.2 shows the distribution map for the regions named ROI1 in Chapter 7 and referred to samples LW_T, LW_R and EW_T. The cell wall thickness is calculated on the dry volumes. The histograms represent the surface of wood as a function of the cell wall thickness. We observe that the sample with lower porosity, i.e. EW1 (φ=78%), presents an average cell wall thickness of 3.7 μm. In contrast, the highest average cell wall thickness is found in LW2 (φ=45%) and in LW_T (φ=54%) and is equal to 7.5 μm. The cell wall thickness decreases almost linearly with the sample porosity, as shown in Figure A.3.

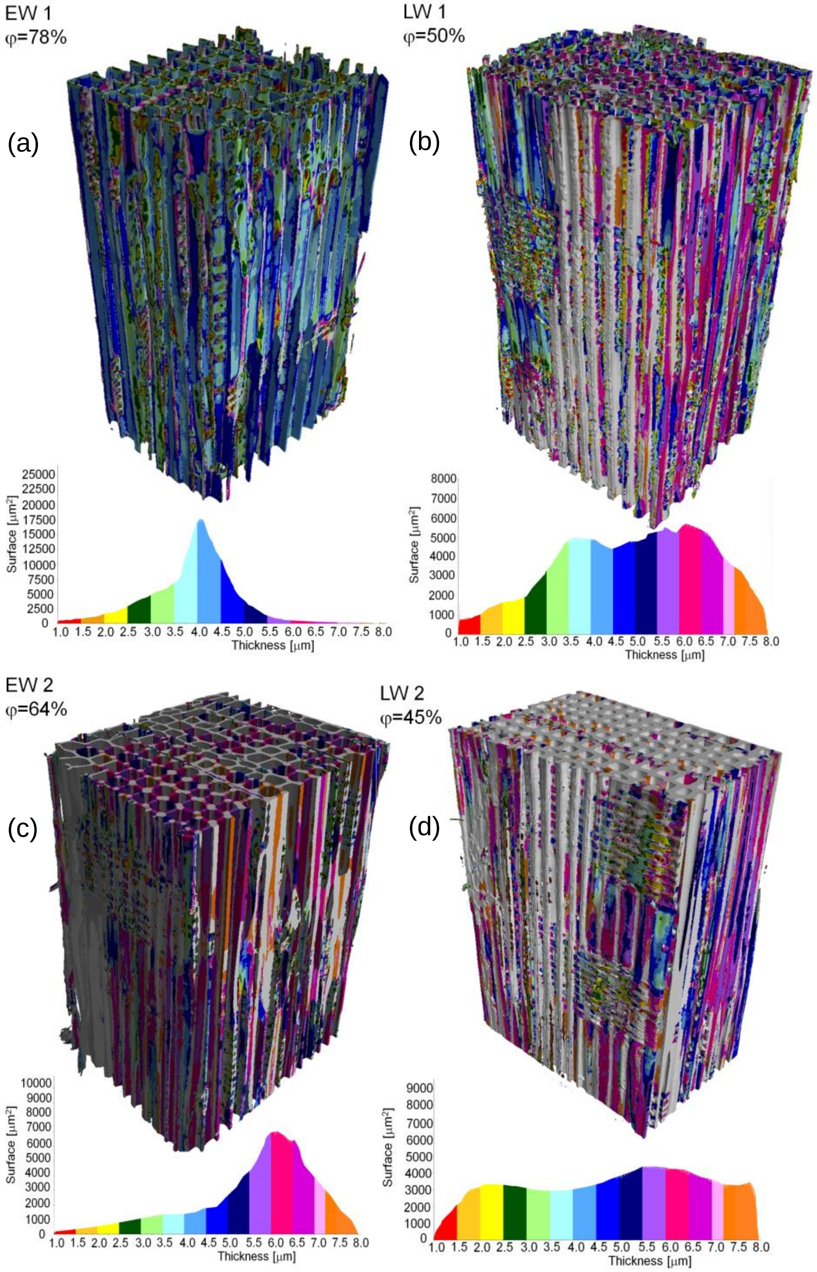

Figure A.1: 3D distribution map of the cell wall thickness of homogeneous wood samples with different porosity. Samples analysed in Chapter 5.

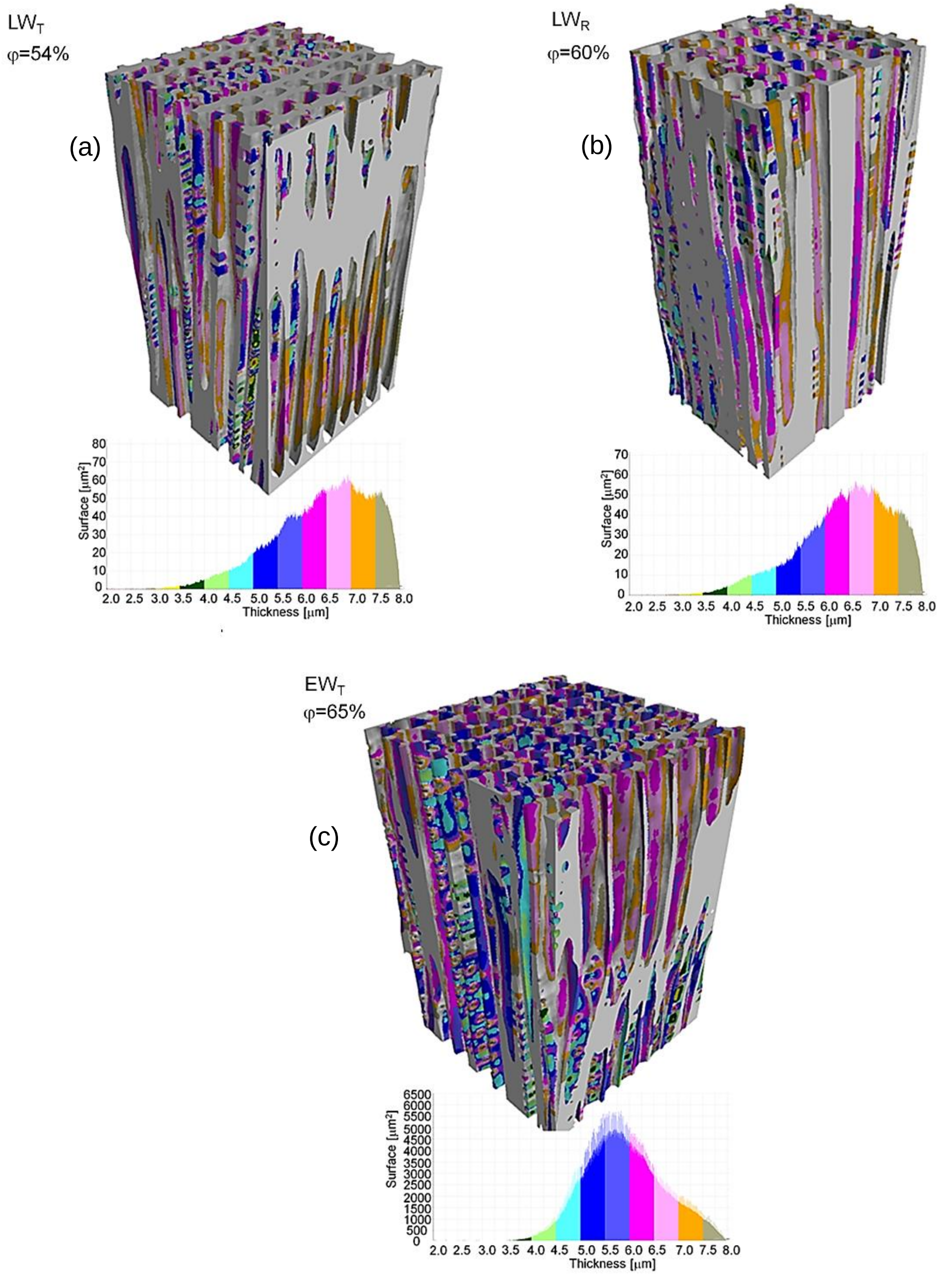

Figure A.2: 3Ddistribution map of the cell wall thickness of regions ROI1 of three homogeneous samples with different porosity. Samples analysed in Chapter 7.

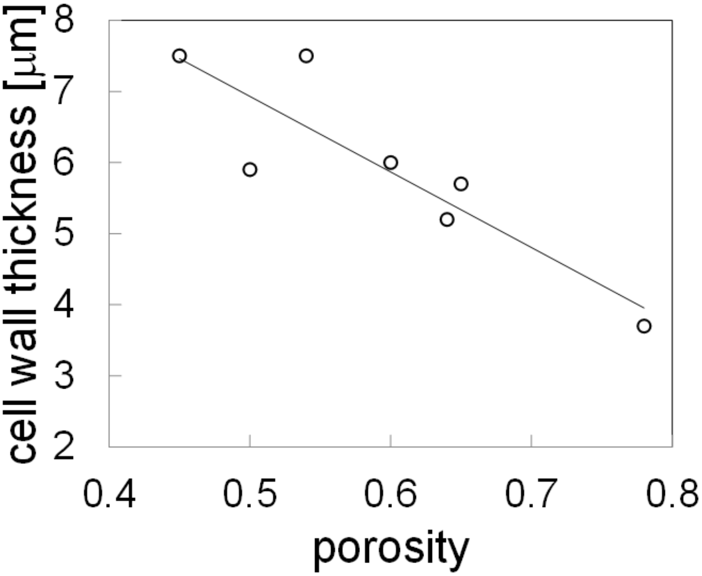

Figure A.3: Average cell wall thickness versus porosity. The line represents the best fit. The values are plotted for the 7 samples visualised above, with porosity ranging between 45% and 78%.

Bibliography

Abd-Elmoniem, K. Z., Stuber, M., & Prince, J. L. (2008). Direct three- dimensional myocardial strain tensor quantification and tracking using zHARP☆. *Medical Image Analysis*, 12(6), 778–786. doi:10.1016/j.media.2008.03.008

Ashby, M. (2013). Designing architectured materials. *Scripta Materialia*, *68*(1), 4–7. doi:10.1016/j.scriptamat.2012.04.033

Bankman, I. N. (2009). *Handbook of medical image processing and analysis*. Amsterdam: Elsevier/Academic Press.

Barrett, J. F., & Keat, N. (2004). Artifacts in CT: Recognition and Avoidance. *RadioGraphics*, *24*(6), 1679–1691. doi:10.1148/rg.246045065

Baruchel, J., Buffiere, J.-Y., Cloetens, P., Di Michiel, M., Ferrie, E., Ludwig, W., Salvo, L. (2006). Advances in synchrotron radiation microtomography. *Scripta Materialia*, *55*(1), 41–46. doi:10.1016/j.scriptamat.2006.02.012

Beer (1852). Bestimmung der Absorption des rothen Lichts in farbigen Flüssigkeiten, *Annalen der Physik und Chemie*, vol. 86, pp. 78–88.

Beever, D. K., & Valentine, L. (2007). Studies on the sorption of moisture by polymers. II. The cellulose-cellulose acetate system. *Journal of Applied Chemistry*, *8*(2), 103–107. doi:10.1002/jctb.5010080204

Bernsen, J. (1986). Dynamic Thresholding of Grey-Level Images. In *Proc. of the 8th Int. Conf. on Pattern Recognition* (pp. 1251–1255). Paris, France.

Bertaud, F. (2002). Evaluation of acid methanolysis for analysis of wood hemicelluloses and pectins. *Carbohydrate Polymers*, *48*(3), 319–324. doi:10.1016/S0144-8617(01)00249-1

Bertaud, F., & Holmbom, B. (2004). Chemical composition of earlywood and latewood in Norway spruce heartwood, sapwood and transition zone wood. *Wood Science and Technology*, *38*(4), 245–256. doi:10.1007/s00226-004-0241-9

Berthold, J., Desbrières, J., Rinaudo, M., & Salmén, L. (1994). Types of adsorbed water in relation to the ionic groups and their counter-ions for some cellulose derivatives. *Polymer*, *35*(26), 5729–5736. doi:10.1016/S0032-3861(05)80048-5

Berthold, J., Rinaudo, M., & Salmeń, L. (1996). Association of water to polar groups; estimations by an adsorption model for ligno-cellulosic materials. *Colloids and Surfaces A: Physicochemical and Engineering Aspects*, *112*(2–3), 117–129. doi:10.1016/0927-7757(95)03419-6

Bolton, A. J., Jardine, P., Vine, M. H., & Walker, J. C. F. (1974). The Swelling of Wood under Mechanical Restraint. *Holzforschung*, *28*(4), 138–145. doi:10.1515/hfsg.1974.28.4.138

Bolton, A. J., & Petty, J. A. (1977). Variation of Susceptibility to Aspiration of Bordered Pits in Conifer Wood. *Journal of Experimental Botany*, *28*(4), 935–941. doi:10.1093/jxb/28.4.935

Bonse, U., Johnson, Q., Nichols, M., Nusshardt, R., Krasnicki, S., & Kinney, J. (1986). High resolution tomography with chemical specificity. *Nuclear Instruments and Methods in Physics Research Section A: Accelerators, Spectrometers, Detectors and Associated Equipment*, *246*(1-3), 644–648. doi:10.1016/0168-9002(86)90167-1

Boone, M., De Witte, Y., Dierick, M., Van den Bulcke, J., Vlassenbroeck, J., Van Hoorebeke L., (2009). Practical use of the modified Bronnikov algorithm in micro-CT. *Nuclear Instruments and Methods in Physics Research Section B: Beam Interactions with Materials and Atoms, 267* (7), 1182-1186, doi:10.1016/j.nimb.2009.01.129

Boone, M. N., De Witte, Y., Dierick, M., Almeida, A., & Van Hoorebeke, L. (2012). Improved Signal-to-Noise Ratio in Laboratory-Based Phase Contrast Tomography. *Microscopy and Microanalysis*, *18*(2), 399–405. doi:10.1017/S1431927611012529

Brabant, L., Vlassenbroeck, J., Boone, M., Cnudde, V., Dewanckele, J., & Van Hoorebeke, L. (2011). Morpho+: a Software Package for the Three-Dimensional Analysis of X-ray Computed Tomography Data. In *International Symposium on Digital Industrial Radiology and Computed Tomography - Poster 28*. Berlin, Germany.

Brandstrom, J. (2001). Micro-and ultrastructural aspects of Norway spruce tracheids: a review. *Iawa Journal*, *22*(4), 333–354.

Bratasz, Ł., Kozłowska, A., & Kozłowski, R. (2012). Analysis of water adsorption by wood using the Guggenheim-Anderson-de Boer equation. *European Journal of Wood and Wood Products*, *70*(4), 445–451. doi:10.1007/s00107-011-0571-x

Bronnikov, A. V. (1999). Reconstruction formulas in phase-contrast tomography. *Optics Communications*, *171*(4–6), 239–244. doi:10.1016/S0030-4018(99)00575-1

Bronnikov, A. V. (2002). Theory of quantitative phase-contrast computed tomography. *Journal of the Optical Society of America A*, *19*(3), 472–480. doi:10.1364/JOSAA.19.000472

Bronnikov, A. V. (2006). Phase-contrast CT: fundamental theorem and fast image reconstruction algorithms. In *Proc. SPIE*, *6318*, 27–33. doi:10.1117/12.679389

Brown, L. G. (1992). A survey of image registration techniques. *ACM Computing Surveys*, *24*(4), 325–376. doi:10.1145/146370.146374

Burgert, I., & Fratzl, P. (2009). Plants control the properties and actuation of their organs through the orientation of cellulose fibrils in their cell walls. *Integrative and Comparative Biology*, *49*(1), 69–79. doi:10.1093/icb/icp026

Canny, J. (1986). A Computational Approach to Edge Detection. *IEEE Transactions on Pattern Analysis and Machine Intelligence*, *PAMI-8*(6), 679–698. doi:10.1109/TPAMI.1986.4767851

Carlquist, S. (2007). Bordered pits in ray cells and axial parenchyma: the histology of conduction, storage, and strength in living wood cells. *Botanical Journal of the Linnean Society*, *153*(2), 157–168. doi:10.1111/j.1095-8339.2006.00608.x

Centre for X-ray Tomography, Ghent University. (2014). *Octopus - Octopus Reconstruction*. Retrieved August 23, 2014, from http://www.octopusreconstruction.com/en/software/octopus_reconstruction

Chan, T. F., & Vese, L. A. (2001). Active contours without edges. *IEEE Transactions on Image Processing*, *10*(2), 266–277. doi:10.1109/83.902291

Chao, W., Harteneck, B. D., Liddle, J. A., Anderson, E. H., & Attwood, D. T. (2005). Soft X-ray microscopy at a spatial resolution better than 15 nm. *Nature*, *435*(7046), 1210–1213. doi:10.1038/nature03719

Choat, B., Brodie, T. W., Cobb, A. R., Zwieniecki, M. A., & Holbrook, N. M. (2006). Direct measurements of intervessel pit membrane hydraulic resistance in two angiosperm tree species. *American Journal of Botany*, *93*(7), 993–1000. doi:10.3732/ajb.93.7.993

Choong, P. E. T., & Tesoro, F. O. (1989). Relationship of capillary pressure and water saturation in wood. *Wood Science and Technology*, *23*(2), 139–150. doi:10.1007/BF00350936

Christensen, G., & Kelsey, K. (1958). The sorption of water vapour by the constituents of wood: determination of sorption isotherms. *Australian Journal of Applied Science*, *9*(3), 265–282.

Christensen, G. N., & Kelsey, K. E. (1959a). The rate of sorption of water vapor by wood. *Holz als Roh- und Werkstoff*, *17*(5), 178–188. doi:10.1007/BF02608810

Christensen, G. N., & Kelsey, K. E. (1959b). The sorption of water vapor by the constituents of wood. *Holz als Roh- und Werkstoff*, *17*(5), 189–203. doi:10.1007/BF02608811

Chu, Y. S., Yi, J. M., De Carlo, F., Shen, Q., Lee, W.-K., Wu, H. J., Margaritondo, G. (2008). Hard-x-ray microscopy with Fresnel zone plates reaches 40 nm Rayleigh resolution. *Applied Physics Letters*, *92*(10), 103119. doi:10.1063/1.2857476

Cloetens, P., Ludwig, W., Baruchel, J., Van Dyck, D., Van Landuyt, J., Guigay, J. P., & Schlenker, M. (1999). Holotomography: Quantitative phase tomography with micrometer resolution using hard synchrotron radiation x rays. *Applied Physics Letters*, *75*(19), 2912–2914. doi:10.1063/1.125225

Cnudde, V., & Boone, M. N. (2013). High-resolution X-ray computed tomography in geosciences: A review of the current technology and applications. *Earth-Science Reviews*, *123*, 1–17. doi:10.1016/j.earscirev.2013.04.003

Cnudde, V., & Jacobs, P. J. S. (2004). Monitoring of weathering and conservation of building materials through non-destructive X-ray computed microtomography. *Environmental Geology*, *46*(3-4), 477–485. doi:10.1007/s00254-004-1049-5

Cohan, L. H. (1938). Sorption Hysteresis and the Vapor Pressure of Concave Surfaces. *Journal of the American Chemical Society*, *60*(2), 433–435. doi:10.1021/ja01269a058

Collignon, A., Maes, F., Delaere, D., Vandermeulen, D., Suetens, P., & Marchal, G. (1995). Automated multi-modality image registration based on information theory. In *Information processing in medical imaging* (Vol. 3, pp. 263–274). Retrieved from https://mirc.uzleuven.be/download/public/MIC/publications/929/paper.pdf

Collins, D. L., & Evans, A. C. (1997). Animal: Validation and Applications of Nonlinear Registration-Based Segmentation. *International Journal of Pattern Recognition and Artificial Intelligence*, *11*(08), 1271–1294. doi:10.1142/S0218001497000597

Comstock, G. (1970). Directional Permeability Of Softwoods. *Wood and Fiber Science*, *1*(4), 283–289.

David, C., Weitkamp, T., Pfeiffer, F., Diaz, A., Bruder, J., Rohbeck, T., … Cloetens, P. (2007). Hard X-ray phase imaging and tomography using a grating interferometer. *Spectrochimica Acta Part B: Atomic Spectroscopy*, *62*(6-7), 626–630. doi:10.1016/j.sab.2007.03.001

De Man, B., Nuyts, J., Dupont, P., Marchal, G., & Suetens, P. (1998). Metal streak artifacts in X-ray computed tomography: a simulation study. *IEEE Nuclear Science Symposium, Conference Record*, *3*, 1860–1865. doi:10.1109/NSSMIC.1998.773898

De Witte, Y. (2010). *Improved and practically feasible reconstruction methods for high resolution x-ray tomography* (Thesis). Universiteit Gent. Retrieved from https://biblio.ugent.be/publication/1002586/file/1886809.pdf

De Witte, Y., Boone, M., Vlassenbroeck, J., Dierick, M., & Van Hoorebeke, L. (2009). Bronnikov-aided correction for x-ray computed tomography. *Journal of the Optical Society of America A*, *26*(4), 890–894. doi:10.1364/JOSAA.26.000890

Defrise, M., Noo, F., Clackdoyle, R., & Kudo, H. (2006). Truncated Hilbert transform and image reconstruction from limited tomographic data. *Inverse Problems*, *22*(3), 1037–1053. doi:10.1088/0266-5611/22/3/019

Derome, D., Griffa, M., Koebel, M., & Carmeliet, J. (2011). Hysteretic swelling of wood at cellular scale probed by phase-contrast X-ray tomography. *Journal of Structural Biology*, *173*(1), 180–190. doi:10.1016/j.jsb.2010.08.011

Derome, D., Rafsanjani, A., Patera, A., Guyer, R., & Carmeliet, J. (2012). Hygromorphic behaviour of cellular material: hysteretic swelling and shrinkage of wood probed by phase contrast X-ray tomography. *Philosophical Magazine*, *92*(28-30), 3680–3698. doi:10.1080/14786435.2012.715248

Dierick, M., Van Loo, D., Masschaele, B., Van den Bulcke, J., Van Acker, J., Cnudde, V. and Van Hoorebeke, L. Recent micro-CT scanner developments at UGCT. *Nuclear Instruments and Methods in Physics Research Section B: Beam Interactions with Materials and Atoms*; 324 (0), p. 35-40.

Dinwoodie, J. M. (1981). *Timber, its nature and behaviour*. New York: Van Nostrand Reinhold.

Domec J.C., Lachenbruch B. & Meinzer F.C. (2006). Bordered pit structure and function determine spatial patterns of air-seeding thresholds in xylem of Douglas-fir (Pseudotsuga menziesii; Pinaceae) trees. *American Journal of Botany*, *93*(11), 1588–1600.

Dornheim, L., Tönnies, K. D., & Dixon, K. (2005). Automatic Segmentation of the Left Ventricle in 3D SPECT Data by Registration with a Dynamic Anatomic Model. In J. S. Duncan & G. Gerig (Eds.), *Medical Image Computing and Computer-Assisted Intervention – MICCAI 2005* (pp. 335–342). Springer Berlin Heidelberg. Retrieved from http://link.springer.com/chapter/10.1007/11566465_42

Downes, G. M., Ward, J. V., & Turvey, N. D. (1991). Lignin distribution across tracheid cell walls of poorly lignified wood from deformed copper deficient Pinus radiata (D. Don). *Wood Science and Technology*, *25*(1), 7–14. doi:10.1007/BF00195552

Elliott, J. C., & Dover, S. D. (1982). X-ray microtomography. *Journal of Microscopy*, *126*(2), 211–213. doi:10.1111/j.1365-2818.1982.tb00376.x

Elliott, J. C., & Dover, S. D. (1985). X-ray microscopy using computerized axial tomography. *Journal of Microscopy*, *138*(3), 329–331. doi:10.1111/j.1365-2818.1985.tb02627.x

EN ISO 12571 (2000). Hygrothermal performance of building materials and products — Determination of hygroscopic sorption properties. International Standard Organization, Geneve

Erickson, H. D.; Crawford, R. J. 1959. The effect of seasoning methods on the permeability of wood to liquids. *Proceedings of the American Wood Preservers Association*, *55*(4), 210-219.

FEI Visualization Sciences Group. (2014). *Avizo User's Guide*. *Avizo User's Guide*. Retrieved from http://www.vsg3d.com/sites/default/files/AvizoUsersGuide.pdf

Feldkamp, L. A., Davis, L. C., & Kress, J. W. (1984). Practical cone-beam algorithm. *Journal of the Optical Society of America A*, *1*(6), 612–619. doi:10.1364/JOSAA.1.000612

Fengel, D., & Stoll, M. (1973). Über die Veränderungen des Zellquerschnitts, der Dicke der Zellwand und der Wandschichten von Fichtenholz-Tracheiden innerhalb eines Jahrringes. *Holzforschung - International Journal of the Biology, Chemistry, Physics and Technology of Wood*, *27*(1), 1–7. doi:10.1515/hfsg.1973.27.1.1

Fergus, B. J., Procter, A. R., Scott, J. A. N., & Goring, D. A. I. (1969). The distribution of lignin in sprucewood as determined by ultraviolet microscopy. *Wood Science and Technology*, *3*(2), 117–138. doi:10.1007/BF00639636

Ferris, M. C., Mangasarian, O. L., & Pang, J.-S. (2001). *Complementarity: Applications, Algorithms and Extensions*. Boston, MA: Springer US.

Fujii, T., Lee, S. J., Kuroda, N., and Suzuki, Y. (2001). Conductive function of intervessel pits through a growth ring boundary of Machilus hunbergii. *International Association of Wood Anatomists Journal* 22:1–14.

Flannery, B. P., Deckman, H. W., Roberge, W. G., & D'Amico, K. L. (1987). Three-Dimensional X-ray Microtomography. *Science*, *237*(4821), 1439–1444. doi:10.1126/science.237.4821.1439

Foskey, M., Davis, B., Goyal, L., Chang, S., Chaney, E., Strehl, N., … Joshi, S. (2005). Large deformation three-dimensional image registration in image-guided radiation therapy. *Physics in Medicine and Biology*, *50*(24), 5869–5892. doi:10.1088/0031-9155/50/24/008

Frandsen, H. L. (2007). *Selected Constitutive Models for Simulating the Hygromechanical Response of Wood* (Thesis). Aalborg University. Department of Civil Engineering. http://vbn.aau.dk/ws/files/13648994/Selected_Constitutive_Models_for_Simulating_the_Hygromechanical_Response_of_Wood

Frangi, A. F., Laclaustra, M., & Lamata, P. (2003). A registration-based approach to quantify flow-mediated dilation (FMD) of the brachial artery in ultrasound image sequences. *IEEE Transactions on Medical Imaging*, *22*(11), 1458–1469. doi:10.1109/TMI.2003.819278

Fu, D., & Kuduvalli, G. (2008). A fast, accurate, and automatic 2D–3D image registration for image-guided cranial radiosurgery. *Medical Physics*, *35*(5), 2180. doi:10.1118/1.2903431

Fuchs, A., Schreyer, A., Feuerbach, S., & Korb, J. (2004). A new technique for termite monitoring using computer tomography and endoscopy. *International Journal of Pest Management*, *50*(1), 63–66. doi:10.1080/0967087032000159300

Fujikawa, S., & Ishida, S. (1974). Membrane structure of bordered pit on the tangential wall of tracheid of Coniferae species. *Mokuzai Gakkaishi Journal of the Japan Wood Research Society*, *20*(3), 103–110.

Gao, Y., Sandhu, R., Fichtinger, G., & Tannenbaum, A. R. (2010). A Coupled Global Registration and Segmentation Framework With Application to Magnetic Resonance Prostate Imagery. *IEEE Transactions on Medical Imaging*, *29*(10), 1781–1794. doi:10.1109/TMI.2010.2052065

Gering, D. T., Nabavi, A., Kikinis, R., Grimson, W. E. L., Hata, N., Everett, P., … Wells, W. M. (1999). An Integrated Visualization System for Surgical Planning and Guidance Using Image Fusion and Interventional Imaging. In C. Taylor & A. Colchester (Eds.), *Medical Image Computing and Computer-Assisted Intervention – MICCAI'99* (pp. 809–819). Springer Berlin Heidelberg. Retrieved from http://link.springer.com/chapter/10.1007/10704282_88

Gering, D. T., Nabavi, A., Kikinis, R., Hata, N., O'Donnell, L. J., Grimson, W. E. L., … Wells, W. M. (2001). An integrated visualization system for surgical planning and guidance using image fusion and an open MR. *Journal of Magnetic Resonance Imaging*, *13*(6), 967–975. doi:10.1002/jmri.1139

Gibson, L. J., & Ashby, M. F. (1999). *Cellular solids: structure and properties*. Cambridge; New York: Cambridge University Press.

Gibson, L. J., Ashby, M. F., & Harley, B. A. (2010). *Cellular materials in nature and medicine*. Cambridge; New York: Cambridge University Press.

Gilboy, W. B. (1984). X- and γ-ray tomography in NDE applications. *Nuclear Instruments and Methods in Physics Research*, *221*(1), 193–200. doi:10.1016/0167-5087(84)90199-6

Gilboy, W. B., Foster, J., & Folkard, M. (1982). A tomographic gamma-ray scanner for industrial applications. *Nuclear Instruments and Methods in Physics Research*, *193*(1-2), 209–214. doi:10.1016/0029-554X(82)90698-X

Gjerdrum, P., & Bernabei, M. (2007). Three-dimensional model for size and location of resin pockets in stems of Norway spruce. *Holz Als Roh- Und Werkstoff*, *65*(3), 201–208. doi:10.1007/s00107-006-0158-0

Goldstein, H., Poole, C. P., & Safko, J. L. (2002). *Classical mechanics*. San Francisco: Addison Wesley.

Gooya, A., Biros, G., & Davatzikos, C. (2011). Deformable Registration of Glioma Images Using EM Algorithm and Diffusion Reaction Modeling. *IEEE Transactions on Medical Imaging*, *30*(2), 375–390. doi:10.1109/TMI.2010.2078833

Gorelick, S., Vila-Comamala, J., Guzenko, V., Mokso, R., Stampanoni, M., & David, C. (2010). Direct e-beam writing of high aspect ratio nanostructures in PMMA: A tool for diffractive X-ray optics fabrication. *Microelectronic Engineering*, *87*(5-8), 1052–1056. doi:10.1016/j.mee.2009.11.091

Gupta, S., Chauhan, R. C., & Saxena S. C., (2005). Locally adaptive wavelet domain Bayesian processor for denoising medical ultrasound images using speckle modelling based on rayleigh distribution. *Proc. IEEE Vision, Image and Signal* Processing, 152 (1), 129–135.

Griffin, D. M. (1977). Water Potential and Wood-Decay Fungi. *Annual Review of Phytopathology*, *15*(1), 319–329. doi:10.1146/annurev.py.15.090177.001535

Grodzins, L. (1983). Optimum energies for X-ray transmission tomography of small samples. *Nuclear Instruments & Methods in Physics Research, Section A: Accelerators, Spectrometers, Detectors, and Associated Equipment*, *206*(3), 541–545.

Grosland, N. M., Bafna, R., & Magnotta, V. A. (2009). Automated hexahedral meshing of anatomic structures using deformable registration. *Computer Methods in Biomechanics and Biomedical Engineering*, *12*(1), 35–43. doi:10.1080/10255840802136143

Groso, A., Abela, R., & Stampanoni, M. (2006). Implementation of a fast method for high resolution phase contrast tomography. *Optics Express*, *14*(18), 8103–8110. doi:10.1364/OE.14.008103

Groso, A., Stampanoni, M., Abela, R., Schneider, P., Linga, S., & Müller, R. (2006). Phase contrast tomography: An alternative approach. *Applied Physics Letters*, *88*(21), 214104. doi:10.1063/1.2207221

Gu, H., Zink-Sharp, A., & Sell, J. (2001). Hypothesis on the role of cell wall structure in differential transverse shrinkage of wood. *Holz Als Roh- Und Werkstoff*, *59*(6), 436–442. doi:10.1007/s001070100240

Guyer, R. A., Kim, H. A., Derome, D., Carmeliet, J., & TenCate, J. (2011). Hysteresis in modeling of poroelastic systems: Quasistatic equilibrium. *Physical Review E*, *83*(6). doi:10.1103/PhysRevE.83.061408

Haberthür, D., Hintermüller, C., Marone, F., Schittny, J. C., & Stampanoni, M. (2010). Radiation dose optimized lateral expansion of the field of view in synchrotron radiation X-ray tomographic microscopy. *Journal of Synchrotron Radiation*, *17*(5), 590–599. doi:10.1107/S0909049510019618

Harris, C., & Stephens, M. (1988). A combined corner and edge detector. In Alvey vision conference, *15*, 50. Manchester, UK. http://courses.daiict.ac.in/pluginfile.php/13002/mod_resource/content/0/References/harris1988.pdf

Hernandez, R. E. (1993): Influence of moisture sorption on the compressive properties of hardwoods. Wood Fiber Sci. 25(1): 103-111

Hernandez, R., & Bizon, M. (1994). Changes In Shrinkage And Tangential Compression Strength Of Sugar Maple Below And Above The Fiber Saturation Point. *Wood and Fiber Science*, *26*(3), 360–369.

Hill, C. A. S., Forster, S. C., Farahani, M. R. M., Hale, M. D. C., Ormondroyd, G. A., & Williams, G. R. (2005). An investigation of cell wall micropore blocking as a possible mechanism for the decay resistance of anhydride modified wood. *International Biodeterioration & Biodegradation*, *55*(1), 69–76. doi:10.1016/j.ibiod.2004.07.003

Hittmeier, M. E. (1967). Effect of structural direction and initial moisture content on swelling rate of wood. *Wood Science and Technology*, *1*(2), 109–121. doi:10.1007/BF00353383

Holmberg, S., Persson, K., & Petersson, H. (1999). Nonlinear mechanical behaviour and analysis of wood and fibre materials. *Computers & Structures*, *72*(4–5), 459–480. doi:10.1016/S0045-7949(98)00331-9

Huang, X., Ren, J., Guiraudon, G., Boughner, D., & Peters, T. M. (2009). Rapid Dynamic Image Registration of the Beating Heart for Diagnosis and Surgical Navigation. *IEEE Transactions on Medical Imaging*, *28*(11), 1802–1814. doi:10.1109/TMI.2009.2024684

Hubbell, J. H., & Seltzer, S. M. (1995). Tables of x-ray mass attenuation coefficients and mass energy-absorption coefficients from 1 keV to 20 MeV for Elements Z = 1 to 92 and 48 Additional Substances of Dosimetric Interest. *National Institute of Standards and Technology*.

Ibanez, L., Schroeder, W., Ng, L., & Cates, J. (2005). *ITK software guide*. Clifton Park, NY: Kitware, Inc.

Ingle, J. D. J.; Crouch, S. R. (1988). *Spectrochemical Analysis*. New Jersey: Prentice Hall.

Isgum, I., Staring, M., Rutten, A., Prokop, M., Viergever, M. A., & van Ginneken, B. (2009). Multi-Atlas-Based Segmentation With Local Decision Fusion - Application to Cardiac and Aortic Segmentation in CT Scans. *IEEE Transactions on Medical Imaging*, *28*(7), 1000–1010. doi:10.1109/TMI.2008.2011480

Ishiyama, C., & Higo, Y. (2002). Effects of humidity on Young’s modulus in poly(methyl methacrylate). *Journal of Polymer Science Part B: Polymer Physics*, *40*(5), 460–465. doi:10.1002/polb.10107

Ishizuka, K., & Allman, B. (2005a). Phase measurement in electron microscopy using the transport of intensity equation. *Microscopy Today*, *5* (3), 22–24.

Ishizuka, K., & Allman, B. (2005b). Phase measurement of atomic resolution image using transport of intensity equation. *Journal of Electron Microscopy*, *54*(3), 191–197. doi:10.1093/jmicro/dfi024

Jakubek, J., Holy, T., Jakubek, M., Vavrik, D., & Vykydal, Z. (2006). Experimental system for high resolution X-ray transmission radiography. *Nuclear Instruments and Methods in Physics Research Section A: Accelerators, Spectrometers, Detectors and Associated Equipment*, *563*(1), 278–281. doi:10.1016/j.nima.2006.01.033

Jenkinson, M., & Smith, S. (2001). A global optimisation method for robust affine registration of brain images. *Medical Image Analysis*, *5*(2), 143–156. doi:10.1016/S1361-8415(01)00036-6

Jensen, T. H. (2010). *Refraction and scattering based x-ray imaging* (Thesis). University of Copenhangen. http://nexim.nbi.ku.dk/documents/phd_thesis_torben_jensen.pdf.

Johansson, I., & Edberg, K. (1987). *Studies on the permeability of Norway spruce. The International research Group on wood preservation*. IRG/WP/2295.

Johnson, D. B., Moore, W. E., & Zank, L. C. (1961). The spectrophotometric determination of lignin in small wood samples. *TAPPI Journal*, *44*(11), 793–798.

Joly, C., Gauthier, R., & Escoubes, M. (1996). Partial masking of cellulosic fiber hydrophilicity for composite applications. Water sorption by chemically modified fibers. *Journal of Applied Polymer Science*, *61*(1), 57–69. doi:10.1002/(SICI)1097-4628(19960705)61:1<57::AID-APP7>3.0.CO;2-T

Keckes, J., Burgert, I., Frühmann, K., Müller, M., Kölln, K., Hamilton, M., … Fratzl, P. (2003). Cell-wall recovery after irreversible deformation of wood. *Nature Materials*, *2*(12), 810–813. doi:10.1038/nmat1019

Keith, C. T. (1971). Observations on the anatomy and fine structure of the trabeculae of Sanio. *IAWA Bull*, *3*, 3–11.

Keunecke, D., Novosseletz, K., Lanvermann, C., Mannes, D., & Niemz, P. (2012). Combination of X-ray and digital image correlation for the analysis of moisture-induced strain in wood: opportunities and challenges. *European Journal of Wood and Wood Products*, *70*(4), 407–413. doi:10.1007/s00107-011-0573-8

Keylwerth, R. (1962). Untersuchungen über freie und behinderte Quellung von Holz—Erste Mitteilung: Freie Quellung. *Holz als Roh- und Werkstoff*, *20*(7), 252–259. doi:10.1007/BF02604681

Klein, S., Staring, M., Murphy, K., Viergever, M. A., & Pluim, J. (2010). elastix: A Toolbox for Intensity-Based Medical Image Registration. *IEEE Transactions on Medical Imaging*, *29*(1), 196–205. doi:10.1109/TMI.2009.2035616

Kollmann, F. F. P., & Côté, W. A. (1968). *Principles of Wood Science and Technology I Solid Wood*. Berlin, Heidelberg: Springer Berlin Heidelberg.

Koran, Z. 1974. Intertracheid pitting in the radial walls of Black Spruce tracheids. Wood Fiber Sci. *7*(2), 111–115.

Kulasinski, K., Keten, S., Churakov, S. V., Guyer, R., Carmeliet, J., & Derome, D. (2014). Molecular mechanism of moisture-induced transition in amorphous cellulose. *Submitted to ACS Macro Letters*.

Lacroix, H. (2007). *Thermohygroelastic properties of polymethylmethacrylate*. Philips Research Europe. Retrieved from http://repository.tudelft.nl/assets/uuid:94888e8c-ec36-4239-ac1b-7c24b5746eaf/TN-2007-00440.pdf

Langer, M., Cloetens, P., Guigay, J.-P., & Peyrin, F. (2008). Quantitative comparison of direct phase retrieval algorithms in in-line phase tomography. *Medical Physics*, *35*(10), 4556–4566. doi:10.1118/1.2975224

Lavely, W. C., Scarfone, C., Cevikalp, H., Li, R., Byrne, D. W., Cmelak, A. J., … Fitzpatrick, J. M. (2004). Phantom validation of coregistration of PET and CT for image-guided radiotherapy. *Medical Physics*, *31*(5), 1083–1092. doi:10.1118/1.1688041

Lee, S., Wolberg, G., & Shin, S. Y. (1997). Scattered data interpolation with multilevel B-splines. *IEEE Transactions on Visualization and Computer Graphics*, *3*(3), 228–244. doi:10.1109/2945.620490

Lee, S.-J., & Kim, Y. (2008). In vivo Visualization of the Water-refilling Process in Xylem Vessels Using X-ray Micro-imaging. *Annals of Botany*, *101*(4), 595–602. doi:10.1093/aob/mcm312

Li, Q., & Renneckar, S. (2011). Supramolecular Structure Characterization of Molecularly Thin Cellulose I Nanoparticles. *Biomacromolecules*, *12*(3), 650–659. doi:10.1021/bm101315y

Liese, W., & Bauch, J. (1967). On the closure of bordered pits in conifers. *Wood Science and Technology*, *1*(1), 1–13. doi:10.1007/BF00592252

Lloyd, J. A. (1978). Distribution of extractives in Pinus radiate earlywood and latewood. *New Zealand Journal of Forestry Science*, *8*(2), 288–294.

Ma, Q., & Rudolph, V. (2006). Dimensional Change Behavior of Caribbean Pine Using an Environmental Scanning Electron Microscope. *Drying Technology*, *24*(11), 1397–1403. doi:10.1080/07373930600952743

Mader, K., Marone, F., Hintermuller, C., Mikuljan, G., Isenegger, A., & Stampanoni, M. (2011). High-throughput full-automatic synchrotron-based tomographic microscopy. *Journal of Synchrotron Radiation*, *18*(2), 117–124. doi:10.1107/S0909049510047370

Madonna, C., Quintal, B., Frehner, M., Almqvist, B., Tisato, N., Pistone, M., … Saenger, E. (2013). Synchrotron-based X-ray tomographic microscopy for rock physics investigations. *Geophysics*, *78*(1), D53–D64. doi:10.1190/geo2012-0113.1

Mäkinen, H., Jyske, T., & Saranpää, P. (2008). Variation of tracheid length within annual rings of Scots pine and Norway spruce. *Holzforschung*, *62*(1), 123–128. doi:10.1515/HF.2008.018

Maksimov, D., Hesser, J., Brockmann, C., Jochum, S., Dietz, T., Schnitzer, A., … Diehl, S. (2009). Graph-Matching Based CTA. *IEEE Transactions on Medical Imaging*, *28*(12), 1940–1954. doi:10.1109/TMI.2009.2026370

Mannes, D., Marone, F., Lehmann, E., Stampanoni, M., & Niemz, P. (2010). Application areas of synchrotron radiation tomographic microscopy for wood research. *Wood Science and Technology*, *44*(1), 67–84. doi:10.1007/s00226-009-0257-2

Marone, F., Mokso, R., Modregger, P., Fife, J., Pinzer, B., Thüring, T., … Lai, B. (2011). Present and Future X-ray Tomographic Microscopy at TOMCAT, *10th international conference on x-ray microscopy*, *1365*, 116-119. doi:10.1063/1.3625318

Marone, F., & Stampanoni, M. (2012). Regridding reconstruction algorithm for real-time tomographic imaging. *Journal of Synchrotron Radiation*, *19*(6), 1029–1037. doi:10.1107/S0909049512032864

Martin, S., Daanen, V., & Troccaz, J. (2008). Atlas-based prostate segmentation using an hybrid registration. *International Journal of Computer Assisted Radiology and Surgery*, *3*(6), 485–492. doi:10.1007/s11548-008-0247-0

Masschaele, B. C., Cnudde, V., Dierick, M., Jacobs, P., Van Hoorebeke, L., & Vlassenbroeck, J. (2007). UGCT: New X-ray radiography and tomography facility. *Nuclear Instruments and Methods in Physics Research Section A: Accelerators, Spectrometers, Detectors and Associated Equipment*, *580*(1), 266–269. doi:10.1016/j.nima.2007.05.099

Miller, K., Wittek, A., Joldes, G., Horton, A., Dutta-Roy, T., Berger, J., & Morriss, L. (2010). Modelling brain deformations for computer-integrated neurosurgery. *International Journal for Numerical Methods in Biomedical Engineering*, *26*(1), 117–138. doi:10.1002/cnm.1260

Mises, R. v. (1913). Mechanik der festen Körper im plastisch- deformablen Zustand. *Nachrichten von der Gesellschaft der Wissenschaften zu Göttingen, Mathematisch-Physikalische Klasse*, *1913*, 582–592.

Modén, C. S., & Berglund, L. A. (2008). Elastic deformation mechanisms of softwoods in radial tension – Cell wall bending or stretching? *Holzforschung*, *62*(5), 562–568. doi:10.1515/HF.2008.082

Mokso, R., Quaroni, L., Marone, F., Irvine, S., Vila-Comamala, J., Blanke, A., & Stampanoni, M. (2012). X-ray mosaic nanotomography of large microorganisms. *Journal of Structural Biology*, *177*(2), 233–238. doi:10.1016/j.jsb.2011.12.014

Moliński, W., & Roszyk, E. (2010). Restriction of swelling of wood subjected to bending stress and moistening in the compressed zone. *Acta Sci Pol Silv Colendar Rat Ind Lignar*, *9*(1), 35–43.

Momose, A., Takeda, T., Itai, Y. & Hirano, K. (1996). Phase-contrast x-ray computed tomography for observing biological soft tissues, *Nature Medicine*, *2*(4), 473-475, ISSN 1078-8956.

Münch, B., Trtik, P., Marone, F., & Stampanoni, M. (2009). Stripe and ring artifact removal with combined wavelet—Fourier filtering. *Optics Express*, *17*(10), 8567–8591. doi:10.1364/OE.17.008567

Murata, K., & Masuda, M. (2001). Observation of the swelling behavior of coniferous cells using a confocal scanning laser microscope and a digital image correlation method. *Materials Science Research International*, *7*(3), 200–205.

Murata, K., & Masuda, M. (2006). Microscopic observation of transverse swelling of latewood tracheid: effect of macroscopic/mesoscopic structure. *Journal of Wood Science*, *52*(4), 283–289. doi:10.1007/s10086-005-0760-5

Nakamura, K., Hatakeyama, T., & Hatakeyama, H. (1981). Studies on Bound Water of Cellulose by Differential Scanning Calorimetry. *Textile Research Journal*, *51*(9), 607–613. doi:10.1177/004051758105100909

Narayanamurti, D., & Mahajan, P. C. (1956). Rheology of wood — Part II. The swelling and shrinkage of wood under mechanical restraint. *Applied Scientific Research, Section A*, *5*(6), 389–410. doi:10.1007/BF03184601

Niemz, P. (1993). Physik des Holzes und der Holzwerkstoffe.

Niemz, P., Guzik, M., & Lühmann, A. (1993). Der Einfluss von Strukturfehlern in Holz auf das Quell- und Schwindverhalten von Holz. Teil 1: Der Einfluss von Druckholz bei Fichte. *Holzforschung Und Holzverwertung*, *45*(2), 36–37.

Nocedal, J., & Wright, S. J. (2006). *Numerical optimization*. New York: Springer.

Ohtani, J. (1985). SEM observations on trabeculae in Abies sachalinensis. *IAWA Bull*, *6* (1), 43–51.

Otsu, N. (1979). A Threshold Selection Method from Gray-Level Histograms. *IEEE Transactions on Systems, Man, and Cybernetics*, *9*(1), 62–66. doi:10.1109/TSMC.1979.4310076

Paganin, D., Mayo, S. C., Gureyev, T. E., Miller, P. R., & Wilkins, S. W. (2002). Simultaneous phase and amplitude extraction from a single defocused image of a homogeneous object. *Journal of Microscopy*, *206*(1), 33–40. doi:10.1046/j.1365-2818.2002.01010.x

Pang, S., & Herritsch, A. (2005). Physical properties of earlywood and latewood of Pinus radiata D. Don: Anisotropic shrinkage, equilibrium moisture content and fibre saturation point. *Holzforschung*, *59*(6), 654–661. doi:10.1515/HF.2005.105

Patera, A. (2007). *Sistemi matematico-fisici per la ricerca di noduli polmonari in immagini CT* (Thesis). Università del Salento, Salento, Italy.

Patera, A., Derome, D., Griffa, M., & Carmeliet, J. (2013). Hysteresis in swelling and in sorption of wood tissue. *Journal of Structural Biology*, *182*(3), 226–234. doi:10.1016/j.jsb.2013.03.003

Perstorper, M., Johansson, M., Kliger, R., & Johansson, G. (2001). Distortion of Norway spruce timber Part 1. Variation of relevant wood properties. *Holz Als Roh- Und Werkstoff*, *59*(1-2), 94–103. doi:10.1007/s001070050481

Peterzol, A., Olivo, A., Rigon, L., Pani, S., & Dreossi, D. (2005). The effects of the imaging system on the validity limits of the ray-optical approach to phase contrast imaging. *Medical Physics*, *32*(12), 3617. doi:10.1118/1.2126207

Petrou, M., & Bosdogianni, P. (2004). *Image Processing*. Chichester, UK: John Wiley & Sons, Ltd. Retrieved from http://doi.wiley.com/10.1002/0470841907

Petty, J. A. (1970). The relation of wood structure to preservative treatment. In *The Wood We Grow*, 29–35. Oxford: Oxford University Press.

Petty, J. A. (1972). The Aspiration of Bordered Pits in Conifer Wood. *Proceedings of the Royal Society B: Biological Sciences*, *181*(1065), 395–406. doi:10.1098/rspb.1972.0057

Petty, J. A., & Preston, R. D. (1969). The Removal of Air from Wood. *Holzforschung - International Journal of the Biology, Chemistry, Physics and Technology of Wood*, *23*(1), 9–15. doi:10.1515/hfsg.1969.23.1.9

Pfeiffer, K.-F. G. (2004). *Evaluation of the Medipix detectors for medical X-ray imaging, with special consideration of mammography* (Thesis). Friedrich-Alexander-Universität Erlangen-Nürnberg. Retrieved from http://www.pi4.nat.uni-erlangen.de/novel-detectors/publications/phd-diplomathesis/pfeiffer_dr.pdf

Phillips, E. W. J. (1933). Movement of the Pit Membrane in Coniferous Woods, with Special Reference to Preservative Treatment. *Forestry*, *7*(2), 109–120.

Pieper, S., Halle, M., & Kikinis, R. (2004). 3D Slicer. In *Proceedings of the 3rd IEEE International Symposium on Biomedical Imgaing: From Nano to Macro* (Vol. 2, pp. 632–635). IEEE. doi:10.1109/ISBI.2004.1398617

Pieper, S., Lorensen, B., Schroeder, W., & Kikinis, R. (2006). The NA-MIC Kit: ITK, VTK, Pipelines, Grids and 3D Slicer as An Open Platform for the Medical Image Computing Community. In *Proceedings of the 3rd IEEE International Symposium on Biomedical Imaging: From Nano to Macro*, 698–701. IEEE. doi:10.1109/ISBI.2006.1625012

Pittermann, J., Sperry, J., Hacke, U. G., Wheeler, J. K., & Sikkema, E. H. (2005). Torus-Margo Pits Help Conifers Compete with Angiosperms. *Science*, *310*(5756), 1924–1924. doi:10.1126/science.1120479

Pluim, J. P. W., Maintz, J. B. A., & Viergever, M. A. (2003). Mutual-information-based registration of medical images: a survey. *IEEE Transactions on Medical Imaging*, *22*(8), 986–1004. doi:10.1109/TMI.2003.815867

Požgaj, A., Chovanec, D., Kurjatko, S., & Babiak, M. (1997). Wood structure and properties.(Štruktúra a vlastnosti dreva). Bratislava. *Priroda*, *486*.

Quirk, J. (1984). Shrinkage and Related Properties of Douglas-Fir Cell Walls. *Wood and Fiber Science*, *16*(1), 115–133.

Rafsanjani, A., Derome, D., & Carmeliet, J. (2012). The role of geometrical disorder on swelling anisotropy of cellular solids. *Mechanics of Materials*, *55*(0), 49–59. doi:10.1016/j.mechmat.2012.08.002

Rafsanjani, A., Derome, D., & Carmeliet, J. (2013). Micromechanics investigation of hygro-elastic behavior of cellular materials with multi-layered cell walls. *Composite Structures*, *95*(0), 607–611. doi:10.1016/j.compstruct.2012.08.017

Rafsanjani, A., Derome, D., Wittel, F. K., & Carmeliet, J. (2012). Computational up-scaling of anisotropic swelling and mechanical behavior of hierarchical cellular materials. *Composites Science and Technology*, *72*(6), 744–751. doi:10.1016/j.compscitech.2012.02.001

Rafsanjani, A., Stiefel, M., Jefimovs, K., Mokso, R., Derome, D., & Carmeliet, J. (2014). Hygroscopic swelling and shrinkage of latewood cell wall micropillars reveal ultrastructural anisotropy. *Journal of The Royal Society Interface*, *11*(95), 20140126. doi:10.1098/rsif.2014.0126

Raghavan, R., Adusumalli, R.-B., Buerki, G., Hansen, S., Zimmermann, T., & Michler, J. (2012). Deformation of the compound middle lamella in spruce latewood by micro-pillar compression of double cell walls. *Journal of Materials Science*, *47*(16), 6125–6130. doi:10.1007/s10853-012-6531-y

Rajendra, K. C. (2007, September 16). *An introduction to wood drying*. Text. Retrieved August 23, 2014, from http://www.forestrynepal.org/article/rajendra-kc/2411

Roberts, L. G. (1963). *Machine perception of three-dimensional solids* (Thesis). Massachusetts Institute of Technology. Retrieved from http://dspace.mit.edu/handle/1721.1/11589

Rozenbaum, O. (2011). 3-D characterization of weathered building limestones by high resolution synchrotron X-ray microtomography. *Science of The Total Environment*, *409*(10), 1959–1966. doi:10.1016/j.scitotenv.2011.02.014

Rueckert, D., Sonoda, L. I., Hayes, C., Hill, D. L. G., Leach, M. O., & Hawkes, D. J. (1999). Nonrigid registration using free-form deformations: application to breast MR images. *IEEE Transactions on Medical Imaging*, *18*(8), 712–721. doi:10.1109/42.796284

Saadatfar, M., Sheppard, A. P., Senden, T. J., & Kabla, A. J. (2012). Mapping forces in a 3D elastic assembly of grains. *Journal of the Mechanics and Physics of Solids*, *60*(1), 55–66. doi:10.1016/j.jmps.2011.10.001

Sakagami, H., Matsumura, J., & Oda, K. (2007). Shrinkage of tracheid cells with desorption visualized by confocal laser scanning microscopy. *Iawa Journal*, *28*(1), 29–37.

Sato, T., Ikeda, O., Yamakoshi, Y., & Tsubouchi, M. (1981). X-ray tomography for microstructural objects. *Applied Optics*, *20*(22), 3880. doi:10.1364/AO.20.003880

Schindelin, J., Arganda-Carreras, I., Frise, E., Kaynig, V., Longair, M., Pietzsch, T., … Cardona, A. (2012). Fiji: an open-source platform for biological-image analysis. *Nature Methods*, *9*(7), 676–682. doi:10.1038/nmeth.2019

Schneider, P., Levchuk, A., & Müller, R. (2010). Automated micro-compression device for dynamic image-guided failure assessment of bone ultrastructure and bone microdamage. *Biomedizinische Technik/Biomedical Engineering*, *55*(Suppl 1), 8–10. doi:10.1515/bmt.2010.703

Seltzer, S. (1989). Electron and positron stopping powers of materials database version 2.0. *NIST Standard Reference Database*, *7*.

Shanno, D. F. (1970). Conditioning of quasi-Newton methods for function minimization. *Mathematics of Computation*, *24*(111), 647–656. doi:10.1090/S0025-5718-1970-0274029-X

Shen, J., Chen, C. C., & Sauer, J. A. (1985). Effects of sorbed water on properties of low and high molecular weight PMMA: 1. Deformation and fracture behaviour. *Polymer*, *26*(4), 511–518. doi:10.1016/0032-3861(85)90150-8

Siau, J.F. (1995). Wood: influence of moisture on physical properties. Department of wood science and forest products. Keene, Virginia Polytechnic Institute and State University.

Sijbers, J., & Postnov, A. (2004). Reduction of ring artefacts in high resolution micro-CT reconstructions. *Physics in Medicine and Biology*, *49*(14), N247–N253. doi:10.1088/0031-9155/49/14/N06

Simpson, W. T., & Skaar, C. (1968). *Effect of restrained swelling on wood moisture content*. U.S.D.A. Forest Service Research note FPL-0196.

Skyba, Oleksandr. (2008). *Durability and physical properties of thermo-hygro-mechanically (THM)-densified wood* (Thesis). ETH Zürich. http://dx.doi.org/10.3929/ethz-a-005685999

Smith DB. (1985) Image reconstruction from cone-beam projections: necessary and sufficient conditions and reconstruction methods. *IEEE transactions on medical imaging*, M1-4, pp.14-25, ISSN 0278-0062.

Srndovic, Stevanic Jasna (2008). Ultrastructure of the Primary Cell Wall of Softwood Fibres Studied using Dynamic FT-IR Spectroscopy. Trita-CHE-Report. Series ISSN: 1654-1081

Stamm A. J. (1952) Surface properties of cellulosic materials. In Wise L.E., *Jahn E.C. (Eds) Wood Chemistry, NewYork, Reinhold Publ. Co.,* 691-816.

Stamm, A. (1970). Maximum Effective Pit Pore Radii Of The Heartwood And Sapwood Of Six Softwoods As Affected By Drying And Resoaking. *Wood and Fiber Science*, *1*(4), 263–269.

Stamm, A. J. (1964). *Wood and cellulose science*. New York: The Ronald Press Company.

Stampanoni, M., Groso, A., Isenegger, A., Mikuljan, G., Chen, Q., Bertrand, A., … Abela, R. (2006). Trends in synchrotron-based tomographic imaging: the SLS experience. In U. Bonse (Ed.), (p. 63180M–63180M–14). doi:10.1117/12.679497

Stampanoni, M., Mokso, R., Marone, F., Vila-Comamala, J., Gorelick, S., Trtik, P., … David, C. (2010). Phase-contrast tomography at the nanoscale using hard x rays. *Physical Review B*, *81*(14), 140105. doi:10.1103/PhysRevB.81.140105

Staring, M., van der Heide, U. A., Klein, S., Viergever, M. A., & Pluim, J. (2009). Registration of Cervical MRI Using Multifeature Mutual Information. *IEEE Transactions on Medical Imaging*, *28*(9), 1412–1421. doi:10.1109/TMI.2009.2016560

Stevanic Srndovic, J. (2008). *Ultrastructure of the Primary Cell Wall of Softwood Fibres Studied using Dynamic FT-IR Spectroscopy* (Thesis). KTH Royal Institute of Technology, Stockholm.

Stone, J. E., & Scallan, D. (1967). Effect of component removal upon porous structure of cell wall of wood. II. Swelling in water and fiber saturation point. *TAPPI Journal*, *50*(10), 35–42.

Studholme, C., Hill, D. L. G., & Hawkes, D. J. (1999). An overlap invariant entropy measure of 3D medical image alignment. *Pattern Recognition*, *32*(1), 71–86. doi:10.1016/S0031-3203(98)00091-0

Sundberg, A., Sundberg, K., Lillandt, C., & Holmbom, B. (1996). Determination of hemicelluloses and pectins in wood and pulp fibres by acid methanolysis and gas chromatography. *Nordic Pulp and Paper Research Journal*, *11*(04), 216–219. doi:10.3183/NPPRJ-1996-11-04-p216-219

Szeliski, R., & Coughlan, J. (1997). Spline-Based Image Registration. *International Journal of Computer Vision*, *22*(3), 199–218. doi:10.1023/A:1007996332012

Taina, I. A., Heck, R. J., & Elliot, T. R. (2008). Application of X-ray computed tomography to soil science: A literature review. *Canadian Journal of Soil Science*, *88*(1), 1–19. doi:10.4141/CJSS06027

Tanaka, T., Avramidis, S., & Shida, S. (2009). Evaluation of moisture content distribution in wood by soft X-ray imaging. *Journal of Wood Science*, *55*(1), 69–73. doi:10.1007/s10086-008-0997-x

Teague, M. R. (1983). Deterministic phase retrieval: a Green's function solution. *Journal of the Optical Society of America*, *73*(11), 1434. doi:10.1364/JOSA.73.001434

Tobolsky, A. V., & McLoughlin, J. R. (1952). Elastoviscous properties of polyisobutylene. V. The transition region. *Journal of Polymer Science*, *8*(5), 543–553. doi:10.1002/pol.1952.120080512

Turbell, H. (2001). *Cone-Beam Reconstruction Using Filtered Backprojection* (Thesis). Linköping University. Retrieved from http://www.diva-portal.org/smash/record.jsf?pid=diva2:302800

Turkulin, H., Holzer, L., Richter, K., & Sell, J. (2005). Application of the ESEM Technique in Wood Research. Part II. Comparison of Operational Modes. *Wood and Fiber Science*, *37*(4), 565–573.

Tynnyi, A. N., Mikitishin, S. I., Velikovskii, A. A., Khomitskii, Y. N., & Kolevatov, Y. A. (1967). Effect of X-rays on the strength of polymethylmethacrylate. *Soviet Materials Science*, *3*(1), 31–33. doi:10.1007/BF00716639

Urquhart, A. R., and Williams A. M. (1924). The moisture relations of cotton: The effect of temperature on the absorption of water by soda-boiled cotton. Journal of the Textile Institute *15*(12), 559

Van den Bulcke, J., Boone, M., Van Acker, J., & Van Hoorebeke, L. (2009). Three-Dimensional X-Ray Imaging and Analysis of Fungi on and in Wood. *Microscopy and Microanalysis*, *15*(5), 395–402. doi:10.1017/S1431927609990419

Van den Bulcke, J., Masschaele, B., Dierick, M., Acker, J. V., Stevens, M., & Hoorebeke, L. V. (2008). Three-dimensional imaging and analysis of infested coated wood with X-ray submicron CT. *International Biodeterioration & Biodegradation*, *61*(3), 278–286. doi:10.1016/j.ibiod.2007.09.004

Vartiainen, I., Mokso, R., Stampanoni, M., & David, C. (2014). Halo suppression in full-field x-ray Zernike phase contrast microscopy. *Optics Letters*, *39*(6), 1601–1604. doi:10.1364/OL.39.001601

Vintila, E. (1939). Studies on density and shrinkage of earlywood and latewood in conifers. *Holz als Roh- und Werkstoff*, *2*(10), 345–357. doi:10.1007/BF02604760

Viola, P. A. (1995). *Alignment by maximization of mutual information* (Thesis). Massachusetts Institute of Technology. Retrieved from http://dspace.mit.edu/handle/1721.1/9918

Virta, J., Koponen, S., & Absetz, I. (2006). Measurement of swelling stresses in spruce (Picea abies) samples. *Building and Environment*, *41*(8), 1014–1018. doi:10.1016/j.buildenv.2005.10.012

Vlassenbroeck, J. (2009). *Advances in laboratory-based X-ray microtomography*. Ghent University, Ghent, Belgium.

Vlassenbroeck, J., Masschaele, B., Cnudde, V., Dierick, M., Pieters, K., Van Hoorebeke, L., & Jacobs, P. (2006). Octopus 8: A High Performance Tomographic Reconstruction Package for X-ray Tube and Synchrotron micro-CT. In J. Desrues, G. Viggiani, & P. Bsuelle (Eds.), *Advances in X-ray Tomography for Geomaterials* (pp. 167–173). London, UK: ISTE.

Wadsö, L. (1988). Bordered pit diffusion. *Report TVBM*. Retrieved from http://www.lunduniversity.lu.se/o.o.i.s?id=24732&postid=1290494

Wahba, G. (1990). *Spline Models for Observational Data*. Society for Industrial and Applied Mathematics. Retrieved from http://epubs.siam.org/doi/book/10.1137/1.9781611970128

Watanabe, U., Norimoto, M., Fujita, M., & Gril, J. (1998). Transverse shrinkage anisotropy of coniferous wood investigated by the power spectrum analysis. *Journal of Wood Science*, *44*(1), 9–14. doi:10.1007/BF00521868

Weitkamp, T., Haas, D., Wegrzynek, D., & Rack, A. (2011). ANKAphase : software for single-distance phase retrieval from inline X-ray phase-contrast radiographs. *Journal of Synchrotron Radiation*, *18*(4), 617–629. doi:10.1107/S0909049511002895

Wildenschild, D., Vaz, C. M. ., Rivers, M. L., Rikard, D., & Christensen, B. S. B. (2002). Using X-ray computed tomography in hydrology: systems, resolutions, and limitations. *Journal of Hydrology*, *267*(3-4), 285–297. doi:10.1016/S0022-1694(02)00157-9

Wimmer, R., & McLaughlin, S. B. (1994). Possible relationships between chemistry and mechanical properties in the microstructure of red spruce xylem. In *Tree-Rings, Environment and Humanity: Proceedings of the International Conference.* Tucson, Arizona, *114*(G1), 659-668.

Wyawahare, M. V., Patil, P. M., Abhyankar, H. K., & others. (2009). Image registration techniques: an overview. *International Journal of Signal Processing, Image Processing and Pattern Recognition*, *2*(3), 11–28.

Yao, J. (1969). Shrinkage properties of second-growth southern yellow pine. *Wood Science and Technology*, *3*(1), 25–39. doi:10.1007/BF00349982

Zabler, S., Rack, A., Manke, I., Thermann, K., Tiedemann, J., Harthill, N., & Riesemeier, H. (2008). High-resolution tomography of cracks, voids and micro-structure in greywacke and limestone. *Journal of Structural Geology*, *30*(7), 876–887. doi:10.1016/j.jsg.2008.03.002

Zamyatin, A. A., Taguchi, K., & Silver, M. D. (2005). Helical cone beam CT with an asymmetrical detector. *Medical Physics*, *32*(10), 3117. doi:10.1118/1.2047784

Zauner, M., Keunecke, D., Mokso, R., Stampanoni, M., & Niemz, P. (2012). Synchrotron-based tomographic microscopy (SbTM) of wood: development of a testing device and observation of plastic deformation of uniaxially compressed Norway spruce samples. *Holzforschung*, *66*(8), 973–979. doi:10.1515/hf-2011-0192

Zhuang, X., Rhode, K. S., Razavi, R. S., Hawkes, D. J., & Ourselin, S. (2010). A Registration-Based Propagation Framework for Automatic Whole Heart Segmentation of Cardiac MRI. *IEEE Transactions on Medical Imaging*, *29*(9), 1612–1625. doi:10.1109/TMI.2010.2047112

Zillig, W. (2009). *Moisture transport in wood using a multiscale approach* (Thesis). Katholieke Universiteit Leuven. https://lirias.kuleuven.be/handle/123456789/233941